Physical properties of Fe-C-S and Fe-S alloys under planetary core condition

Bin Zhao

Sorbonne Université

Ecole doctorale: Ecole Doctorale 397 - Physique et Chimie des Matériaux

Physical properties of Fe-C-S and Fe-S alloys under planetary core conditions

Par Bin ZHAO

Dirigée par Daniele ANTONANGELI et Guillaume MORARD

Présentée et soutenue publiquement le 2 décembre 2022

Devant un jury composé de :

Mme. Nathalie Bolfan-Casanova	Directrice de recherche CNRS - Université Clermont-Auvergne	Rapporteuse
M. Dan Frost	Professor - University of Bayreuth	Rapporteur
Mme. Nadege Hilairet	Chargée de recherche CNRS - Université de Lille	Examinatrice
M. Mark Wieczorek	Directeur de recherche CNRS - Université de la Côte d'Azur	Examinateur
Mme. Livia Bove	Directrice de recherche CNRS - Sorbonne Université	Examinatrice
M. Nicolas Rambaux	Maître de conférences - Sorbonne Université	Examinateur
M. Guillaume Morard	chargé de recherche CNRS - Université Grenoble Alpes	Directeur de thèse
M. Daniele Antonangeli	directeur de recherche CNRS - Sorbonne Université	Directeur de thèse

Abstract

Planetary space missions are fundamental to improve our understanding of the deep interiors of the terrestrial planets and moons. Fostered by an increased amount of geophysical observations, advance models have been put forward concerning structure and dynamics of their iron-rich core. To this end, experimental data on the properties of Fe-alloys at relevant pressure and temperature conditions are much needed.

The Moon is the closest terrestrial body to the Earth, and also the most well constrained thanks to the numerous space missions, including landers and orbiting spacecrafts. However, if current models are in overall good agreement for what concerns the crust and the mantle (at depth less than 1200 km), large discrepancies and uncertainties remain for the core region. Regarding core's composition, sulfur and carbon are considered the two most abundant light elements in the Moon's core but, given the lack of knowledge of Fe-C-S alloy's properties, the core of the Moon is generally modeled as either a binary Fe-S or Fe-C. This work aimed at overcoming this limitation by providing the necessary dataset to discuss the properties of the Moon's core on the basis of the ternary Fe-C-S system. Local structure and density of liquid Fe-C-S alloys were studied *in situ* by X-ray diffraction and absorption experiments up to 5 GPa and at temperatures between 1600 K and 1900 K. Miscibility of liquid Fe-C-S alloys was studied by quench experiments between 2 and 6 GPa at 1650 K and 2000 K, respectively. The obtained data were employed to build a thermodynamic model of the density of liquid Fe-C-S alloys as a function of pressure, temperature, and light element content. This model, together with information on the miscibility gap, are used to discuss the light element content in the Moon's core.

Moving further out in the solar system, among the Galilean satellites of Jupiter, Europa, Io, and Ganymede are considered highly differentiated. With limited information available, their cores were considered to be composed of an Fe-S alloy. Fe_3S_2 was suggested as a potential solid phase forming by secular cooling of the S-rich liquid core, but its structure, lattice parameters, and stability limits were unknown. As such, as part of this PhD work, the properties of Fe-S compounds were studied by in situ X-ray diffraction from 11 to 15 GPa and from room temperature to melting. Stability field of Fe_3S_2 and its structural properties were determined, which indicate that Fe_3S_2 is unlikely to be present in the core of Europa, Io, or Ganymede, but that it could form upon crystallization of S-rich Fe-S liquid cores in the range 12 to 20 GPa.

Content

Chapter 1 Liquid iron alloys in the context of planetary cores

1.1 Terrestrial planets and their metallic cores

The four inner planets of the solar system, i.e. Mercury, Venus, Earth and Mars are called terrestrial (or telluric) planets because they possess an Earth-like differentiated internal structure composed of a central metallic core surrounded by a silicate mantle, and a thin, chemically differentiated crust. Other planetary bodies of the Solar system, such as the dwarf planets Ceres and Pluto, or satellites such as the Moon (the only natural satellite of the Earth), Deimos and Phobos (satellites of Mars) or Io (satellite of Jupiter) are also considered to have a terrestrial structure. Several exoplanets such as Corot 7b or Gliese 581g are also expected to have an Earth-like structure, but being larger and more massive, are generally referred to as Super-Earths. Terrestrial planets share not only a similar inner structure but also an overall comparable core composition – iron alloyed with nickel and lighter elements, which could include H, C, S, O, Si.

As this PhD thesis aims at the study of iron alloys at pressure and temperature conditions directly relevant for small-sized planetary bodies, the case of the Moon and the telluric satellites of Jupiter will be addressed with some more detail below.

1.1.1 The Moon

As today, the Moon is believed to have formed by a large off-center (not center-targeted) collision of a Mars-sized planetary body (also called Theia) to the proto-Earth 4.5 billion years (Ga) ago, called the Giant Impact hypothesis (Cameron and Ward, 1976; Hartmann and Davis, 1975). This hypothesis didn't prevail over the other three traditional ideas (fission (Wise, 1963), capture (Singer, 1970), and binary accretion (Herbert et al., 1986)) until the Conference on the Origin of the Moon in 1984. There are two major lines of evidence that support this idea: (i) the Earth-Moon system possesses a significantly high angular momentum compared to the other terrestrial planets, the energy of which could be accounted for by a giant impact (Cameron, 2001; Canup and Asphaug, 2001); (ii) the identical isotopic ratio of Moon and Earth, which indicates a common origin (Lugmair and Shukolyukov, 1998; Wiechert et al., 2001; Touboul et al., 2007; Zhang et al., 2012;

Mougel et al., 2018). Due to the high energy of the collision, the Moon was largely molten at the beginning of its formation, with a thick magma ocean (up to 1000 km) (Elkins-Tanton et al., 2011). During the following tens of million years, the plagioclase floated up to the surface and crystallized, finally forming the crust (Elkins-Tanton et al., 2011; Lin et al., 2017), while the progressive solidification of the deep lunar magma ocean makes up the mantle. Paleomagnetic and tungsten isotopic studies suggest the metallic core have formed a few hundred million years later (Runcorn, 1996; Touboul et al., 2007). The differentiated three-layer model consisting of crust, mantle, and core, similar to the Earth, has been accepted as the most basic structure of the Moon (Fig 1.1).

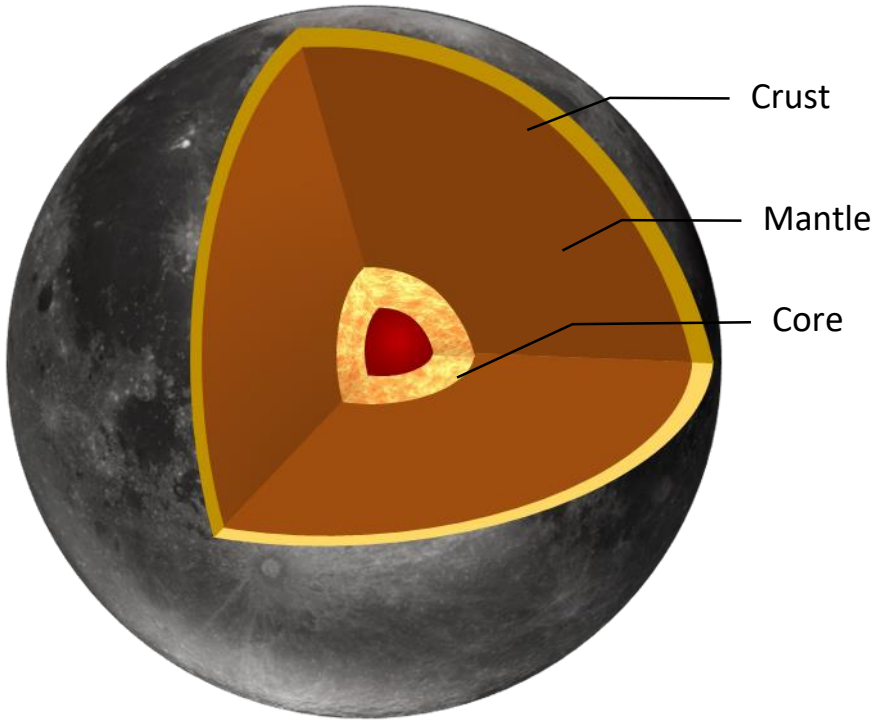

Fig. 1.1 The widely accepted three-layer model of the Moon's internal structure. The dark red area represents a potential inner core.

The rapid development of space technology in the second half of the past century led to a gain in the knowledge of the Moon's internal structure at an unprecedentedly high rate. On 4 October 1959, the Soviet Luna 3 spacecraft first achieved to photograph the surface of the far side of the Moon, which was a milestone in lunar exploration history. During the following tens of years, intensive lunar programs were carried out, by which plenty of soil samples were returned to Earth

(Papike et al., 2018; Qian et al., 2021), considerable geodetic (e.g. Konopliv et al., 1998; Williams et al., 2014) and topographic (Qian et al., 2021) data were collected by orbiting spacecrafts, and, numerous moonquakes (Nakamura et al., 1973 and 1974) were recorded by the seismometer network installed during Apollo missions. Integrating all the independent observables and extensive information permitted to propose an overall internal structure of the Moon, with some physical properties — such as density, sound velocity, and depth of interfaces— directly obtained for each of the basic layers (Tompkins and Pieters, 1999; Gagnepain-Beyneix et al., 2006; Khan et al., 2014; Garcia et al., 2019). Fig 1.2 shows a summary made by Garcia et al., (2019) of the density, compressional and shear wave velocities as a function of depth according to selected studies. As quite evident, the current models are in good agreement for what concerns the Moon's crust and mantle (at depth less than 1200 km), but large discrepancies and uncertainties remain for the core region. As indicated by the shear sound velocity, in some models the core is fully molten, while in others it has a solid inner core (shears waves do not propagate in liquids). This depends on the way the models are built, which in turn implies that the current observables, although the more and more accurate, are not yet enough to allow establishing a unique Moon's model. In particular, the density, ranging from ~4 to 8 g/cm^3 in the deepest area, would relate to significant differences in the possible compositions.

Recently, we are witnessing a renewed interest for the exploration of the Moon, with numerous robotic and crewed lunar missions proposed or under development by various countries, and *in primis* the NASA Artemis program [https://www.nasa.gov/specials/artemis/] and Chang'E 6 by CNSA. Further observations and further data are expected to come providing further constraints on current understanding of lunar formation, structure and evolution.

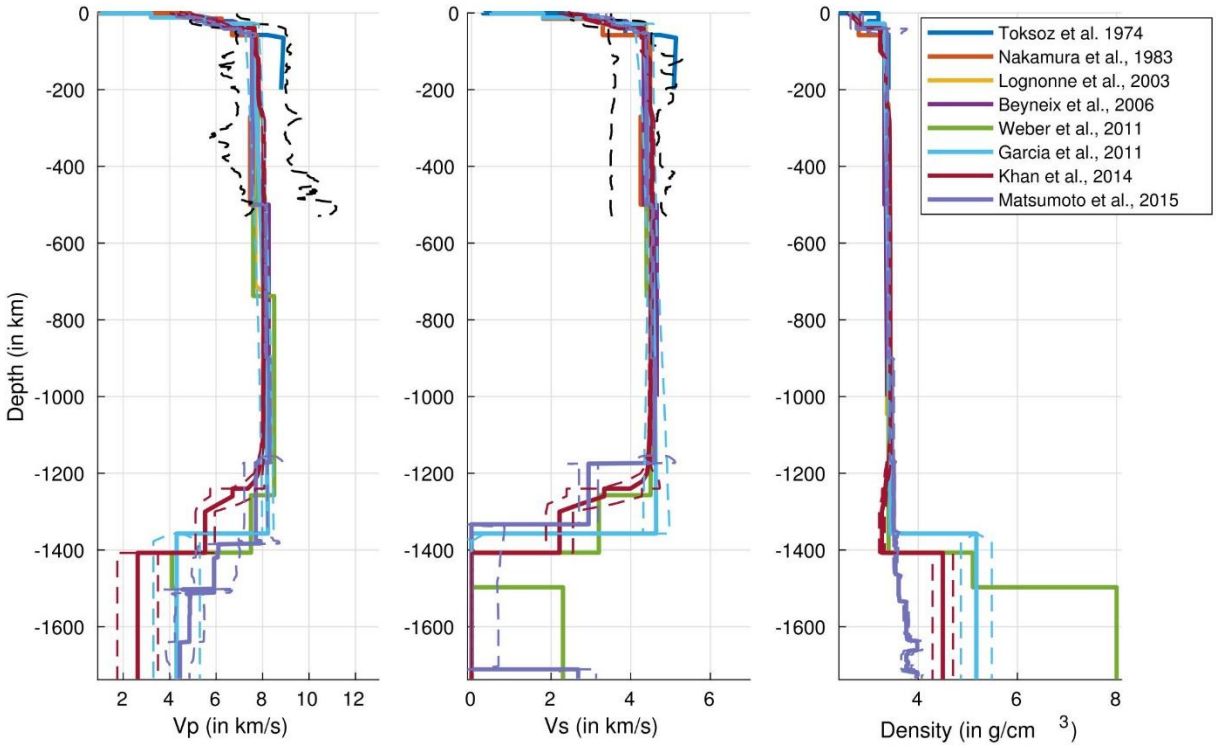

Fig. 1.2 Compressional and shear sound velocity and density as a function of depth within the Moon according to various models. The dash lines represent the uncertainties where available. The black dashed curves in the first 500 km range indicate the sound velocity contours with highest probability density extracted from Khan and Mosegaard, 2002. The figure is from Garcia et al. (2019).

Focusing on the Moon's core, primary object of interest in this thesis, discrepancies exist regarding its physical properties (e.g. Hood et al., 1999; Weber et al., 2011; Viswanathan et al., 2019; Nakamura et al., 1973 and 1974) and chemical composition (e.g. Steenstra et al., 2017a and 2017b). The absence of clear detection of seismic waves passing through the core argues for the fact that a fluid region exists in the deep interior (Nakamura et al., 1973). Combining the electro-magnetic sounding data (Hood et al., 1999) with the fact that the lunar samples from the surface are iron-depleted (Lucey et al., 1995), the notion that the core consists of mainly iron is now largely accepted, but the possible existence of a solid inner core, as suggested by some seismic studies (Weber et al., 2011) remains unconfirmed, and not favored by analysis of the moment of inertia (Williams et al., 2014; Morard et al., 2018). On the other hand, the paleomagnetic studies show the existence of a global magnetic field up to 3.6 Ga ago (Cisowski et al., 1983), with a strength of the order of 100 mT (Fuller and Cisowski, 1987), and a plausible mechanism accounting for this is a long-term core dynamo (Stevenson et al., 1983) sustained by the growth of a solid inner

core (Laneuville et al., 2014; Mighani et al., 2020). Since the core dynamo was considered to cease sometime between 1.92 and 0.8 Ga ago by analyzing the Apollo breccias (Mighani et al., 2020), other mechanisms accounting for the core dynamo have been thought less possible, due to the less sustainability. For instance, thermal convention would sustain a core dynamo only until ~3.5 Ga ago (Laneuville et al., 2014), and a dynamo driven by mantle precession is able to persist until sometime between ~3.4 and 2.0 Ga (Dwyer et al., 2011).

Thanks to the lunar missions carried out during the past three decades (e.g. Lunar Laser Ranging, Viswanathan et al., 2019; Dickey et al., 1994 and GRAIL, Wieczorek et al., 2013; Williams et al., 2014), planetary data (including mass, gravity, mean density, and mean moment of inertia) have been obtained with unprecedented accuracy, allowing improved geodetic constraints. Regarding the core, a few consensuses have been reached: (1) The mean core density, needed to account for the measured moment of inertia, is below that of pure iron; (2) Sulfur (Laneuville et al., 2014; Rai and Westrenen 2014) and carbon (Steenstra et al., 2017b) have been widely considered as two major candidates incorporated with iron in the Moon's core, because of their effectiveness in decreasing the density (Morard et al., 2018; Xu et al., 2021) and the melting point of pure iron (Buono and Walker, 2011; Fei and Brosh, 2014), as well as of their high solubility in iron (Morard et al., 2018; Fei and Brosh, 2014); (3) The core radius has been restrained to a relatively narrow range from ~340 km to ~400 km by electromagnetic sounding (Hood et al., 1999) and seismic and geodetic data inversion (Garcia et al., 2019), with few studies pushing the uncertainties down to almost 10 km (e.g. Viswanathan et al., 2019).

1.1.2 Galilean Satellites of Jupiter

Jupiter, with its four Galilean satellites, Europa, Io, Ganymede, and Callisto, has been long thought of as a 'miniature solar system'. These satellites were considered to have formed by condensation and accretion in the subnebula around Jupiter, similar to the solar system (Pollack and Fanale, 1982), while their internal structure was not really constrained until measurements of gravity and magnetic field by the Galileo spacecraft, starting 1995. The four satellites have a comparable size, with radii ranging from R=1565 km for Europa to 2631 km for Ganymede, with the central pressure ranging from ~6 GPa to ~10 GPa. Among the four bodies, Europa, Io, and Ganymede are believed to be differentiated, possessing a rocky mantle and a metallic core, shown in Fig. 1.3.

Although the gravity constraints require the existence of denser cores likely made of iron alloys for Europa, Io, and Ganymede, their chemical composition and states remain unknown. Sulfur was always favored as light element, when not considered as the only light element for discussions and modelling. For example, Anderson et al. (1998) assumed that the core size of Europa could account for 50% of its radius if the core is composed of a binary Fe-FeS alloy at the eutectic composition. Later on, Anderson et al. (2001) provided two core models for Io: the radius would be either 550~900 km for a core made by eutectic Fe-FeS, or 350-600 km for a core made by pure Fe. Almost all the current models of the Galilean satellites have been established on the basis of data reported by the Galileo and Voyager missions and are relatively simple, with many properties far from being well understood. The launch of the JUpiter ICy moons Explorer (JUICE) mission by the European Space Agency in planned in 2023. One of the objectives of this mission is to probe the gravity field of Europa, Ganymede and Callisto, allowing for an improved understanding of their internal mass distribution and hence of the internal structure of these potentially highly differentiated planetary bodies.

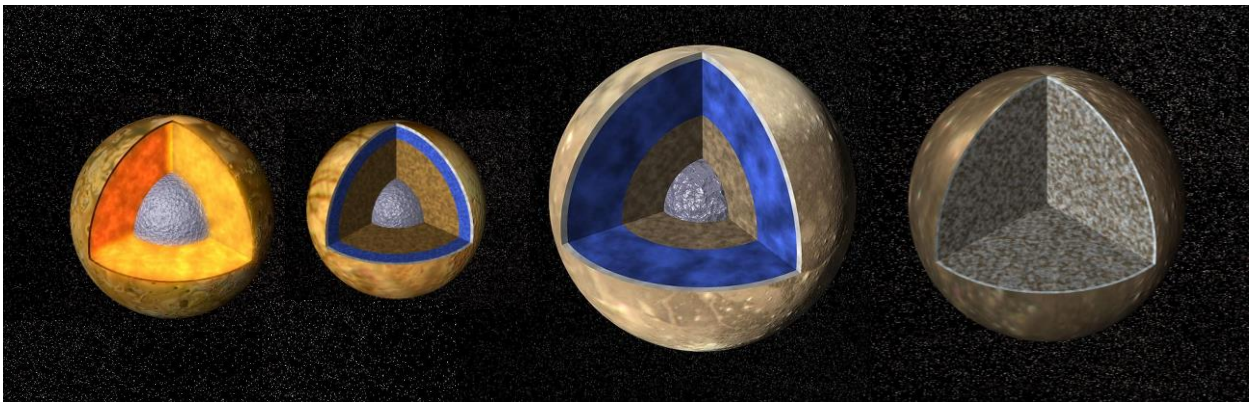

Fig. 1.3 Internal structure of the Galilean satellites, Io, Europa, Ganymede, and Callisto from left to right, rescaled with respect to their actual sizes. Figures are from Jet Propulsion Laboratory, NASA [https://www.jpl.nasa.gov/images]. A metallic core distinct from the mantle is visible for Io, Europa, and Ganymede (central sphere), while the interior of Callisto is a mixture of rocks, metal, and ice. Europa and Ganymede have a water shall (blue layer), with an unknown liquid water – ice ratio, located at an undefined depth.

Sulfur is always favored as the main light element in the core of those outer-solar-system planetary bodies due to a more oxidized environment. If sulfur is the only light element, or account for a

large proportion of the light elements incorporated in their cores, knowledge of the phase diagram of the Fe-S system at pertinent pressures is critical to model crystallization and assess the stable solid phases. In fact, several solid phases intermediated between Fe and FeS, such as Fe_3S_2 and Fe_3S, have been reported to be stable at pressures of direct relevance for the cores of the Galilean satellites of Jupiter, while exact phase boundaries and physical properties are not clear. On one hand, the precise transition conditions for these intermediate phases determine whether they would be produced during the core crystallization. On the other hand, once one or more intermediate phases form during the core crystallization, their physical properties would be key information for understanding the core properties.

1.2 State of art of the properties of the iron alloys at pertinent conditions

Since iron and iron alloys are the main candidates for the core constituents of terrestrial planetary body, there have been a large amount of studies concerning the high-pressure and high-temperature (HP-HT) physical properties (phase diagram, melting curve, density, sound velocity and thermo-elasticity of solid and liquid phases, etc.) of binary iron alloys, i.e. iron with light elements such as O, Si, S, and C (e.g. Morard et al., 2007) , and, to a less extent, on ternary iron alloys such as Fe-C-S and Fe-O-S (e.g. Tsuno et al., 2007) at conditions relevant for small- and middle-sized bodies.

Here the melting curve and the physical properties of liquid Fe-S, Fe-C, and Fe-C-S will be reviewed.

1.2.1 Phase diagram and melting curve

All the terrestrial planets are expected to have experienced extensive melting during their formation and differentiation, and, depending on their thermal history, they might have crystallized (or will crystallize in the future) a solid core. The Earth has been proved to possess a solid inner core while there is not yet firm evidence for the core status of other terrestrial planetary bodies. Therefore, the melting curves (liquidi and solidi) of iron alloys, especially on the Fe-rich side, are important information to help restrain the core status (estimating the temperature) or temperature

(estimating the status). The knowledge of the slope of the solidus, in comparison to the adiabatic gradient is also of primary interest, as this controls the crystallization regime.

As the occurrence of melting can be detected by observation of the texture of recovered samples, in principle, experiments devoted to melting measurements could be simply carried out with a pressure - and temperature - generating device, and melting curves can be precisely determined if the P-T conditions are well constrained by reliable calibrations, without requiring more complex *in situ* experiments. Accordingly, the booming of high-pressure techniques has led to the publications of a considerable amount of data on Fe-C, Fe-S and Fe-C-S melting relations at high pressure since 1970s.

The first high-pressure melting experiments for Fe-S was conducted in a single stage apparatus by Brett and Bell, 1969. The phase diagram at 3 GPa has been determined by analyzing the recovered samples. With the rapid development of multi-anvil apparatus and other high pressure devices, more results have been published (e.g. Usselman, 1975). The experimental results on the eutectic melting of Fe-FeS is summarized in Fig.1.4. Large discrepancies among existing studies could be explained by large uncertainties on the temperature determination, in particular in the in early experiments. The Fe-FeS binary phase diagram was studied by Fei et al. (1997 and 2000) over an extended pressure range, revealing a peculiar evolution of liquidus with respect to pressure up to 20 GPa, and several intermediate Fe-S compounds at high pressures (Fig 1.5). Buono et al. (2011) conducted melting experiments at 6 GPa and established a thermodynamic model by integrating all the available melting data. As today, a great number of works have been dedicated to the melting properties of the Fe-FeS system under moderate pressure. However, discrepancies still remain, especially for the data with opposite trends below 15 GPa. While most early studies suggest a constantly increasing melting temperature with pressure, some later work by Fei and Morard found the melting temperature decrease with pressure below 15 GPa followed by an increase at higher pressure. Errors on the temperature may be attributed to different measurement techniques.

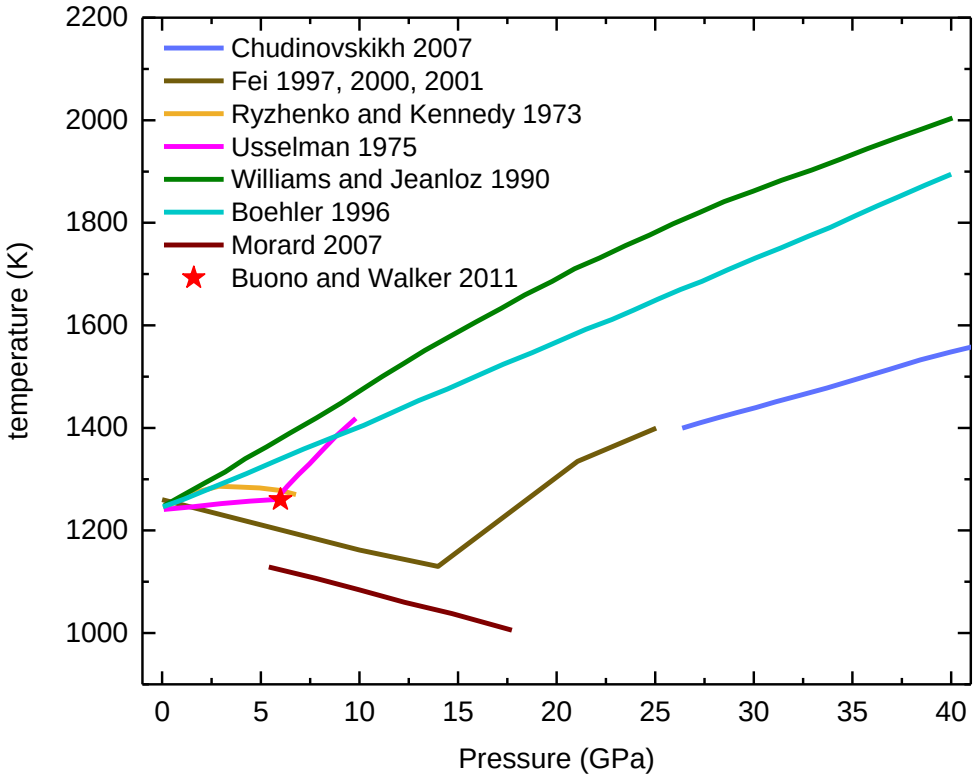

Fig. 1.4 Eutectic melting temperature of Fe-FeS at pressures below 40 GPa. All the curves are interpolated from experimental data. discrepancies are visible in the various studies and often related to the different methods. For instance, temperature is determined by the Planck's radiati function for DAC (Diamond Anvil Cell) experiments in Boehler, 1996, and by thermocouples in a large-volume device Usselman, 1975.

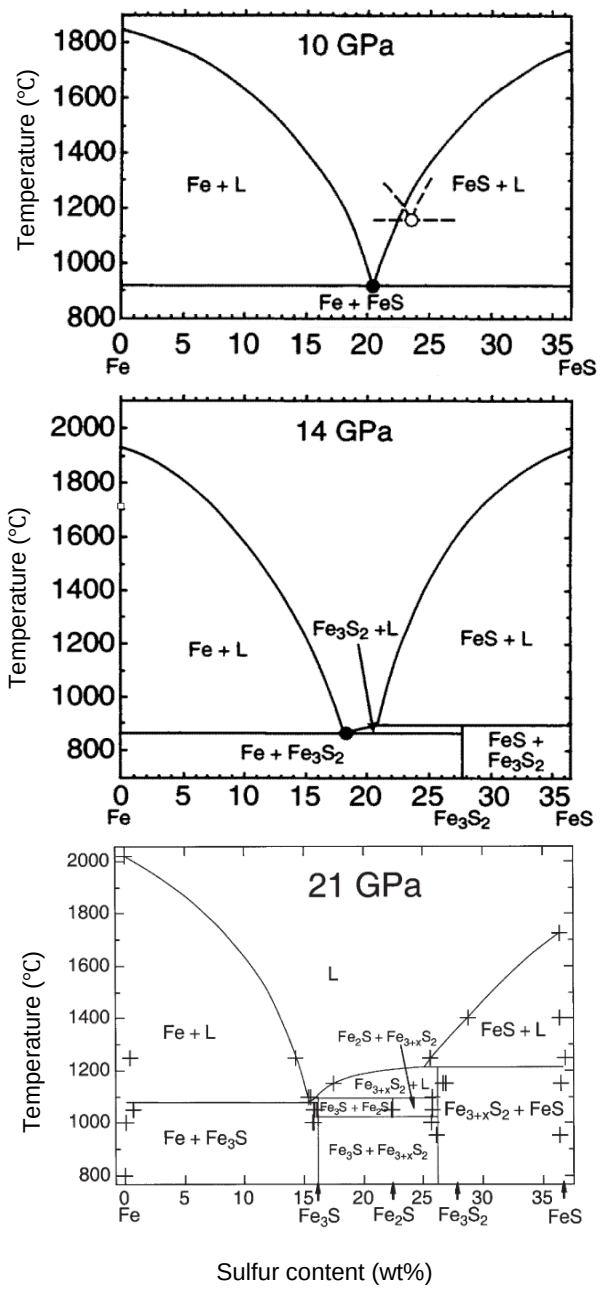

Fig. 1.5 The phase diagram of Fe-FeS under moderate pressures. Plots are from Fei et al. (1997 and 2000). The Phase diagrams of Fe-S were studied by in-situ X-ray diffraction at 10 GPa and 14 GPa, and by analyzing the recovered samples for the 21 GPa runs. The eutectic melting temperature was found to have a minimum at 14 GPa. It's worth stressing that above 14 GPa, an intermediate Fe-S compound stabilizes at high temperature as highlighted by the new peaks in diffraction pattern. This new phase was afterward identified as Fe_3S_2 by microprobe analysis. Above 21 GPa, one more intermediate Fe-S compound, Fe_3S was discovered by the analysis on the recovered samples.

The first study on phase diagram of Fe-C under pressure was conducted two years after that of Fe-S (Strong and Chrenko, 1971), and reported a marked increase of the melting temperature with pressure. More results concerning the melting relation have been reported since 1990s (e.g. Hirayama et al.,1993; Chabot et al., 2008). Systematical studies on the evolution of the phase diagram with pressure was conducted by Nakajima et al. (2009), with a specific focus on C-rich side, and by Fei and Brosh. (2014), covering the pressure range from 5 GPa to 20 GPa. These results are shown in Fig.1.6.

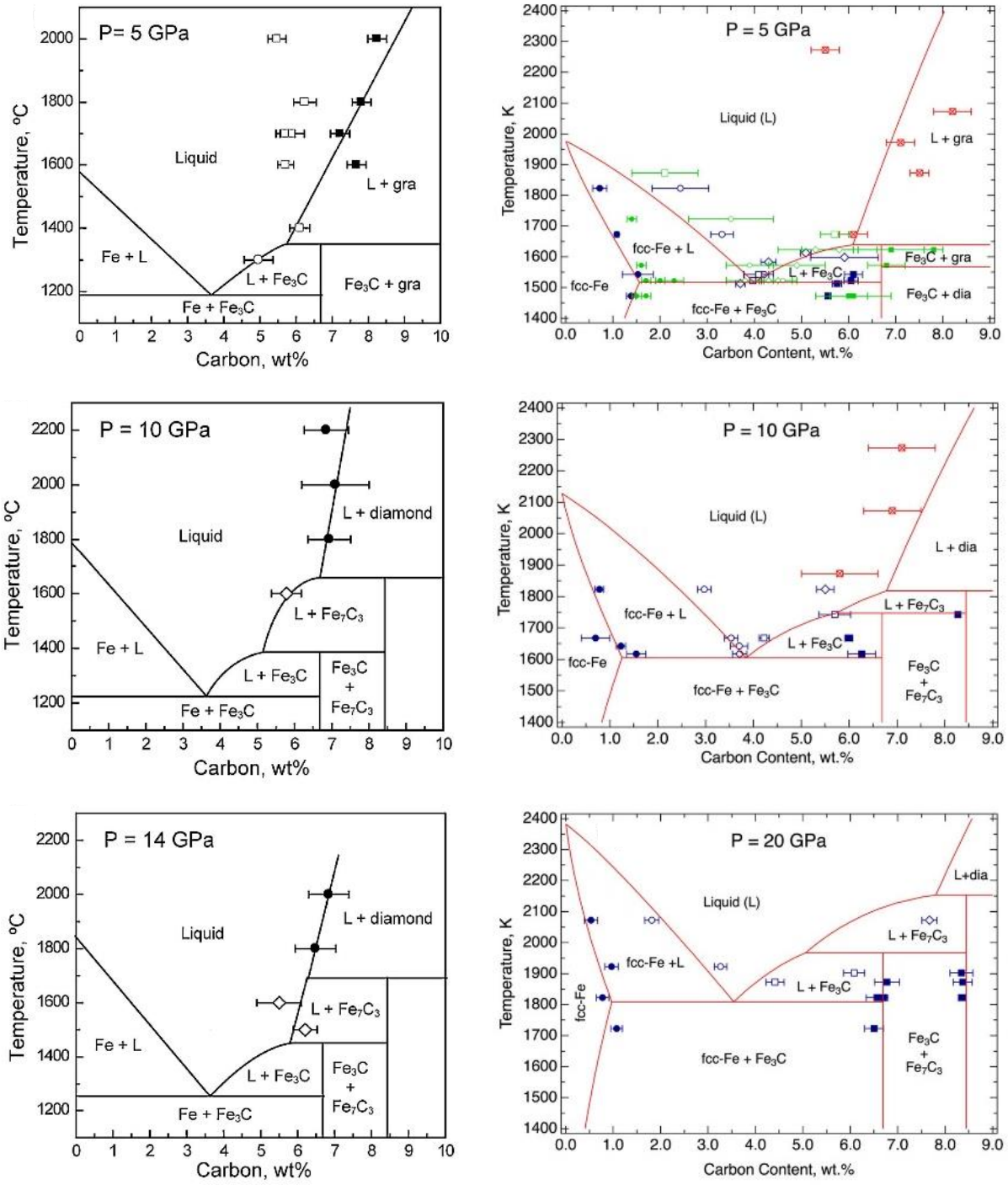

Fig.1.6 Phase diagrams of Fe-Fe10wt%C in the 5-20 GPa range. Images are from Nakajima et al. (2009) (left column) and Fei and Brosh (2014) (right column). Note that Nakajima's results contain only their own data on C-rich side of Fe-C, while the phase diagrams of Fei are thermodynamic models based on their experimental data at 5 GPa (green), the data of Nakajima et al. (2009) (red), and Chabot et al. (2008) (dark blue).

Similar to Fe-FeS, the phase diagram and melting relations of Fe-C are thus well constrained. Conversely, the data on the melting relations in the ternary Fe-C-S remain limited, mainly due to the complexity of the ternary system. There are only a few published studies on the melting of Fe-C-S. Two starting compositions on C-rich side, Fe-5 wt%C-5 wt%S (hereafter referred to as 'Fe-5C-5S') and Fe-5C-15S were studied by Dasgupta et al. (2009), showing that an iron carbide, Fe3C or Fe_7C_3 depending on the pressure, is the only solid phase just below the liquidus. The solidus and liquidus of the two compounds were interpolated from 2 to 6 GPa and are shown in Fig. 1.7. Later on, the melting of four more compounds was reported in the pressure range of 3.5-20 GPa (Deng et al., 2013). For the two C-poor samples, the first crystallizing phase was found to be metallic Fe instead of iron carbide. These results indicate that carbon content still plays a significant role in the crystallization regime of liquid Fe-C-S. However, data are still spurious to determine the eutectic melting or the liquidus surface for the ternary at pertinent pressures for planetary cores.

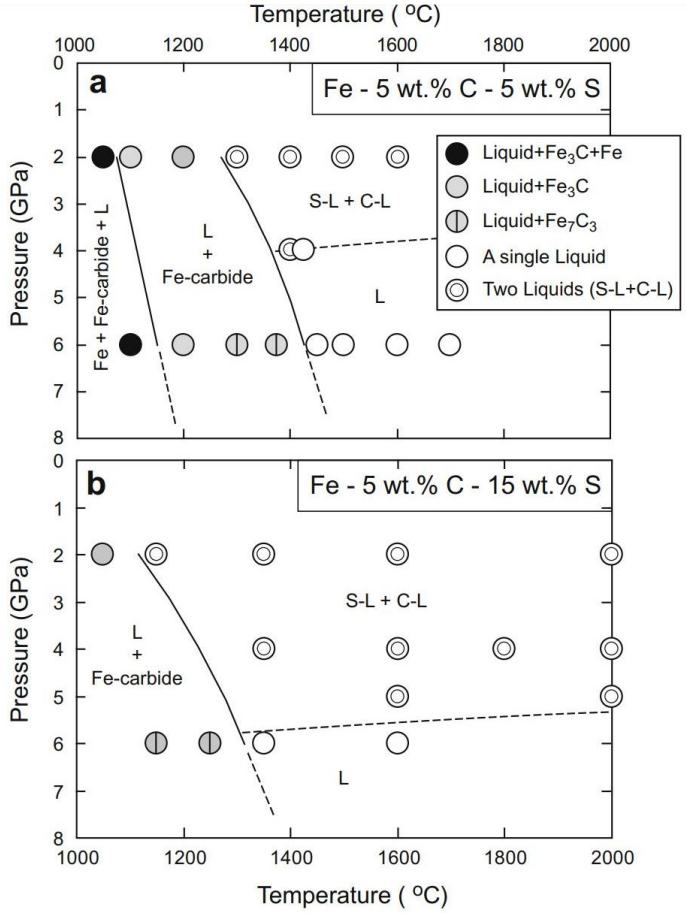

Fig 1.7 Melting relationships of Fe-5C-5S and Fe-5C-15S. The plot is from Dasgupta et al. (2009). Solid lines and dashed lines are inferred boundary for different phases. The two-liquid areas indicate the C-rich and S-rich liquids are immiscible at low pressure.

1.2.2 Density of the liquid phase

Early studies have focused on the density of liquid iron and some binary iron alloys at ambient pressure. Density of liquid iron has been intensively studied by various methods, and the values with the methods at 1550 ℃ are summarized in table 1.1. A part of the experimental data for liquid iron were integrated and examined by Assael et al. (2006) to build a standard, shown in Fig. 1.8.

Table 1.1 Density of liquid iron at 1550 ℃ from literature

References	Measurement method	Density (kg/m^3)
Hixson et al., 1990	Sessile drop	6970
Jimbo and Cramb, 1993	Sessile drop	7124
Vertman et al., 1964	Sessile drop	7020
Lucas, 1960	Maximum bubble pressure	7020
Frohberg and Weber., 1964	Maximum bubble pressure	7060
Dragomir et al., 1964	Maximum bubble pressure	7000
Saito et al., 1969	Maximum bubble pressure	7030
Kirshenbaum and Cahill, 1962	Archimedean	7000
Morita et al., 1970	Archimedean	7130
Lucas, 1972	Archimedean	7170
Adachi et al., 1970	Levitation	6950

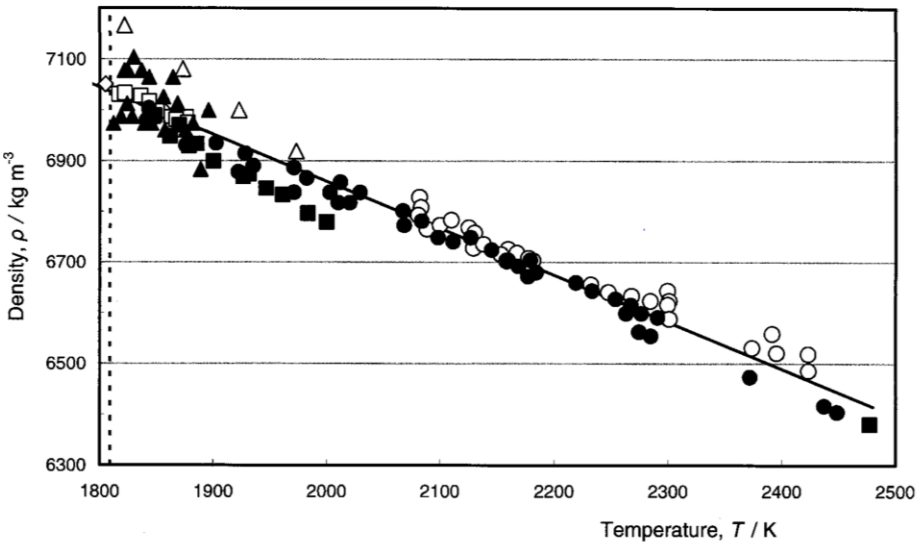

Fig. 1.8 Density as a function of temperature (the solid curve) at ambient pressure made by Assael et al. (2006). Discrete data are from experiments. Open rhombuses: Brillo and Egry, 2004; Open squares: Sato, 2003; Open triangles: Lucas, 1972; Open circles: Saito et al., 1969; Closed squares: Lucas, 1960; Closed triangles: Frohberg and Weber, 1964; Closed circles: Kirshenbaum and Cahill, 1962.

The density of liquid Fe-S at 1900 K as a function of sulfur content at ambient pressure was summarized by Morard et al. (2018), shown in Fig. 1.9. The thermodynamic model built in this study (the solid curve) is in good agreement with the experimentally determined results of Nagamori et al. (1969) and that from molecular dynamics simulations of Kuskov et al. (2006), but large discrepancies are indicated compared to the *ab initio* calculations (Jing et al., 2014; Nishida et al., 2016). The results of Nishida et al. (2016) were extrapolated from 4 GPa, so a deviation could happen. The density of Jing et al. (2014) was calculated from elastic parameters, which could generate large uncertainties due to the transmission error.

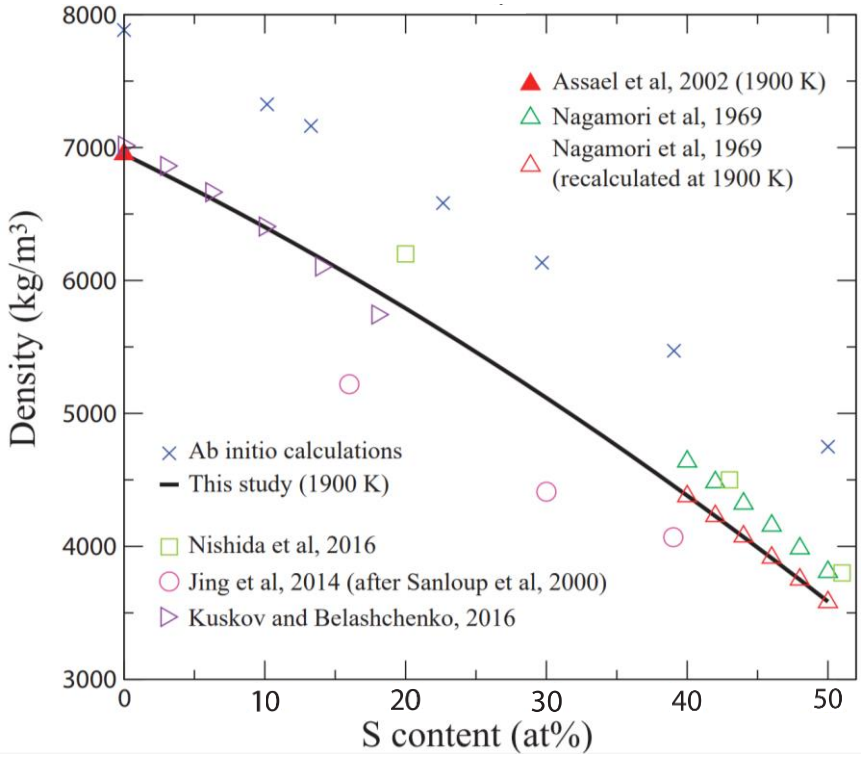

Fig. 1.9 Ambient-pressure density of liquid Fe-S alloys as a function of sulfur content at 1900 K. The plot is made by Morard et al. (2018). The solid curve is thermodynamic model built with pure-iron data from Assael et al. (2006) and S-rich liquid data from Nagamori et al. (1969).

Regarding the density of liquid Fe-C alloys at ambient pressure, a study has measured the density of a series of iron-graphite mixtures from melting using the sessile drop method (Jimbo and Cramb, 1993). With the volumes of the drop determined by the symmetry, the liquid density was extracted at each temperature stage, and a density function of temperature and carbon content was thus built with the experimental results.

When it comes to high pressures, the measurement of liquid density has been for long time, and to certain extent still today, extremely challenging due to the significant technical difficulties. Especially for pure iron, the density at high pressure or the equation of state has never been directly determined by experiments, because of not only the technical challenges, but also the fact that the purity of liquid iron is strongly affected by the surrounding materials of the high pressure assemblies. For iron alloys, liquid densities at high pressure were mainly obtained from the equation of state with experimentally-determined zero-pressure bulk modulus and its inferred derivative to pressure (e.g. Stolper et al., 1981), and by molecular dynamics simulations (e.g. Woodcock et al, 1976) before 2000s. Regarding the experimental approaches, the 'sink/float' method was the most effective way of measuring the liquid density under pressure, bracketed between the densities of the sinking/floating markers placed in the sample capsule. This method was originally employed for silicate melts (e.g. Herzberg et al., 1982), and improved by Balog et al. (2001 and 2003), and first applied to liquid Fe-10S. More recently, the density of a series of Fe-S compounds was measured by the same method (Nishida et al., 2008).

With the emergence of third generations of synchrotron radiation sources, various techniques combining high-brilliance X-rays with various high-pressure apparatus have become available, and since then, measurements of liquid densities of iron alloys have seen a booming. For instance, using the *in-situ* X-ray absorption method, the density of Fe-10S, Fe-20S, and Fe-27S was studied from 1.5 GPa to 6.2 GPa and 1500 K to 1780 K (Sanloup et al., 2000) and the density of liquid FeS was measured up to 3.8 GPa and 1800 K (Nishida et al., 2011). Later on, *in situ* X-ray diffraction has also been employed to measure the liquid density. Fe-S with various S content was studied below 10 GPa by Morard et al. (2018) and Xu et al. (2021). In Morard et al. (2018), an equation of state and a mixing model were developed to determine the density as a function of S content and pressure. Xu et al. (2021) proposed models for thermal expansion coefficient as a function of S content. A summary of developed models and selected datasets of the Fe-S system

is illustrated in Fig. 1.10. While data still show some scattering, the effect of S is overall well accounted by the models, and the incorporation of sulfur into liquid iron has been proven to considerably decrease the density of the alloy.

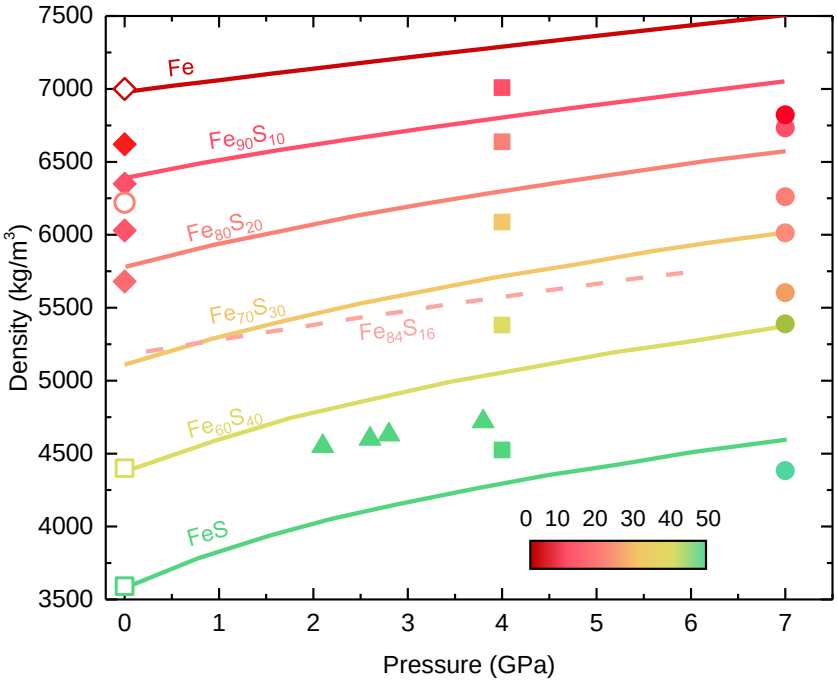

Fig.1.10 Density of Fe-S liquids as a function of pressure around 1900K. The solid curves equations of state of $Fe_{90}S_{10}$, $Fe_{80}S_{20}$, $Fe_{70}S_{30}$, $Fe_{60}S_{40}$, and FeS at 1900 K obtained fitting the experimental data by Morard et al. (2018). The dash curve is a EOS of $Fe_{84}S_{16}$ at 1770 K by Sanloup et al. (2000). Solid squares, and triangles are experimental data from Nishida et al. (2008 and 2011), respectively. Solid circles are obtained by interpolation or extrapolation of the experimental data of Xu et al. (2021). Zero-pressure data are from Assael et al. (2006) (open rhombus), Kuskov and Belashchenko (2016) (solid diamonds), Nagamori et al. (1969) (open squares), and Nishda et al. (2016) (open circle), which have been corrected to 1900 K. The sulfur content is color-coded (see color bar in the graph).

Studies on density of liquid Fe-C alloys appeared after those on Fe-S, and, with the exception of Morard et al. (2017), all the data are from *in-situ* X-ray absorption experiments. Terasaki et al. (2010) employed Fe_3C powder as starting material, and obtained the liquid density up to 9.5 GPa and 1973 K. Although the error bars are large, these are the first results published for Fe-C. Fe-5.7C and Fe-3.5C were later on studied by Sanloup et al. (2011) and Shimoyama et al. (2013) up to 7.8 GPa and 6.8 GPa. In particular, the temperature dependence of the density was determined by Shimoyama et al. (2013) from 1500 K to 2200 K. All the published data for Fe-C around 1900

K together with that of pure liquid Fe are summarized in Fig 1.11. Compared to sulfur, carbon has a smaller effect on the density of liquid iron. Noteworthy, a phase transition of Fe-C liquids was observed around 5 GPa by a density leap (Shimoyama et al., 2013), and afterwards supported by a subtle structure change (Shibazaki et al., 2015; Chen and Wang, 2020).

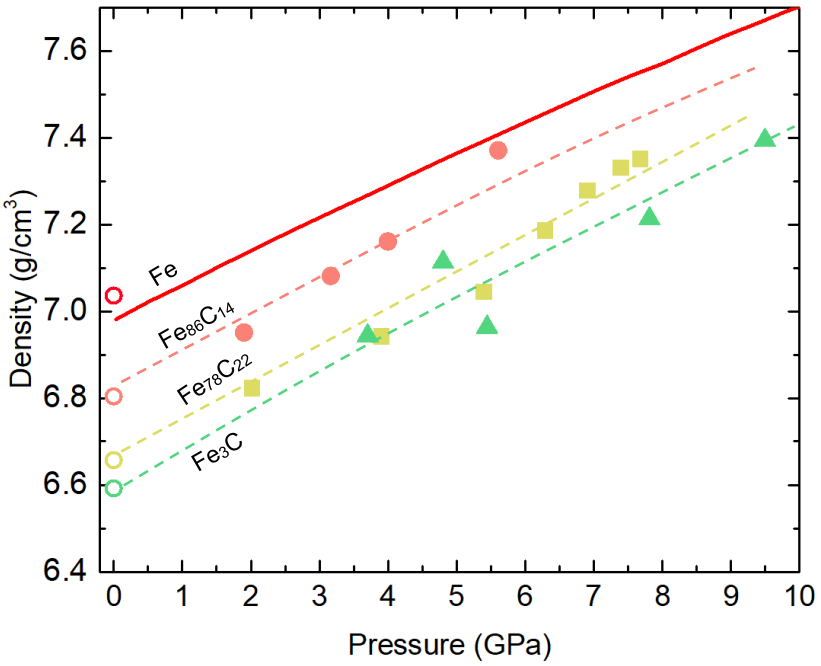

Fig. 1.11 Density as a function of pressure for Fe-C liquids around 1900K. The solid line represents results for pure iron from Anderson and Arhens, 1994. Open and filled points are experimental results at ambient pressure and high pressure with the composition annotated nearby (Jimbo and Cramb, 1993; Terasaki et al., 2010; Sanloup et al., 2011; Shimoyama et al., 2016). Dashed curves are guides for eyes.

Noteworthy, no density data of liquid Fe-C-S ternary alloys have been published yet. The density determination of liquid alloys in the ternary Fe-C-S system, and the modelling of the data are two main parts of this thesis work.

1.2.3 Liquid local structure

Differently from crystals, liquids do not have a long-range structure, and exhibit only short-range orders, i.e. order at distances comparable to interatomic distances (for a more detailed discussion please refer to Chapter 4). Fig.1.12 shows a schematic diagram of the structure of gas, liquid,

amorphous, and crystalline materials, in which the pair distribution function represents an overall probability distribution of other atoms to an arbitrary one as a function of *r*, and the structure factor describes how the materials scatter the incident radiation. A detailed description about structure factor, pair distribution function, and their relations are provided in 4.2. From structure factor $S(Q)$ and pair distribution function $g(r)$, the structures of different phases are easily discerned. Focusing our attention on liquids, the $g(r)$ shows a defined structure only in the low r region, related to the local maxima of the atomic distribution, which is characteristic of the short-range order of the liquid. With increasing distance, the distribution function approaches 1, indicating that the order no longer exists in the long range.

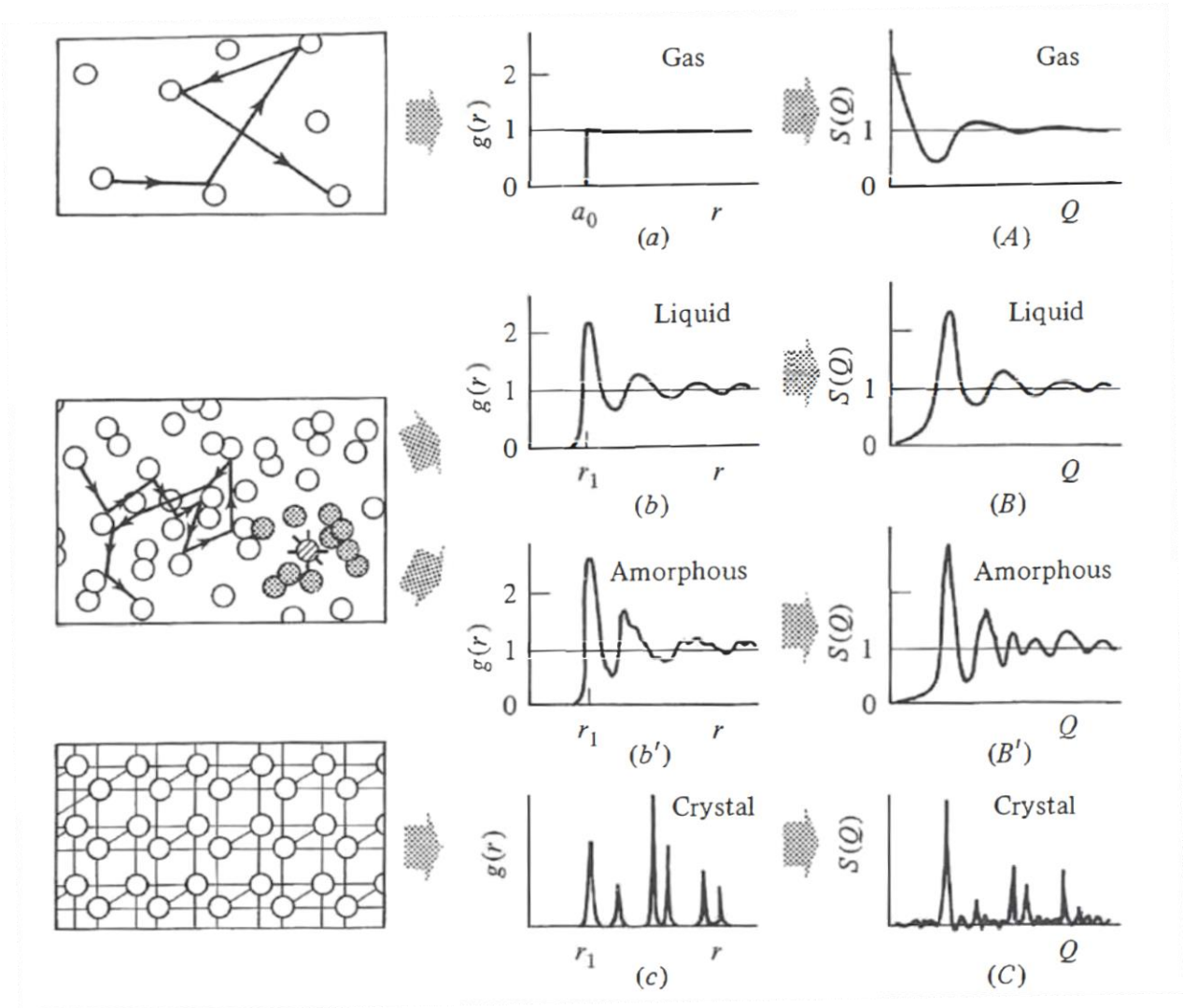

Fig.1.12 Schematic view of the structure of gases, liquids, amorphous substances, and crystals and corresponding pair distribution function $g(r)$ and structure factors $S(Q)$. The graph is from Waseda (1980).

The local structure of Fe-C and Fe-S has been studied by *in-situ* X-ray diffraction (e.g. Shibazaki and Kono, 2018) as well as by ab-initio calculations (e.g. Ohmura et al., 2020). Regarding sulfur, the addition of a small amount of S (up to 18.1 at% according to Xu et al. (2021)) was demonstrated not to modify the local organization of the liquid Fe, while the structure of Fe-S alloys shows the less and less order with increasing S content from 23.5 to 50 at%S (Shibazaki and Kono, 2018). As shown in Fig. 1.13(a), the second oscillation onward become less clear, indicating the disturbed local structure. Similar effect was also observed by Xu et al. (2021) starting from 25.1 at%S, and the structure becomes poorly organized for the most S-rich liquid, $Fe_{48.8}S_{51.2}$, in good agreement with the former study. On the other hand, C inclusion shows minor effects on the liquid structure, which remains relatively highly ordered up to 25 at% of C (Fig. 1.13(b)). This different behavior was attributed to the relative size of sulfur and carbon atoms. With a larger ionic radius, sulfur atoms would cause a larger perturbation to Fe-Fe bonds (Morard et al., 2018), while smaller C atoms don't. Regarding the insertion mechanisms, both sulfur and carbon are generally considered as interstitial elements as they very slightly extend the position of the first and second oscillations in the $g(r)$. However, a recent *ab initio* calculation argued for sulfur to be a substitutional element as the atomic volume stays constant with increased S content at 140 GPa and 5000K, indicating a pressure and temperature dependence of the incorporation mechanics (Ohmura et al., 2020).

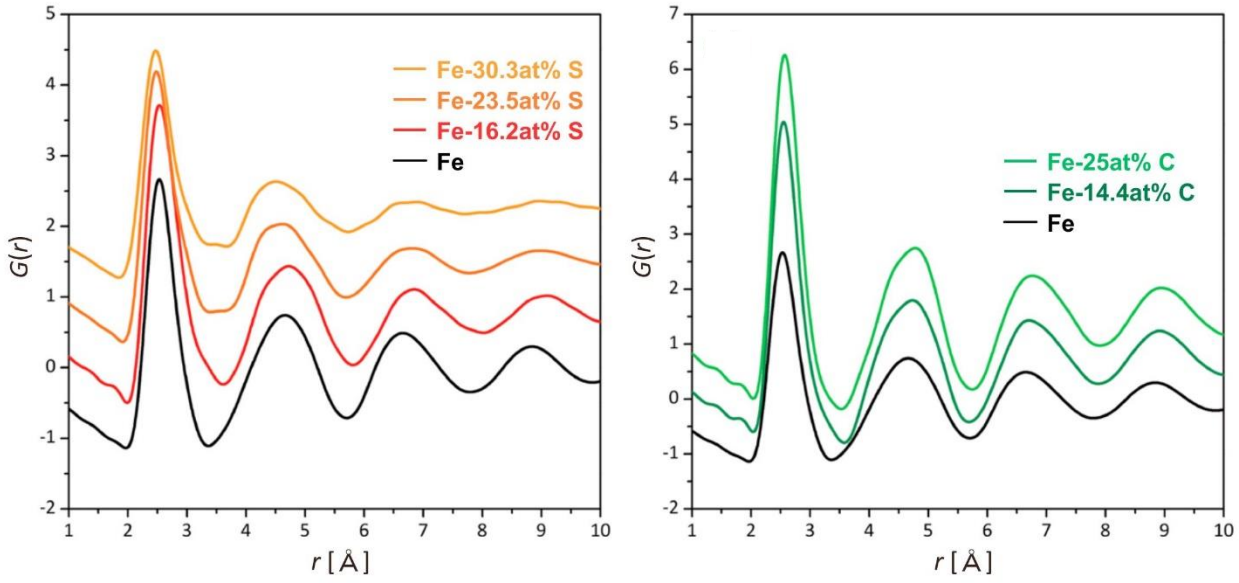

Fig.1.13 Pair distribution function of Fe-S (left) and Fe-C (right) liquids for increasing S or C content (bottom to top). The plot is from Shibazaki and Kono (2018). The oscillations from the second one onward

become the less and less marked for alloys with 23.5 at%S or more, while the structure remains essentially unchanged for the here-considered Fe-C liquids.

Similar to the case of density, currently there is no study addressing the structure of ternary Fe-C-S liquids, which is going to be studied by *in-situ* X-ray diffraction in this thesis work.

1.2.4 Sound velocity of liquids

Only compressional waves can propagate in liquids. The compressional sound velocity of liquids can be either determined by experiments, such as ultrasonic techniques, or by calculation with necessary thermo-elastic parameters. Here, only experimental results are presented. By ultrasonic interferometry, the sound velocity of liquid Fe-S was measured up to 8.2 GPa and 2000 K (Jing et al., 2014; Nishida et al., 2016), and the results are shown in Fig 1.14. While there is a slight disagreement on the absolute values, both studies indicate a less effect of sulfur on the sound velocity of pure iron with pressure increases.

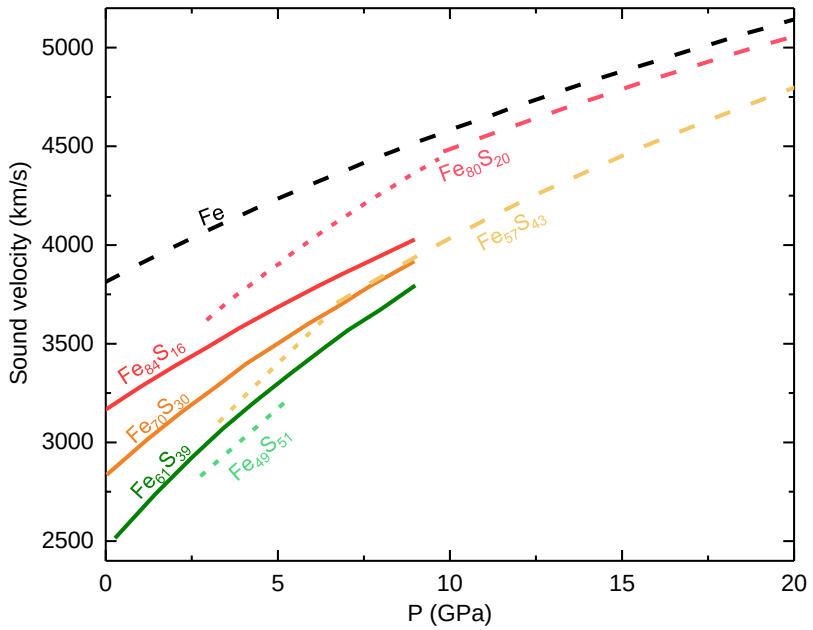

Fig. 1.14 Sound velocity as a function of pressure between 1573 K and 1973 K. Solid curves are velocity profiles estimated from experimental data by Jing et al. (2014). Short-dashed curves and dashed curves are interpolation of experimental data of low-pressure phase and high-pressure phase by Nishida et al. (2020). The chemical composition is annotated beside the curves.

Ultrasonic experiments have been also performed on Fe-C liquids. Sound velocity of Fe-3.5C was measured in a cubic press up to 3.4 GPa by Shimoyama et al. (2016), and results are shown in Fig. 1.15. The extrapolated value to ambient pressure is in good agreement with the ambient-pressure data. Although a reduction in the measured velocities with increasing temperature dependence is reported, all the data are quite close to the velocity of pure iron. The influence of C on the sound velocity of liquid iron is thus considered very limited, even though data are limited to only one compound. Up to date, no sound velocity data either from experiments or from calculations have been reported yet for Fe-C-S alloys. In this study, the sound velocity of liquid Fe-C-S alloys is going to be calculated starting from the measured density and thermo-elastic parameters.

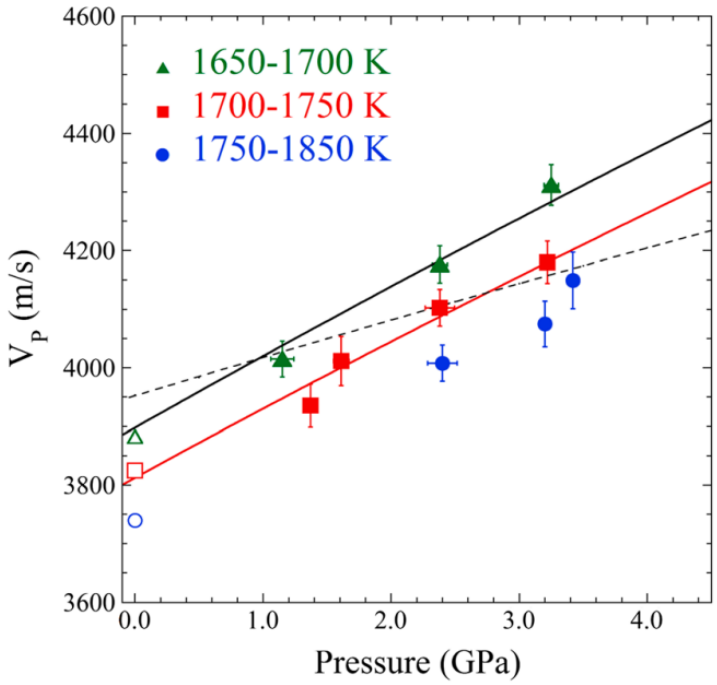

Fig. 1.15 Sound velocity as a function of pressure for $Fe_{86}C_{14}$ from Shimoyama et al. (2016). Solid and open symbols represent, respectively, experimental results at high pressure and ambient pressure data reported by Pronin et al. (1964). Red solid curve is a fit to the data in 1700-1750 K. Black solid and dash curve corresponds respectively to iron data at 1700 K (Jing et al., 2014) and along the adiabat with a potential temperature of 1811K (Anderson and Arhens, 1994).

1.2.5 Interest of structural and thermo-elastic properties of liquid iron alloys for planetary science

As addressed above, the majority of studies on the structural and thermo-elastic properties of liquid iron alloys are limited below 10 GPa. Accordingly, these results are generally used to model the core of small planetary bodies of the solar system such as the Moon and Jupiter's satellites, and sometimes extrapolated to address small planets such as Mercury and Mars. For instance, sound velocity and density measurements of solid Fe in combination with measurements on liquid Fe-S have been used to reinterpret seismic travel time reported in Weber et al. (2011) to propose a density, velocity and compositional model for the Moon's core (Antonangeli et al., 2015). Sulfur estimation in the liquid core based on acoustic data range between 3-6 wt% (Antonangeli et al., 2015), 1-7 wt% (Jing et al., 2014) and 10.5 wt% (Nishida et al., 2016), while less than 6 wt%S (Rai and Westrenen, 2014) was advocated on the basis of metal-silicate partitioning experiments. Alternatively, if C is the dominant light element, a lunar core made by a binary Fe-C alloy could contain 0.6-4.8 wt% of C, as reported by a simulation study on the early magma ocean (Steenstra et al., 2017b). However, almost all the discussions and interpretations of the observations are restrained to binary systems as the direct consequence of the lack of knowledge of the properties of multicomponent alloys (e.g. Fe-C-S), with partial exception concerning the melting and miscibility behavior as few data are availiable (Corgne et al., 2008; Dasgupta et al., 2009). Because of the plausibility of a multi-component core, the physical properties of the Fe-C-S alloy at high pressure and high temperature would be key information for an improved understanding of core composition, and thus formation and thermal evolution of the metallic core of small telluric bodies.

1.3 The aims of the current work

This thesis work aims at providing tighter constraints on the light element content in the Moon's core, modeled on the basis of a more realistic ternary Fe-C-S system. Indeed, if the core were partially molten, a solid inner core composed of Fe (+C) or iron-carbide, would be surrounded by a liquid outer core made of Fe-C-S. Otherwise, if the core were fully molten, this would be either a homogeneous Fe-C-S alloy, or a two-layers structure, with an inner carbon-rich and sulfur-depleted layer, and an outer layer sulfur-rich and carbon-depleted. The immiscibility-induced core

stratification would happen only if the bulk chemical composition of the core lies in the immiscible region of Fe-C-S liquid.

If the Moon is the target of our primary interest, the gained knowledge on the properties of the ternary Fe-C-S system can also be used to address the properties of telluric planetary cores with respect to their size and composition, encompassing pressures expected at the center of Ganymede and including pressures already pertinent for the core of Mercury.

To address the properties of an Fe-C-S liquid core, be this the entire core or an outer core surrounding a solid inner core, the structure of a series of liquid Fe-C-S alloys was studied *in-situ* at high pressure and high temperature by X-ray diffraction, while the density of the samples was extracted both by analysis of the X-ray diffraction pattern and both by X-ray absorption profiles. The co-effect of sulfur and carbon on the structure of liquid iron was investigated and compared to the individual effect of sulfur or carbon. The density obtained from the two methods were compared and discussed. As a key goal of this work, the densities as a function of pressure of alloys with different S and C content were employed to develop a mixing model for liquid Fe-C-S alloy. This thermodynamic model was in turn used to constraint the C and S concentration needed in the Moon's core to account for the geodetic observations. The measured densities and the thermo-elastic parameters obtained fitting the pressure-volume relations at high temperature also allow the calculation of the compressional sound velocity. In order to establish a precise mixing model, samples spanning over a large range of sulfur content were required as starting material because sulfur is much more soluble in liquid iron than carbon. The starting compositions selected for this thesis work were Fe-1.5C-4S, Fe-1.5C-8S, Fe-1.5C-15S, Fe-1.5C-22S, Fe-1.5C-30S, Fe-3C-4S, and Fe-3C-8S. In addition, to test the accuracy of the diffraction method to derive density we have also performed some preliminary experiments on elemental aluminum as benchmark case.

To discuss the possibility of liquid core stratification due to the immiscibility of Fe-C-S liquids, we performed a series of laboratory experiments in which samples quenched at high pressure and high temperature were recovered and analyzed to determine the miscibility gap, and how this vary with pressure and temperature. The obtained miscibility gaps combined with geodetic data could place strong constraints to the core composition. For this purpose, starting compositions were specifically selected across the expected miscibility gap, with gradual increase of sulfur and carbon

content. A first compositional series was set ranging from $Fe_{0.83}C_{0.05}S_{0.12}$ to $Fe_{0.4}C_{0.3}S_{0.3}$. This series of samples was found reach the carbon solubility limit, and several experimental failures occurred due to the sample leaking when melting in the BN capsule. Therefore, a second series of composition was considered, ranging from $Fe_{0.81}C_{0.06}S_{0.13}$, to $Fe_{0.49}C_{0.25}S_{0.26}$, with overall less carbon content in the starting composition and a sapphire ring was inserted in the capsule to retain the liquid. The two series of starting composition for the miscibility experiments are shown together with samples used for density measurements in Fig 1.16.

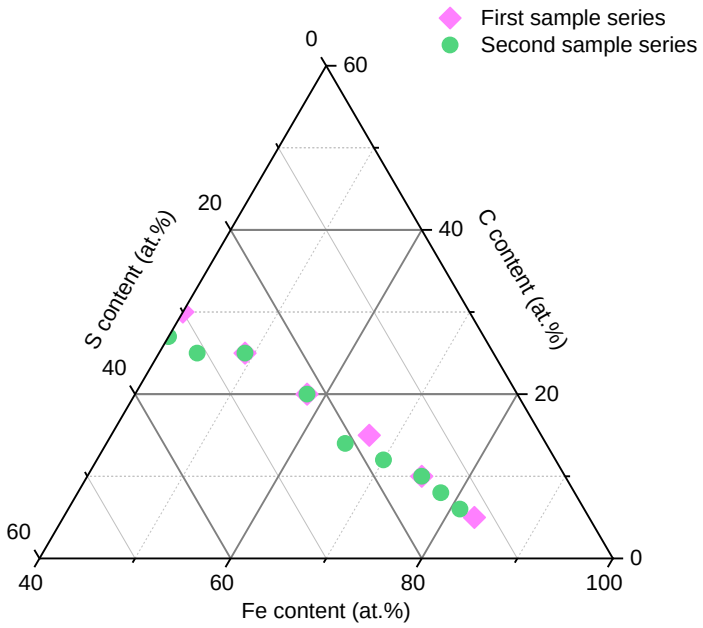

Fig. 1.16 The two series of starting compositions for miscibility experiments. There is overall less carbon content in the second series in order not to reach too fast the carbon solubility limit.

In this thesis work we also studied the phase diagram of Fe-S above 10 GPa by *in-situ* X-ray diffraction with a specific interest for the stable solid phases. Indeed, as already mentioned, an Fe_3S_2 phase intermediate between Fe and FeS was found by Fei et al. (1997) to form above 14 GPa, but the exact stabilization conditions, the lattice parameters, and the equation of state remain unclear. Four starting compositions encompassing the stoichiometric composition of Fe_3S_2 (corresponding to Fe-27S) were selected to investigate the phase diagram of Fe-S at 10-15 GPa and the conditions of formation of the intermediate phase: Fe-15S, Fe-20S, Fe-25S, and Fe-30S.

Once the diffraction peaks of this phase are correctly indexed, it is possible to determine how the lattice parameters evolve with pressure or temperature and thus its equation of state. The properties of this intermediate Fe-S phase are pertinent to discuss the crystallization regime of the core of planetary objects such as Ganymede, or middle-sized telluric planetary bodies such Mercury, as core crystallization is often invoked to explain the magnetic field (e.g. Breuer et al., 2015).

The following chapters will be dedicated to present the experimental and theoretical methods in some detail (chapter 2), full descriptions of the work on liquid Fe-C-S alloys (chapter 3) with implications on the Moon's core (chapter 4), and the properties of Fe-S compounds with some discussions (chapter 5).

Chapter 2 Experimental and theoretical methods

High-pressure experiments are needed to probe properties of materials at conditions existing within planetary interiors, and are the only way to perform studies in such conditions other than *ab initio* calculations.

In this chapter, the experimental techniques applied in this thesis work are presented, addressing the high-pressure generation devices and associated pressure and temperature metrology, as well as the employed experimental techniques. At first, the large volume presses and the corresponding methods for P-T determination are presented. Then, three X-ray techniques that we have employed for density and structure study are described in some detail, including the employed experimental protocols.

The second part of the chapter is devoted to the introduction of the notion of local liquid structure and its relation with diffraction signals, to the description of density determination from liquid diffuse scattering signal and absorption profile. At the end a thermodynamic model based on asymmetric Margules formulism is presented.

2.1 High pressure generation

Being the pressure a force over a surface, high pressure can be obtained either by applying large forces, either by decreasing the area over which the force is applied. Devices for pressure generation can be classified in large-volume presses and small-volume devices (typically Diamond Anvil Cell) based on the cell volume. Paris-Edinburgh cell (PEC) and multi-anvil apparatus (MAA) are two kinds of large volume devices, both used in this study, which can routinely cover pressure range between 1 to 30 GPa. Thanks to the relatively larger sample chamber (up to several mm^3), they are more easily manipulated and the large volume offers advantages (e.g. in terms of signal) for *in situ* measurements. Furthermore, they allow reliable heating by resistive furnaces. Small volume devices such as diamond anvil cell, or dynamic compression, such as laser-driven shock compression, which could reach higher pressures, of the order of hundreds of GPa but, since not used in this study, they will not be presented here.

2.1.1 Paris-Edinburgh cell

PEC was originally designed for neutron scattering experiments, and then adapted for X-ray scattering (Besson et al., 1992). With a number of novel models developed during the recent years, PECs are now compatible with various X-ray in-situ experiments (Morard et al., 2018; Sanloup et al., 2011; Philippe et al., 2016; Boulard et al., 2020). For instance, the recently developed Rotating Tomography Paris-Edinburgh cell (RoToPEc) and Ultrafast Tomography Paris-Edinburgh cell (UToPEc) are two modules specifically designed for tomography study at high temperature and high pressure. In particular, the UToPEc, employed in this study, has an enlarged opening angle of 165 °, allowing high-resolution tomography and reconstruction almost without any obvious artefacts. Assembled with a fast rotational stage at bottom, a tomography containing 900 projections takes only 1s for rotations over 180 ° (Giovenco et al., 2021). Fig.2.1 shows a picture of the UToPEc. The main body, made of stainless steel, serves as a holder and compressor to a pair of anvils. The assembly is put between the anvils, and the pressure is generated by an external hydraulic pump. The highest reachable pressure largely depends on the size of the assembly. Pressure of 10 GPa can be typically reached with the 7-mm (in diameter) assembly, while with 5-mm assemblies the maximum pressure is up to 16 GPa.

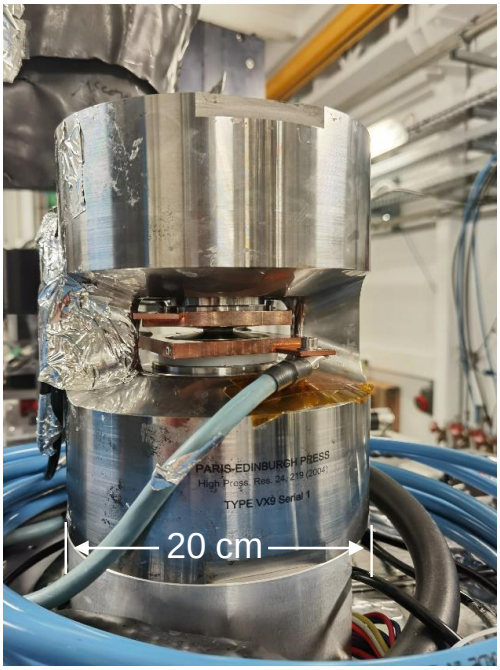

Fig. 2.1 Picture of a UToPEc installed on the PSICHE beamline at SOLEIL. The main body is made of steel, with a large opening angle of 165 °.

A schematic of the press assembly is shown in Fig. 2.2, although more complex assemblies have been used in other studies for special purposes (Jing et al., 2014; Knibbe et al., 2021). A gasket, a sample chamber, and a heater with electrodes at its two ends, are the main elements. 7-mm assemblies coupled with tungsten carbide anvils and 5-mm assemblies equipped with sintered-diamond anvils were used in this study for pressure generation up to about 5 GPa and 14 GPa, respectively. For in situ X-ray experiments, ideally, materials for gaskets should be transparent to X-ray. While some early experiments used TiZr alloy (Marshall and Francis, 2002) (transparent to neutrons) or pyrophyllite (Besson et al., 1992) for gasket, boron epoxy has become the most frequently used material (Giovenco et al., 2021; Knibbe et al., 2021) for X-ray experiments. The material for capsules should not only be transparent but also not reactive with the sample and electrically insulating. Capsule material normally includes hBN, MgO, sapphire or diamond, here listed for increasing hardness. The softer hBN can provide more hydrostatic compression, so it is generally preferred for most of the experiments on solid or liquid samples. For X-ray absorption experiments, a hard diamond capsule is necessary to maintain the shape of the sample at high pressure (e.g. Sanloup et al., 2011; Knibbe et al., 2021).

The pressure range reachable with these setups covers the pressures within the core of the small telluric planetary bodies of the solar system, including the Moon, Europa and Io, as well as the pressure within the core of larger bodies with mantle made by mixture of water and silicates, such as Ganymede.

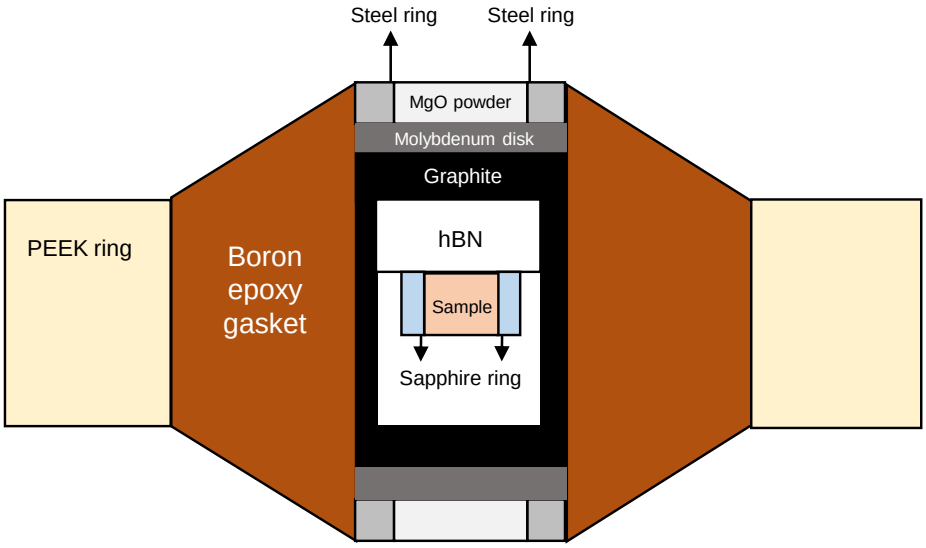

Fig 2.2 Schematic of a classical PE assembly.

2.1.2 Multi-Anvil Apparatus

The first MAA was invented by Tracy Hall with the goal to synthesize diamonds (Hall, 1958). It was a tetrahedral press driven by four hydraulic rams. Although this MAA has not been used during the last four decades, it initiated the development of various kinds of MAAs. The pressure coverage and the ability to combine with *in situ* synchrotron measurement have made today the developed MAAs excellent tools for mineralogy study (Utsumi, et al., 1998; Mueller et al., 2006 and 2007). There are several types of MAA currently in use, with Kawai-type MAA the most widely used. These MAAs are introduced here below.

2.1.2.1 Kawai-type MAA

This is a 6-8 multi-anvil in which the six first-stage anvils, driven by hydraulic rams, compress eight cubic second-stage anvils, each with a corner truncated to accommodate an octahedral cell as shown in Fig.2.3. This press can routinely generate ~40 GPa at maximum using tungsten carbide second-stage anvils (Ishii et al., 2016), with the highest pressure record of 109 GPa obtained using sintered-diamond anvils (Yamazaki et al., 2014). The truncation size of the anvil is another factor controlling the achievable pressure. The highest pressure is generated using the smallest-truncated second-stage anvils, which accommodate assemblies sized only 0.5-1 mm (Ohtani et al., 1989). For experiments up to around 5 GPa, the target pressure for liquids in this study, a set of 14/8 sized anvils were used, where 14 mm is the edge length of the cube after truncation, and 8 mm the side length of the truncated regular triangle. More in general, cubic size could range from 10 to 54 mm (Frost et al., 2004; Kondo et al., 1993), and the 11 different truncation sizes most commonly used are 0.5, 1.0, 1.5, 2.0, 3, 3.5, 4, 5, 8, 11, and 17mm (Ohtani et al., 1989; Frost et al., 2004; Shimomura et al., 1992), selected depending on the target pressure.

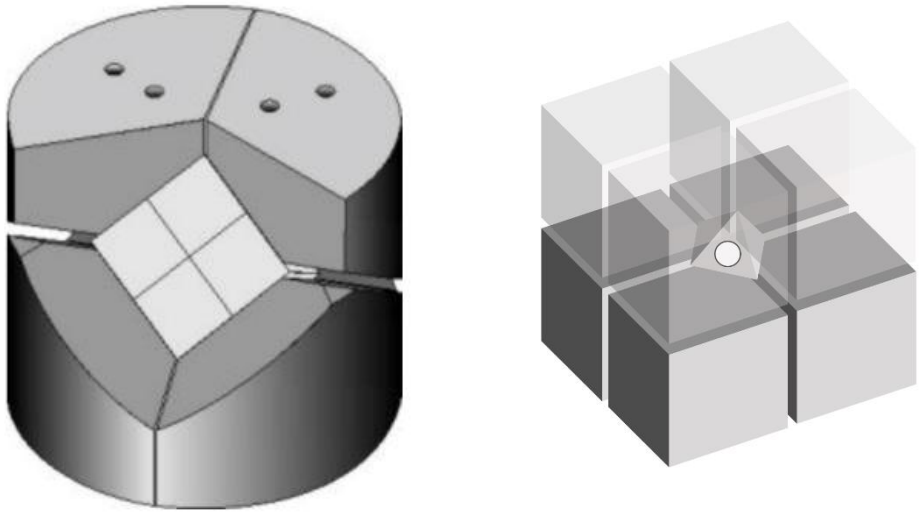

Fig. 2.3 Schematic of the 6-8 multi-anvil press (a) and the cell compressed by the second-stage cubes (b).

2.1.2.2 Other types MAA

Other types of MAA, such as the DIA-type apparatus (or cubic anvil apparatus) and its advanced version, deformation-DIA (or D-DIA) apparatus as well as its combination with 6-6 or 6-8 assemblies, have been also widely used during the last tens of years.

The original DIA-type apparatus uses four horizontal and two vertical anvils driven by hydraulic pressing. Compared to the Kawai-type apparatus, its larger anvil gaps make it particularly useful for *in situ* synchrotron X-ray experiments. It has been used in the studies of structure, density, and viscosity for melts (Rutter et al., 2002; Katayama et al., 2004; Yamada et al., 2007; Arima et al., 2007) and elasticity for Earth's materials (Li et al., 2004).

The deformation-DIA apparatus was developed by Wang et al. (2003), with the vertical anvils connected to two differential rams located inside the guide blocks, so that it allows deformation experiments in uniaxial geometry under pressure. This system has been therefore used in a number of rheology studies (Nishiyama et al., 2007; Wenk et al., 2005; Li et al., 2008). After several years of the appearance of the D-DIA apparatus, a new MA 6-6 assembly was first reported by Nishiyama (Nishiyama et al., 2008), in which a cubic cage is applied to guide the movement of

the six second-anvils. The alignment of the anvils can thus be maintained precisely to high pressure. In addition, it allows a quick replacement of the anvils with different truncation sizes, which is very functional to optimize operations, as needed for limited beam time experiments. The deformation DIA-type press with the developed MA 6-6 assembly is shown in Fig. 2.4.

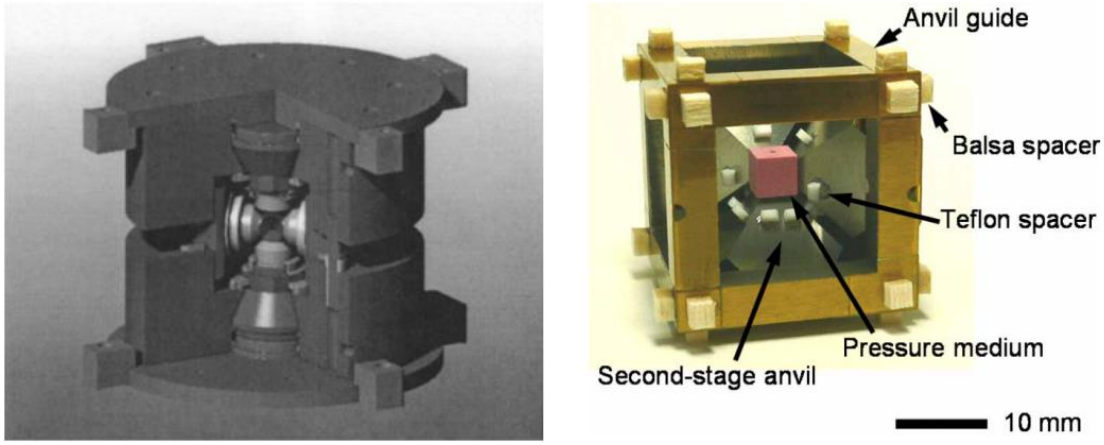

Fig. 2.4 Cutaway of a D-DIA apparatus and a photography MA 6-6 assembly. Pictures are from Wang et al. (2003) and Kawazoe et al. (2010), respectively.

2.1.2.3 High temperature generation in MAA

Similar to PEC, in MAA experiments high temperature can be generated by a resistive heater inside the cell (Fig.2.2). Classic materials for the heater are graphite (Shimomura et al., 1992), $LaCrO_3$ (Frost et al., 2004), and metallic foils with high melting points, such as rhenium (Ishii et al., 2016). Graphite and $LaCrO_3$ furnace have been proven to provide homogenous heating and to be able to reach T >2500 K and 2900 K, respectively. However, it should be noted that pressure-induce transformation of graphite into diamond prevents effective uses at pressures above ~11 GPa).

Many methods allow to directly or indirectly determine pressure and temperature and they will be discussed in some detail in section 2.2.

2.2 Temperature and pressure measurement/determination in high pressure experiments

2.2.1 Temperature measurement/determination

Temperature determination in PEC and MAA can be classified into two main methods: (i) temperature reading from a thermocouple inserted in the assembly; (ii) using an empirical temperature vs. power calibration curve.

Temperature measurement by thermocouples is based on the Peltier effect (Spanner, 1951), and exploits the electric potential difference across the conjunction of two dissimilar metallic wires. This potential difference depends on the temperature difference between the conjunction and the open ends, the materials of the wire, and the pressure (Li et al., 2003). Commercialized thermocouples always have a code indicating the compositions and a recommended range of utilization (Powell, 1974). The tungsten-rhenium alloy thermocouples, for instance the Type-C thermocouple (W5%Re-W26%Re), can tolerate temperature up to 2300 ℃, which makes them amongst the most preferred in PE cell and MAA experiments for geoscience studies (e.g. Ishii et al., 2016). This type of thermocouple is also used in high-temperature diamond anvil cell (DAC) experiments with an external heater (Bassett et al., 1993; Dubrovinskaia and Dubrovinsky, 2003). The thermocouple should be placed as close as possible to the sample to minimize errors due to the temperature gradient inside the cell.

Sometimes it is not possible, or not desirable, to accommodate a thermocouple, either because of space limitations and potential interaction with the sample, or because of the structure of the assembly (Parker et al., 2010; Morard et al., 2018). In these cases, the temperature can be determined in two ways. One is to conduct a calibration run with a thermocouple inserted in the selected assembly, but without sample, and the obtained temperature as a function of power is used in the subsequent runs using same assembly (Kono et al., 2014). The other is a non-destructive method exploiting equation-of-state cross-calibration by using at least two standard materials as calibrants, with their unit-cell volume measured as a function of the heating power. This could be achieved by either a dedicated calibration run with only the calibrants, or by having the calibrants beside the sample in all the runs. Although having the calibrants next to the sample allows determination of both the sample's temperature and pressure, it is not suitable for the study of liquid samples, as the calibrants may physically or chemically interact with the liquid sample during experiments, affecting the quality of the obtained data. This cross-calibration method has

proved sufficient precision for simultaneous estimates of temperature and pressure (Crichton and Mezouar, 2002), with the most frequently used standard materials hBN, MgO, NaCl, Pt, and Au.

In this study, temperature as a function of power was obtained by a calibration run performed before the sample loading, in which the non-destructive cross-calibration method was employed based on the equation of state of standard materials, with their unit cell volumes measured at each power step. Specifically, Pt, MgO, and BN were adopted as calibrants in PSICHE beamline, and NaCl and MgO in ID-27 beamline. As an example, the temperature curves obtained from calibration runs in SOLEIL are shown in Fig. 2.5. The precision at low temperature by this method is limited by the internal stress introduced by the large stiffness difference of platinum and hBN. The stress is relaxed with the temperature increase, as highlighted by the modification of the slope around 300 W in Fig. 2.5. In this study the calibration is employed only above 300 W, where the error for temperature is estimated to be ±100 K.

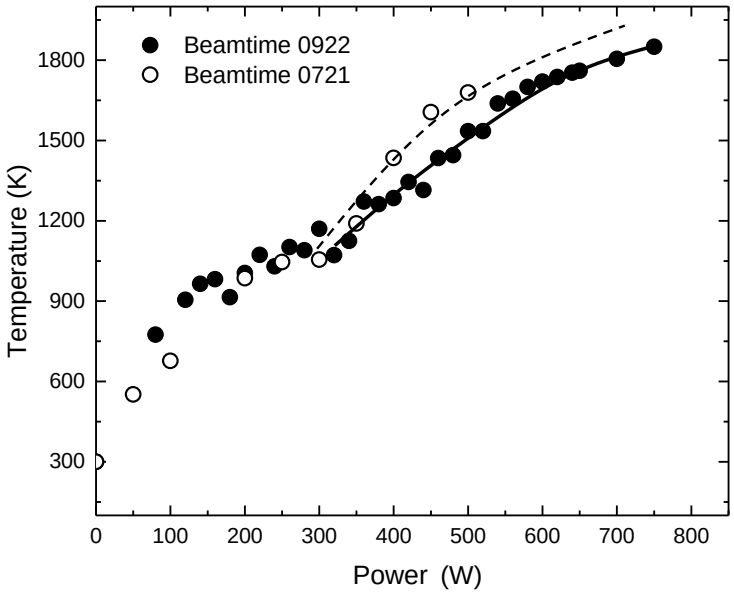

Fig. 2.5 The temperature as a function of power in the two beamtimes by cross calibration using hBN and platinum as standards. Based on the thermal equations of state, a pair of unit-cell volumes of hBN and platinum will produce a unique set of pressure and temperature, which is called cross calibration.

2.2.2 Pressure measurement/determination

With synchrotron radiation, the pressure in the cell can be directly determined by the measured unit-cell volume of some standard materials such as hBN, NaCl, and Pt, whose thermal equation

of state is well known, provided the temperature measurements by a thermocouple (Xu et al., 2021). For experiments where thermocouples are not compatible/desirable, as mentioned in the previous section, a cross calibration could be adopted with the use of two or three standard materials with well-known thermal equations of state.

In ex-situ experiments, the relationship between the cell pressure and hydraulic pressure relies in calibrations runs performed in advance. Room-temperature pressure calibration is achieved by detecting the resistive jump at phase transition points of some metals and minerals, such as Bi and ZnS, while high-temperature calibration is commonly obtained by well-known phase transitions pressure of minerals such as the coesite-stishovite transition point at 9.6 GPa and 1400 ℃ (Walter et al., 1995; Shatskiy et al., 2011).

2.3 High pressure techniques used in this study

2.3.1 *In situ* X-ray diffraction

X-ray diffraction is a robust technique for the identification of crystalline materials, determination of phases, lattice parameters, crystallite sizes, and preferred orientations of crystalline samples, as well as for structural analysis of amorphous materials and liquids (Holder et al., 2019). If a monochromatic X-ray beam impinges on a crystalline solid, the intensity maxima on the diffraction pattern follow the Bragg's law (Waseda et al., 2011)

$$n\lambda = 2dsin\theta \tag{2.1}$$

Where n is an integer, λ the wavelength of the X-ray, d the interplanar distance, and θ the diffraction angle. Once looking at the Bragg's law, it becomes clear that measurements can be performed in angle-dispersive or energy-dispersive mode.

The angle-dispersive diffraction is the most widely used approach because in laboratory experiments the photon energy of the X-ray is usually fixed to the emission line of the material used as the anode, with copper, cobalt, molybdenum and silver amongst the most classical options. When not specified otherwise, powder XRD usually refers to the angle-dispersive diffraction.

Differently, in synchrotron facilities, the light source is generated by bending magnets or insertion devices placed along a storage ring, so that photons with a wide range of energy can be generated. This wide-range light source is referred to as 'white beam', with which energy-dispersive diffraction measurements can be carried out. Out of this 'white beam', crystal monochromators can select photons of certain energy if a monochromatic beam is needed. A new method combining the angle and energy dispersive diffraction was developed for structural analysis of liquid and amorphous materials, where energy dispersive patterns are collected over a range of 2θ angles (Wang et al., 2004). This method, called CAESAR (Combined Angle- and Energy-dispersive Structure Analysis and Refinement), proved high-performance in quantitative structure and lattice property studies. More details will be given in the following subsections.

2.3.1.1 Angle-dispersive diffraction at ID-27 beamline

At synchrotron diffraction beamlines, the employed X-ray beam is generally at higher energy compared to the common Cu Kα energy (8.04 keV corresponding to a wavelength of 0.1541 nm). This is particularly suitable for experiments performed over a limited 2θ range (high-pressure environment often comes with limited angular aperture), or for massive sample environments (as MAA or PEC are). The working energy for operation in our experiments at the ID27 beamline of ESRF, France, is 33.17 keV (i.e 0.3738 nm, Iodine K-edge), selected by a Si(111) channel cut monochromator. Tungsten carbide slits were used to collimate the size of incident beam to 50 by 50 μm. Soller slits located between the sample and the detector allow efficiently filtering out the background signal from the environment, thus enabling high quality data acquisition (Morard et al., 2011). To reach higher pressure, smaller 5-mm assemblies coupled with sintered-diamond anvils were used in our experiments performed on ID27. The 5-mm assemblies have a same internal structure as 7-mm ones (introduced in 2.1), using the BN as sample capsule, but with the size of each part decreased. Mixed powder of MgO and NaCl were put beside the sample as P-T calibrants. The wavelength of the light source was set to be 0.3738 nm, and the diffractometer was calibrated using the LaB6 as standard before experiments.

Experiments were performed by bringing at first the sample to target pressure by cold compression, and then, the sample was heated up. Angle-dispersive X-ray diffraction patterns were taken on the sample and calibrants for increasing temperature at steps of 20 W, until melting. P-T condition was determined by the cross calibration by the unit-cell volumes of MgO and NaCl which were

placed close to the sample or well mixed in the sample. The diffracted beam went through a double-layer Soller-Slit that filters out the background from scattering and was collected by a Pilatus CdTe 3M detector with an exposure time of 30s. Fig. 2.6 shows the 2D diffraction image of LaB_6 standard material collected at ID-27 and the corresponding radial-averaged diffraction pattern.

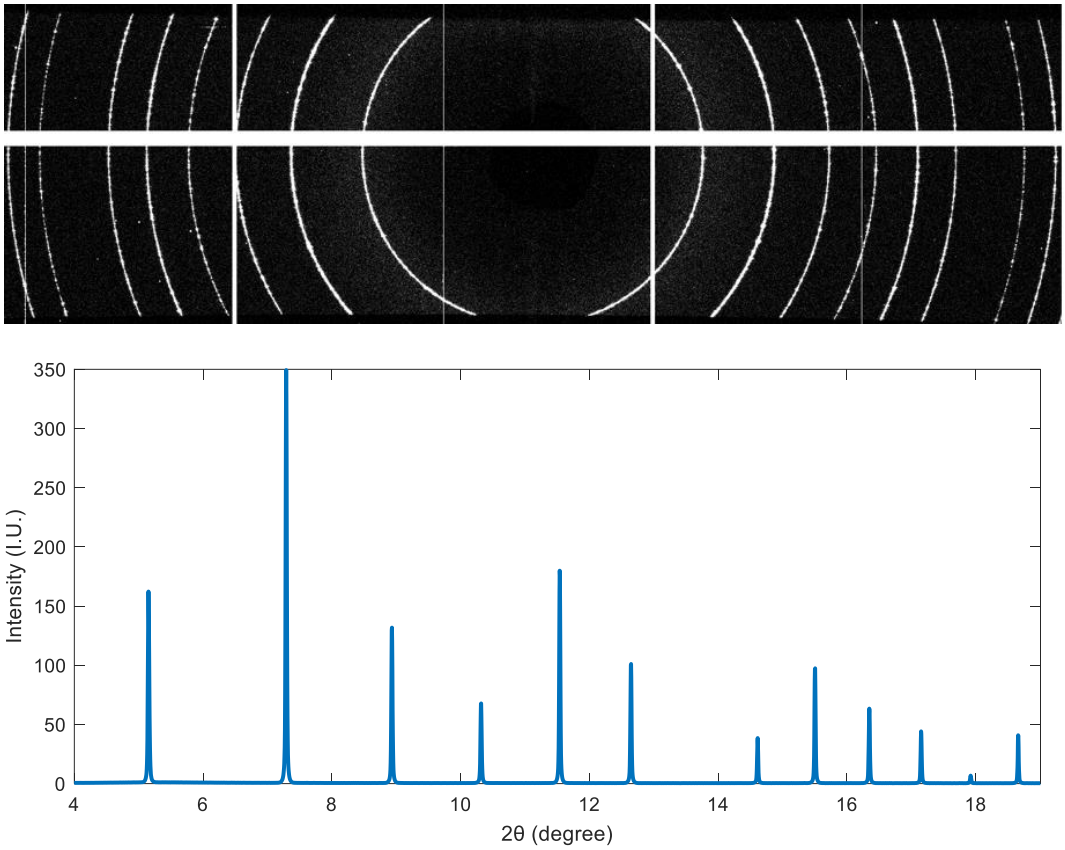

Fig. 2.6 Diffraction image of LaB_6 and its radial-averaged diffraction pattern collected for λ= 0.3738 nm

2.3.1.2 CAESAR at PSICHE beamline

The advent of machines of third generation for synchrotron radiation made available high-brilliance X-ray over a wide range of photon energy. To make full use of the photon source and obtain high quality diffraction data, the CAESAR technique, in which energy dispersive diffraction is taken over a range of 2θ angles, was developed and first reported in 2004 (Wang et al., 2004). This technique has been initially implemented at the Advanced Photon Source, Chicago, USA, and used in particular for investigation of the structure and density of liquid and amorphous

systems (e.g. Shibazaki et al., 2015; Shibazaki and Kono, 2018; Ikuta et al., 2016; Prescher et al., 2017). The obtained diffraction spectrum is a two-dimensional intensity (I) distribution as a function of 2θ and energy, and can be rearranged as I *vs*. d-spacing or I vs. Q (exchange wave-vector). The method was first developed by Funakoshi in his PhD work (Funakoshi, 1997, PhD thesis). In the case of liquids, glasses or other amorphous samples, this spectrum contains the information of quantified local atomic distribution, from which the density of the liquid could be extracted. Details are provided in the next section.

Since 2017 the CAESAR technique has been also implemented at the PSICHE beamline of Synchrotron SOLEIL (Coati et al., 2017; King et al., 2022). Figure 2.7 shows a picture of the setup we used.

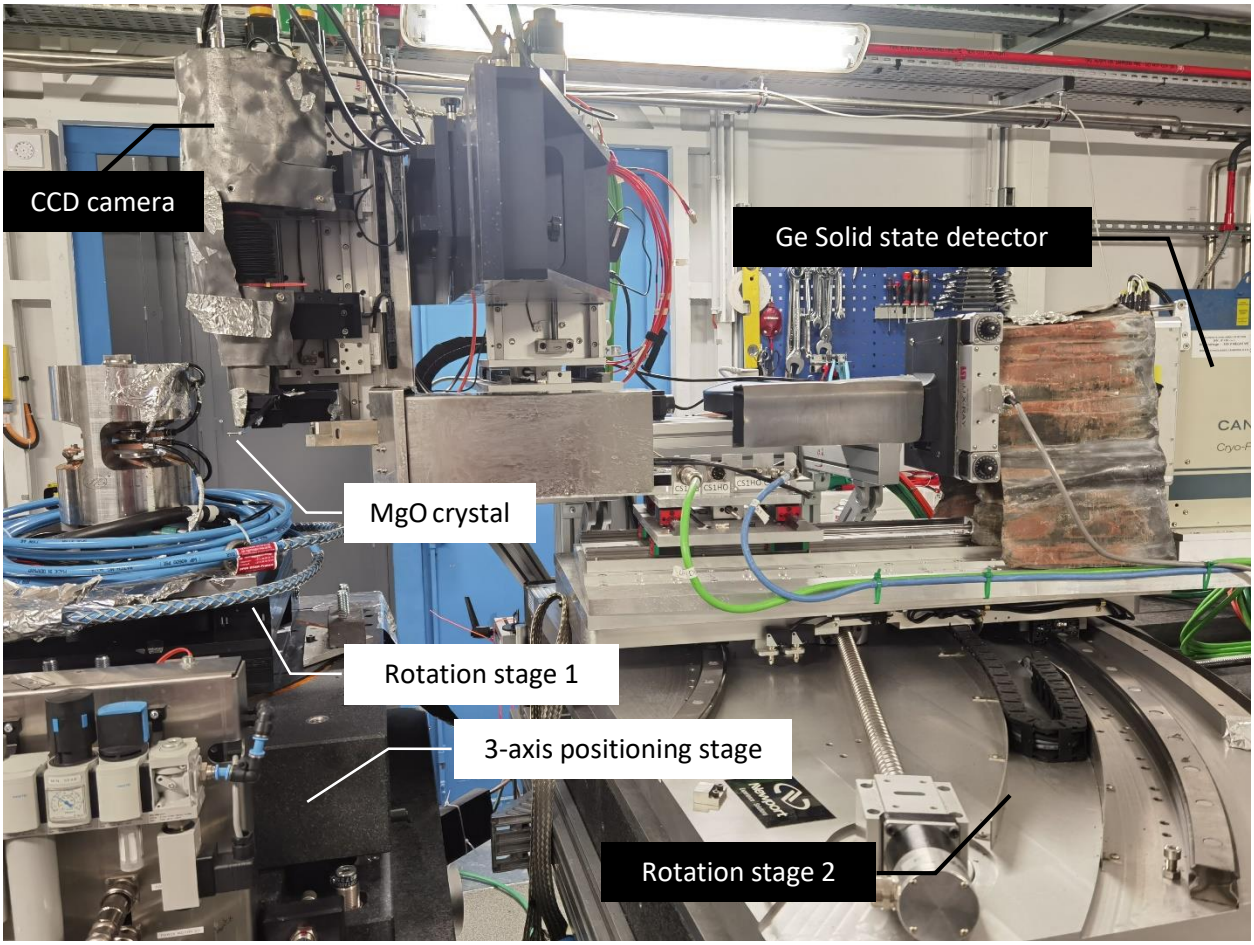

Fig. 2.7 The experimental setup at Psiche beamline. During this thesis work the beamline was operated in three different modes: 1) The Ge solid-state detector mounted on the rotation stage collects the energy dispersive X-ray diffraction pattern at different angles for CAESAR mode; 2) The CCD camera collects the projection at different angles of the sample mounted on the rotation stage 1 for tomography; and 3) The

intensity of selected diffraction peaks of MgO are collected while the sample horizontally is scanned by moving the positioning stage, and employed to determine the sample absorption profile.

The *in situ* synchrotron X-ray diffraction experiments were carried out in a UToPEC (Boulard et al., 2018). The samples were loaded to a 7-mm PEC assembly consisting of a sapphire ring (in the high-pressure runs in beamtime 0922) or a hBN capsule, a graphite furnace, and a boron epoxy gasket (please refer to Fig.2.2. for a schematic of the assembly). Sapphire is an ideal material serving as the inner capsule because of its hardness, which allows holding the samples' geometry and retaining liquids at extreme conditions. The sample should be located at the center of the assembly along the vertical direction, to ensure its accessibility when the gap between the two anvils shrinks under pressure. Pressure was generated by a pair of tungsten carbide anvils driven by a hydraulic pump, while temperature was increased by increasing power in the resistive heater The pressure media hBN, clinging to the sample, also served as the pressure marker, with the unit cell volume of which the pressure was calculated using its thermal equation of state. The high brilliance white x-ray beam from a superconducting wiggler, with the photon energy from 10 keV to 90 keV, is collimated to 22×50 μm^2 (vertical horizontal) by two slits before the sample. The diffracted beam is collected by 7 solid-state Ge detectors perpendicularly arranged in a row. The energies were calibrated using characteristic fluorescence X-ray lines of Mo, Sn, Ba, Sm and Au. The 2θ angle was calibrated at 8◦ using a 7 μm thick Au foil with a precision of ±0.003◦.

Experiments were first carried out on a testing material, aluminum, since density data for liquid aluminum have been reported using a similar technique (Ikuta et al., 2016), and then followed by the Fe-C-S alloys. Sample information and results for the test run are provided in appendix A. During the experiments, samples were first brought to target pressure by initial cold compression, followed by heating up at a rate of ~100 K/min. The status of the sample was checked every 50 W by energy dispersive diffraction pattern collected starting from 300 W. The appearance of a diffuse signal pins the onset of melting, while the total disappearance of sharp peaks indicates a fully molten status. An example of the diffraction patterns collected upon heating is shown in Fig. 2.8. When the samples were fully molten (typically at 550 W), we took a diffraction pattern of the pressure marker (hBN). Then a CAESAR scan was performed combining the angle-dispersive diffraction pattern from 10 keV to 90 keV collected at various 2θ angles (from 2.5 ° to 29.1 ° with a 0.2 ° step). During the rotation of the stage, the detector collected the signal diffracting from a

fixed sample volume by the controlled movement of slits between the sample and detectors. The counting time for 2.5-12 °, 12-20 °, and 20-29.1 °were 5s, 10s, and 20s, respectively, so the whole scan took a total exposure time of about 20 minutes. In most cases this procedure was repeated with increased heating power (by 100 W and 200 W), yielding three density points at different conditions for each run. At the end of the heating run, temperature was quenched and samples recovered for *ex situ* analysis.

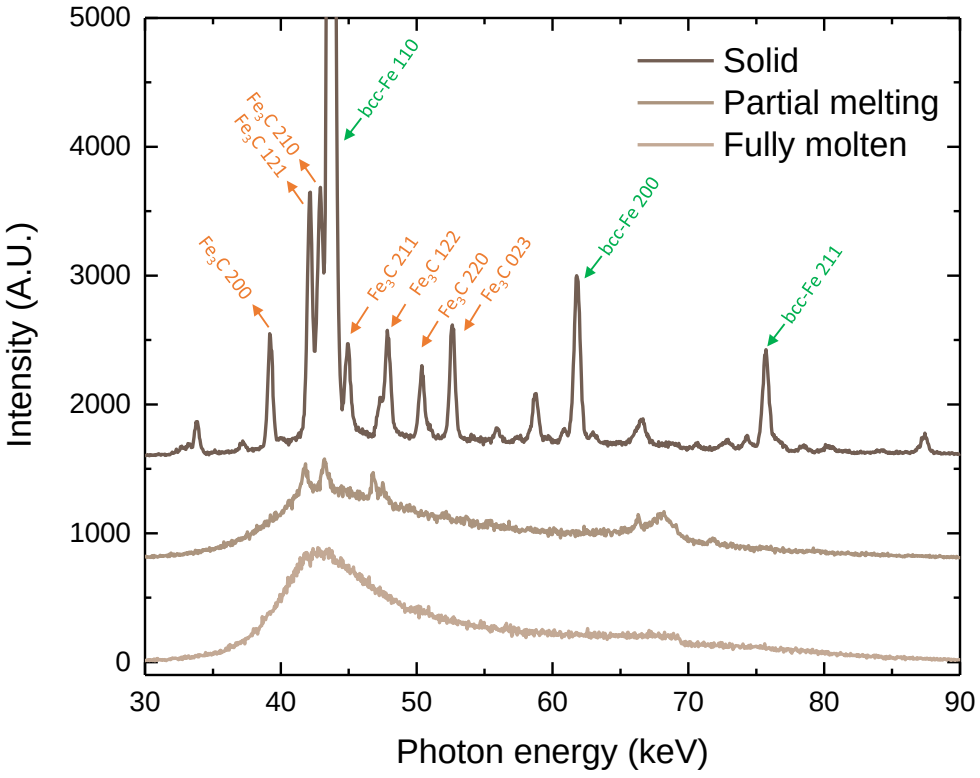

Fig. 2.8 Energy dispersive X-ray diffraction pattern collected on an Fe-C-S sample at 2.8 GPa upon heating. The pattern of the solid is taken at 300 W (1190 K), with the main peaks from solid phases annotated. FeS was not detected probably due to the smaller atomic proportion. Initial melting occurred at 400 W (1340 K) and the fully molten status was observed from 550 W (1600 K).

2.3.2 *In situ* X-ray absorption at PSICHE beamline

Scattering and photoelectric absorption occur when X-rays interact with a sample. Due to this interaction, X-rays are attenuated as they pass through the sample. The incoming intensity I_0, and the attenuated intensity I after going through a distance x are related by the Beer-lambert law:

$$I = I_0 e^{-\mu\rho x} \tag{2.2}$$

where μ is the mass absorption coefficient, which depends on the substance and on the X-ray energy, and ρ the density of the sample (Nishida et al., 2011). The X-ray energy is related to its wavelength by $E = hc/\lambda$, with h the Planck constant, and c the speed of light in vacuum. For the same X-ray energy, denser substances normally have larger mass absorption coefficients, while for the same material, absorption decreases with the increasing energy of the X-ray (Fig. 2.9).

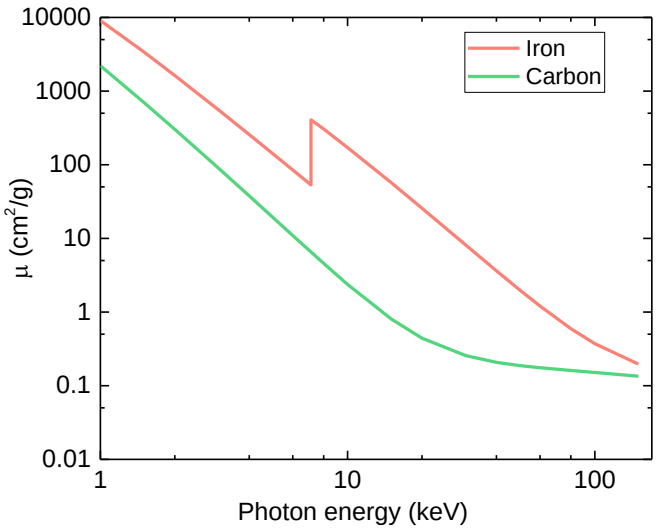

Fig. 2.9 Mass absorption coefficient of iron and carbon as a function of photon energy. The data are from NIST (National Institute of Standards and Technology) Standard Reference Database 126. The observed kink in Fe absorption is the absorption K-edge.

For mixtures and compounds, the mass absorption can be obtained by a weighted sum of the mass absorption of the composing elements:

$$\mu = \sum_i w_i \mu_i \tag{2.3}$$

If the sample is surrounded by other materials (high-pressure cell or other sample environment), these also contribute to the absorption. In these cases, what is generally measured is the absorption profile of the whole assembly, including the sample, capsule, and background. Known the

geometry of the assembly, the product $\mu\rho$ of the sample can be extracted (Terasaki et al., 2010; Henry et al., 2022).

PSCICHE beamline is conceived to be able to rapidly change the setup to be able to perform not only diffraction but also absorption measurements on the same sample at same pressure and temperature conditions. In our experimental protocol, after each diffraction acquisition, the optic system was switched to absorption mode for absorption profile collection. In this mode, the vertical size of beam source is reduced to 10 microns by closing the slits, and an MgO polycrystalline specimen was added in the beam path, between the sample and the detector (see Fig. 2.10). After penetrating the sample, x-rays went through the MgO crystal and generated diffraction patterns, whose intensity is exploited to reconstruct the absorption profile. The advantage of this setup is that that neither further optic components nor detectors were needed and diffraction mode and absorption mode share the same general optics layout. In practice, the detectors were fixed at a diffraction angle 2θ=9 °, where two intense diffraction peaks of MgO appear at photon energy equal to 37.5 keV (200) and 53.5 keV (220). The absorption profiles collected at both the two energies allow the density extraction, but in practice, only the one at 37.5 keV was employed because the maximum contrast enables a more precise fitting of the data (Henry et al, 2022).

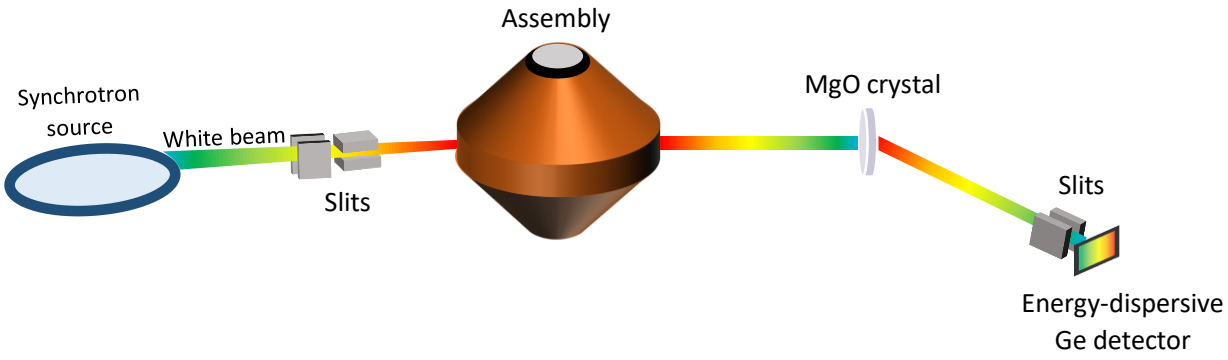

Fig. 2.10 A schematic of the setup and beam path for absorption profile acquisition.

The whole exposure takes about 10 minutes, covering a range of horizontal scan from -1.1 mm to 1.1 mm with respect to the sample center, with a resolution of 0.02 mm. Same as CAESAR acquisition, the 7 detectors individually collect data, remarkably increasing the signal to noise ratio. The collected absorption profile was the fitted to the Beer-Lambert law. The fitting process

strongly relies on the geometry of the assembly, so an absorption acquisition is always followed by a tomography scan to check the geometry of the sample. The use of a hard sapphire capsule is therefore favored for such applications.

2.3.3 *In situ* X-ray computed-tomography (XCT) at PSICHE beamline

As a non-destructive detection or imaging technique, XCT is widely used in medicine (e.g. Pan et al., 2008), industry (e.g. De Chiffre et al., 2014), and geoscience (e.g. Mees et al., 2003). All the applications share a same theory: X-rays go through the sample (or body) and generate a two dimensional projection, with the intensity (often visualized as a grayscale) depending on the attenuation. The more attenuative portions are brighter and the less attenuative are darker. With the rotation of the sample (or of the X-ray source), a large amount of 2-D images at different angles are collected. Based on the Radon transform, these 2-D images are processed to produce a 3-D volume rendering (Deans, 2007), which is called 'Tomography reconstruction'.

In geoscience, XCT can be combined with various high pressure techniques to investigate the sample *in situ* at extreme conditions. For example, structural phase transitions of iron at high pressure and high temperature were recently studied in a Paris-Edinburge cell (Boulard et al., 2020). Furthermore, the geometry, homogeneity, and volume of the sample are also visible, provided enough absorption contrast between the sample and the surrounding materials. As mentioned in section 2.1.1, the UToPEC has an extended opening angle of 165 °compared to the standard four-column PE press (135 °), allowing a high-quality tomography imaging (while the 15 ° missing angle will still cause some subtle artefacts). A Paganin correction (Paganin et al., 2001) can be applied to minimize the ring artefacts.

In this study, tomography data collected at high pressure and high temperature and the 3-D rendering are used to assess sample geometry, melting and to support the analysis and interpretation of the diffraction and absorption measurements. Therefore, radiography or tomography imaging is always performed in combination with CAESAR and absorption as a supporting technique. Different from the white beam used in CAESAR and absorption acquisition, the optic path for tomography includes a series of filters and an x-ray mirror on the incident side as high pass and low pass energy filters, leaving a spectrum with a peak flux around 25 keV, and an energy band around a desired value ($\Delta E/E$ typically 0.1), which forms a 'pink beam' (King et al., 2016). The setup is shown in Fig. 2.11. The use of optic filters and an X-ray mirror do not

affect the original white beam flux at such an energy range, compared to the low transmission rate around 0.1% if using a monochromator. The high flux of the 'pink beam' ensures the quality of imaging and meanwhile eliminates the beam hardening artefacts caused by the strong attenuation of low-energy photons.

On the receiving side, a single crystal scintillator (YAG, LSO, or LuAG) transforms the X-ray into visible light. A mirror is located between the CCD camera and the scintillator to reflect the visible beams vertically to avoid the direct incoming beams to damage the electronics. The used Hamamatsu Orca Flash4.0s CMOS camera allows a maximum frame rate of 100 frames/s. While the PEC is rotating, 1500 radiographs at different angles can be recorded in a few seconds, which allows high-quality 3-D reconstruction renderings.

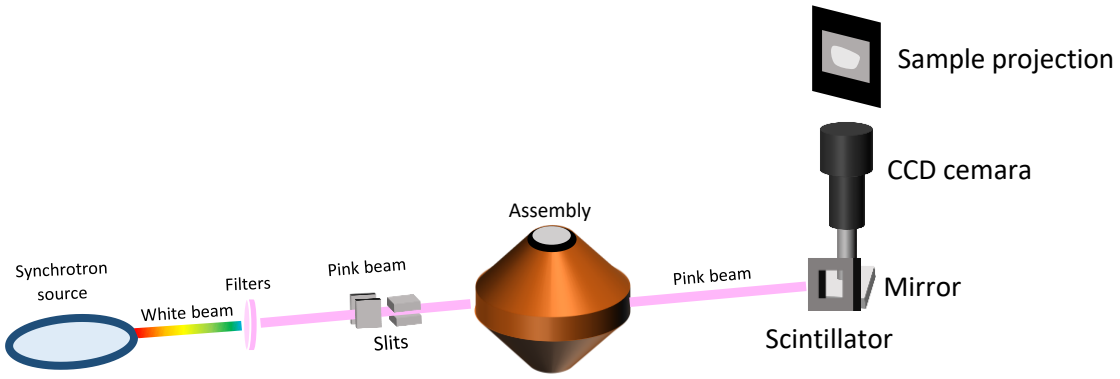

Fig. 2.11 A schematic of the setup and beam path for tomography acquisition.

The tomography images were integrated by the *ImageJ* software, and the 3-D volume rendering was reconstructed by the *Blob 3D* software. The tomography images served as important evidence for judging the status of the sample, such as the phase, homogeneity, deformation, leak, etc. Fig. 2.12 is an example of a liquid sample in a BN capsule at high temperature and pressure, and its 3-D reconstruction. Fig. 2.13 shows the evolution a liquid sample in a sapphire capsule with the temperature increase.

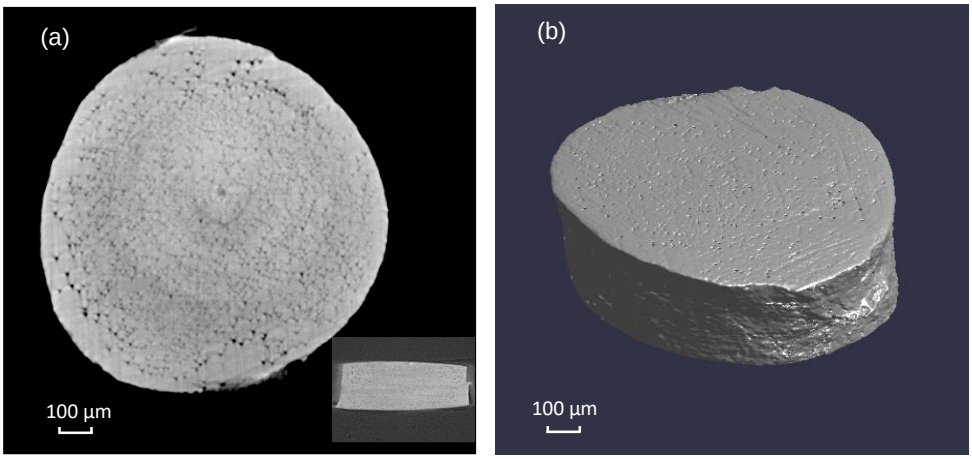

Fig. 2.12 (a) Reconstructed horizontal slice viewed from the top and from the side (inset) of Fe-5 wt%C inside a BN capsule, obtained using the software *ImageJ*. (b) 3D volume rendering of the sample by software *Blob 3D*.

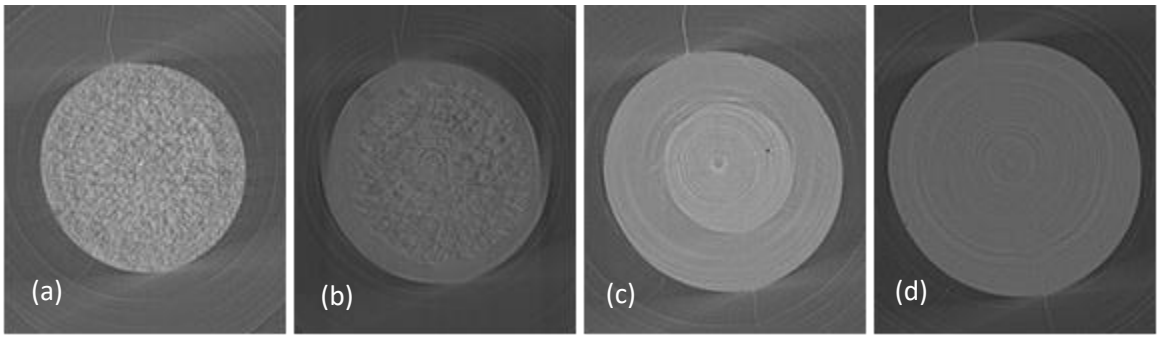

Fig. 2.13 The horizontal slice of an Fe-C-S sample in a sapphire capsule at 2.6 GPa upon heating. (a) Solid sample composed of Fe, FeS, and Fe_3C powders. (b) Onset of the melting. (c) 2 immiscible liquids with the bright Fe-rich part in the center and the dark S-rich part around. (d) The liquid became miscible at a higher temperature.

2.3.4 Quench experiments

Certain physical properties, including phase diagram, elemental diffusion, partitioning, melting temperature and liquid-liquid immiscibility can be studied even without in-situ diagnostics. Liquid samples will reach an equilibration relatively fast (normally tens of seconds) (Thibault and Walter, 1995) after having reached a fixed temperature and pressure, both in terms of homogeneity, textures, or miscibility. If a sample experiences a fast quench from liquid to solid phase at this condition, the textures and miscibility status will be retained since there is not enough time to re-equilibrate. Thus the recovered samples can be studied by imaging and analytical techniques, such

as scanning electron microscopy or electron microprobe, to study its chemical and physical properties. These are often called ‘cook-and-look’ experiments.

The ‘cook-and-look’ experiments are usually performed in the context of geophysical studies to determine the phase transition of minerals (Kanzaki, 1991; Kojitani et al., 2007), and miscibility of liquid compounds and mixtures (Corgne et al., 2008; Dasgupta et al., 2009). Large-volume pressure devices, such as Multi-anvil presses, Piston cylinders, and Paris-Edinburgh presses, are more often employed. Switching off the DC power supply, combined with an effective cooling system, can cool down the sample from the experimental conditions down to ambient temperature in few seconds, leaving the high-T phases or texture unchanged.

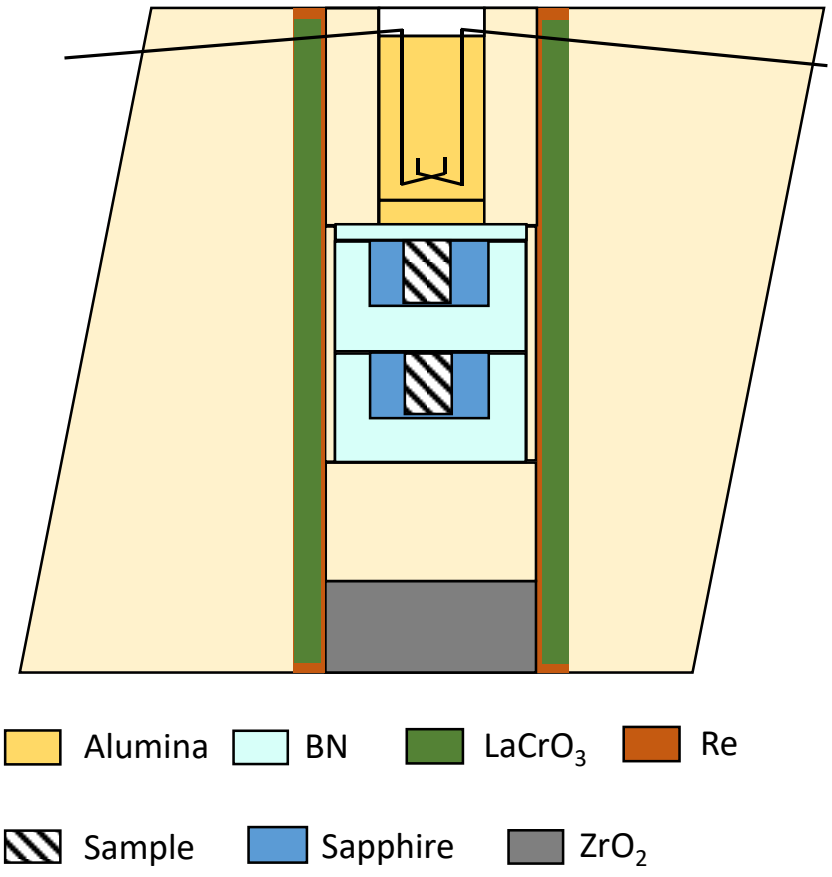

Fig. 2.14 A schematic of the of the MA 14-8 assemblies used at in IMPMC.

For miscibility study of Fe-C-S alloys, a first series of "cook-and-look" experiments were carried out in a multi-anvil press with the 18/11 assemblies at the Laboratoire Magmas et Volcans (LMV), Clermont-Ferrand, and a second series with 14/8 assemblies at the Institut de minéralogie, de physique des matériaux et de cosmochimie (IMPMC), Paris. As the first series of samples experiencing severe leak after melting in the BN capsule, a sapphire ring was employed for the second series of experiments at IMPMC. $LaCrO_3$ sleeves and Re foils were employed as heaters for runs at LMV and IMPMC, respectively. In both cases, type-C W/Re thermocouples were placed on the top of the capsule to monitor the temperature, and the pressure exerted on the sample defined by the hydraulic pressure based on a calibration curve. The schematic of the assembly used at IMPMC is shown in Fig. 2.14. Similar to the protocol used for PE cell, the samples were first the cold compressed, and then the temperature was raised at an average rate of 100K/min by increasing the power in the resistive heater. In the early experiments without a sapphire ring, after melting, the liquid samples often reached the furnace and destroyed it in a few seconds, while for the runs with a sapphire ring, the samples were kept either at 1650K or 2000K for tens of seconds before quench, which is achieved by switching off the power.

After experiments, all the recovered samples from both PE cell and MA press were mounted in epoxy resin and polished for analysis.

2.4. Liquid structure and its relation with diffraction signals

Unlike the crystal state in which the position of all the atoms are well located around equilibrium positions, liquids exhibit only short range order, with fluctuation in terms of atomic distribution, and this fluctuation disappears at long distance. The common concepts of crystal structure and symmetry are no longer suitable for liquids. Instead, the concept of distribution function is usually employed to characterize the liquid structure.

To introduce the distribution function, we consider first the one-dimension case. Assuming N atoms located a positions $x_1, x_2, \ldots, x_N$ in the region from 0 to L, as shown in Fig. 2.15, the one-body density at any arbitrary position can be written as

$$\rho_1(x) = \sum_{1}^{N} \delta(x - x_i) \tag{2.4}$$

where the $\delta(x - x_i)$ is the δ-function suggested by Dirac. The total atomic number N is thus equal to the integration of the number density:

$$\int_0^L \rho_1(x)dx = N \tag{2.5}$$

Similarly, we consider the pairs of the atoms for the two-body density (such as (x_1, x_2), (x_1, x_3), ..., (x_1, x_N)). In this case the two-body density number is written as

$$\rho_2(x, x') = \sum_{i=1}^{N} \sum_{j=1 \neq i}^{N} \delta(x - x_i)\, \delta(x - x_j) \tag{2.6}$$

Since the total pair quantity is $N(N-1)$, we obtain the following relation:

$$\int_0^L \int_0^L \rho_2(x, x')\, dxdx' = N(N-1) \tag{2.7}$$

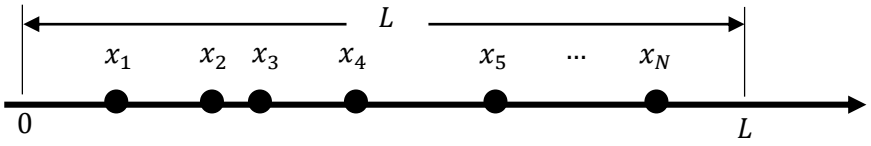

Fig 2.15 Schematic distribution of N atoms in a line

When it is extended to the real space, the atomic positions are replaced by $\boldsymbol{r}_1, \boldsymbol{r}_2, \boldsymbol{r}_3, \ldots, \boldsymbol{r}_N$., where $\boldsymbol{r}_i$ is the position vector pointing at the *i*-th atom. Rewriting the Eq. (2.4-2.7), we obtain the following equations:

$$\rho_1(\boldsymbol{r}) = \sum_{1}^{N} \delta(\boldsymbol{r} - \boldsymbol{r}_i) \tag{2.8}$$

$$\rho_2(\boldsymbol{r}, \boldsymbol{r}') = \sum_{i=1}^{N} \sum_{j=1 \neq i}^{N} \delta(\boldsymbol{r} - \boldsymbol{r}_i)\, \delta(\boldsymbol{r} - \boldsymbol{r}_j) \tag{2.9}$$

$$\int_V \rho_1(\boldsymbol{r})dv = N \tag{2.10}$$

$$\int_V \int_V \rho_2(\boldsymbol{r}, \boldsymbol{r}')\, dvdv' = N(N-1) \tag{2.11}$$

The above discussion is based on one set of $\boldsymbol{r}_1, \boldsymbol{r}_2, \boldsymbol{r}_3, \ldots, \boldsymbol{r}_N$. Next, we assume this quantities $\boldsymbol{r}_1, \boldsymbol{r}_2, \boldsymbol{r}_3, \ldots, \boldsymbol{r}_N$ have various values. In these cases, the potential energy of the system has the following form

$$\Phi = \phi(\boldsymbol{r}_1, \boldsymbol{r}_2, \boldsymbol{r}_3, \ldots, \boldsymbol{r}_N) \tag{2.12}$$

According to the statistical mechanics, the probability of finding the atomic positions $\boldsymbol{r}_1, \boldsymbol{r}_2, \boldsymbol{r}_3, \ldots, \boldsymbol{r}_N$ in the small volumes $dv_1, dv_2, dv_3, \ldots, dv_N$ is proportional to the factor

$$\exp[-\Phi/k_B T]\, dv_1, dv_2, dv_3, \ldots, dv_N \tag{2.13}$$

where k_B is the Boltzmann constant and T the temperature. Using the probability factor, we can consider the average of the quantity in Eq. (2.10) and Eq. (2.11). This process is denoted by $\langle\ \rangle_{Avg}$, and Eq. (2.10) and Eq. (2.11) are rewritten as

$$\int_V n_1(\boldsymbol{r})dv = N \tag{2.14}$$

$$\int_V \int_V n_2(\boldsymbol{r}, \boldsymbol{r}')\, dvdv' = N(N-1) \tag{2.15}$$

with

$$\langle \rho_1(\boldsymbol{r}) \rangle_{Avg} = n_1(\boldsymbol{r}) \tag{2.16}$$

$$\langle \rho_2(\boldsymbol{r}, \boldsymbol{r}') \rangle_{Avg} = n_2(\boldsymbol{r}, \boldsymbol{r}') \tag{2.17}$$

Here *n* is called density function. Combining the Eq. (2.14) and Eq. (2.15), we have the following relation:

$$\int_V n_2\,(\boldsymbol{r},\boldsymbol{r}')dv' = (N-1)\,n_1(\boldsymbol{r}) \tag{2.18}$$

Next, we define the function $g(\boldsymbol{r},\boldsymbol{r}')$ in last equation

$$n_2(\boldsymbol{r},\boldsymbol{r}') = n_1(\boldsymbol{r})g(\boldsymbol{r},\boldsymbol{r}') \tag{2.19}$$

Since in a homogeneous system the one-body density function is independent of $\boldsymbol{r}$, it is denoted as ρ_0, so that

$$n_1(\boldsymbol{r}) = \rho_0, \qquad \rho_0 = N/V \tag{2.20}$$

Therefore, $n_2(\boldsymbol{r},\boldsymbol{r}')$ is a function of only r $= |\boldsymbol{r}-\boldsymbol{r}'|$ and

$$n_2(r) = \rho_0 g(r) \tag{2.21}$$

The $g(r)$ is called pair distribution function and generally used to characterize the local structure of liquids.

As the density function approach the average density as r increase, the following relation holds:

$$\lim_{r\to\infty} g(r) = 1 \tag{2.22}$$

Next, we talk about the relationship between the liquid structure and the diffraction pattern we collect from experiments.

With the wave vector of incident and scattered beam denoted as $\boldsymbol{Q_{in}}$ and $\boldsymbol{Q}_{out}$, the scattering momentum Q is obtained by

$$Q = |\boldsymbol{Q_{in}} - \boldsymbol{Q}_{out}| = 4\pi sin\theta/\lambda \tag{2.23}$$

where θ is half the scattering angle and λ the wavelength of the beam.

The $I(Q)$ collected during experiments can be written as the sum of three parts, the coherent and incoherent scattering signal from the sample, and the background from surrounding materials:

$$I_{meas}(Q) = \frac{1}{\alpha}[I_{coh}(Q) + I_{incoh}(Q) + bI_{bkg}(Q)] \tag{2.24}$$

where $I_{meas}(Q)$ is the measured signal, $I_{coh}(Q)$ and $I_{incoh}(Q)$ the coherent and incoherent scattering signal from the sample, $I_{bkg}(Q)$ the background signal from surroundings, α the normalization factor, and b the background factor. Thus, the coherent scattering term is written as:

$$I_{coh}(Q) = \alpha I_{meas}(Q) - I_{incoh}(Q) - bI_{bkg}(Q) \tag{2.25}$$

Following the definition by Eggert, 2002, the coherent scattering intensity $I_{\mathrm{coh}}(q)$ of a polyatomic material is expressed as

$$I_{coh}(Q) = N\sum_{p} f_p^2(Q) + N\sum_{p}\sum_{q}\int_{S} f_p(Q)f_q(Q)\rho_{p,q}(r)\frac{sinQr}{Qr}dV \tag{2.26}$$

where N is the total number of compositional units in the sample, $f(Q)$ the atomic factor of the corresponding atom, $\rho(r)$ the average atomic density function, and r the distance between two atoms. Similar to the two-component system described in Waseda 1980, we define the following functions for multi-component cases (Morard et al., 2007 and 2014):

$$\frac{1}{N}\sum_{p} f_p^2(Q) = \sum_{i} X_i f_i^2(Q) = \langle f^2 \rangle \tag{2.27}$$

$$\frac{1}{N}\sum_{p}\sum_{q} f_p(Q)\, f_q(Q) = \sum_{i}\sum_{j} X_i f_i(Q)\, X_j f_j(Q) = \langle f \rangle^2 \tag{2.28}$$

$$\sum_{p}\sum_{q} X_p X_q f_p(Q)\, f_q(Q)\, \rho_{p,q}(r)/\langle f \rangle^2 = \rho(r) \tag{2.29}$$

where X_i is the atomic content of element i. Then the coherent signal is defined as

$$I_{coh}(Q) = \langle f^2 \rangle + \langle f \rangle^2 \times \int_0^\infty 4\pi r^2 [\rho(r) - \rho_0] \frac{sinQr}{Qr} dr \tag{2.30}$$

where ρ_0 is the average atomic density. Following the Faber-Ziman definition, the structure factor $S(Q)$ is given by the equation

$$\begin{aligned} S(Q) = \frac{I_{coh}(Q) - (\langle f^2 \rangle - \langle f \rangle^2)}{\langle f \rangle^2} &= \frac{[\alpha I_{meas}(Q) - I_{incoh}(Q)] - (\langle f^2 \rangle - \langle f \rangle^2)}{\langle f \rangle^2} \\ &= 1 + \int_0^\infty 4\pi r^2 [\rho(r) - \rho_0] \frac{sinQr}{Qr} dr \end{aligned} \tag{2.31}$$

The normalization factor α can be determined following the procedure in Krogh-Moe, 1956 and Normal, 1957, used for the normalization of diffraction signal collected over a limited Q range. The α is determined by the following equation

$$\alpha = \frac{-2\pi^2 \rho_0 + \int_0^{Q_{max}} \frac{I_{incoh}(Q) + \langle f^2 \rangle}{\langle f \rangle^2} Q^2 dQ}{\int_0^{Q_{max}} \frac{I_{meas}(Q)}{\langle f \rangle^2} Q^2 dQ} \tag{2.32}$$

where the Q_{max} is the maximum scattering momentum the experiments reached. After a Fourier transform, the structure factor is transformed to the atomic distribution in the real space:

$$F(r) \equiv 4\pi r[\rho(r) - \rho_0] = \frac{2}{\pi} \int_0^{Q_{max}} Q[S(Q) - 1] \sin(Qr) dQ \tag{2.33}$$

where $F(r)$ is called distribution function, and '≡' represents definition. The pair distribution can be thus calculated as

$$g(r) \equiv \frac{\rho(r)}{\rho_0} = 1 + \frac{F(r)}{4\pi r \rho_0} \tag{2.34}$$

2.5 Density from diffraction – CAESAR data treatment

The raw CAESAR data consist in a 2-dimensional plot with the intensity as a function of 2θ and energy. To eliminate the effect due to the different exposure time depending the angle range (see section 2.3.1 and Fig.2.16 (a)), the I (2θ, energy) must go through a pre-normalization process to generate the pattern with normalized exposure time (Fig. 2.16 (b)). After the pre-normalization, the effect related to the non-uniform spectral content of the incoming beam, due to the source and optics, was considered. In particular, as shown in Fig. 2.16 (c), the intensity below 30 keV and at energy higher than 70 keV is too weak so that the obtained diffraction signal in these two energy ranges results too noisy. The diffraction pattern was therefore normalized with respect to the intensity spectrum of the incoming beam, truncating the signal above and below the selected energy threshold. The 2-dimensional plot was then converted in a 1-dimensional plot showing the intensity as a function of Q ready for structure analysis. Fig. 2.17 shows the filtered spectrum and the final $I(Q)$. It's worth to stress that the high-brilliance light source of Synchrotron SOLEIL and the available setup at PSICHE beamline allows obtaining data over large energy and 2θ range, enabling an extended Q range up to 20 $Å^{-1}$. This permits accessing to more information concerning local structure of liquids and amorphous systems compared to the regular angle-dispersive diffraction.

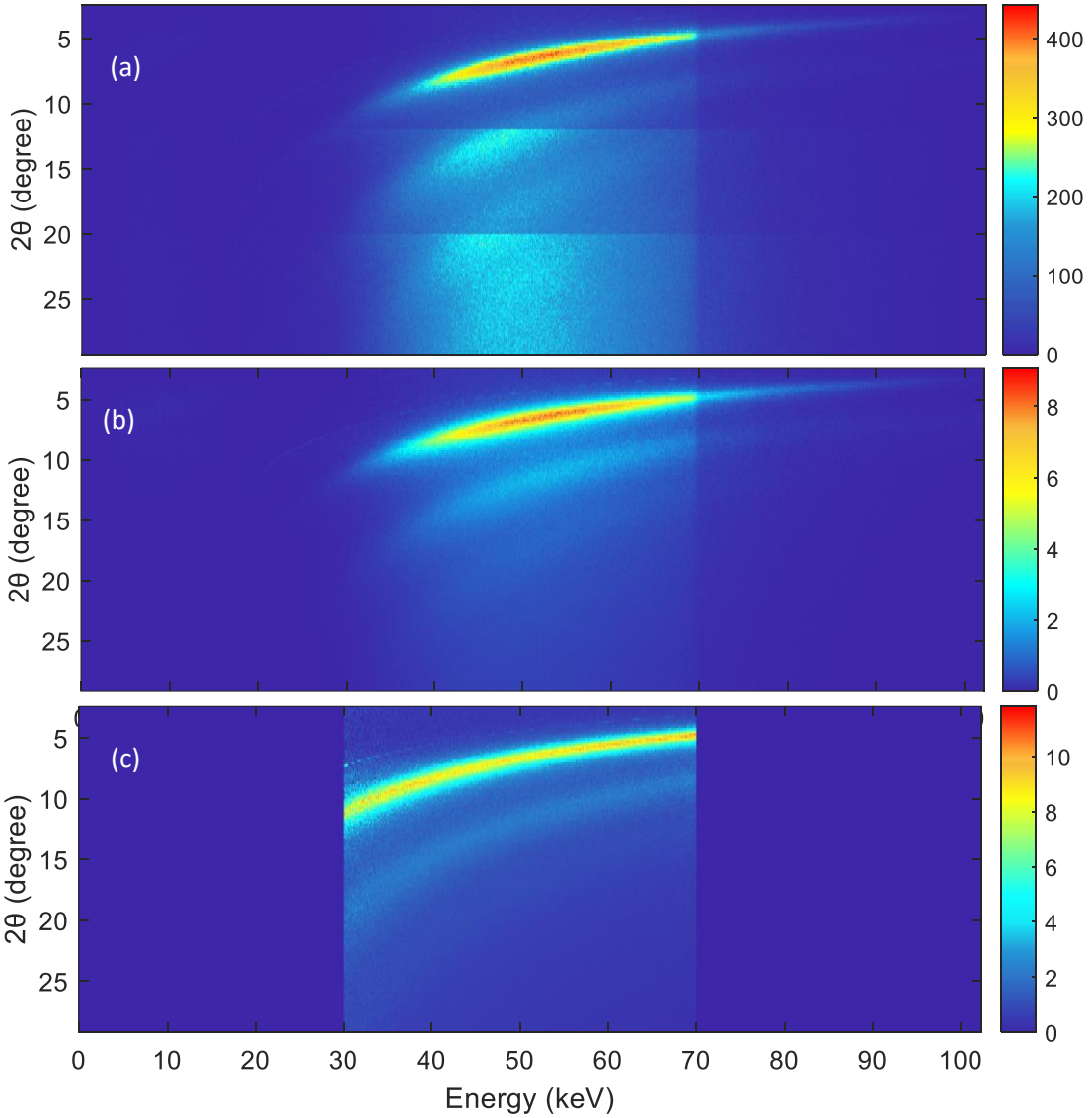

Fig. 2.16 The procedure for raw CAESAR data treatment of an Fe-C-S sample at 3.7 GPa and 1850 K. (a) The raw data of intensity as a function of 2θ and photon energy are collected with different exposure time in three angle ranges, *i.e.* 5s, 10s, and 20s for 2.5-12 °, 12-20 °, and 20-29.1 °, respectively. (b) The pattern is pre-normalized taking into account the exposure time and diffracting volume. (c) The pattern of intensity is then normalized with respect to the energy spectrum of the incoming beam.

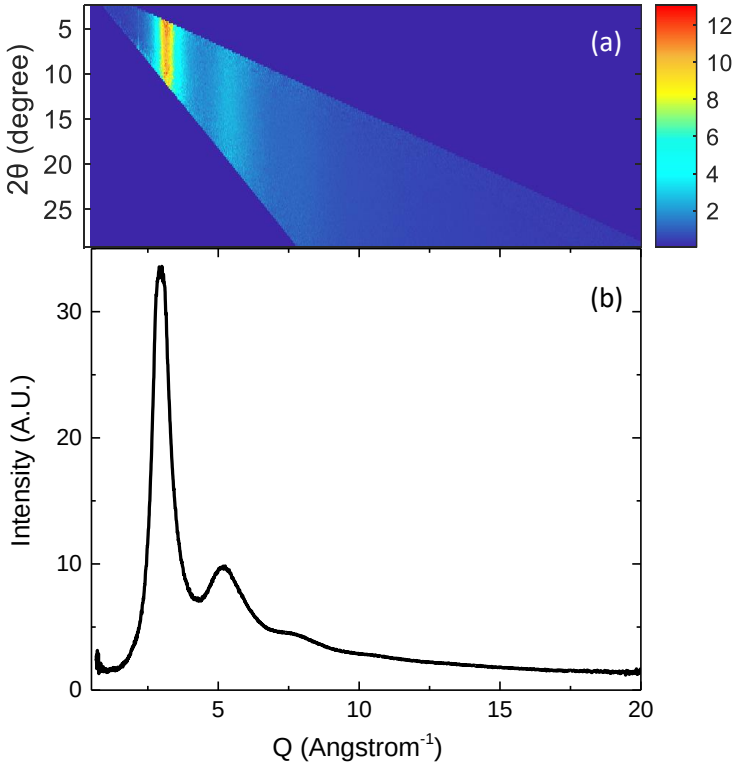

Fig. 2.17 Re-arrangement of the CAESAR data. (a) The pattern of intensity as a function of *Q* and 2θ re-arranged from the CAESAR data. (b) The intensity as a function of *Q* by taking the average intensity at each *Q* value in (a).

The obtained $I(Q)$ was analyzed by the Python-based program Amorpheus (Boccato et al., 2022) to calculate the structure factor and pair distribution function, according to the procedure described in section 2.4. To extract the average density we followed the approach detailed in (refs). In brief, we focus on a limited *r* range and the low-r portion of $F(r)$ and $g(r)$. Since no atom exists within a certain distance (r_{min}) to another one because of the repulsive force, the $\rho(r)$ equals to 0 in this range, which results in

$$g(r) = 0 \ (r < r_{min}) \tag{2.35}$$

$$F(r) = -4\pi r \rho_0 (r < r_{min}) \tag{2.36}$$

The $F(r)$ becomes linear in this range and its slope determines the density. In practice an iterative procedure is needed to reduce the oscillation in the low *r* region, and the $S(Q)$ at $i+1$th iteration is calculated by the inverse Fourier transform:

$$S_{i+1}(Q) = S_i(Q)\left[1 - \frac{1}{Q}\int_0^{r_{min}} \Delta F_i(r)\sin(Qr)\,dr\right] \tag{2.37}$$

with the $\Delta F(r)$ in the first iteration using an estimated initial value ρ_0:

$$\Delta F_0(r) = -F_0(r) - 4\pi r\rho_0 \tag{2.38}$$

The number of iterations is set to 5 to ensure the convergence. Fig. 2.18 shows the iteration procedure for the distribution function $F(r)$ for an example case.

The final average atomic density is determined by minimizing a figure of merit:

$$\chi^2(r_{min}, Q_{max}, \rho_0) = \int_0^{r_{min}} [\Delta F(r)]^2 dr \tag{2.39}$$

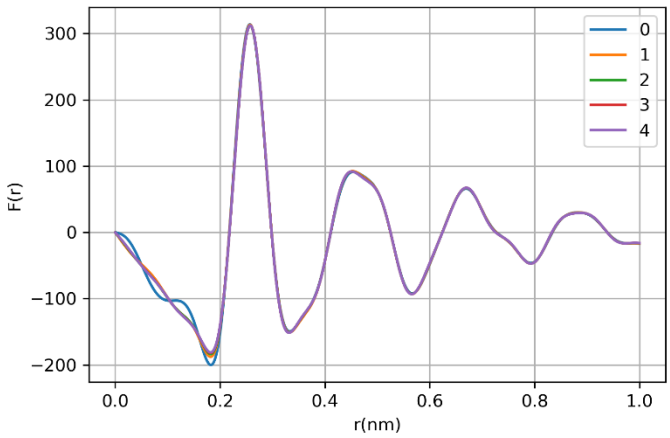

Fig. 2.18 The iterative procedure for the minimization of the oscillations in the low-r portion of the distribution function $F(r)$. Typically converge is attained after the 2nd iterations, and $F(r)$ becomes a straight line for $r < r_{min}$., while it is not affected at $r > r_{min}$. This example is for an Fe-C-S sample at 3.7 GPa and 1850 K.

In this way the value of ρ_0 is determined for a given pair of r_{min} and Q_{max} when the χ^2 reaches the minimum. A double loop on r_{min} and Q_{max} is usually done to search for the minimum of χ^2.

All the inputs including the background, energy range, r_{min}, and Q_{max} have an impact on the results of the inversion. Here we discuss how the selection of the inputs influences the structure and density.

(1) Energy range

The energy range should be first determined during the raw data treatment. As mentioned in the beginning of this section, in our case only the signal in a range from 30-70 keV was retained because of the intensity profile of the incoming beam. Figure 2.19 shows the *I*(*Q*) when choosing a wider energy range, as large as 20-100 keV. After numerous tests, the 30-70 keV range has been selected as the preferred energy range, since this minimizes the noise while cutting at minimum the collected data.

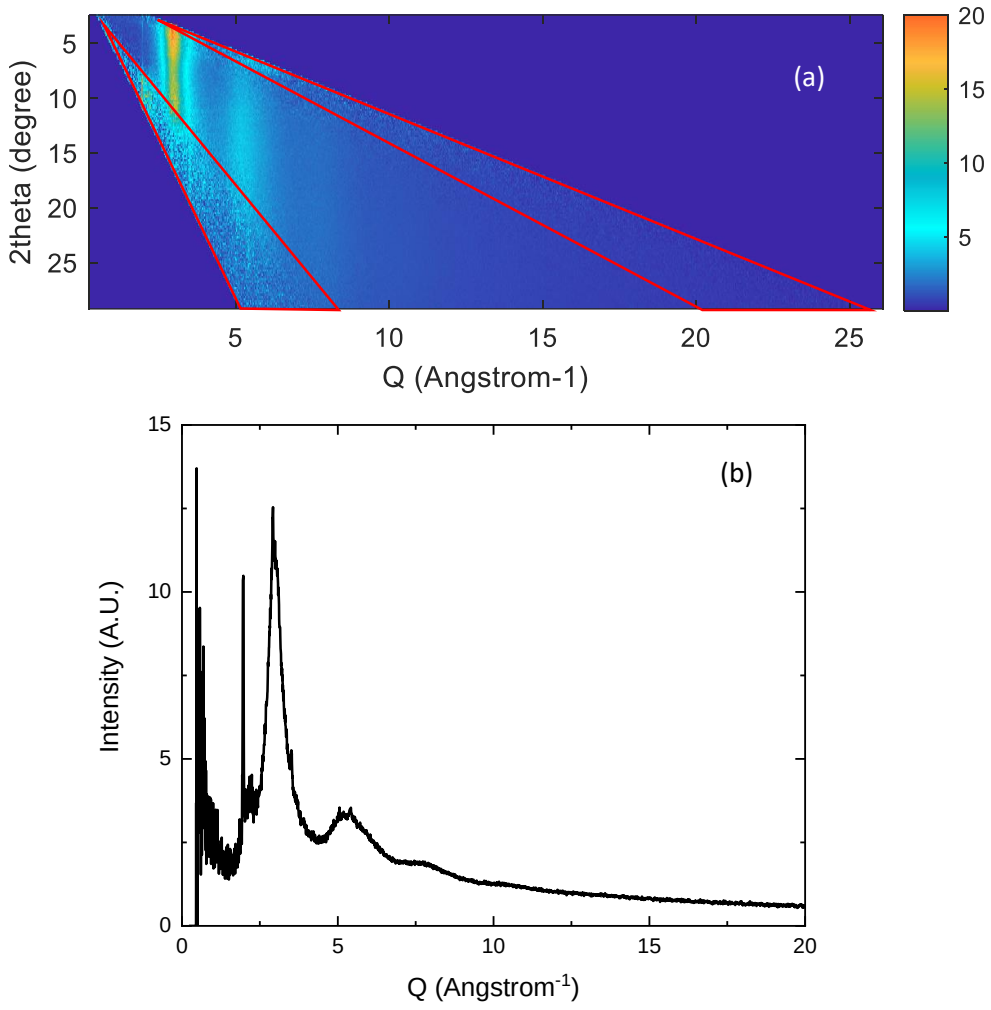

Fig. 2.19 Re-arranged CAESAR pattern (a) and the corresponding $I(Q)$ (b) when considering the energy range 20-100 keV. Compared to the pattern in Fig. 2.17 the pattern is much more noisy. The noise arises from the low-energy and high-energy signals (shown by the red triangles), affected by the limited incoming flux due to the spectral content of the source. This is directly reflected on the derived $I(Q)$, especially at low Q.

(2) Background

After having obtained a suitable diffraction pattern $I(Q)$, the background should be considered. Generally speaking, within the background we include all signals except the coherent scattering from the sample, thus including incoherent scattering from the sample, scattering from the surroundings, and absorption by the sample. As shown in Fig. 2.20, the incorrect subtraction of the background would led after iterations to the deviation of the $g(r)$ and $S(Q)$ in the range of $r > r_{min}$. If the signal is a pure coherent scattering, the iterations should affect only in the low-r range (see Fig. 2.18 and Fig. 2.20), as result of the cut-off effect of $S(Q)$ with limited Q range during the Fourier transform.

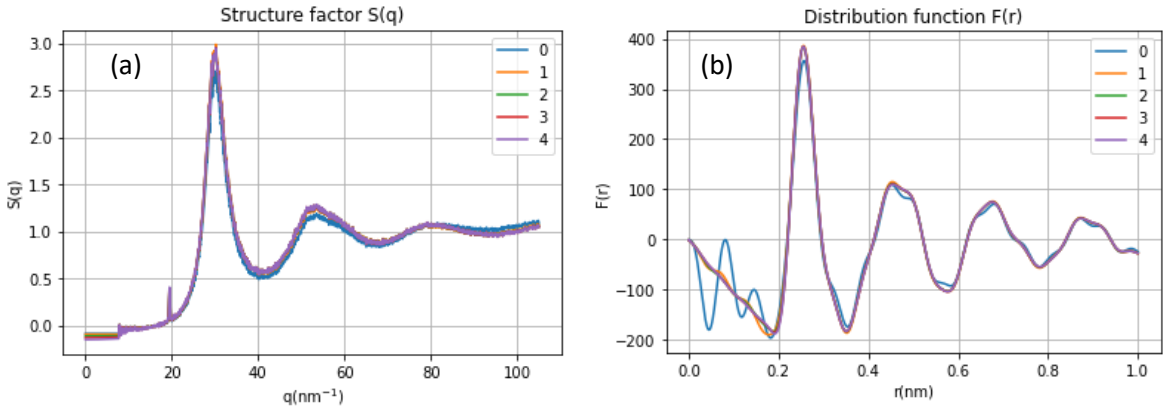

Fig. 2.20 (a) The structure factor of an Fe-C-S sample at 2.15 GPa and 1895 K as an example. (b) The distribution function after Fourier transform. If the background is not properly removed, differently from what shown in Fig. 2.20, the iterations lead to deviations of both $S(Q)$ and $F(r)$ from the original values for $r > r_{min}$. This distortion will reflect into the slope of the low-r region in $F(r)$, thus the density.

In order to evaluate the background, we acquired a CAESAR scan on both an empty cell and a cell with solid sample before melting. The background extracted from the two scans is shown in Fig. 2.21. While the background from an empty cell contains only the component of scattering from the surroundings, we can consider that the background taken from the cell with a solid sample also accounts for incoherent scattering from the sample and self-absorption. The $S(Q)$ and $g(r)$ after

iterations also supports the notion that the background extracted from solid sample works well for the analysis of all the liquid samples investigated in this work. Fig. 2.22 shows an example of the $S(Q)$ and $g(r)$ after the background subtraction *i.e.* processed assuming the signal coming only from pure coherent scattering. Compared to Fig. 2.20, there is almost no deviation on the $S(Q)$ and $g(r)$ in $r > r_{min}$.

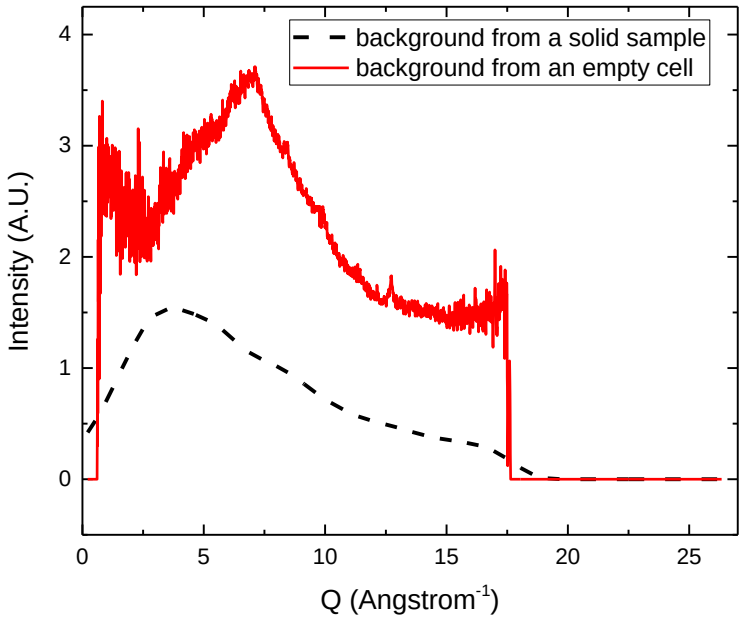

Fig. 2.21 The background extracted from a solid sample and that from an empty cell. The high frequency noises in the background from the sample have been filtered out.

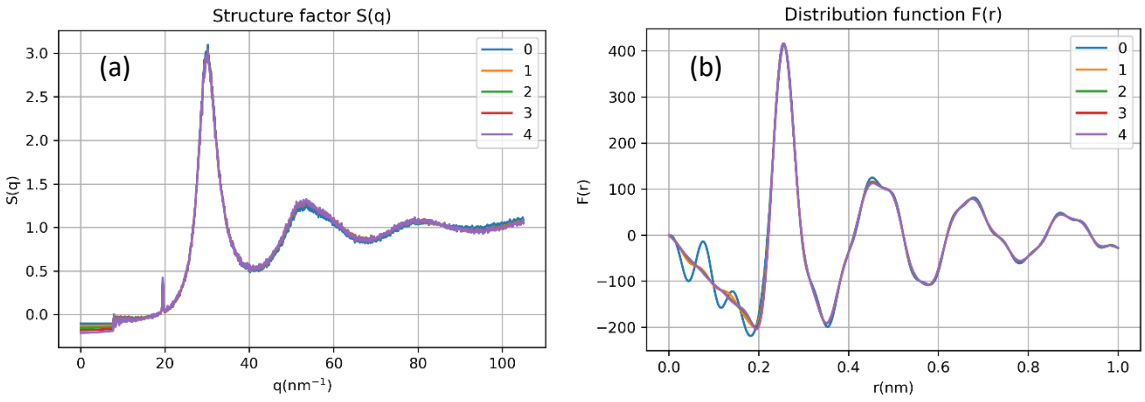

Fig. 2.22 The structure factor (a) and distribution function (b) of an Fe-C-S sample at 2.15 GPa and 1895 K (same as in Fig. 2.20) after the subtraction of the background. There is much less deviation compared with Fig. 2.20, although some issue related to residual background remains. Possibly this arises from subtle

differences in the background from each sample due to the composition difference, compression status, etc. This residual background yields an overall limited uncertainty on the density, which can be neglected.

(3) r_{min} and Q_{max}

r_{min} and Q_{max} is a pair of the input parameters to be refined when running the Amorpheus software. For each given value of r_{min}, and Q_{max}, the ρ_0 and corresponding χ^2 are calculated, so that all the parameters are fixed when χ^2 reaches a minimum. However, it is interesting to consider how the local minima in χ^2 (and corresponding densities) vary when considering different r_{min} or Q_{max} as shown in Fig. 2.23. In fact, even though χ^2 reaches a minimum at several r_{min} value, nor all r_{min} are equivalent as can be judged from the shape of $g(r)$. For the "correct" r_{min} value, the $g(r)$ in the low r region is flat and starts to increase at $r = r_{min}$, otherwise the $g(r)$ shows a distortion around $r = r_{min}$, which makes no physical sense. With a wrong r_{min} we note large difference in the density determined from the correct r_{min}. In other words, the correct r_{min} is crucial for a reliable density determination.

In terms of Q_{max}, the value of χ^2 shows periodically local minima over a range of Q_{max}, which is attributed to the shape of $I(Q)$ and the preferred cut at a certain Q values (and hence the shape after the Fourier transform). To minimize the χ^2, Q_{max} should be chosen with full oscillations included or excluded. In theory, the selection of Q_{max} won't significantly affect the density, because the cut-off effect is not prominent if one further full oscillation is included or not (for instance choosing Q_{max}= 78 or 103) and after iterations the $g(r)$ regularly converges. For instance, in the example here considered, the obtained atomic density are 83.8, 82.8, and 83.2 at Q_{max}= 78, 103, and 132, respectively (see Fig. 2.23 (b)). Given the limited effect on density, for the purpose of this work and for consistency, the Q_{max} around 80 yielding the minimum value of χ^2 is employed for all the samples.

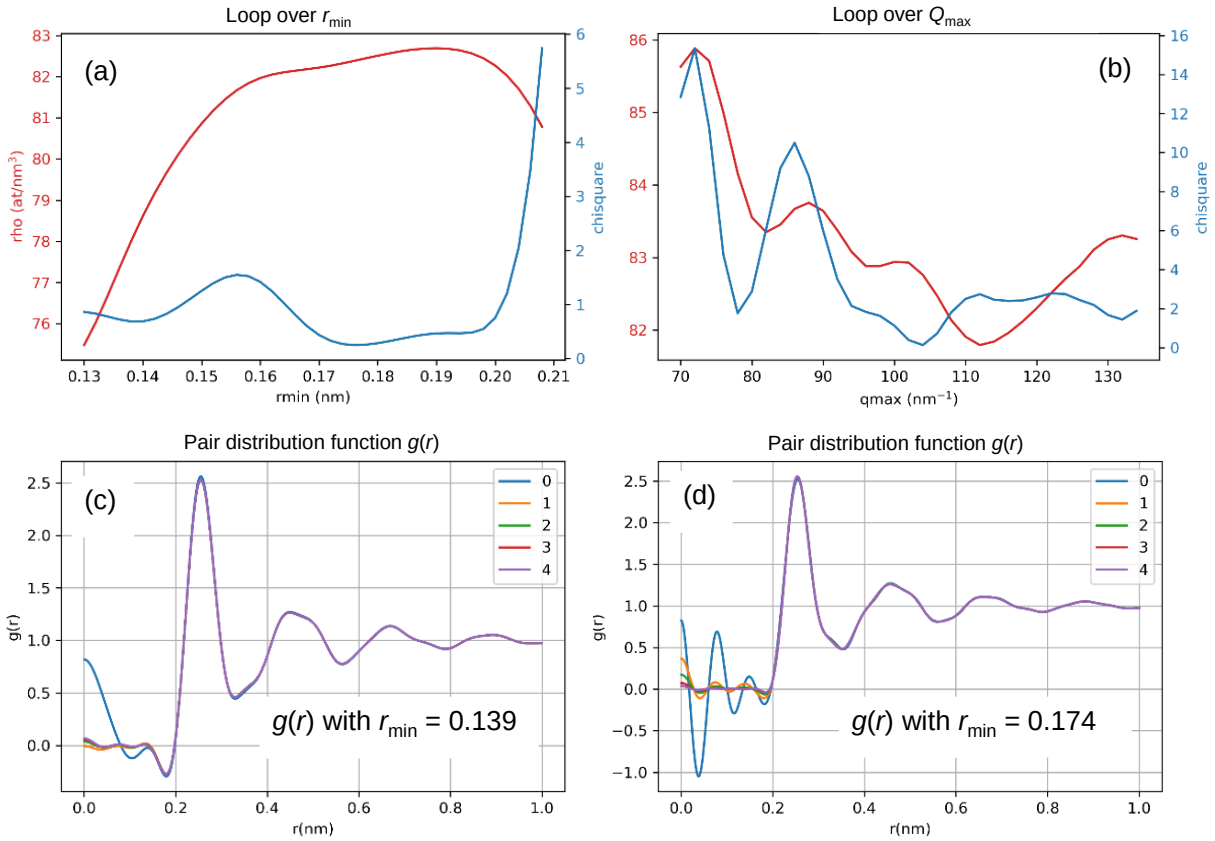

Fig. 2.23 (a) A loop for searching for $r_{\min}$ that yields the minimum of χ^2 with a given Q_{max}. (b) A loop for searching for Q_{max} that yields the minimum of χ^2 with a given r_{min}. The $\chi^2$is shown in blue and the corresponding atomic density in red. In the loop over r_{min}, the χ^2 reaches the minimum at 0.139 nm and 0.174 nm respectively, while in the loop over Q_{max}, the χ^2 reaches the minimum periodically at Q=78, 103, and 132. (c) and (d) The pair distribution function calculated with an r_{min} =0.139 and 0.174, respectively.

It is worth noting that Fig 2.23 is employed to illustrate only the independent effect of $r_{\min}$ and Q_{max} on the χ^2. In practice, a double-loop over $r_{\min}$ and Q_{max} is carried out to seek the minimum of χ^2, which generates a 3-D plot shown in Fig. 2.24.

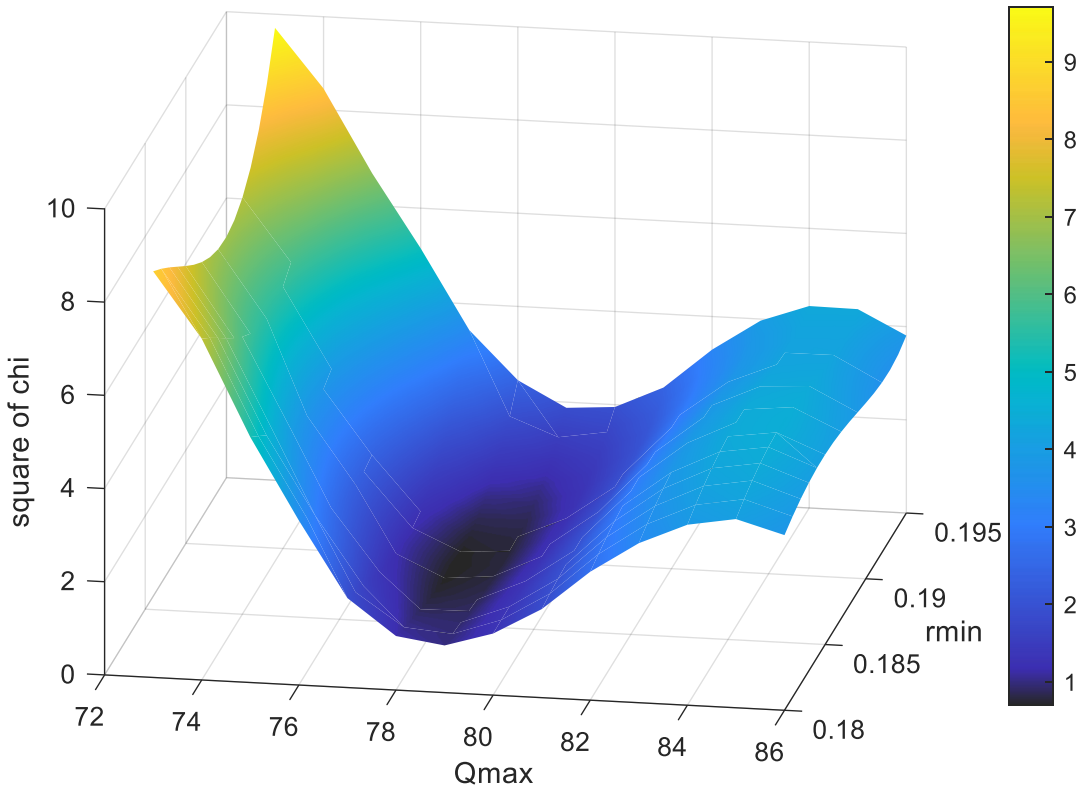

Fig. 2.24 The loop for searching the minimum of χ^2 over a series of r_{min} for an Fe-C-S sample. The χ^2 reaches a local minimum when the r_{min} = 0.182 nm and Q_{max}=79 nm^{-1}, where the atomic density equals to 81.8, and the massive density 6780 kg/m^3.

2.6 Density from X-ray absorption – absorption profile treatment

Based on the Beer-Lambert law, and considering independent absorption by sample, capsule and environment, the ratio of the transmitted intensity over the incident intensity can be written according to Eq. (2.2) as follow:

$$\frac{I}{I_0} = \exp(-\mu_s\rho_s t_s - \mu_c\rho_c t_c - \mu_e\rho_e t_e) \tag{2.40}$$

where the subscripts *s*, *c*, and *e* represent sample, capsule, and environment, respectively.

In practice, the contribution from environment was observed to be negligible. Considering the geometry of the cylindrical capsule and sample, with the center noted by X_c, the intensity as a function of distance to the center could be written as

$$I = \begin{cases} I_0 \exp\left(-2\mu_c\rho_c\left(\sqrt{R-(x-X_c)^2}-\sqrt{r-(x-X_c)^2}\right)-2\mu_s\rho_s\sqrt{r-(x-X_c)^2}\right) & x < r \\ I_0 \exp\left(-2\mu_c\rho_c\left(\sqrt{R-(x-X_c)^2}\right)\right) & r < x < R \\ I_0 & x > R \end{cases} \quad (2.41)$$

where R and r are the radius of capsule and sample determined by the tomography at experimental condition, x is the distance to the sample center. Fig 2.25 shows the details of the geometry. The value of $\mu_c\rho_c$ and $\mu_s\rho_s$ can thus be determined by the fitting procedure. Fig. 2.26 is an example of raw data compared with the fitted data.

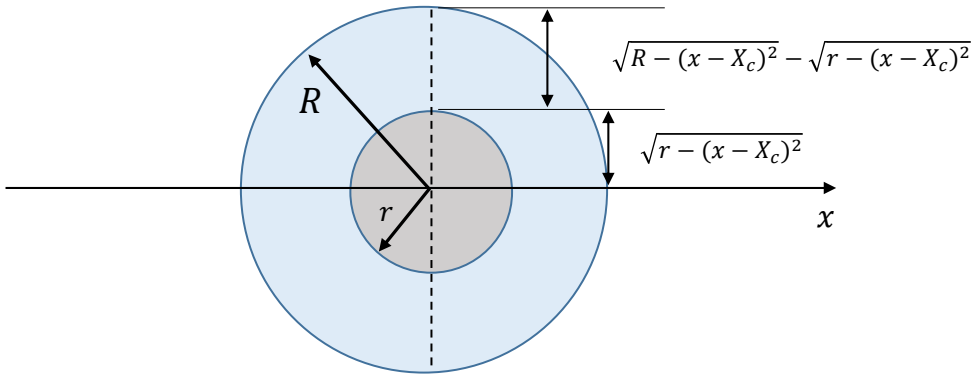

Fig. 2.25 Schematic of the assembly geometry. The cylindrical sample is shown in grey at the center, and the sapphire ring is shown in light blue. The intensity of collected beam is dependent on the thickness of each part indicated.

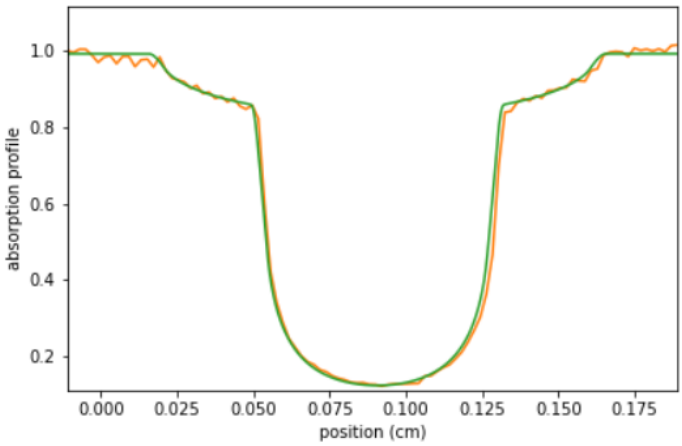

Fig. 2.26 Absorption profile after normalization (orange) in comparison with fitted data (green). This example is for an Fe-C-S sample at 4.92 GPa and 1610 K.

To extract the density of samples from the product $\mu_s\rho_s$, the value of μ_s is needed. The μ_s was estimated in two ways. The first approach is based on the formalism of the massive absorption coefficient of compounds in Eq. (2.3), with the μ of each component taken from the NIST Standard Reference Database. In the second approach we can calculate μ from an absorption scan and a diffraction pattern on solid before melting, which independently and respectively provide the product $\mu_s\rho_s$, and the density ρ_s of the solid sample. In the latter case, under the assumption than the mass absorption coefficient for a given compound does not significantly vary upon melting, the density of liquid samples at experimental conditions can be calculated by

$$\rho_{P,T} = \frac{(\mu\rho)_{P,T}}{(\mu\rho)_S/\rho_S} \tag{2.42}$$

where the subscript s represents the solid sample. Before melting, the sample density ρ_S is calculated from the measured unit-cell volume of each component extracted by diffraction and their known molar proportion.

2.7 The Margules formulism for liquid mixtures

2.7.1 Thermal equation of state

Several formalisms are used to characterize the volume as a function of pressure at constant temperature. Two widely used formalisms are the third-order Birch-Murnaghan equation of state (e.g. Poirier and Tarantola, 1998) and the Vinet equation of state (e.g. Vinet et al., 1986 and 1987). The former is written as:

$$P(V) = \frac{3}{2}K_0\left[\left(\frac{V_0}{V}\right)^{\frac{7}{3}} - \left(\frac{V_0}{V}\right)^{\frac{5}{3}}\right]\left\{1 + \frac{3}{4}(K' - 4)\left[\left(\frac{V_0}{V}\right)^{\frac{2}{3}} - 1\right]\right\} \quad (2.43)$$

and the latter as:

$$P(V) = 3K_0\left[\left(\frac{V_0}{V}\right)^{\frac{2}{3}} - \left(\frac{V_0}{V}\right)^{\frac{1}{3}}\right] exp\left\{\frac{3}{2}(K' - 1)\left[1 - \left(\frac{V_0}{V}\right)^{-\frac{1}{3}}\right]\right\} \quad (2.44)$$

where the V is the volume under pressure, V_0 and K_0 the volume and bulk modulus at zero pressure and reference temperature (normally room temperature), and K' the pressure derivative of bulk modulus. The Vinet EOS was originally developed for solids and later proven valid for modelling the low-temperature parameters of liquid metals (e.g. Komabayashi 2014; Knibbe et al., 2021). Here we also employ the Vinet formalism for Fe-C and Fe-S and their room-temperature parameters from literature.

As well, there are various thermal models to characterize the volume evolution at high temperature, which could be classified in three categories depending on the compression and heating route assumed in the model to link the reference P, T point to the considered P, T point. They are summarized in the table below. As indicated, various models are used in isochoric heating after cold compression, which differ in the way they account for the thermal pressure. As the thermal pressure is always produced during the heating, this formalism category does not allow to model the data at low pressure and high temperature simultaneously (e.g. Dorogokupets et al., 2007;

Miozzi et al., 2020). The hot compression after an isobaric heating (normally at ambient pressure) models the thermal expansion coefficient in the heating process, and the bulk modulus and its first derivative in the hot compression, all as a function of the temperature. Interested readers are referred to the bibliography.

Table 2.1 Various thermal models applied to different compression and heating routes

Route	Models
Cold compression→Isochoric heating	Holland-Powell model (e.g. Angel et al., 2017); Mie-Gruneisen-Debye (e.g. Miozzi et al., 2020); Einstein model (Dorogokupets et al., 2017)
Cold compression→Isobaric heating	Anderson-Gruneisen (e.g. Komabayashi 2014)
Isobaric heating→ Hot compression	Modified EOS (e.g. Zhao et al., 1997)

The Anderson-Gruneisen formalism adopted in this study is presented here in some more detail. In the Anderson-Gruneisen formalism, the thermal expansion is dependent on pressure, but not on temperature, and the value under pressure is evaluated by the Anderson-Gruneisen parameter δ_T (Boehler et al., 1990; Anderson et al., 1992),

$$\delta_T \equiv (\partial ln\alpha/\partial lnV)_T \tag{2.45}$$

and

$$\delta_T = \delta_0 \eta^{\kappa} \tag{2.46}$$

where δ_0 is the value of δ_T at 1 bar, $\eta = V/V_0$, and κ is a dimensionless thermos-elastic parameter. Eq. (2.45) and (2.46) yield

$$\frac{\alpha}{\alpha_0} = exp\left[-\frac{\delta_0}{\kappa}(1-\eta^{\kappa})\right] \tag{2.47}$$

where α_0 is the thermal expansion coefficient at 1 bar.

2.7.2 The mixing of solutions

2.7.2.1 Gibbs energy and mixing models

Considering a binary system as example, the composition of the system can vary from pure component A to B, with the Gibbs energy defined by the following equation

$$G = x_A G_A + x_B G_B + G_{mix} \tag{2.48}$$

G is the Gibbs energy of the system, and the components A and B are often called end members. The G_{mix} is called Gibbs energy of mixing, shown by the difference between the Gibbs energy of the system with the weighted sum of the Gibbs energy of the end members in Fig. 2.27. One significant source of the Gibbs energy of mixing is the mixing entropy of the two components, $RT(x_A \ln x_A + x_B \ln x_B)$, where R is the gas constant and T the temperature in K. A solution with the only entropy as the Gibbs energy of mixing is regarded as an ideal mixing. The Gibbs energy of a binary system based on ideal mixing can be thus expressed as

$$G = x_A G_A + x_B G_B + RT(x_A \ln x_A + x_B \ln x_B) \tag{2.49}$$

Differentiating the Gibbs energy yield the volume of the binary solution:

$$V = x_A V_A + x_B V_B \tag{2.50}$$

There are also other contributions to the Gibbs energy, called excess Gibbs energy. In fact, the excess contribution widely exists when mixing liquids (e.g. Morard et al., 2018), which can be defined in different ways depending on different models. This sort of model is called non-ideal mixing model. Accordingly, there will be an excess term for volume if derived with respect to pressure (more thoroughly discussed in the next section). The characteristic shape of the Gibbs energy with an excess contribution is also shown in Fig. 2.27. The next section will discuss a specific non-ideal mixing model adopted in this study.

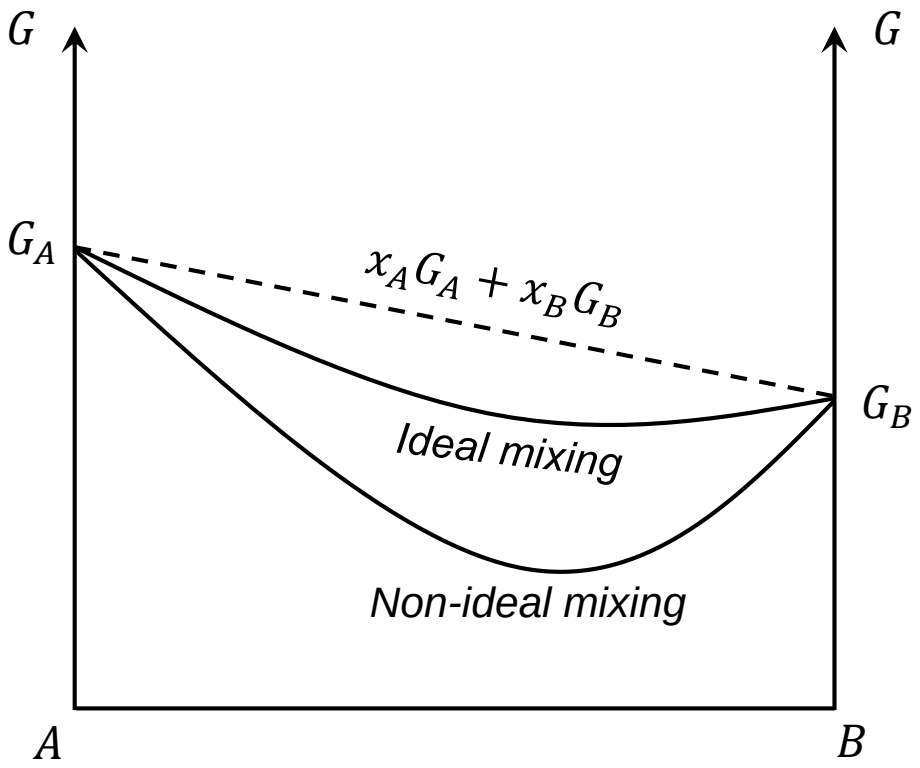

Fig. 2.27. Characteristic shapes Gibbs energy of ideal mixing and non-ideal mixing.

2.7.2.2 The Margules formalism for liquid mixtures

In an asymmetric Margules formulation, the non-ideality of the Gibbs energy of the component *i* of a mixture is described by the addition of an excess contribution:

$$G_i = G_{i0} + G_{i,ex}(W) \tag{2.51}$$

where G_i is the Gibbs energy of component *i*, G_{i0} the Gibbs energy at standard state, and $G_{i,ex}(W)$ the excessive Gibbs energy. W is the interactive Margules parameter which is assumed linear with pressure and temperature:

$$W(P,T) = W_0 + T \times W_S + P \times W_V \tag{2.52}$$

Deriving the Gibbs energy with respect to pressure, the volume of liquids mixture (here using Fe-C-S as an example) by end members (here using Fe, Fe_3C, and FeS as an example) is written as

$$V_{FeCS} = X_{Fe_3C}V_{Fe_3C} + X_{FeS}V_{FeS} + X_{Fe}V_{Fe} + X_{Fe_3C}V_{ex(\,Fe_3C)} + X_{FeS}V_{ex(\,FeS)} + X_{Fe}V_{ex(\,Fe)} \tag{2.53}$$

The additional terms are excessive contributions to the volume, which are functions of the fraction of each component. For instance, the excessive volume contribution from Fe, *i.e.* $V_{ex(\,Fe)}$ is related to the other end members by:

$$\begin{aligned} V_{ex(\,Fe)} = {} & X_{FeS}^2[W_{V,Fe-FeS} + 2X_{Fe}\left(W_{V,FeS-Fe} - W_{V,Fe-FeS}\right)] \\ & + X_{Fe_3C}^2[W_{V,Fe-Fe_3C} + 2X_{Fe}\left(W_{V,Fe_3C-Fe} - W_{V,Fe-Fe_3C}\right)] \\ & + 2X_{Fe}X_{FeS}X_{Fe_3C}\left(W_{V,FeS-Fe} + W_{V,Fe_3C-Fe}\right) \\ & - 2X_{Fes}X_{Fe_3C}\left(X_{FeS}W_{V,Fe_3C-FeS} + X_{Fe_3C}W_{V,FeS-Fe_3C}\right) \\ & + \frac{X_{Fe_3C}X_{FeS}(1-2X_{Fe})}{2}(W_{V,FeS-Fe} + W_{V,Fe-FeS} + W_{V,Fe_3C-Fe} \\ & + W_{V,Fe-Fe_3C} + W_{V,Fe_3C-FeS} + W_{V,FeS-Fe_3C}) \end{aligned} \tag{2.54}$$

with the ternary interaction term neglected. $W_{V,i-J}$ is the volume interaction Margules parameter, which characterizes the interaction intensity of components *i* and *j* (Tsuno et al., 2011). With the other two counterparts for FeS and Fe_3C, the mixed volumes given by Margules model are shown in Eq. (2.55).

$$\begin{aligned} \mathrm{V}_{Fe-C-S} = {} & \mathrm{X}_{Fe_3C}\mathrm{V}_{Fe_3C} + \mathrm{X}_{FeS}\mathrm{V}_{FeS} + \mathrm{X}_{Fe}V_{Fe} + \mathrm{X}_{Fe}X_{Fe_3C}^2W_{V,Fe-Fe_3C} \\ & + \mathrm{X}_{Fe}X_{FeS}^2W_{V,Fe-FeS} \\ & + X_{Fe_3C}X_{Fe}^2W_{V,Fe_3C-Fe} + X_{Fe_3C}X_{FeS}^2W_{V,Fe_3C-FeS} \\ & + X_{Fes}X_{Fe}^2W_{V,FeS-Fe} + X_{Fes}X_{Fe_3C}^2W_{V,FeS-Fe_3C} \\ & + \frac{X_{Fe}X_{Fe_3C}X_{FeS}\left(3-2X_{Fe}-2X_{Fe_3C}-2X_{FeS}\right)}{2}(W_{V,Fe-Fe_3C} + W_{V,Fe-FeS} \\ & + W_{V,Fe_3C-Fe} + W_{V,Fe_3C-FeS} + W_{V,FeS-Fe} + W_{V,FeS-Fe_3C}) \end{aligned} \tag{2.55}$$

Chapter 3 On the properties of Fe-C-S liquids

This chapter gives a full view of the experimental results for the ternary liquid Fe-C-S alloys, including the properties of the recovered samples, the local structure and density determined following the data-processing methods introduced in chapter 2, and a well-established thermodynamic model. The densities from the two techniques are compared, and both values are used for the establishment of the thermodynamic model, which allow a further discussion on the constraints on the composition of the Moon's core.

3.1 Sample preparation

The Fe-C-S samples are mixtures of iron (99.5%, Alfa Aesar), iron sulfide (FeS, 99.98%, Alfa Aesar), and graphite powders (99%, Alfa Aesar). For each sample, the starting components were weighed, mixed, and ground in an agate mortar for 30 minutes and stored in a vacuum box. Before experiments, the powders were burned in a vacuum furnace at 150 ℃ for a few hours to ensure dehydrated, and loaded to a sapphire or an hBN capsule and pressed to compact.

3.2 Microscopy analysis of the recovered samples

3.2.1 Scanning electron microscopy imaging

Quenched samples were mounted into epoxy resin and polished for SEM and electron microprobe analysis. The micro-structure was analyzed by a ZEISS-ULTRA55 scanning electron microscope at Institut de Minéralogie, de Physique des Matériaux et de Cosmochimie, Sorbonne Université.

An SE2 (Secondary electron) image of the recovered assembly and BSE (Back-scattered electron) images of Fe-C-S samples from *in situ* CAESAR experiments are shown in Fig. 3.1. It shows 2 or 3 phases homogeneously distributed within the whole samples with the S-rich part and S-depleted part exhibiting a strong contrast. Sapphire capsules proved excellent suitability for sealing the liquid sample and keeping its geometry. With the BN serving as lids at the two sides, the pressure inside the capsule is considered almost hydrostatic.

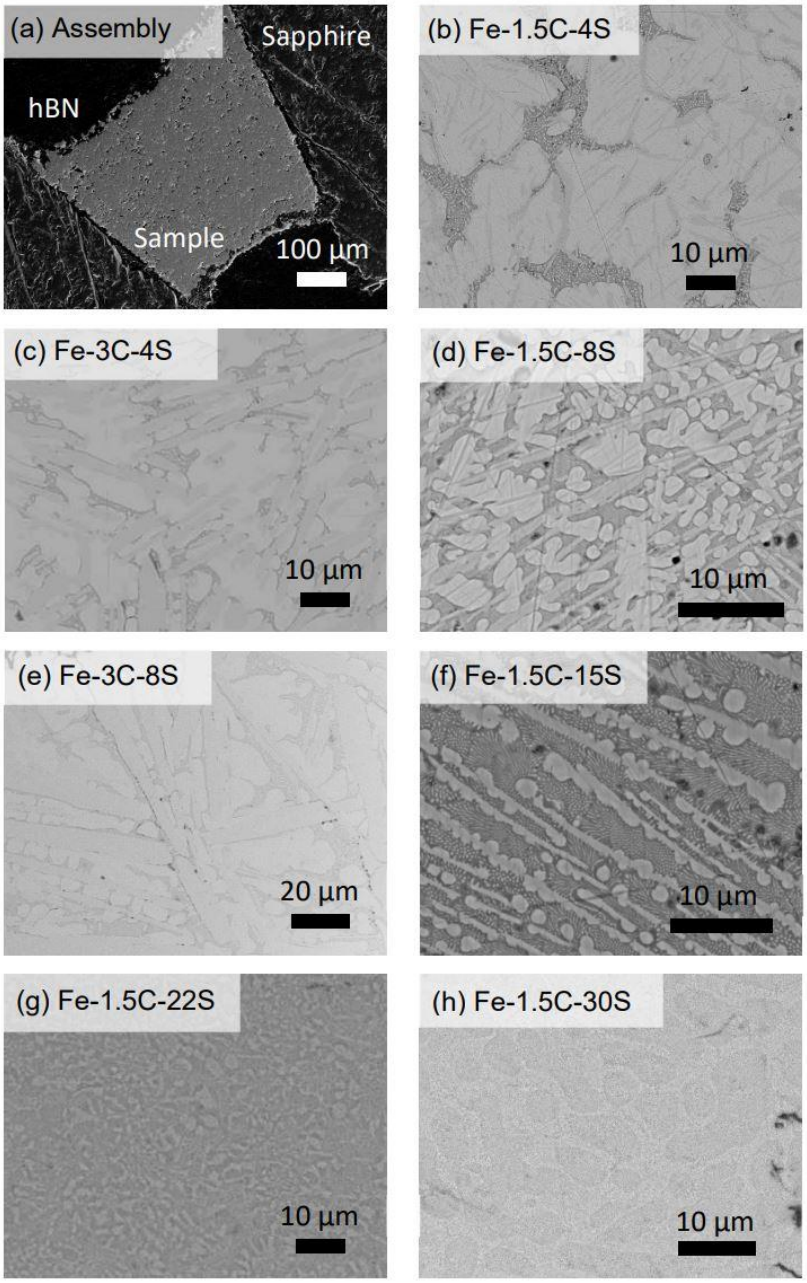

Fig. 3.1 Example of full view of the recovered assembly (a) and backscattered electron images of the Fe-C-S samples (b-h). Two phases are visible in the most sulfur-rich samples (f-h) and three phases in the others (b-e): the darker sulfur-rich region and brighter carbon-rich region in the two phases-samples, and the dark S-rich region, the bright iron-rich region, and the carbon-rich phase with intermediate brightness in the three-phases samples. In the last case, the S-rich and C-rich phase are close to the stoichiometric composition, FeS and Fe_3C, respectively. Looking at texture, this shows a trend with the increase of sulfur (>15 wt%): the lamellar-shaped C-rich phase and Fe-rich phases were replaced by a single medium carbon-rich phase.

Regarding the miscibility experiments, due to leaks, not all the samples could be recovered from the runs performed in LMV. Fig 3.2 shows some of the recovered samples from 1600K and 4 GPa (in particular those having retained a regular shape). Six loadings with different starting compositions were conducted in each run (multi-capsule assembly), without having marked the location of each of the six starting compositions. Liquid immiscibility can be identified in (a) and (b), while (c) shows a miscible sample. As holes are found in most of the samples, we can assume that graphite grains coexisted with the melt, but could not be measured as these got detached during the polishing.

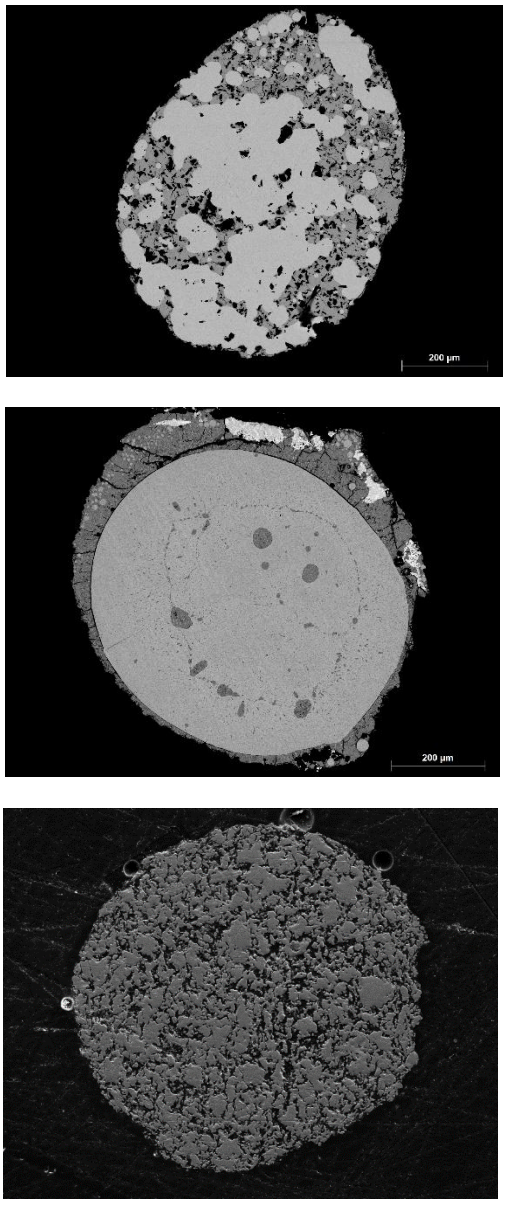

Fig. 3.2 Three samples with regular shapes recovered from 4 GPa and 1600K. (a) and (b) show liquid-immiscible samples and (c) shows a miscible sample. For (a) and (b), the brighter portions are regions with higher density, composed of Fe-C, while the darker portions correspond to quenched Fe-S liquid with lower density. The denser parts are expected to will gather at the center of the sample as shown in (b), which in turn implies that sample (a) might not be fully equilibrated. In (c), no contrast is visible over the whole sample, except holes, in black, indicating that the sample is quenched from a miscible liquid. The black parts observed in (a) and (c) over the entire sample, where graphite grains were inferred to exist but got detached during the polishing.

The BSE images of the samples with representative textures from the runs performed at IMPMC are shown in Fig. 3.3. Similar to runs performed at LMV, carbon-saturated samples were identified by black spots/holes, which was supported by the fact that the hollow spots have been found only in high-carbon-content samples with the known starting composition for each sample image. Samples show three different sorts of recovered textures: miscible, immiscible, and a "critical" status. The texture shown in Fig. 3.3 (C) and (D) is obviously different from that shown in Fig. 3.3 (A), where small C-rich droplets with diameters of 2-5 microns coexist with dendritic texture. In fact, the droplets-like texture have been also found in Fe-S-Si (Sanloup and Fei, 2004; Morard and Katsura, 2010) and Fe-O (Kato and Ringwood, 1989) immiscible liquids with relatively low bulk light element content, which were called emulsion texture, but in those cases, the diameters were overall larger (up to tens of microns), and no dendritic texture existed. The smaller droplets coexisting with dendritic texture found in this study is more like a critical state between miscible and immiscible, and therefore, the bulk composition is expected to be rather close to, or even in the miscibility gap. Accordingly, the small C-rich drops are expected to quench from C-rich liquid, and the dendritic part from homogeneous Fe-C-S liquid.

(a) $Fe_{75}C_{10}S_{15}$ 2000 K 4 GPa

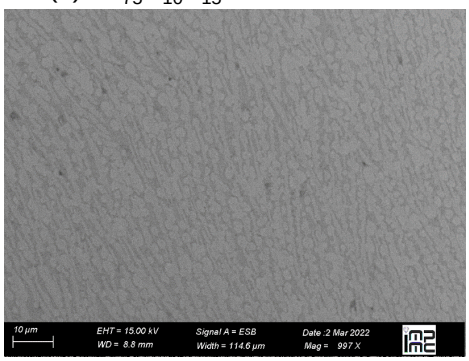

(b) $Fe_{65}C_{14}S_{21}$ 2000 K 4 GPa

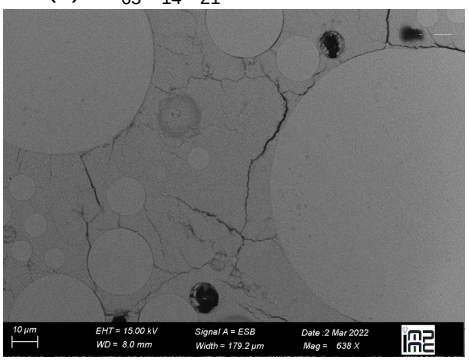

(c) $Fe_{58}C_{20}S_{22}$ 2000 K 5 GPa

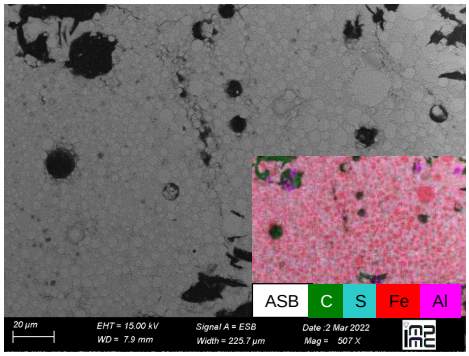

(d) $Fe_{58}C_{20}S_{22}$ 1650 K 4 GPa

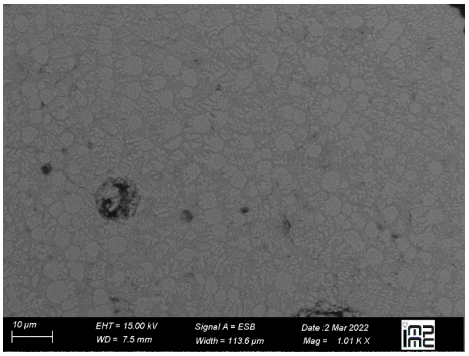

Fig. 3.3 Back-scattered electron (BSE) images representative of textures in the recovered samples. Nominal compositions and experimental conditions are marked on top of each image. (A) Homogeneous texture quenched from single liquid. (B) Quenched sample from two immiscible liquids. The bright carbon-rich droplets are distributed in the darker sulfur-rich liquid. (C) and (D) examples of a critical status between miscible and immiscible liquids, where carbon-rich liquid forms small droplets that exsolve from the sulfur-rich liquid, but do not gather to form large carbon-rich droplets. The inset in (C) is the corresponding EDS map (same probed area), showing chemical concentration of C, S, Fe, and Al.

3.2.2 Electron microprobe analysis

Following SEM analysis, all the samples were also analyzed by electron microprobe in CAMPARIS, Sorbonne University using a CAMECA SX-100 wavelength dispersive spectrometer (WDS). Pure iron, natural pyrite (FeS_2), and synthetic Fe_3C, and Fe_2O_3 were used to calibrate Fe, S, C, and O, respectively. All the standards and samples are coated with platinum with same thickness by controlling the sputtering time (and typically at the same time). In the first analysis, the accelerating voltage and operating current were set as 10 kV and 200 nA. Analysis on 10 different locations are conducted on the standard to average the count rate for the calibration. It has been well known that the carbon content commonly sees an increase with time as it accumulates on the sample surface due to the evaporation of C-bearing organic molecules inside the machine (Fei and Brosh, 2014; Deng et al., 2013). Therefore, nitrogen-cooled cold fingers and an oxygen flux were employed to suppress the evaporation of C-bearing compounds and to create a reactive atmosphere that removes the carbon around the samples. In spite these precaution and care in the measurements, the obtained total weight percent was generally higher than 100%, with a likely overestimated iron content as often near and sometime above 100%, and reasonable carbon and sulfur contents. The table below shows the results of Fe-1.5C-4S as an example.

Table 3.1 A part of EPMA results of Fe-1.5C-4S from CAMPARIS

Probed spot	Carbon (wt%)	Oxygen (wt%)	Sulfur (wt%)	Iron (wt%)	Total (wt%)
1	2.9821	1.3747	0.6533	99.9685	104.9786
2	0.7726	2.0681	0.361	100.9811	104.1828
3	2.7082	1.2303	13.0246	91.5791	108.5422
4	2.3412	0.7766	0.0393	100.5453	103.7024
5	3.0814	2.2214	21.0512	84.2096	110.5635
6	3.4798	1.6664	11.9846	88.1675	105.2983

7	1.5989	1.2929	0.1239	99.3003	102.3159
8	0.9923	1.4022	0.0304	100.6158	103.0406

Great efforts have been made to figure out the reason and solve the problem. The potential error sources were considered to be the selection of accelerating voltage, the composition error of the standards, and issues related to the coating layer. We also stress that we have been among the first users of CAMPARIS to investigate metallic iron samples rather than silicates as most commonly done.

Regarding the selection of accelerating voltage, to detect the Kα of Fe at 6.4 keV, a minimum voltage of 10 kV is needed. As a matter of fact, 15 kV is more commonly used for iron alloys in similar studies reported in literature (e.g. Chabot et al., 2008; Deng et al., 2013). The employed accelerating voltage here (10 kV) is around the threshold where the characteristic X-ray of iron can be detected, which could produce artefacts on the count rate. However, the results obtained in the following measurements, for which we employed an increased accelerating voltage of 15 kV, have not been significantly better. The selection of accelerating voltage is therefore here considered not to be a crucial factor.

Concerning standards, since the standard for sulfur is natural pyrite, we could not *a priori* discard the possibility that some impurities are present. Accordingly, we conducted both EDS (energy dispersive spectrometer) and WDS (wavelength dispersive spectrometer) on the pyrite standard, with carbon coating, and both indicated it as pure FeS_2. The possibility of error from the standard has also been ruled out.

Finally, we consider source of errors coming from the coating. Analysis of iron and pyrite standards with carbon coating showed a total weight percent very close to 100%, with a remarkable decrease in iron content. Similarly, good results are obtained for our Fe-S samples (detailed in another part of this Ph.D. thesis). The anomalously high count rate on iron content is thus ascribed reasonably to the Pt coating. We can speculate that either the platinum film causes artifacts on the count rate of iron, or that the detector of the microprobe does not function well with the platinum coating.

In view of the problems we were facing with CAMPARIS, and in parallel to the diagnostic work reported above, we decided to have analysis performed elsewhere. Because of the expertise and

experience on the analysis of C-bearing metals, the composition of the recovered samples from were also quantified in the Earth and Planets Laboratory, Carnegie Institution for Science, with a JEOL8530F electron microprobe operated at an accelerating voltage of 15 kV and beam current of 20 nA (for samples from *in situ* experiments) and 30 nA (for samples from quench experiments). The samples were coated with iridium. A calibration curve for carbon analysis was established based on the C Kα intensity of Fe_7C_3, Fe_3C, a C-bearing NIST steel Fe-1wt%C, and pure Fe, and is shown in Fig. 3.4. For samples from *in situ* experiments, a focused beam sized a few micron was first employed to measure the composition of each phase in the samples, and a defocused beam sized $30\times30\mu m^2$ was then employed to measure the bulk composition. For samples from quench experiments, a $30\times30\mu m^2$ defocused beam was applied to all the samples for each phase. The phase-sorted or/and bulk composition of all samples from *in situ* and quench experiments are shown in Table 3.2 and 3.3 respectively. It is worth noting that the iron carbide phase recovered from *in situ* runs shows less carbon content than that of Fe_3C, indicative of the presence of are carbon defects, as already reported in previous studies (Walker et al., 2013; Fei and Brosh, 2014).

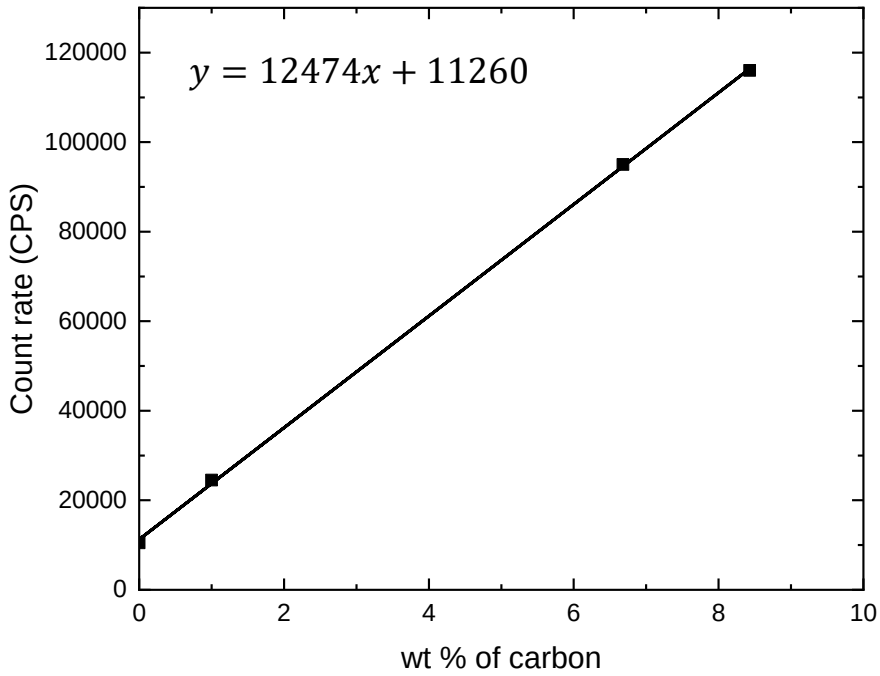

Fig. 3.4 Carbon count rate in the Fe and Fe-C standards. The linear fit is used as a calibration for the correction of carbon content in the samples.

Table 3.2 EPMA results of samples from *in situ* experiments.

Starting composition	Weight percent				Total	Notes
	Fe	C	S	O[d]		
Beamtime0720						
Fe-1.5C-4S-1 $Fe_{84.9}C_{11.6}S_{3.5}$	97.87(0.36)	1.43(0.52)	0.02(0.01)	0.08(0.02)	99.40(0.34)	Fe-rich phase
	93.1(0.98)	6.09 (0.65)	0.52 (0.67)	0.05(0.01)	99.77(0.26)	C-rich phase
	69.48(2.06)	1.23(0.53)	27.35(1.87)	0.25(0.05)	98.34(0.64)	S-rich phase
	95.88(3.62)	2.81(1.29)	2.28(3.21)	0.11(0.02)	101.08(0.83)	Bulk composition
Fe-1.5C-4S-2 $Fe_{85.5}C_{12.9}S_{1.6}$	97.82(0.83)	0.90(0.24)	0.03(0.01)	0.09(0.05)	98.83(0.65)	Fe-rich phase
	91.72(0.49)	6.08(0.31)	1.13(0.77)	0.09(0.05)	99.02(0.30)	C-rich phase
	67.58(2.73)	0.97(0.11)	29.24(2.48)	0.28(0.13)	98.07(0.45)	S-rich phase
	95.50(1.03)	3.11(0.46)	1.04(0.55)	0.53(0.10)	100.18(0.54)	Bulk composition
Fe-3C-4S $Fe_{81.3}C_{14.3}S_{4.4}$	98.73(0.25)	1.11(0.13)	0.02(0.01)	0(0)	99.86(0.18)	Fe-rich phase
	93.53(0.21)	7.19(0.26)	0.02(0.01)	0(0)	100.74(0.17)	C-rich phase
	65.79(1.69)	1.03(0.14)	30.88(1.99)	0.10(0.03)	97.80(0.54)	S-rich phase
	94.06(2.44)	3.55(1.07)	2.98(2.10)	0.15(0.20)	100.75(0.55)	Bulk composition
Fe-3C-8S $Fe_{76.5}C_{18}S_{5.5}$	97.13(0.19)	0.94(0.12)	0.03(0.01)	0(0)	98.11(0.22)	Fe-rich phase
	92.78(0.11)	6.60(0.19)	0.02(0.01)	0.01(0.01)	99.41(0.26)	C-rich phase
	67.58(4.05)	1.06(0.26)	30.11(4.00)	0.08(0.02)	98.85(0.33)	S-rich phase
	91.91(2.02)	4.64(1.29)	3.78(3.04)	0.48(0.14)	100.81(0.75)	Bulk composition
Beamtime0921						
Fe-1.5C-4S-3[a] $Fe_{81.6}C_{12.3}S_{6.1}$	/	/	/	/	/	Recovery failure
Fe-1.5C-8S $Fe_{74.8}C_{11.5}S_{13.7}$	96.66(0.44)	1.17(0.15)	0.34(0.30)	0.03(0.03)	98.20(0.14)	Fe-rich phase
	90.17(1.91)	6.22(1.02)	3.53(2.65)	0.12(0.09)	100.05(1.61)	C-rich phase
	75.96(1.14)	1.23(0.48)	21.09(1.24)	0.27(0.09)	98.55(0.89)	S-rich phase
	87.79(0.96)	2.89(0.28)	9.25(1.32)	0.06(0.06)	99.98(0.98)	Bulk composition
Fe-1.5C-15S[b] $Fe_{66.7}C_{11.}S_{22.1}$	86.29(3.21)	5.15(1.53)	7.96(3.43)	0.24(0.17)	99.65(1.73)	C-rich phase
	73.68(0.60)	1.41(0.28)	22.13(0.89)	0.64(0.35)	97.87(0.42)	S-rich phase
	80.77(0.5)	2.91(0.44)	15.40(0.70)	0(0)	99.09(0.31)	Bulk composition
Fe-1.5C-22S-1[c] $Fe_{59.1}C_{10.6}S_{30.3}$	74.66(0.74)	2.88(0.64)	21.98(0.49)	0.13(0.02)	99.65(0.96)	Bulk composition
Fe-1.5C-22S-2[c] $Fe_{60.7}C_{9.2}S_{30.1}$	75.49(0.41)	2.45(0.37)	21.55(0.22)	0.16(0.03)	99.65(0.44)	Bulk composition
Fe-1.5C-30S[c] $Fe_{47.5}C_{16.3}S_{36.2}$	67.62(0.95)	4.97(0.25)	29.55(1.10)	0(0)	102.13(0.42)	Bulk composition

[a] Recovery was not possible due to a blowout during the decompression.

[b] The Fe_3C phase visible in BSE image was not detected by microprobe due to the very small size of the grains, comparable to, when not smaller than the size of the focused beam.

[c] The texture of the two most S-rich sample is characterized by very small grains that do not allow distinguishing between C-rich and S-rich zones, therefore only the bulk composition is provided.

[d] The reported trace oxygen is thought from sample's oxidization occurred after the synchrotron experiments (July 2020 and September 2021) in the time lapse between SEM analysis (right after synchrotron experiments) and electron microprobe analysis (April 2022) as the O amounts from two beamtimes are comparable if not slightly larger for *Beamtime0720*, indicating the use of sapphire rings in the second beamtime did not produce O contamination.

Table 3.3 EPMA results of the samples from quench experiments

Starting composition	Pressure	Phase assemblage	Weight percent				Total	Notes
			Fe	C	S	O		
1650-K runs								
$Fe_{81}C_6S_{13}$	2 GPa	1 liquid	88.17(0.34)	2.05(0.23)	9.42(0.40)	0.67(0.05)	100.3(0.39)	Bulk composition
$Fe_{78}C_8S_{14}$	2 GPa	/	/	/	/	/	/	Contaminated by thermocouple
$Fe_{70}C_{12}S_{18}$	4 GPa	1 liquid + graphite	83.74(0.56)	2.02(0.25)	15.42(0.65)	0.98(0.21)	102.16(0.33)	Bulk composition
$Fe_{65}C_{14}S_{21}$	4 GPa	1 liquid + graphite	81.37(1.10)	1.39(0.26)	17.78(1.16)	0.88(0.14)	101.42(0.47)	Bulk composition
$Fe_{58}C_{20}S_{22}$	4 GPa	1 liquid* + graphite	77.75(1.00)	1.19(0.25)	22.04(1.09)	0.92(0.11)	101.90(0.40)	Bulk composition
$Fe_{49}C_{25}S_{26}$	4 GPa	1 liquid + graphite	73.93(0.40)	0.32(0.12)	27.83(0.50)	0.99(0.15)	103.06(0.51)	Bulk composition
2000-K runs								
$Fe_{81}C_6S_{13}$	2 GPa	1 liquid	88.16(9.62)	1.20(1.10)	10.72(10.56)	0.45(0.17)	100.53(0.80)	Bulk composition
$Fe_{78}C_8S_{14}$	2 GPa	2 liquids	70.17(1.54)	0.07(0.11)	26.72(2.00)	0.56(0.07)	97.52(0.66)	S-rich
			93.43(0.10)	2.97(0.14)	2.73(0.15)	0.45(0.08)	99.58(0.13)	C-rich
$Fe_{75}C_{10}S_{15}$	2 GPa	2 liquids	70.70(0.54)	0.57(0.21)	25.07(0.89)	1.44(0.25)	97.79(0.24)	S-rich
			93.25(0.39)	3.71(0.20)	2.08(0.06)	0.39(0.06)	99.43(0.47)	C-rich
$Fe_{75}C_{10}S_{15}$	4 GPa	1 liquid	83.30(6.95)	2.07(1.72)	13.68(8.29)	0.69(0.34)	99.75(1.22)	Bulk composition
$Fe_{70}C1_2S_{18}$	4 GPa	2 liquids + graphite	72.42(0.23)	0.20(0.04)	24.30(0.27)	0.78(0.08)	97.70(0.21)	S-rich
			92.45(0.14)	4.10(0.09)	1.85(0.05)	0.35(0.08)	98.75(0.18)	C-rich
$Fe_{65}C_{14}S_{21}$	4 GPa	2 liquids + graphite	72.32(0.49)	0.24(0.21)	25.14(0.66)	0.92(0.09)	98.63(0.22)	S-rich
			92.93(0.34)	3.95(0.16)	1.96(0.21)	0.32(0.05)	99.16(0.39)	C-rich
$Fe_{65}C_{14}S_{21}$	5 GPa	1 liquid + graphite	81.14(6.22)	1.01(0.52)	15.54(6.80)	0.62(0.30)	98.31(0.92)	Bulk composition
$Fe_{58}C_{20}S_{22}$	5 GPa	1 liquid* + graphite	77.14(8.13)	1.12(1.25)	19.85(9.59)	0.75(0.36)	98.86(1.38)	Bulk composition
$Fe_{44}C_{25}S_{31}$	6 GPa	1 liquid + graphite	72.41(3.22)	0(0)	27.46(3.59)	0.96(0.27)	100.83(0.64)	Bulk composition

* Samples with a special texture including dendritic texture and small C-rich droplets, which is thought to be a critical status between miscible and immiscible.

3.3 Local structure and density from CAESAR data

Fig. 3.5 (a) shows the obtained pair correlation function $g(r)$ (or radial distribution function for isotropic media such as the liquids of the present study) together with partial $g(r)$ from calculations available in literature. Oscillations in the $g(r)$s become less pronounced for samples with 22.1 at.%S or more, consistent with previous studies on Fe-S binary liquids (Shibazaki and Kono, 2018, Morard et al., 2018, Xu et al., 2021), where the liquids were reported to show a more disordered structure for S content of 23.5 at.%S, 29.4 at.%S, and 25.1 at.%S, respectively. On the other hand, inclusion of up to 18 at.% of carbon in the ternary liquid seems not to have a detectable impact on the local structure, as signatures of the second and third coordination shells are still distinguishable. The modification of the structure is controlled by the interstitial inclusion of more massive S atoms that perturb the Fe-Fe network, while smaller C atoms can enter in interstitial sites between Fe atoms without much affecting the local structure. This is further supported by the variation in the atomic density shown in Fig. 3.6. The atomic density with increasing S or C content shows opposite trends, highlighting the different effect of sulfur and carbon. Conversely, we note that the atomic density of Fe-Si liquids does not significantly change with Si content, as Si atoms substitute iron atoms.

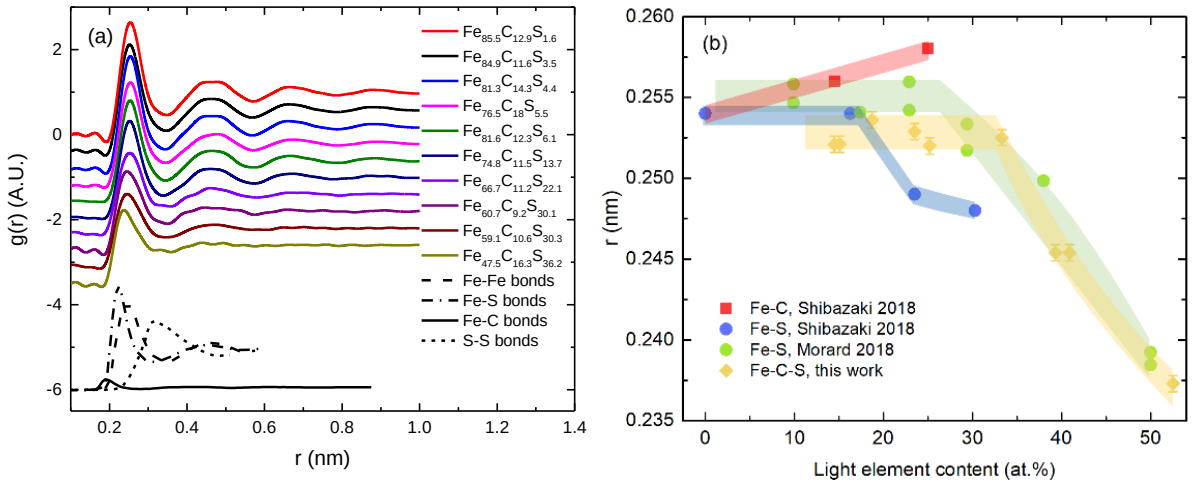

Fig. 3.5 (a) Radial distribution function measured for Fe-C-S ternary liquids in the 1-5 GPa and 1700-1900 K range. Data are shown for increasing sulfur content (from the top to bottom) and compared to the partial $g(r)$ showing the individual contribution of Fe-Fe, Fe-S, and S-S bonds, calculated for a binary Fe-S liquid alloy with 23 at.%S (Morard et al., 2018), and the partial $g(r)$ illustrating the Fe-C bonds calculated for a binary Fe-C alloy with 20 at.%C (Lai et al., 2017). (b) First peak positions of the ternary alloys in comparison with results obtained for binary Fe-C and Fe-S at similar P-T condition (1.5-5.2 GPa and 1600-

1980 K in Morard 2018, and 3-5 GPa, 1600-2000 K in Shibazaki 2018). Colored bands are guides for the eye.

The most prominent feature in the $g(r)$ is the position (r_1) and intensity of the first peak, corresponding to the first coordination sphere. r_1 as a function of total light element content is plotted in Fig. 3.5 (b) and compared with results from literature obtained for binary liquids. Within the experimental uncertainties the r_1 value of Fe-S liquids is not observed to vary with S content for S addition up to ~20-25 at.%, while it significantly decreases for larger concentration. As suggested by calculated partial $g(r)$, this is likely due to the increased contribution of the shorter and covalent Fe-S bonds (Fig. 3.5 (a)). Since the scattering intensity is proportional to the square of the atomic number, the contribution from Fe-Fe and Fe-S bonds in the case of $Fe_{66.7}C_{11.2}S_{22.1}$ account, respectively, for ~65% and ~27% of the total signal (see Morard et al., 2008 and references there in), while the contribution from other bonds is negligible. Therefore, the formation of shorter Fe-S bonds moves the first peak position of the total $g(r)$ towards lower r, while other bonds hardly have a visible effect. For binary Fe-C liquids, the addition of carbon seems to move r_1 towards higher values according to available experimental data (Shibazaki and Kono, 2018), in apparent contrast with molecular dynamic calculations that indicate short Fe-C bonds (Lai et al., 2017). This discrepancy may imply that the addition of carbon might have a more complex perturbation effect other than simply forming the Fe-C bonds.

Our results of r_1 as a function of total light element content follow a trend qualitatively similar to that reported for the binary Fe-S by Morard et al. (2018) and Shibazaki and Kono (2018), with a closer agreement with values reported in the former. The similar trend of Fe-S and Fe-C-S liquids for the same total light element content indicates that the Fe-S bonds still play a dominant role in determining the structure of the ternary liquid, and that up to 18 at.% of C, C does not modify the two-regime behavior observed for binary Fe-S liquid alloys, nor the light element threshold defining the change in the regime. Thus, in this context C seems to play the same role as S in decreasing the r_1 value, in agreement with the calculated length of Fe-C bonds (Lai et al., 2017), but in apparent contrast with the experimental r_1 value reported for the Fe-C liquids (Shibazaki and Kono, 2018).

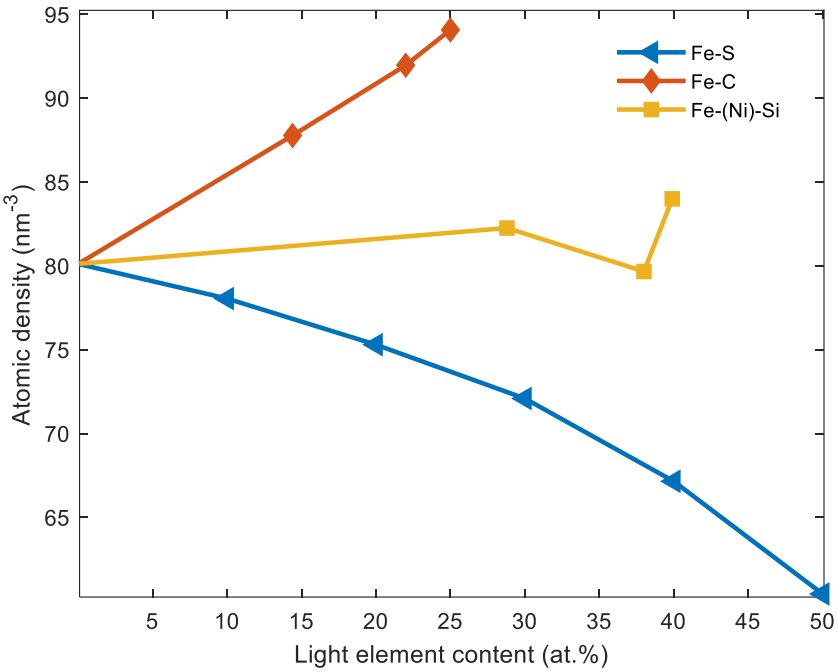

Fig. 3.6 Atomic density of Fe-C, Fe-S, Fe(-Ni)-Si liquid calculated at 5 GPa from massive density following a formalism $\rho_{at} = \rho * N_A/M$, where ρ is the massive density, N_A the Avogadro number, and M the molar mass. The liquid Fe density is from Komabayashi 2014 at 1900K. Fe-C data are from Terasaki et al. (2010) ($Fe_{75}C_{25}$), Sanloup et al. (2011) ($Fe_{78}C_{22}$), and Shimoyama et al. (2013) ($Fe_{86}C_{14}$) corrected to 1923K. Fe-S data are from Morard et al. (2018) at 1900K. Fe(-Ni)-Si data are from Sanloup et al. (2004) ($Fe_{71}Si_{29}$ and $Fe_{60}Si_{40}$) and Terasaki et al. (2019) ($Fe_{52}Ni_{10}Si_{38}$) at 1900K.

Table 3.4 summarizes the densities obtained from the analysis of the g(r) at the experimental P-T conditions. Densities obtained by diffraction and by absorption are consistent, with remarkable agreement in the cases of S-rich samples (e.g. measurements on $Fe_{60.7}C_{9.2}S_{30.1}$ and $Fe_{47.5}C_{16.3}S_{36.2}$), and a difference never exceeding 8% (measurements on $Fe_{74.8}C_{11.5}S_{13.7}$). When the two methods provide slightly dissimilar results, densities measured by diffraction are systematically below that measured by absorption. A possible reason is that collected diffraction signal is contributed from a sulfur-rich portion of the sample. In fact, the diffraction method would be more sensitive to local inhomogeneity compared to absorption if the diffracting volume is comparable in scale to the size of inhomogeneous regions (a few tens of microns). On the other hand, as the absorption profile is taken on the whole sample, the error from local inhomogeneity has been almost eliminated (*i.e.* the massive absorption coefficient is averaged). Finally, and irrespective of the above consideration, we note that the both values are used to build the thermodynamic model.

Table 3.4 Composition of the samples, experimental P-T conditions, density obtained by analysis of the CAESAR data at experimental conditions and recalculated at the reference temperature of 1850 K.

Nominal composition	Atomic proportion (%)			Exp. T (K)	Pressure (GPa)	ρ by diffraction (kg/m^3)	ρ extrapolated to 1850K (kg/m^3)
	Fe	C	S				
Beamtime0720							
Fe-1.5C-4S	87.2	6.4	6.4	1690	1.06	6550	6590
				1895	2.15	6640	6670
Fe-3C-4S	81.6	12.3	6.1	1722	2.29	6500	6660
				1895	2.09	6510	6580
Fe-3C-8S	76.2	11.9	11.9	1625	2.52	6300	6260
				1895	2.17	6220	6220
Beamtime0922							
Fe-1.5C-4S	87.2	6.4	6.4	1760	3.86	6470	6300
				1850	3.70	6370	6370
Fe-1.5C-8S	81.2	6.3	12.5	1610	4.92	6310	6240
				1720	4.70	6260	6200
				1805	4.57	6170	6150
Fe-1.5C-15S	71.6	6.0	22.4	1760	3.72	/	/
				1850	3.62	5680	5680
Fe-1.5C-22S	62.8	5.7	31.5	1760	3.44	5120	5100
				1850	3.31	5200	5200
				1760	4.76	/	/
				1850	4.35	5540	5540
Fe-1.5C-30S	53.6	5.5	40.9	1760	4.7	5030	5000
				1850	4.42	5080	5080

3.4 Density calculation from absorption profile

Absorption measurements were only conducted in the second of the two synchrotron beamtimes, high-pressure runs (*Beamtime0922*). The densities determined using the μ according to the two protocols detailed in section 2.6 are shown in Table 3.5. Densities from the two methods yield about 10% discrepancy. This large discrepancy originated from different μ determination may indicate that the theoretical μ value estimated according Eq. (2.3), with the μ of each component taken from the NIST Standard Reference Database, is no longer appropriate for samples under

high P-T conditions, when the absorption profiles could include a component from the scattering of the gasket/capsule or in general spourious contribution from the surrounding materials. Therefore, the μ determined for the hot solid samples before melting are assumed to be a good proxy for μ of the corresponding liquids and adopted in the analysis that yields the densities that are used for further discussion.

Table 3.5 Composition of the samples, experimental P-T conditions, density from absorption at experimental conditions and recalculated at the reference temperature of 1850 K.

Beamtime0922								
Nominal composition	$\mu_s\rho_s$ (cm^{-1})	T (K)	P (GPa)	μ from literature (cm^2/g)	ρ (kg/m^3)	μ from solid samples (cm^2/g)	ρ (kg/m^3)	ρ rescaled to 1850K (kg/m^3)
Fe-1.5C-4S	25.75	1760	3.86	4.09	6300	3.77	6830	6790
	24.34	1850	3.70		5950		6460	6460
Fe-1.5C-8S	26.00	1610	4.92	3.97	6550	3.88	6710	6610
	25.69	1720	4.70		6470		6630	6570
	25.39	1805	4.57		6400		6550	6530
Fe-1.5C-15S	21.15	1760	3.72	3.76	5630	3.56	5950	5920
	21.45	1850	3.62		5700		6030	6030
Fe-1.5C-22S	17.38	1760	3.44	3.55	4900	3.32	5220	5200
	17.32	1850	3.31		4880		5200	5200
	18.62	1760	4.76		5250		5590	5560
	18.36	1850	4.35		5170		5510	5510
Fe-1.5C-30S	15.01	1760	4.7	3.31	4530	2.92	5140	5110
	14.78	1850	4.42		4470		5060	5060

3.5 Comparison of density from diffraction and absorption measurements

Densities obtained by diffraction and by absorption are summarized in Table 3.6. Obtained values are consistent, with remarkable agreement in the cases of S-rich samples (e.g. measurements on $Fe_{60.7}C_{9.2}S_{30.1}$ and $Fe_{47.5}C_{16.3}S_{36.2}$), and a difference never exceeding 8% (measurements on

$Fe_{74.8}C_{11.5}S_{13.7}$). When the two methods provide slightly dissimilar results, densities measured by diffraction are systematically below that measured by absorption. Density estimated by analysis of CAESAR data in a benchmark run conducted on Al (see Appendix A) is observed consistent with literature data, although there is no result from absorption to compare with. Samples' texture is possibly at the origin of this difference. The liquid Al is homogeneous even at microscopic scale as single component. Conversely, in Fe-C-S samples local compositional heterogeneities at micron scale cannot be ruled out, even though the sample is generally homogeneous. Diffraction signal might have a contribution from a sulfur-rich portion of the sample (the size of the S-rich portions in recovered samples are observed to be up to 10 μm wide, comparable to the size of the diffracted volume), which would yield to lower density than the whole sample. On the other hand, as the absorption profile is taken on the whole sample, the error from local inhomogeneity is almost eliminated (i.e. the massive absorption coefficient is averaged).

Table 3.6 Samples' composition, experimental P-T conditions, measured density and density rescaled to 1850 K, for both diffraction and absorption experiments.

Atomic proportion (%)			Exp. T (K)	Pressure (GPa)	ρ by diffraction (kg/m^3)	ρ rescaled to 1850K (kg/m^3)	ρ by absorption (kg/m^3)	ρ rescaled to 1850K (kg/m^3)
Fe	C	S						
Beamtime0720								
84.9	11.6	3.5	1895	2.15	6780	6800	/	/
85.5	12.9	1.6	1690	1.06	6900	6800	/	/
81.3	14.3	4.4	1722	2.29	6740	6680	/	/
			1895	2.09	6600	6620	/	/
76.5	18.0	5.5	1625	2.52	6590	6490	/	/
			1895	2.17	6430	6460	/	/
Beamtime0921								
81.6	12.3	6.1	1760	3.86	6550	6510	6830	6790
			1850	3.70	6460	6460	6460	6460
74.8	11.5	13.7	1610	4.92	6200	6110	6710	6610
			1720	4.70	6180	6130	6630	6570
			1805	4.57	6110	6100	6550	6530
66.7	11.2	22.1	1760	3.72	/	/	5950	5920
			1850	3.62	5620	5620	6030	6030

59.1	10.6	30.3	1760	3.44	5020	4990	5220	5200
			1850	3.31	5160	5160	5200	5200
60.7	9.2	30.1	1760	4.76	/	/	5590	5560
			1850	4.35	5550	5550	5510	5510
47.5	16.3	36.2	1760	4.7	/	/	5140	5110
			1850	4.42	4970	4970	5060	5060

Irrespective of the above consideration, since, as already mentioned, density obtained by the two technique are overall consistent, all values are used to build the thermodynamic model (see next section).

3.6 The thermodynamic model

A non-ideal mixing model for Fe-C-S liquid was built based on the Margules formulation described in section 2.7 and constrained by the density data determined from our experiments. Fe, FeS and Fe_3C are adopted as the end members, with their EOS parameters provided in Table 3.7.

Table 3.7 Thermal elastic parameters for Fe, Fe_3C, and FeS

Parameters	**Fe[a]**	**Fe_3C[b]**	**FeS[b]**
$V(P_0, T_0)$ (cm^3/mol)	6.88	26.68	22.96
K_{T0} (GPa)	148	75.66	17.02
K_T'	5.8	7.98	5.92
δ_T	5.1	9.43	5.92
$\alpha(P_0)$ ($10^{-5}K^{-1}$)	9	9.59	11.9
κ	0.56	0.56	1.4
γ	1.73[c]	1.7	1.3
T_0(K)	298	1723	1650

a. Parameters from Komabayashi (2014).
b. Parameters refitted by Knibbe et al. (2021).
c. Parameters from Anderson and Ahrens (1994).

Fitting the density data to the Margules formalism (Eq. 2.55) yields the six volume interaction Margules parameters shown in Table 3.8. Starting from the modeled ternary volume, all relevant thermodynamic properties of Fe-C-S solutions can be computed according standard thermodynamic relations.

Table 3.8 Fitted interaction Margules parameters

$W_{V,Fe-Fe_3C}$	0.2 ±0.2
W_{V,Fe_3C-Fe}	0 ±0.2
$W_{V,Fe-FeS}$	-2.2 ±0.4
$W_{V,FeS-Fe}$	-1.0 ±0.4
W_{V,Fe_3C-FeS}	-3.0 ±0.2
$W_{V,FeS-Fe_3C}$	0.8 ±0.2

* All the parameters are in cm^3/mol

The thermal expansion coefficients of each composition can be calculated according its definition:

$$\alpha = \left(\frac{1}{V}\right)\left(\frac{\partial V}{\partial T}\right) \tag{3.1}$$

For comparison, the density measured at different experimental conditions are rescaled at the reference value of 1850K by making use of the thermal expansion coefficients, and the comparisons between ideal and non-ideal models are shown in Fig. 3.7. The fitted Margules parameters for Fe and Fe_3C are close to 0 indicating that Fe and Fe_3C mix almost ideally at here-considered conditions. Comparing to the ideal mixing model in Fig. 3.7 (a), the densities provided by Margules model in Fig. 3.7 (b) are in overall better agreement with the experimental data. Also, note that ternary alloy with high light element content at low pressure (< 3 GPa) proved to be immiscible, hence only high-pressure data were collected for the sulfur-rich samples. Finally, we stress that although the here-established mixing model well account for the available experimental data and is suitable for density calculations for the Fe-C-S liquid system as a function of pressure and/or composition in the 0-5 GPa range, it may no longer be valid at higher pressure, since the density discontinuity of Fe-C liquid due to a phase transition at 5.2 GPa (Sanloup et al., 2000).

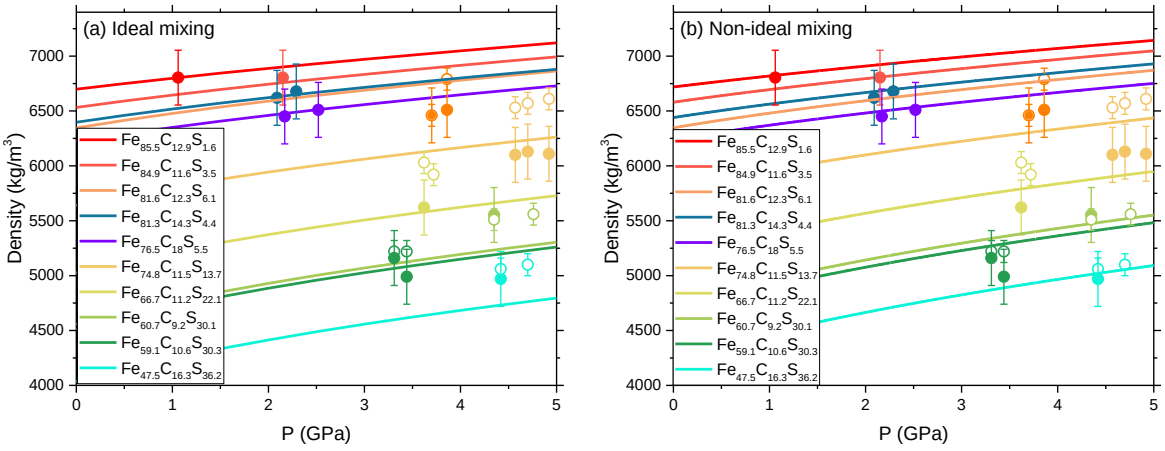

Fig. 3.7 Density at 1850 K computed for selected compositions in the liquid Fe-C-S ternary system according to ideal (a) and non-ideal (b) thermodynamic models. (a) Ideal mixing model constructed based on the properties of Fe, Fe_3C and FeS end members (Table 3.7). (b) Non-ideal mixing model based on the Margules mixing rule. Open circles and filled circles are, respectively, results from absorption and diffraction measurements. The experimental uncertainties are mainly from the limited Q range, self-absorption, and r_{min} fluctuation in the case of diffraction, and from minor sample deformation and fitting procedure for absorption.

The density calculated for the liquid Fe-C-S ternary alloys at 5 GPa as a function of the light element content is shown in Fig. 3.8 (a) and compared with data for binary Fe-S and Fe-C alloys from literature. The uncertainties are from the fitting of the Margules parameters, which yielded ±35 - ±75 kg/m^3 on the density. The most recent studies on Fe-S liquid by diffraction (Morard et al., 2018) and absorption (Terasaki et al., 2019) are in good agreement and provide higher density compared to earlier studies (Sanloup et al.,2000), while results on Fe-C liquid by absorption are all within mutual uncertainties (Terasaki et al., 2010; Sanloup et al., 2011; Shimoyama et al., 2013). The density of Fe-C-S alloys plots in between those of binary alloys, indicating a co-effect of sulfur and carbon in decreasing the density of pure iron. As alloys with high light element content reach the miscibility limit at low pressure (see Dasgupta et al., 2009), the carbon content considered in this study is restricted to less than 18 at.%, so to model a homogeneous ternary liquid. The density is thus largely controlled by the sulfur content, with the effect due to carbon inclusion minor as the direct consequence of the limited proportion of carbon in the modeled alloys.

The compressional sound velocity v_p of liquid Fe-C-S alloys, and specifically of the ten compositions investigated in this study, can be calculated at 5 GPa and 1850 K in an internally consistent way based on our thermodynamic model, following the equation

$$v_p = \sqrt{\frac{K_T(1+\alpha\gamma T)}{\rho}} \tag{3.2}$$

where γ is the Grüneisen parameter, α the thermal expansion coefficient calculated by Eq. (3.1), ρ the extrapolated density of the ternary alloy by the mixing model, and K_T the isothermal bulk modulus calculated by its definition and the mixing model, Eq. (2.55):

$$K_{1850K,P} = \left[-V\left(\frac{dP}{dV}\right)\right]_{1850K} \tag{3.3}$$

Since there is no experimentally determined γ for liquid Fe-S, Fe-C, or Fe-C-S, the γ of ternary Fe-C-S samples are calculated as:

$$\gamma = \frac{K_T V \alpha}{C_P - K_T V T \alpha^2} \tag{3.4}$$

where the C_P is the heat capacity at constant pressure of the ternary alloys, determined by the values of all the end members:

$$C_P = \frac{\partial(\sum_i x_i\, Q_i)}{\partial T} = \sum_i x_i\, C_{P,i} \tag{3.5}$$

where Q is the amount of heat and the subscript *i* represent each end members. The C_P of Fe, FeS, and Fe_3C are calculated with Eq. (3.4) using the parameters provided in Table 3.7. The calculated thermo-elastic properties are provided in Table 3.9.

Here we note that using other parameterization of the bulk modulus of the alloys (e.g. Chen et al. 2014; Morard et al, 2018) and/or a value of γ=1.72 (e.g. Kuwabara et al., 2016; Shimoyama et al.,

2016) fixed to that experimentally determined for liquid Fe (Anderson and Ahrens, 1994) lead to a ~15% higher compressibility and consequently higher velocities without modifying the reported trend.

Table 3.9 Calculated thermo-elastic properties of all the samples at 1850 K and 5 GPa

Composition	K_T (GPa)	α ($\times 10^{-5}$ K^{-1})	C_P (J/K)	γ	v_p (m/s)
$Fe_{85.5}C_{12.9}S_{1.6}$	90.42	6.68	35.42	1.40	3859
$Fe_{84.9}C_{11.6}S_{3.5}$	92.74	6.67	35.25	1.47	3948
$Fe_{81.6}C_{12.3}S_{6.1}$	83.87	6.45	33.17	1.37	3773
$Fe_{81.3}C_{14.3}S_{4.4}$	89.12	6.39	32.71	1.43	3883
$Fe_{76.5}C_{18}S_{5.5}$	85.15	6.00	29.31	1.39	3820
$Fe_{74.8}C_{11.5}S_{13.7}$	66.41	6.08	29.21	1.15	3415
$Fe_{66.7}C_{11.2}S_{22.1}$	54.83	5.63	24.39	1.14	3211
$Fe_{60.7}C_{9.2}S_{30.1}$	47.89	5.34	21.07	1.08	3090
$Fe_{59.1}C_{10.6}S_{30.3}$	47.70	5.21	19.91	1.11	3103
$Fe_{47.5}C_{16.3}S_{36.2}$	42.21	4.54	12.14	1.39	3043

Fig. 3.8 (b) shows the calculated sound velocity compared with the data from literature for the Fe-S and Fe-C binary systems. The errors are from the fitting of Margules parameters and the uncertainties of γ. The ternary data show some scatter, but follow the trend defined for Fe-S alloys. We also note that the points showing higher values of sound velocity with respect to a linear trend are those with larger C fraction (e.g. the point at x=23.5, for which C content is 18 at%). While difficult to independently address the effect of S and C on velocities, the sound velocity of the liquid ternary alloy would offer a useful reference to model seismic velocities in the Moon's core.

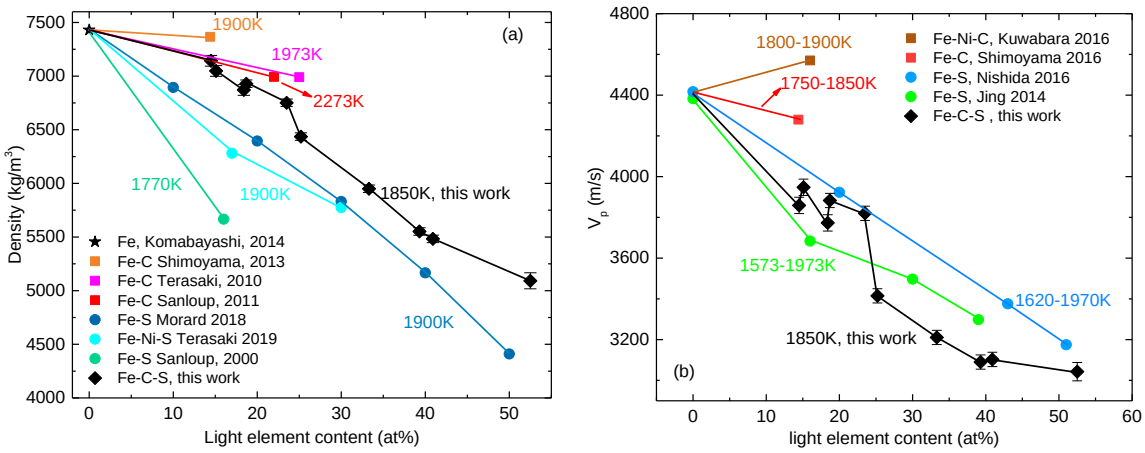

Fig. 3.8 Density (a) and sound velocity (b) at 5 GPa modeled for the ternary Fe-C-S alloys as a function of light element content and compared with data for the binary Fe-S and Fe-C system. The reference temperature for our model is 1850 K, while the temperature of other studies is annotated adjacent to the data with the same color. Lines across the points are guides for the eye.

3.7 Results of miscibility experiments

The miscibility gap of the ternary alloys was studied at two temperatures, 1650K and 2000K to detect a potential temperature effect on the miscibility gap. 1650 K is around the lower limit of the temperature range at which all the samples are fully molten based on the previously reported Fe-C-S melting experiments (Dasgupta et al., 2009; Deng et al., 2013), and 2000 K is around the maximum temperature the available cell assembly can reach. This temperature range also cover core temperatures expected in small terrestrial planetary bodies (e.g. the Moon). The miscibility gaps estimated at 1650 K and 2000 K on the basis of the bulk composition of the miscible products and the phase-sorted composition of the immiscible products are shown in Fig. 3.9.

At 1650 K, all the samples were found to be carbon-saturated, except the most iron-rich one. No typical immiscible texture was observed in these carbon-saturated samples at 4 GPa, indicating that with the graphite powder of the starting material dissolving into the alloy, the liquid composition fast reached the carbon solubility limit before entering the immiscible zone. The sample at critical status implies that miscibility gap and carbon solubility limit should intersect at the composition of the liquid product. The 2-GPa miscibility gap is constrained by only the composition of one miscible product, as the other samples from 2-GPa runs were contaminated by the thermocouple. On the other hand, both miscible and immiscible products were observed from

2000-K runs, with the 2- and 4-GPa miscibility gaps constrained by their composition. At pressures of 5 and 6 GPa, all the samples showed miscible and carbon-saturated texture, including one at the critical status. Similar to the runs at 1650 K, it becomes hard to observe immiscible liquids because the miscibility gap shrinks with increasing pressure and the liquid composition reaches first the carbon solubility limit. Since the carbon solubility increases with temperature it intersects the 5-GPa miscibility gap, as indicated by a recovered sample at critical condition.

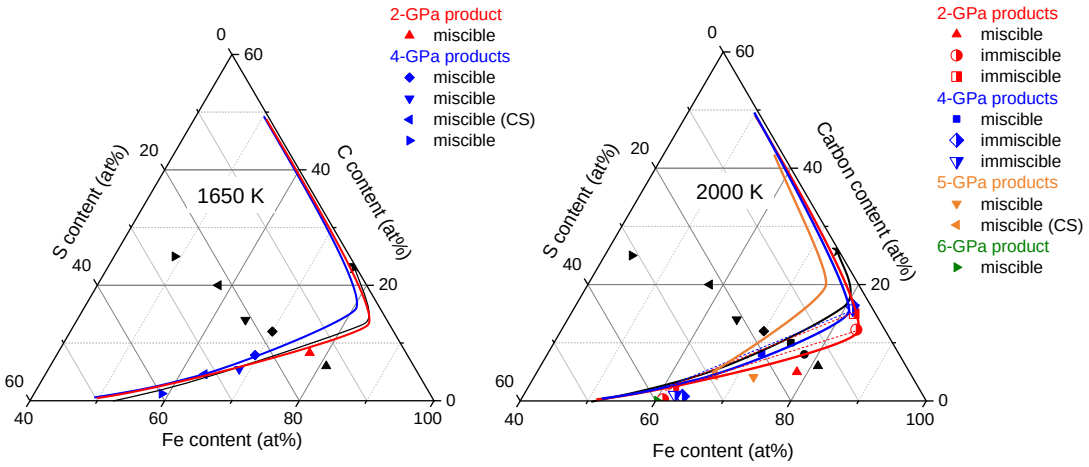

Fig. 3.9 Miscibility gaps of Fe-C-S alloys at 1650 K and 2000 K determined by the composition of recovered samples (color coded for pressure dependence). The black stars are carbon solubility limit in Fe-C liquid at 5 GPa by Fei and Brosh (2014). The other black symbols represent starting compositions, while corresponding colored symbols represent the composition of the corresponding products, with the immiscible ones linked by dashed lines. The black curves are carbon solubility limit in Fe-C-S liquid around 5 GPa, determined by the ternary data and C-saturated ternary liquid composition in this study. In the legends, CS represents critical status.

Compared to the previous studies on the miscibility of Fe-C-S liquid by Corgne et al. (2008) and Dasgupta et al. (2009), our results show an overall lower carbon content in the products, and a reduced closing of the miscibility gaps with pressure. Fig. 3.10 shows the comparison of 2, 4, and 5- GPa miscibility gaps here-constrained with determination by Dasgupta et al. (2009) at similar temperature. As the shape of the miscibility gap is determined by similar protocols in both cases, this large difference on the evolution of the miscibility gaps with pressure is rationalized as a considerable compositional difference of the recovered samples, possibly due to differences in microprobe analysis. Dissimilar duration of high-temperature experiments can be ruled out as

origin for this apparent discrepancy, as the composition of the immiscible products would only move along the miscibility gap with time, but would not modify it.

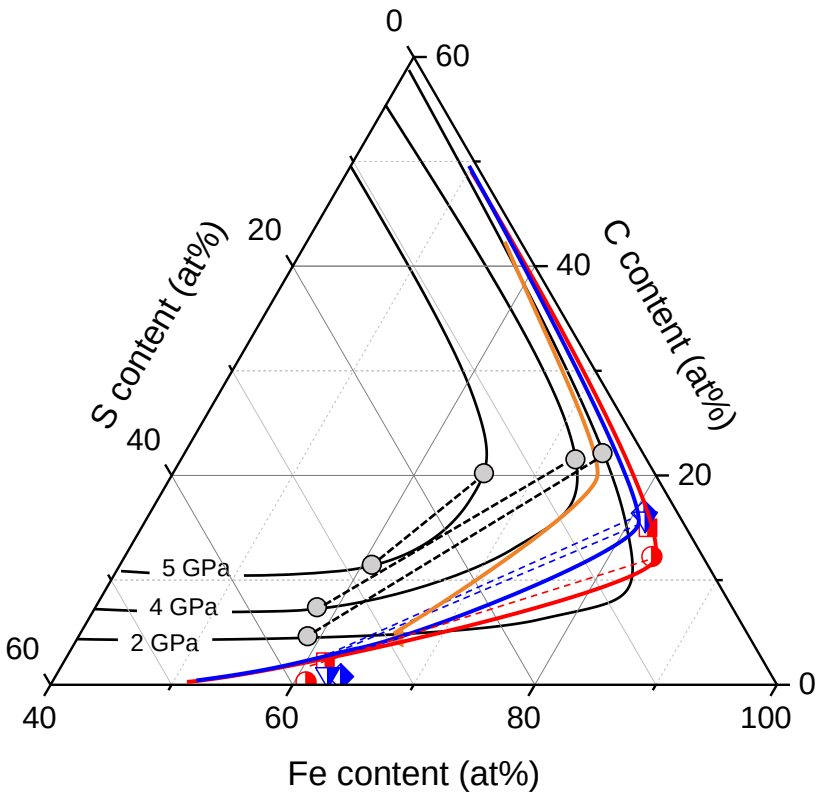

Fig. 3.10 Miscibility gaps at 2, 4 and 5 GPa (in red, blue, and orange, respectively) at 2000 K as obtained in this study in comparison with the results at 1873 K by Dasgupta et al. (2009) (in black). Grey circles are compositions of the phases in the immiscible samples, linked by the black dashed lines.

We also note that the miscibility gaps are essentially the same at 1650 K and 2000 K, while temperature largely affect the carbon solubility limit and, accordingly, the composition of the run products. Due to the higher carbon solubility in Fe-C-S alloys at 2000 K, the composition of Fe-C-S samples enter the immiscible zone after melting and partition to two phases at or below 4 GPa. However, as the carbon solubility limit in Fe-C-S liquid drops below the 4-GPa miscibility gap at 1650 K, immiscibility is hardly observed, since carbon solubility limits the dissolution of graphite in the ternary liquid. Unlike the pressure-induced closure of the miscibility gap above 6 GPa suggested by some studies, we found that in the temperature range of present interest, the miscibility gap of Fe-C-S liquid only moderately shrinks with pressure and remain about constant

with temperature. The composition of the actual products is largely controlled by the carbon solubility limit. If confirmed, terrestrial planets with a carbon- and sulfur-rich fluid core at pressures larger than 5 GPa are not likely to experience liquid partitioning, nor immiscibility-induced core stratification. Conversely, those with a core pressure below 5 GPa, could have a two-liquids Fe-C-S core could at relatively high temperature. However, with the secular cooling of the core, and the consequent reduction of the carbon solubility limit, a transition from two immiscible liquids to a single miscible liquid accompanied by carbon precipitation seems inevitable.

3.8 Summary

Liquid structures and densities of Fe-C-S alloys have been studied by a multi-techniques approach at high pressure and high temperature, up to 5 GPa and 1900 K, over a large range of carbon and sulfur composition. The experimental data were employed to establish a non-ideal thermodynamic solution model for density and other thermo-elastic properties of liquid ternary alloys as a function of pressure and composition, which provides a useful database to discuss the composition of the core of small telluric planetary bodies.

Local structure, density and sound velocity of the ternary Fe-C-S liquids have been compared to those of binary Fe-C and Fe-S liquids. Although both interstitial, S and C differently affect the liquid structure, with $g(r)$ of ternary Fe-C-S liquid very close to the $g(r)$ of binary Fe-S liquid with the same light element content. At first approximation, the local structure of ternary liquids is thus controlled by the S content. Conversely, both density and sound velocity of ternary alloys show a co-effect of carbon and sulfur. With specific regards to density, values of ternary alloys are distributed between the upper and lower values provided, respectively, by Fe-C and Fe-S alloys having the same total amount of light elements. Still, the effect of S is more significant, lowering both density and sound velocities of the ternary Fe-C-S liquids with respect to pure Fe more significantly than C, as evident from the direct comparison of properties of ternary alloys with the same total amount of light elements but different C *vs*. S proportions.

Chapter 4 Constraints on the composition of the Moon's core

4.1 Liquid iron alloys in the Moon's metallic core

Being the Moon a telluric body, its metallic core is expected to be comprised by iron alloyed with nickel and some amount of lighter elements, which could include C, O, Si and S. Moreover, the core should be at least partially molten in line with the moonquake records and geodetic observations (e.g. Lognonné and Johnson, 2007).

When considering iron and iron alloys phase diagrams, the relatively low temperatures of the Moon's interior (*T* between 1300 K and 1900 K, e.g. Wieczorek et al. 2006) point to the Fe-FeS system as the simplest explanation for a liquid iron alloy stable at the thermodynamic conditions of the Moon's core. Furthermore, the depletion of the lunar mantle in siderophile elements possibly relates with presence of sulfur in the core (Rai and Westrenen, 2014). Sulfur has a strong chemical affinity to iron at Moon's core conditions (siderophile behavior), and it is effective in decreasing the density of pure liquid iron (Fig. 3.9 (a)). Accordingly, many compositional models have been put forward for the core of the Moon based on the thermo-elastic properties of Fe-S or Fe-Ni-S liquid alloys (e.g. Nishida et al., 2011; Jing et al., 2014; Antonangeli et al., 2015; Morard et al., 2018; Terasaki et al., 2019).

Other light elements, such as oxygen and silicon, are not expected in significant concentration, as oxygen solubility into iron seems to be relatively low at the pressures pertinent to the Moon's core (Ricolleau et al., 2011), and the oxidizing conditions during the core differentiation do not favor silicon (Kilburn and Wood, 1997). On the other hand, based on silicate/metal partitioning, carbon has been also recently considered as a potential main light element, entering into the Moon's core composition up to 4.8 wt%C (Steesntra et al., 2017b), but the comparatively higher density of liquid Fe-C alloys (Fig. 3.9 (a)) seems difficult to reconcile with the density of the core constrained on the basis of the geodetic data. Similarly, compressional sound velocities of liquid Fe-C and Fe-Ni-C alloys at Moon's core pressure and temperature conditions are higher than that of liquid Fe-S (Fig. 3.9 (b)), with significant implications for the inversion of the seismological data.

Absence of data on the ternary Fe-C-S system so far largely limited the discussion and the models to the binary systems. Current dataset allows a step forward.

4.2 The Fe-C-S system and the Moon's core

The local structure of ternary Fe-C-S liquid here experimentally determined for the first time, show that the shape of the $g(r)$ and in particular the position of the first coordination sphere evolves with increasing light element content following the same trend of Fe-S liquids. As a first order approximation, the limited substitution of sulfur with carbon (~18 at.%) doesn't affect the local structure of the ternary liquid. However, the two elements have different quantitative effects on density and sound velocities (Fig. 3.8). Indeed, S lowers both density and sound velocity of liquid iron more significantly than C, as readily visible from the experimental data of Fe-C and Fe-S with the same atomic proportion.

According to these considerations, assessing the amount of C in the core of the Moon on the sole basis of seismological or geodetical observations constraining density and/or sound velocity is not straightforward. On the other hand, the possibility of carbon as a potential light element existing with sulfur in the Moon's core cannot be ruled out.

Many Moon's models were built by integrating various independent observables, including seismic, electromagnetic, geodetic, and geochemical data. Great efforts have been made to interpret these observables in terms of composition, but discrepancies still exist among studies, in particular concerning the core (Garcia et al., 2019; Viswanathan et al., 2019; Kuskov et al., 2021 and references therein). To discuss the possible content of sulfur and carbon in the Moon's core, a density contour is plotted in Fig. 4.1, where densities proposed by three of the latest Moon's models (see table 4.1 and associated references for more details) are correlated to sulfur and carbon content based on results discussed in Chapter 3. Moon's core is assumed at 5 GPa and 1850 K. Note that in Kuskov 2021 the Moon's core is modeled with a solid inner core surrounded by a liquid outer core, so that the solutions' space reported in Fig. 4.1 corresponds to the C and S content in the outer core, while a fully molten core was assumed in the other two models.

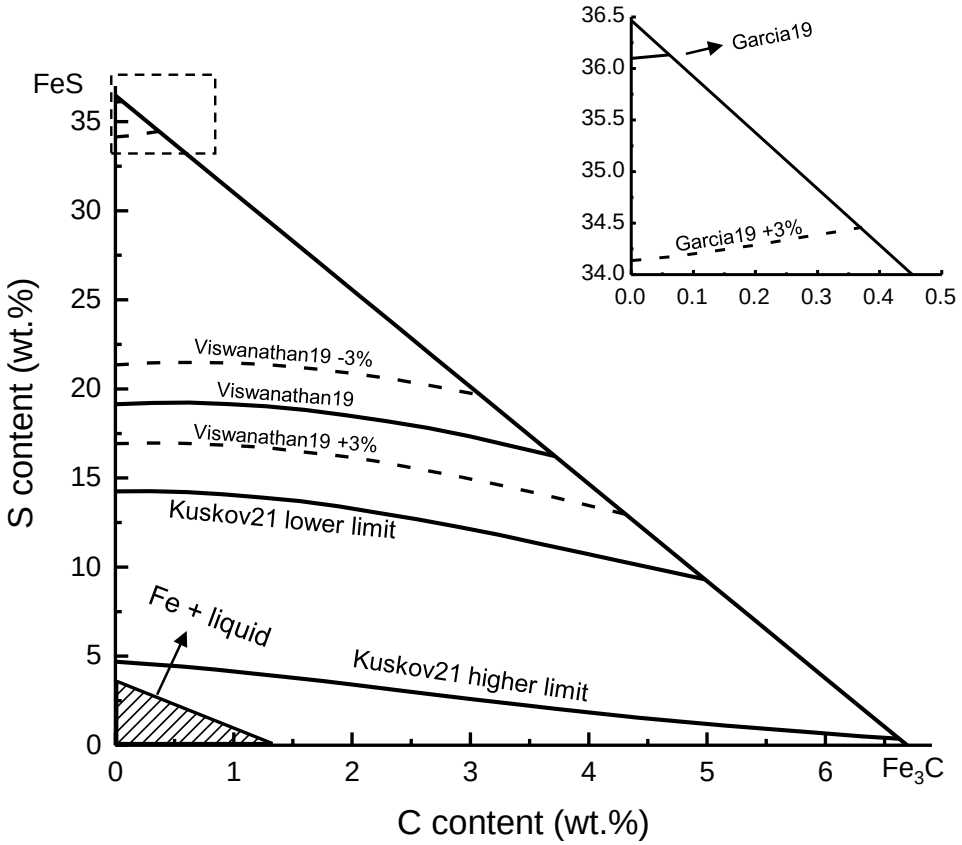

Fig. 4.1 Carbon and sulfur content within the liquid (outer) core assumed at 5 GPa and 1850 K and having density according to three recent Moon's models: Garcia19 (Garcia et al., 2019), Viswanathan19 (Viswanathan et al., 2019), and Kuskov21 (Kuskov et al., 2021). A ±3% variation is considered with respect to the density proposed in Garcia19 and Viswanathan19. Inset: Zoom-in of light element distribution for Garcia19. The shaded triangle shows the composition range for which solid Fe phase (+C at solid solubility limit) is expected in coexistence with Fe-C-S liquid.

Table 4.1 Reference models of the Moon's core here considered for discussion. Garcia19 is from model 2 in Garcia et al. (2019); Viswanathan19 is from Viswanathan et al. (2019), and Kuskov21 is from model E in Kuskov et al. (2021).

	Garcia19	Viswanathan19	Kuskov21
Main data source	Seismic T_s, T_p Geodetic M, I/MR^2, k_2 Electromagnetic ρ_a	Geodetic M, I/MR^2, k_2; Crustal thickness and density	Seismic T_s, T_p Geodetic M, I/MR^2, k_2; Geochemical bulk concentration of FeO and Al_2O_3
Core status	Fully molten	Fully molten	Solid inner core + liquid outer core
Density of the (outer) core	4550 kg/m^3	5812 kg/m^3	6200 – 7000 kg/m^3

While both Garcia19 and Viswanathan19 assume an entirely liquid core, Garcia19 suggests two Moon models with the core density ~22% lower than in Viswanathan19, resulting in a nearly pure FeS core. As the two models in Garcia19 gave quite similar core densities (4480 *vs.* 4550 kg/m^3), the model 2, using an updated geodetic dataset, is taken for discussion here. As Fe, FeS, and Fe_3C were employed as end-members for the thermodynamic model, the mixing limit (*i.e.* the maximum light-element content) is defined by the curve linking FeS and Fe_3C in Fig. 4.1. A ±3% variation with respect to the proposed density in Garcia19 reflects only into a ~2 wt% variation of required sulfur content, while allowing for some carbon (below 0.5 wt%). If this model were confirmed, the required sulfur content would be pinned to 34-36 wt.%, while the carbon content would be constrained by the ternary liquidus as a function of C and S content.

In the model Viswanathan2019, the core oblateness as a function of radius was derived from two models, one with LLR-fitted polar MOI (moment of inertia), and the other with a hydrostatic core model. The overlapped region indicates the core properties compatible with both models, which yield a core radius in the range of 381 ±12 km with a density of 5812 kg/m^3. The proposed density and the corresponding C and S contents are shown in Fig. 4.1. While carbon content spans from 0 to 4.4 wt.%, reaching the miscibility gap (as this model assumes a homogeneous liquid core, the carbon content is not supposed to exceed this limit), and correspondingly, the sulfur content is constrained within 13-23 wt.% (variation of ±3% on the nominal density).

The model Kuskov2021 assumes a partially molten core, with the density of the liquid outer core in the range of 6200-7000 kg/m^3 (and the density of the solid inner core in the range 7500–7700 kg/m^3). The pseudo binary Fe(Ni)-S was considered in this paper, with a solid inner core composed of iron (plus nickel and light elements at trace level) and an outer liquid core made of Fe-S. We can then reconsider this model in the light of our results on the ternary Fe-C-S. Both, Fe and Fe_3C are denser than the Fe-C-S liquids from which they crystallize and would be suitable candidates for an inner core, with the actual crystallizing phase controlled by the bulk concentration of carbon in the liquid.

(i) For a bulk composition on C-poor side, Fe would be the first crystallizing solid phase, leaving a Fe-C-S liquid outer core. Whether an Fe inner core would grow from the center (bottom-up), or Fe formed at the top of the core would snow across the liquid core (top-down) depends on total light element content, an in particular S content (Xu et al., 2021).

(ii) For a bulk composition with intermediate light element content (e.g. Fe-5wt%C-5wt%S, see Dasgupta et al., 2009), Fe_3C would be the first solid phase to crystallize to form a solid inner core, leaving a Fe-C-S liquid outer core until the entire available C is consumed. In a similar manner to previous case, S content is expected to largely control the top-down *vs*. bottom-up crystallization regime.

(iii) For a bulk composition on C-rich side (e.g. Fe-4.35wt%C-7.85wt%S, see Deng et al., 2013), graphite will first form during the core cooling process and float upward to the core-mantle boundary, followed by the crystallization of Fe_3C during the continuous temperature decrease to form an inner core. When applied to the model of Kuskov2021, only the latter stage is considered. Case (iii) can thus be brought back to case to (ii).

Experiments on the Fe-C-S ternary system have supported the above-outlined three crystallization regimes, which are strongly dependent on the bulk C and S content. We stress, however, that with a limited number of experiments conducted only with a few specific compositions, the C threshold between the C-poor and C-rich side, *i.e*. the eutectic point, and how it modifies with sulfur content, remain poorly constrained.

A solid inner core of fcc-iron with the density of 7500-7700 kg/m^3 was proposed in the model of Kuskov2021. In this case, further limits in the amount of light elements, beside the above-

mentioned eutectic, are placed by the liquidus (the existence of an inner core in equilibrium with melt imposes conditions below those at liquidus). Melting experiments in the Fe–S–C system indicate the liquidus temperature to decrease significantly compared to that in the Fe–S binary system by adding a very small amount of carbon into the Fe–S system (Deng et al., 2013). In absence of precise determination of the phase diagram of the Fe-C-S system, the ternary composition at liquidus temperature = 1850 K is estimated as linear interpolation between results for the Fe-C and Fe-S binary systems (Fig. 4.2) and shown as shaded area in the Fe corner in Fig. 4.1. The entire compositional space corresponding to the density of the outer core proposed in Kuskov2021 lies outside this corner for a core at 1850K. In other words, a relatively hot core at 1850 K could hardly support a solid inner core.

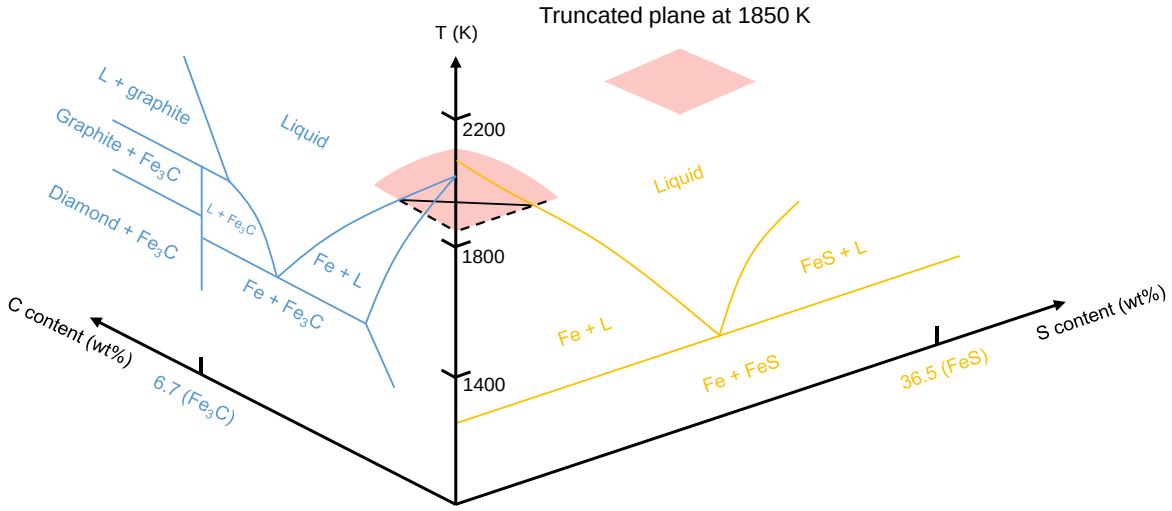

Fig. 4.2 Linear estimate of ternary composition at liquidus temperature = 1850 K from binary phase diagrams of Fe-C and Fe-S. The ternary composition is theoretically determined by the intersection of the liquidus surface of the ternary alloy and the truncated plane at 1850 K. In absence of knowledge of the ternary phase diagram, the composition is here linearly estimated.

If a colder core at 1600 K is assumed, the C and S content at liquidus are expected to significantly increase. When linearly estimated, the compositional space area for which a solid Fe phase (+C at solid solubility limit) coexists with Fe-C-S liquid is remarkably larger (Fig. 4.3). At the same time Fe-C-S liquid is denser at lower temperature, so a larger fraction of light elements is needed to account for the density proposed by the considered Moon's models (Fig. 4.4). Specifically, ~1 wt% more S would be required to justify the densities in Garcia19 and Viswanathan19 if the core is at

1600 K rather than at 1850 K. More interestingly, since the temperature's effect on density is comparatively smaller than on the liquidus composition, the compositional space accounting for the density of the outer core proposed in Kuskov2021 sees now an overlap with the composition range for which a solid Fe(+C) phase coexists with Fe-C-S liquid (Fig. 4.4). In this case, the possible C and S content in the Moon's outer core has a maximum carbon content of 2.8 wt% for a sulfur content of 4 wt%, while sulfur content could be up to 14 wt%, limited by the liquidus composition of Fe-S. We stress, however, that current knowledge of the phase diagram and melting relations of the ternary Fe-C-S system is very limited and the above discussion should not be considered quantitative.

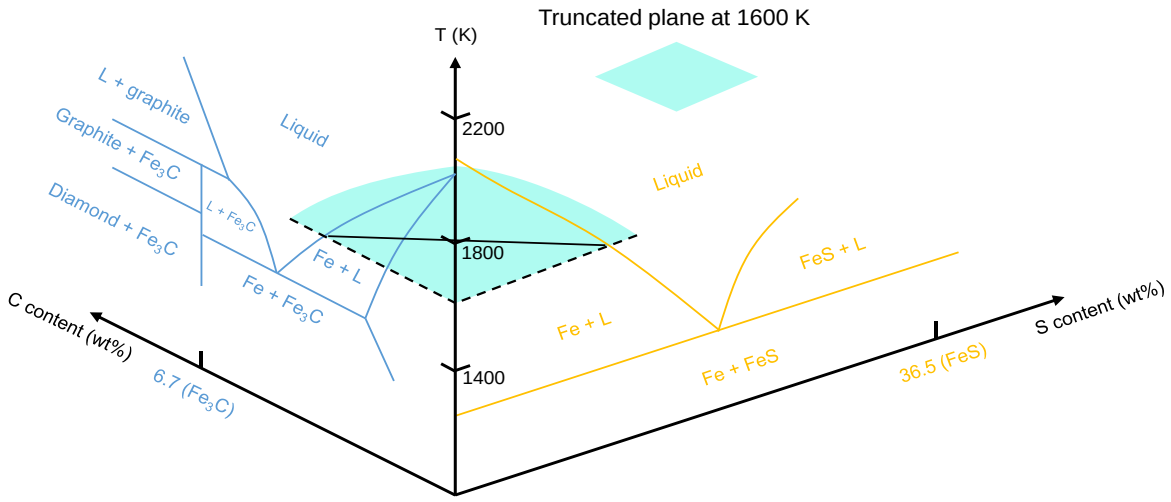

Fig. 4.3 Linear estimate of ternary composition at liquidus temperature = 1600 K from binary phase diagrams of Fe-C and Fe-S. See caption of Fig. 4.2 and text for more details.

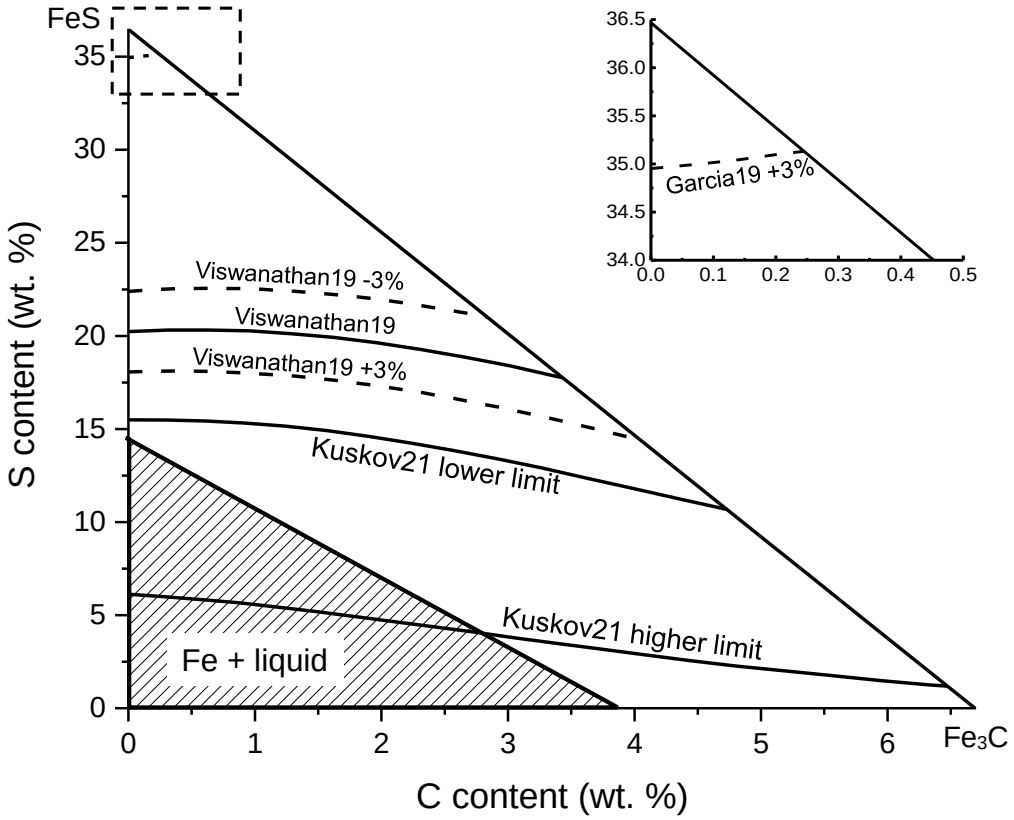

Fig. 4.4 Range of possible carbon and sulfur content within the liquid (outer) core assumed at 5 GPa and 1850 K and having density according to three recent Moon's models: Garcia19 (Garcia et al., 2019), Viswanathan19 (Viswanathan et al., 2019), and Kuskov21 (Kuskov et al., 2021).. A ±3% variation is considered with respect to the density proposed in Garcia19 and Viswanathan19. Inset: Zoom-in of light element distribution for Garcia19. The shaded area shows the composition range for which solid Fe phase (+C at solid solubility limit) is expected in coexistence with Fe-C-S liquid. This compositional space at 1600 K is significantly larger than at 1850 K (see Fig. 4.1) so that the model Kuskov21 now finds possible solutions (overlap of the shaded are with compositional space accounting for outer core density).

4.3 Summary

Based on the acquired knowledge of the thermo-elastic properties of Fe-C-S alloys, and the derived thermodynamic model, we discussed the simultaneous presence of carbon and sulfur in the Moon's core. Three of the latest Moon's models have been considered, which propose different core states (fully molten vs. partially molten) and have quite different core densities, and thus light element content. Carbon, differently from sulfur, is hardly constrained on the sole basis of density and/or

sound velocity. If the Moon's core is assumed to be composed of a homogeneous Fe-C-S liquid, the maximum carbon content is limited by the miscibility gap, here estimated at 5 GPa and 1850 K around 4.4 wt% depending on sulfur content. On the contrary, sulfur estimates on the basis of the proposed densities largely depend upon the considered model and are in a 13-23 wt.% range (Viswanathan et al., 2019) or 34-36 wt.% for model 2 in Garcia et al., 2019), well above upper limits proposed on the basis of core differentiation models (e.g. Rai and van Westrenen, 2014). About 1wt% more S would be required if the core is assumed at 1600 K rather than at 1850 K. This apparent incompatibility between a light, S-rich core advocated by geophysical observations and an S-poor core put ahead by core-differentiation models, metal-silicate partitioning and elemental abundances in the bulk silicate Moon, remains to be addressed. On the other hand, if the core were not fully molten (e.g. model E in Kuskov et al., 2021), in the Fe-C-S system, a solid inner core would be made of Fe or Fe_3C depending on whether the bulk C content is on the C-poor or C-rich side of the eutectic. The currently limited knowledge of the phase diagram and melting properties of the ternary Fe-C-S system allows only for a qualitative discussion. The existence of a solid inner core puts more constraints on core's temperature since it must be below the liquidus. If we assume a core temperature of about 1850 K, the amounts of S and C required to match the outer core density proposed in model E by Kuskov et al. (2021) make the existence of a solid inner core rather unlikely. Lower temperatures would be required to have an inner core. If the core is assumed at 1600 K, as a consequence of the temperature's effect on liquidus composition and in spite of the increased amount of light elements needed to match outer core density, a C-bearing fcc-Fe core in coexistence with a liquid Fe-C-S outer core would be possible, in qualitative agreement with the model of Kuskov21. However, in this case, the light element fraction strongly depends on a detailed understanding of the phase diagram and partial melting properties of the ternary Fe-C-S system, and the knowledge of the bulk composition of the proto-core, for which further studies are needed.

Chapter 5 Structure and compressibility of Fe_3S_2 and FeS under moderate pressures: implications for modeling the core of middle-size planetary bodies

With partial exception of Mercury, it is generally accepted that planetary bodies within the inner-solar-system (i.e. within the snow line) accreted in oxidizing conditions that favor the presence of O and S as alloyed elements in the core (Hillgren et al., 2000). Therefore, Fe-S compounds are main candidates for the core of terrestrial planetary bodies in the inner solar system, in particular concerning solid (inner) cores, due to the limited partitioning of O into solid Fe. The complexity of the Fe-S system at pressures below 20 GPa directly reflects into the fact that the stable structure of solid Fe-S cores critically on the P-T condition. For instance, an intermediate Fe-S phase between Fe and FeS, Fe_3S_2 has been reported stable at 14 GPa by Fei et al. (1997) (Fig. 5.1), replaced by two more iron-rich phases, Fe_2S and Fe_3S, at higher pressures (Fei et al., 2000). The actual stability field the Fe_3S_2 phase is still unclear and its crystal structure unknown.

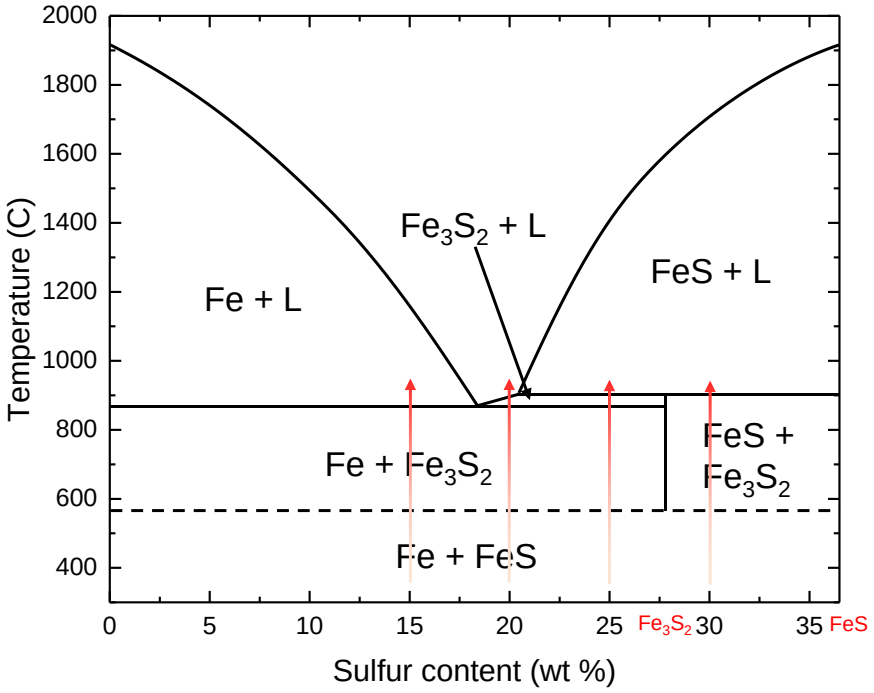

Fig. 5.1 Fe-FeS phase diagram at 14 GPa. The solid curves are phase boundaries based on Fei et al. (1997). The dashed line is the estimated phase boundary for Fe_3S_2. Red arrows show the starting compositions and the heating paths proposed in this study.

This study thus aims at addressing these two aspects of the Fe-FeS phase diagram by *in situ* X-ray diffraction. Furthermore, measurements as a function of pressure and temperature allow constraining the thermo-elastic properties of stable FeS and Fe_3S_2. To these ends, starting compositions with a wide range of sulfur content have been investigated, nominally Fe-15S, Fe-20S, Fe-25S, and Fe-30S (in wt%), as indicated in Fig. 5.1. These starting samples were prepared starting from iron and iron sulfide powders, following protocols similar to those employed for Fe-C-S samples and described in section 3.1. Experiments have been conducted in the pressure range of 11-15 GPa, either from room temperature to melting or from room temperature till target T of 900 K, and quenched, to allow analysis of the quenched melt and quenched solid phases (runs terminated at 900 K). Detailed instrumental parameters have been introduced in section 2.3.1.

5.1 Overview of the *in situ* diffraction data

The experiments include four high-pressure runs around 14 GPa, one on each composition, and one further run on Fe-25S at lower pressure, around 11 GPa, for comparison. Among the high-pressure runs, Fe-15S was heated up until melting. An isothermal decompression was performed on Fe-20S from the target P-T point to investigate the phase stability. Except the molten Fe-15S, all the others runs were quenched from the target temperature of ~900 K to retain the solid phases at experimental conditions. Fig. 5.2 shows the P-T paths followed in the various experiments.

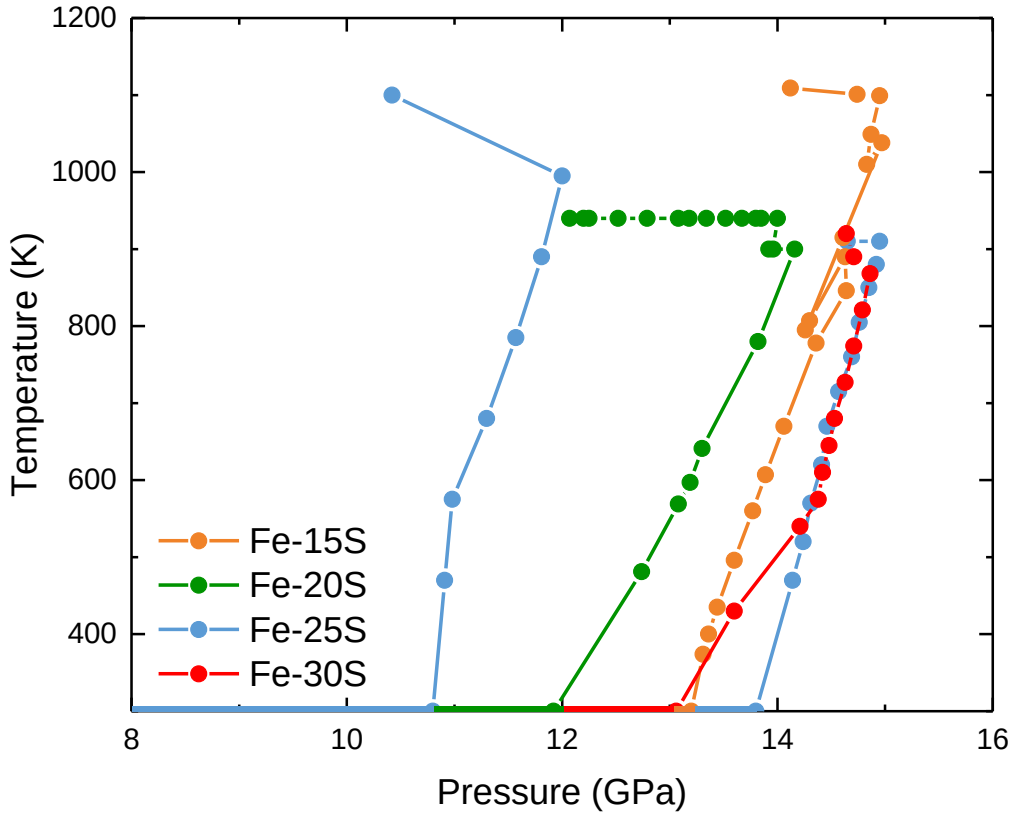

Fig 5.2 Experimental P-T paths for five Fe-S samples. All the samples went through a cold compression followed by step heating. The points indicate the P-T conditions where diffraction patterns were collected.

Fig. 5.3 shows a series of diffraction pattern collected on Fe-15S upon heating. Signal from the NaCl pressure marker was detected all the time. With increasing temperature, a small amount of FeO was detected starting from around 780 K. We consider the MgO cap sealing the capsule as the most likely source of oxygen. We note that Deng et al. (2013) also reported oxidation by MgO at similar P-T condition, and in these experiments MgO served as capsules for Fe-C-S samples. Diffraction peaks from Fe_3S_2 appeared at 890 K, concomitant with the rapid reduction of the intensity of FeS peaks. A phase transition from hcp-Fe to fcc-Fe occurred between 890 K and 1049 K. Fcc-Fe coexisted with Fe_3S_2 until the onset of melting at 1109 K, pinned by the appearance of a diffuse signal. At 1109 K XRD pattern from sample contains only diffuse signal from liquid and sharp peaks from fcc-Fe.

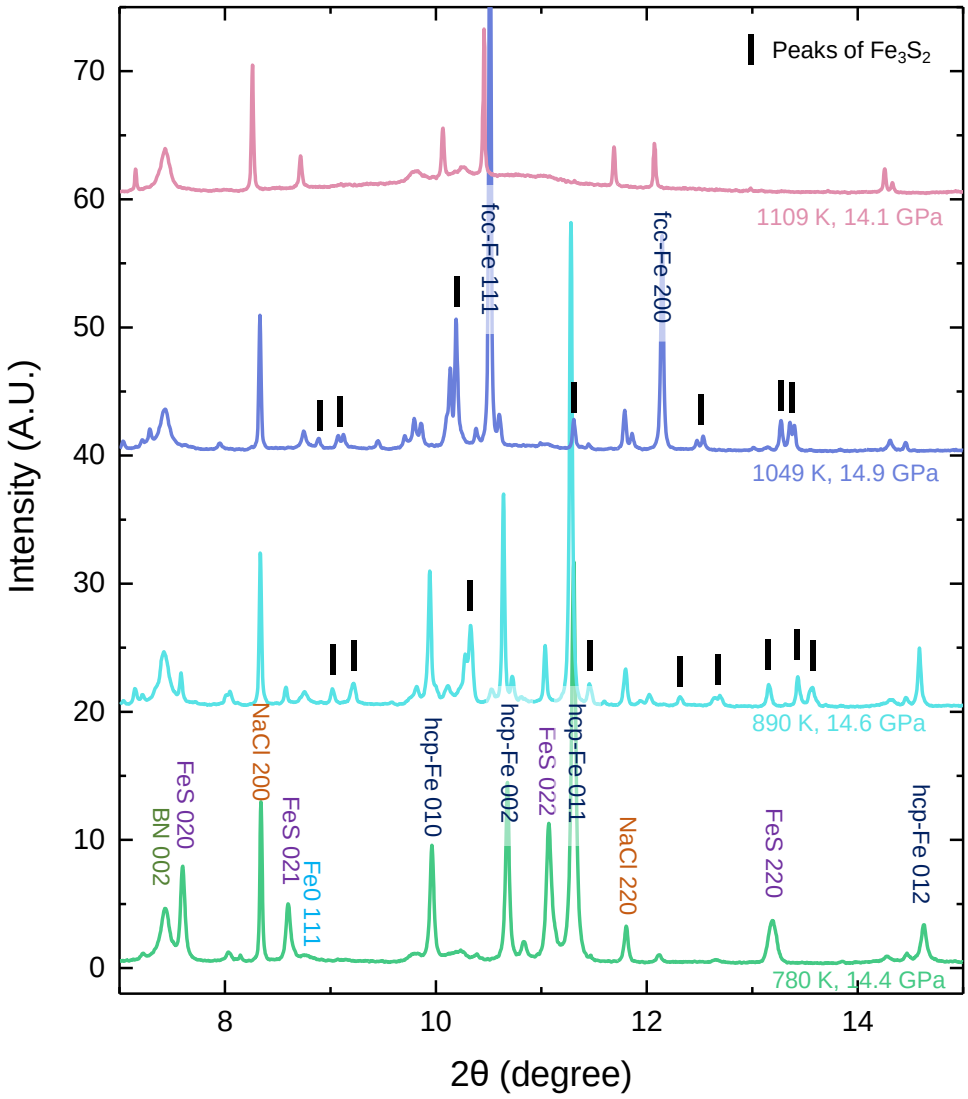

Fig. 5.3 Series of diffraction pattern collected on Fe-15S upon heating. Peaks of NaCl and BN are observed all the time. Reflections from FeO appeared at 780 K and remained visible over the entire explored P-T range. Diffraction signal of Fe_3S_2 appeared at 890 K and disappeared upon melting, once the diffused signal was detected. The phase transition from hcp-Fe to fcc-Fe was observed between 890 K and 1049 K. The partially molten sample at 1109 K only shows diffuse signal from liquid and sharp peaks from fcc-Fe.

Same products, Fe and Fe_3S_2, were observed at ~900K in the run on Fe-20S. Isothermal decompression allowed to estimate the Fe_3S_2 phase stability boundary at P=12.2 GPa, pressure below which the Fe_3S_2 decomposed in fcc-iron and FeS (Fig. 5.4). This phase transition boundary is also supported by the run on Fe-25S, where no Fe_3S_2 was produced up to 12 GPa and 995 K.

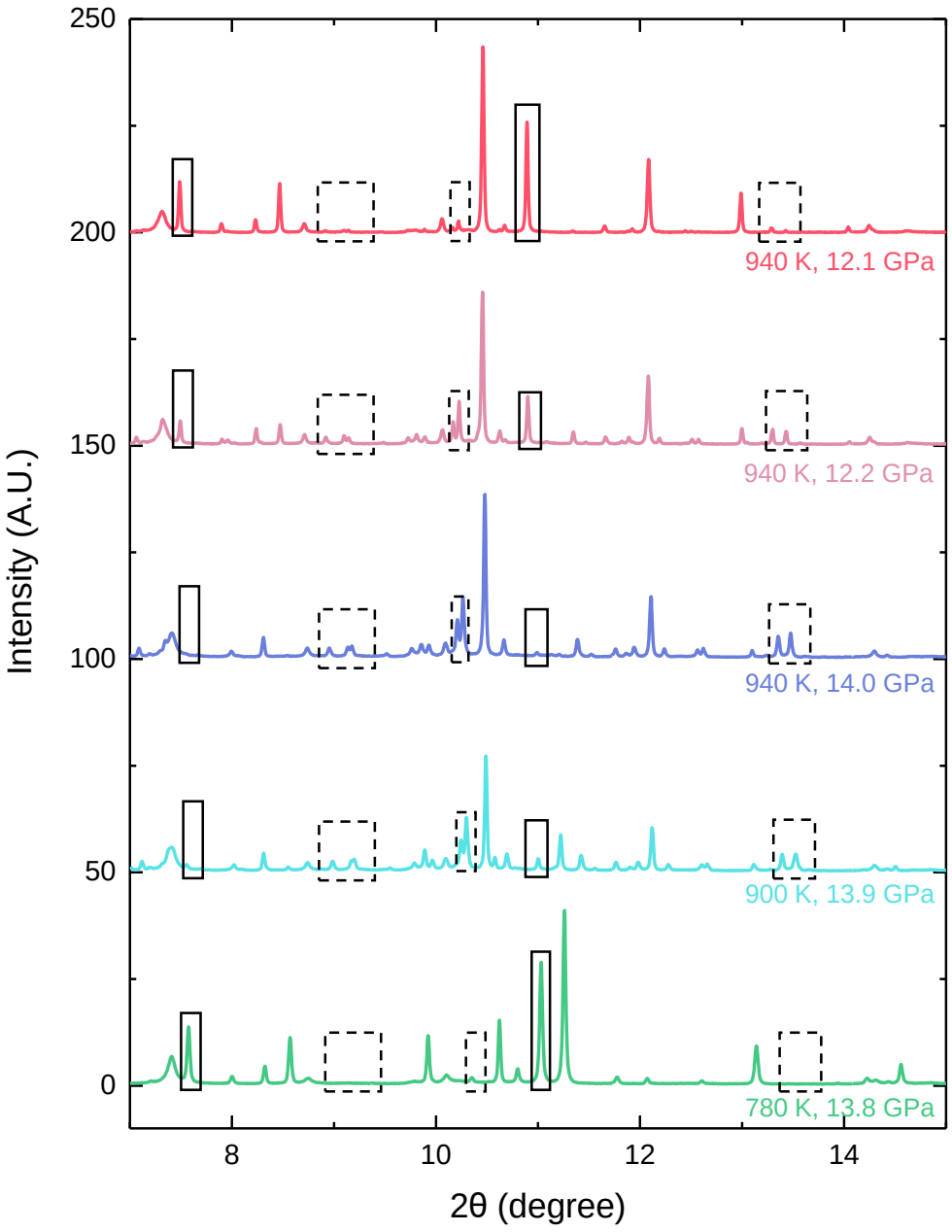

Fig. 5.4 The diffraction pattern sequence of the run on Fe-20S. An almost isobaric heating (from 780 K to 940 K) was followed by an isothermal decompression (from 14 GPa to 12.1 GPa at 940 K). For clarity, peaks characteristic of Fe_3S_2 are highlighted in the dashed boxes, and that of FeS in the solid boxes. Upon heating the sample follows a phase sequence similar to that of Fe-15S discussed above. In particular, as in Fe-15S, the new intermediate phase appeared at 900 K and its diffraction peaks became more pronounced at 940 K. The phase transition from hcp-iron to fcc-iron occurred at 900 K upon heating. With the appearance of Fe_3S_2 the FeS was consumed and its signal disappeared at 940 K, while signal from Fe remained evident. The isothermal decompression path shows that the Fe_3S_2 starts to transform back to Fe and FeS around 12.2 GPa, and the reaction completes at 12.1 GPa.

Fe_3S_2 and FeS were also observed as the products in the high-pressure run on Fe-25S and Fe-30S. It is worth noting that in the run on Fe-25S, Fe + Fe_3S_2 were expected as products, as the stoichiometric Fe_3S_2 has 27.7 wt% of sulfur. Conversely peaks of FeS + Fe_3S_2 were detected up to 1000 K, temperature at which the run was quenched to allow analysis of the recovered solid phases. This unexpected combination of products was attributed to the partial oxidation of iron occurred prior to the transition of Fe_3S_2. The consumption of part of the iron made the actual S fraction in the Fe-S sample larger than 27.7 wt%, leading to the stabilization of FeS together with stoichiometric Fe_3S_2.

A summary of the products from all the runs can be found in the table below.

Table 5.1 Maximum pressure and products of each run

Starting composition	Maximum Pressure (GPa)	Products
Fe-15S	14.97	Fe + Fe_3S_2 + trace FeO
Fe-20S	14.16	Fe+Fe_3S_2 + trace FeO
Fe-25S (low-P)	12.00	Fe+FeS + trace FeO
Fe-25S (High-P)	14.95	FeS+Fe_3S_2 + trace FeO
Fe-30S	14.86	FeS+Fe_3S_2 + trace FeO

5.2 Micro-structure analysis and chemical quantification

All the recovered samples were carbon coated and analyzed by a ZEISS 55 scanning electron microprobe at IMPMC and double-checked with analysis at ISTeP, Sorbonne University. EDS mapping and quantification were also conducted on each sample. The figures below show some representative textures.

The texture of Fe-15S is shown in Fig. 5.5. This run was quenched from partial melting and this is reflected by the simultaneous presence of quenched liquid (the homogeneous area on the left side, next to the MgO cap) with solid grains (on the right side). Fig. 5.5 (b) shows the electron back-scattered image of the solid portion, where two phases coexist. The standardless EDS quantification conducted on the two phases indicates that one of them is Fe_3S_2 and other is an Fe-S compound with sulfur concentration lower than 50 at% (Table 5.2). Possibly, this Fe enrichment

is consequence of signal coming from metallic Fe and a small amount of produced Fe_3S_2 discernable as tiny grains in Fig. 5.5 (b). In addition, an O contamination trace level was detected, in line with the diffraction patterns that showed a small contribution from FeO.

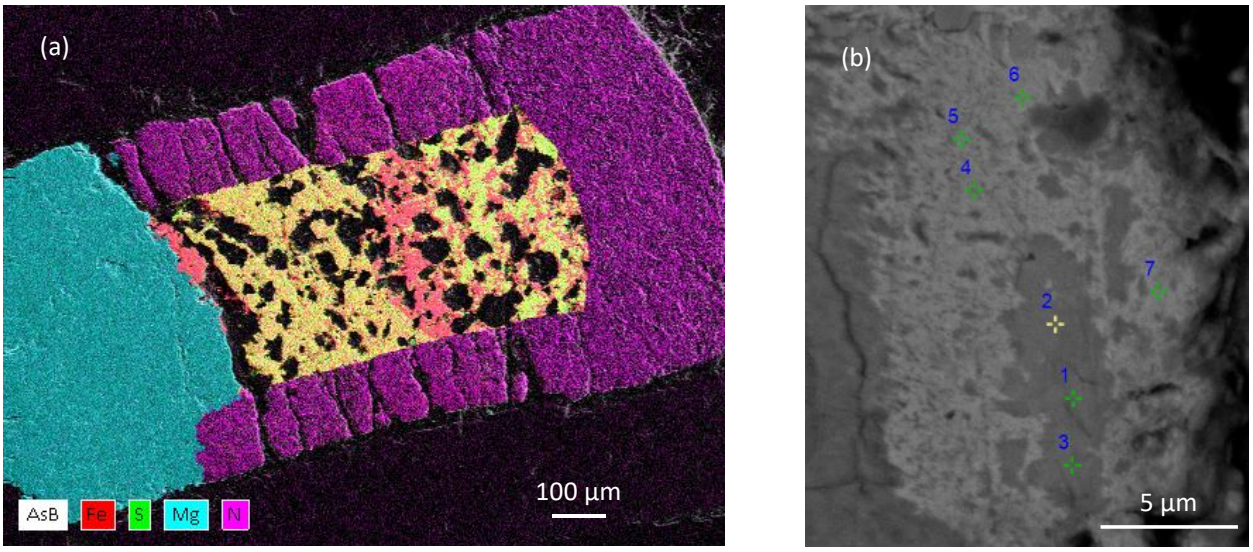

Fig. 5.5 (a) EDS mapping of the recovered assembly from run on Fe-15S. The sample is at the center, while the magenta area corresponds to the BN capsule, and the cyan area to the MgO cap. (b) BSE image focusing on the solid portion of the recovered sample. The numbered points correspond to individual analysis and the resulting phases are indicated in the table 5.2.

Table 5.2 EDS quantification on Fe-15S solid part

Phase	O	S	Fe	Ni	Total*
Fe_3S_2 (point 1-3)	1.94 (0.54)	41.56 (1.63)	56.50 (1.84)	0 (0)	100.00
Fe-S alloy (point 4-7)	0.61(0.50)	28.83(0.71)	70.51(0.79)	0.05(0.05)	100.00

* Standardless EDS analysis, the content has been rescaled and shown in atomic percent.

The BSE image of Fe-20S (Fig. 5.6) shows the coexistence three phases in the recovered sample, the bright Fe grains, dark Fe-O compound, and FeS grains with intermediate brightness. Quantified results are shown in Table 5.3. The Fe-O compound shows a depleted oxygen content compared to stoichiometric FeO, probably due to contribution from a small amount of tiny iron grains, as FeO diffraction peaks exhibit no difference from nominal values until the quench (Fig. 5.4).

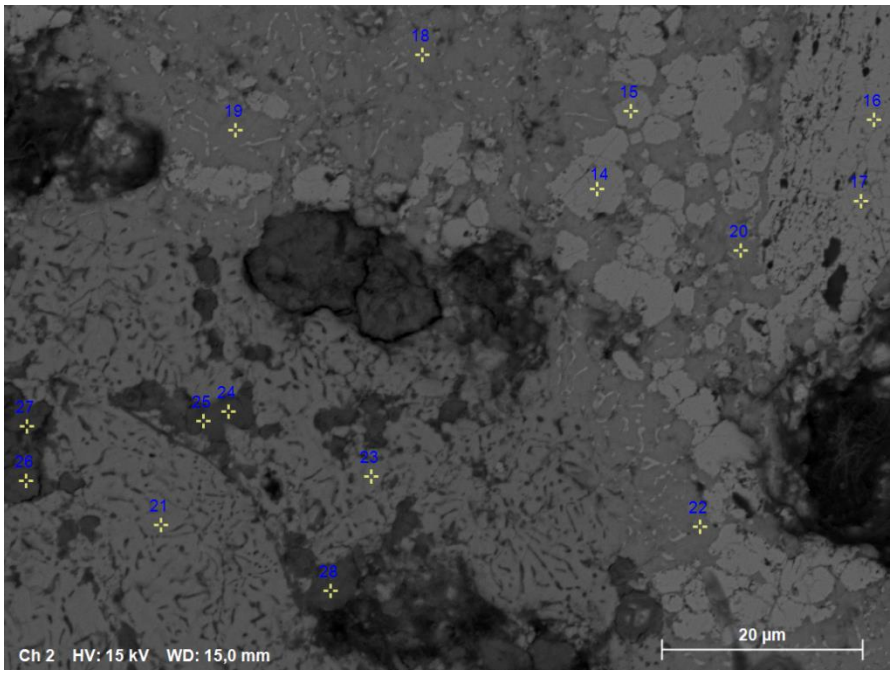

Fig. 5.6 Back-scattered electron image of the recovered sample from run on Fe-20S. Three phases are observed: Fe, FeS and an Fe-O compound having less concentration in O than FeO. Pores could be signature of the NaCl pressure marker that got detached during polishing. The Fe shows two different textures, the larger-sized grains which could be the original grains, and the small spots and traces, which could be formed by the decomposition of Fe_3S_2 during the decompression.

Table 5.3 EDS quantification in atomic percent on products quenched from run on Fe-20S

Phase	O	S	Fe	Ni	Total
Fe (point 14-17)	0 (0)	0.16 (0.06)	99.77 (0.11)	0.07 (0.07)	100.00
FeS (point 18-23)	0.11(0.25)	46.24 (1.26)	53.60 (1.42)	0.05 (0.11)	100.00
Fe-O compound (point 24-28)	30.75(3.10)	2.41 (0.74)	66.78 (3.80)	0.06 (0.04)	100.00

5.3 Structure and lattice parameter of Fe_3S_2 under pressure

Fei et al. (1997) first reported the stabilization of Fe_3S_2 above 14 GPa, but the structure remained unsolved. A study on Ni_3S_2 shows that it has a trigonal structure with R32 symmetry at ambient pressure, and an orthorhombic structure with Cmcm symmetry above 20 GPa (Prewitt et al., 2002). As an analogue, it is possible that Fe_3S_2 exhibits a similar structure. To determine this, the lattice parameters of each phase in the collected diffraction patterns were refined with the GSAS-II

(General Structure Analysis System) package, using the Rietveld method. Fig. 5.7 shows an example of pattern collected in run Fe-20S at 900K, in which the residual peaks belongs to the Fe_3S_2 phase. We compare these peaks extracted from all the patterns observing good consistency in terms of number and position.

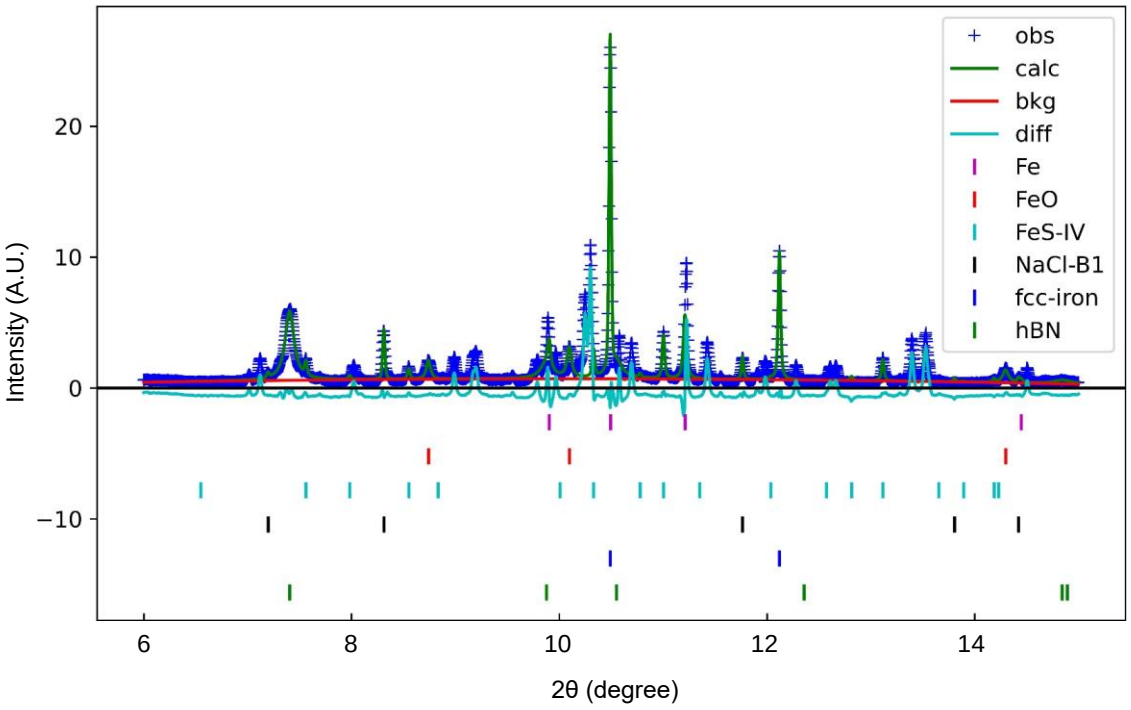

Fig. 5.7 Rietveld refinement of the diffraction pattern collected on Fe-20S at 13.92 GPa and 900K. Among the five components, it is noteworthy that NaCl was added in the mixture as pressure marker and detached during the polishing. Chemical reaction between NaCl and Fe-S mixtures was never observed.

The diffraction patterns were imported to PreDICT software to determine the structure of Fe_3S_2. Fig. 5.8 shows the interface of the software. Using the data of Fe-20S at 900 K and 13.92 GPa as an example, after setting the correct wavelength and selecting all the visible peaks of Fe_3S_2, the fitting is initiated by clicking 'Run DICVOL'. According classic protocols the fitting should be started trying to use high-symmetric crystal structures, such as cubic, and if no solution found, move to a less symmetric structure. In our case, no solutions were found with cubic, tetragonal, or hexagonal, until using orthorhombic.

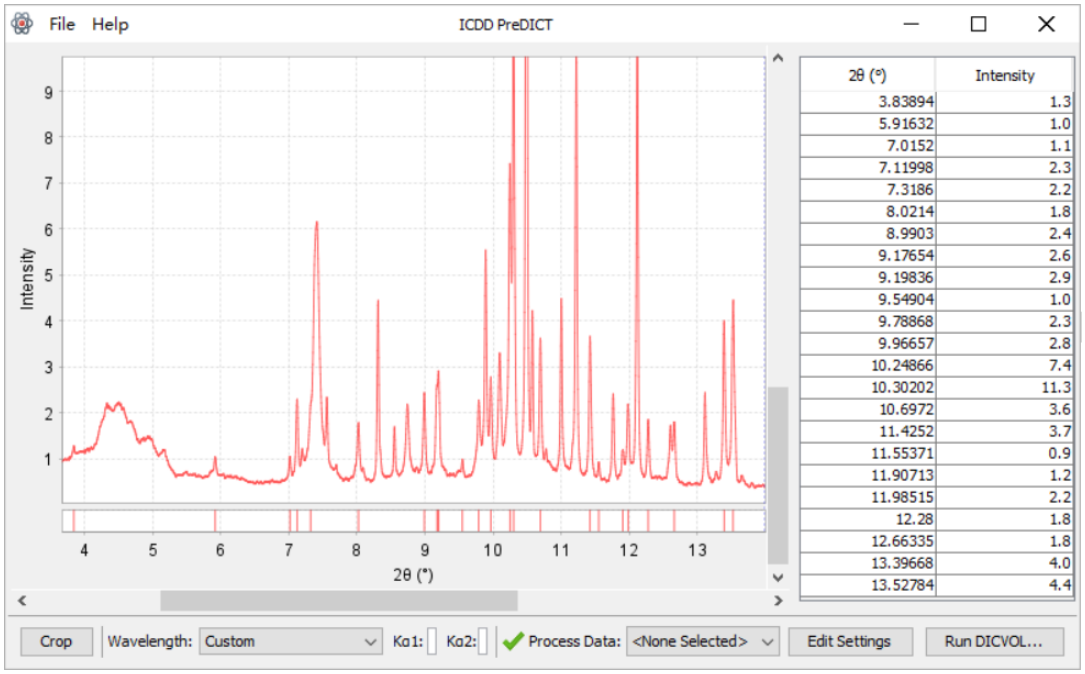

Fig. 5.8 The interface of preDICT with the diffraction pattern of Fe-20S at 900 K and 13.92 GPa. The short red lines below the pattern indicate the positions of peaks belonging to Fe_3S_2.

Fitting the peaks to an orthorhombic structure produced a solution with a=11.139 Å, b=9.531 Å, c=3.171 Å, and the unit-cell volume of 336.65 $Å^3$. The solution is unique and can be reproduced in all the collected diffraction data at comparable P-T conditions. To further determine the point group and space group, the software *CHEKCELL* was used to fit all the visible peaks. There are three point groups, and correspondingly 59 space groups included in the orthorhombic crystal system, and *CHEKCELL* can search for the best matching space group among them by the given peak positions and lattice parameters. Fig. 5.9 shows the interface. By fitting the 34 visible peaks to the 59 space groups, the search function produces three best-estimated space groups, PNA21, PNN2, and PNNM. Noteworthy, each of these three groups foresees several extra peaks here not observed. Using the PNA21 group as example (Fig 5.9), the lower section of the software shows the predicted peaks vs. the observed peaks. Most likely all the extra peaks predicted according to the three space groups are not discernable in the image plate because they are too weak. Therefore, without further experimental data, the space group of Fe_3S_2 cannot be uniquely determined and only constrained to the mentioned three cases.

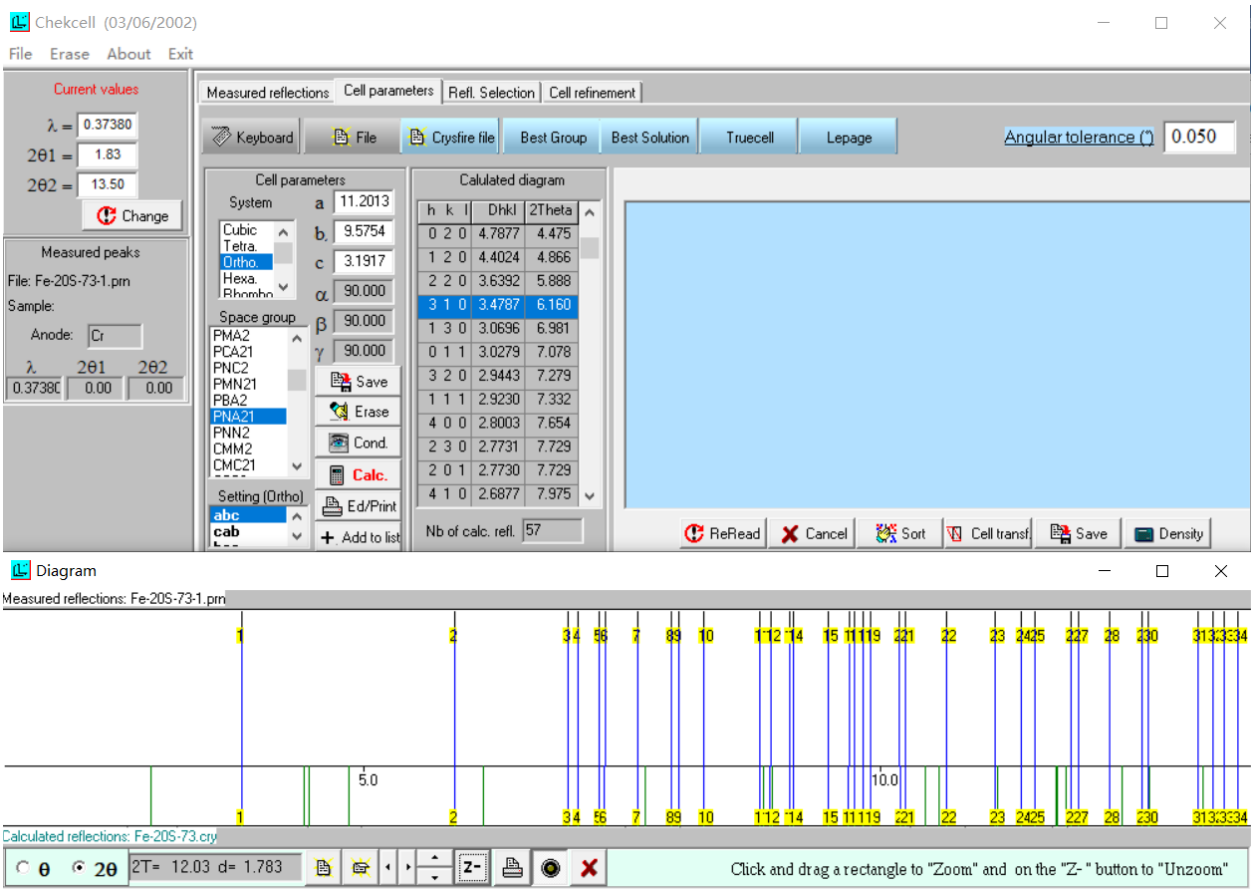

Fig. 5.9 The interface of *CHEKCELL* software. The upper section includes the diffraction and crystal information, and the lower section shows the fitting results (in green) compared to the predicted peak position (in blue) within the given 2θ range.

The unit-cell volume of Fe_3S_2 at experimental conditions are summarized in Table 5.4, and plotted as a function of pressure in Fig. 5.10, which shows as well dependence on pressure over the here-considered T range of the individual lattice parameters.

Table 5.4 Lattice parameters and derived volume of Fe_3S_2 at experimental conditions from each run

Runs	P (GPa)	T (K)	a (Å)	b (Å)	c (Å)	V (Å^3)
Fe-15S	14.3	850	11.101	9.501	3.158	333.09
	14.3	850	11.101	9.501	3.162	333.58
	14.61	915	11.133	9.527	3.173	336.49
	14.97	1038	11.166	9.558	3.189	340.33
	14.83	1010	11.208	9.588	3.203	344.15
	14.87	1049	11.231	9.612	3.213	346.84
	14.95	1099	11.261	9.634	3.222	349.50
	14.74	1101	11.297	9.647	3.227	351.71
Fe-20S	14.16	900	11.127	9.521	3.166	335.39
	13.92	900	11.139	9.531	3.171	336.65
	13.92	900	11.138	9.535	3.172	336.92
	13.96	920	11.147	9.539	3.177	337.83
	14	940	11.168	9.560	3.183	339.82
	13.95	940	11.174	9.555	3.186	340.1
	13.9	940	11.177	9.559	3.186	340.39
	13.85	940	11.178	9.559	3.187	340.51
	13.8	940	11.176	9.560	3.187	340.55
	13.67	940	11.181	9.561	3.188	340.77
	13.52	940	11.184	9.565	3.188	341.08
	13.34	940	11.191	9.568	3.189	341.46
	13.18	940	11.194	9.570	3.189	341.67
	13.08	940	11.198	9.571	3.190	341.90
	12.79	940	11.201	9.575	3.192	342.33
	12.52	940	11.209	9.581	3.193	342.91
	12.25	940	11.218	9.586	3.196	343.63
	12.2	940	11.219	9.590	3.198	344.03
Fe-25S	14.85	850	11.057	9.470	3.143	329.10
	14.92	880	11.148	9.477	3.145	332.29
	14.95	910	11.103	9.504	3.162	333.64

	14.65	910	11.111	9.512	3.164	334.36
Fe-30S	14.71	890	11.123	9.510	3.164	334.71
	14.64	920	11.128	9.521	3.170	335.86
	14.24	920	11.139	9.521	3.175	336.70

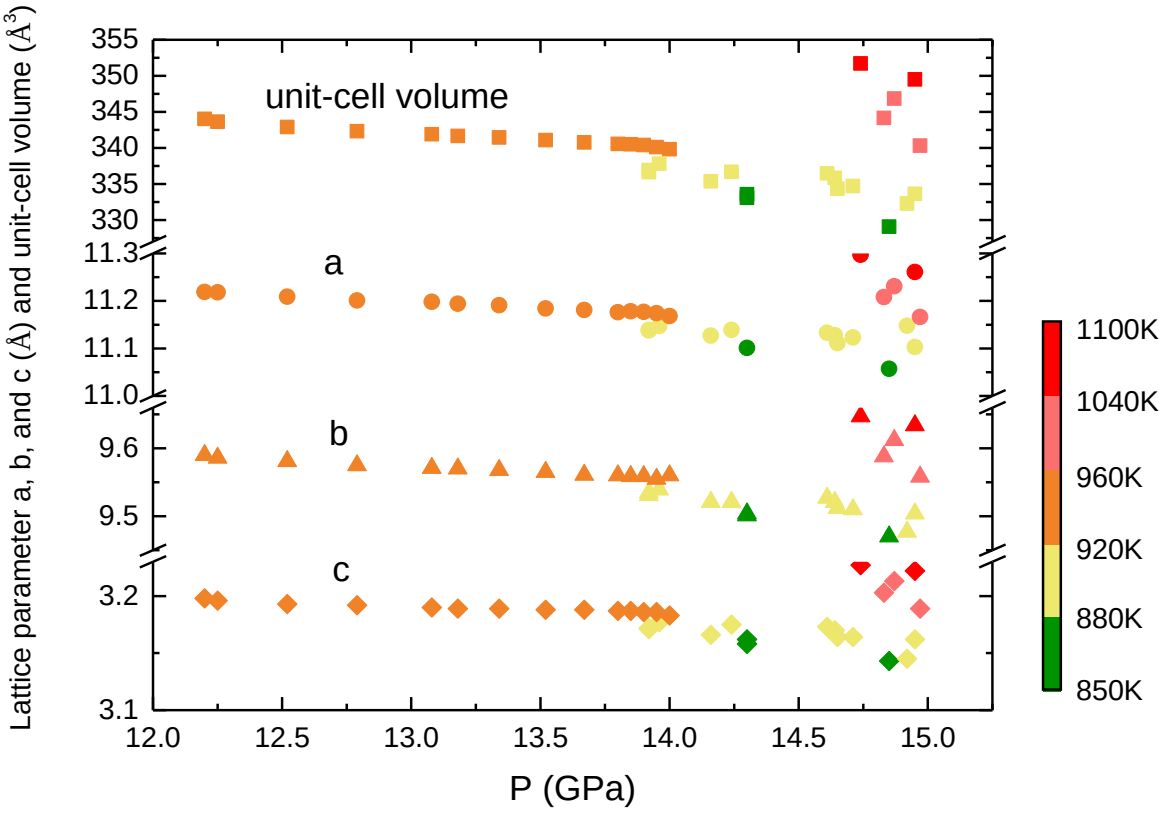

Fig. 5.10 Lattice parameters and unit-cell volume of Fe_3S_2 as a function of pressure in the temperature range from 850 K to 1100 K. Squares represent the unit-cell volumes (in Å^3), while circles, triangles, and diamonds are the values of a, b, and c, respectively.

The density of Fe_3S_2 is related to the unit-cell volume and the molar mass by the relation

$$\rho = \frac{M}{V_{unit-cell} \times N_A/Z} \tag{5.1}$$

where the M is the molar mass, N_A the Avogadro's number, and Z the number of molecules in one unit cell. Common crystals adopt even Z values, such as 4, 6, 8, 12, etc. Without knowing the exact Z value of Fe_3S_2, its density was first estimated by that of the reactants, Fe and FeS, with the following chemical equation, assuming an unchanged volume throughout the reaction:

$$2FeS + Fe = Fe_3S_2 \tag{5.2}$$

For instance, the analysis of the diffraction pattern of Fe-20S at 940 K and 14 GPa allows the determination of all lattice parameters of Fe and Fe_3S_2. Knowing their molar volumes and assuming an unchanged volume during the reaction, the density of the product is computed as 6310 kg/m^3. This density assessment may shed a light on the Z value of Fe_3S_2, as the volume is not expected to change significantly during the reaction. With hypothetic Z values of 4, 6, 8, and 12, the theoretical density computed with Eq. (5.1) are 4520, 6790, 9050, and 13570 kg/m^3, respectively. Consequently, Z = 6 is here considered the most plausible value.

As Fe_3S_2 decomposes to Fe + FeS below 12.2 GPa, and melts above 1100 K, structural information on Fe_3S_2 can be obtained only in a relatively narrow P-T range. The isothermal decompression data allow to determine the isothermal bulk modulus K with respect to pressure at 940 K, but it was not possible to determine as well its pressure derivative K' due to the small pressure range. As such, the data points were fitted to the second-order Birch-Murnaghan equation of state (i.e. the Eq. 2.43 with K' fixed at 4) and the Vinet equation of state (Eq. 2.44) with K' also fixed to 4 for comparison. The fit is shown in figure 5.11 and resulting parameters are summarized in table 5.5. The two fits result in similar pressure dependence of volume and the zero-pressure volume. While there is a large difference on the bulk modulus, the two fits are considered both valid in this narrow pressure range.

Table 5.5 Fitted thermal expansivity and EOS parameters using second-order Birch-Murnaghan and Vinet formalism with K'=4 for Fe_3S_2 at T = 940 K

T_0 (K)	940K	
Formalism	2nd-order Birch-Murnaghan	Vinet
$V_{0(T_0)}$ (Å^3)	372.2 (0.8)	367.3 (0.6)
$K_{0(T_0)}$ (GPa)	129.9 (3.8)	185.2 (4.0)
K'_{T_0}	4[a]	4[a]
α ($\times 10^{-5}$ K^{-1})	26.5[b]	

[a] Fixed value.
[b] The value is determined by the definition of thermal expansion (Eq. 3.1) with the experimental volumes in 14-15 GPa and 850-1100K.

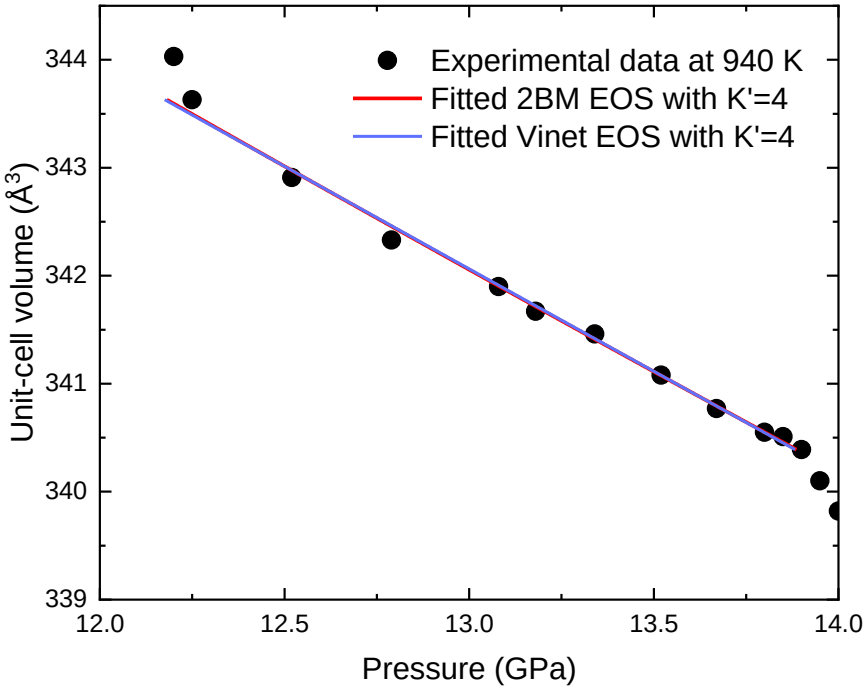

Fig. 5.11 Experimental data and fitted EOS for *K'* fixed to 4. A few points at the two ends of the here-considered pressure range have been removed from the fitting as they showed a variance approaching the phase stability boundary.

5.4 Lattice parameters and compressional behaviors of FeS-IV and FeS-V

The lattice parameters measured for the two phases of FeS, FeS-IV (hexagonal) and FeS-V (NiAs type) observed in run Fe-25S at low and high pressure and in run Fe-30S, are listed in Table 5.6. Using a fundamental NiAs type cell (a_f and c_f) to describe the unit cell of these two phases, $a = 2a_f$ and $c = c_f$ for FeS-IV, and $a = a_f$ and $c = c_f$ for FeS-V (Kusaba et al., 1998).

Table 5.6 Lattice parameters of FeS-IV and FeS-V at experimental P-T conditions

Phase	P (GPa)	T (K)	a/b (Å)	c (Å)	c_f/a_f
Run Fe-25S, low pressure					
FeS-IV	10.91	470	6.537	5.335	1.632
	10.98	575	6.561	5.361	1.634
	11.3	680	6.577	5.185	1.638
	11.57	785	6.593	5.408	1.641
	11.81	890	6.61	5.425	1.641
FeS-V	12	995	3.316	5.447	1.643
	10.42	1100	3.349	5.512	1.646
Run Fe-25S, high pressure					
FeS-IV	14.24	520	6.494	5.295	1.631
	14.31	570	6.494	5.303	1.633
	14.41	620	6.499	5.313	1.636
	14.46	670	6.504	5.326	1.638
	14.57	715	6.506	5.327	1.638
	14.69	760	6.512	5.334	1.638
	14.76	805	6.513	5.336	1.638
	14.85	850	6.514	5.338	1.64
	14.92	880	6.519	5.344	1.64
	14.95	910	6.526	5.352	1.64
Run Fe-30S					
FeS-IV	14.38	575	6.43	5.267	1.638
	14.53	680	6.495	5.322	1.638
	14.63	727	6.504	5.328	1.638
	14.71	774	6.513	5.340	1.64

14.79	821	6.521	5.346	1.64
14.86	868	6.53	5.356	1.64
14.71	890	6.544	5.367	1.64
14.64	920	6.530	5.359	1.642

All the FeS phases show an anisotropic compressibility indicated by the ratio c_f/a_f varying with temperature and pressure.

The low-pressure range from 0 to 8 GPa have been carefully investigated by Kusaba et al. (1998) and the derived dependence of ratio c_f/a_f with pressure and temperature is shown in Fig. 5.12, together with our data on FeS-IV and FeS-V at high pressure and high temperature. Our experimental data show high consistency with the previous studies, and complement published dataset with further results at higher pressures and temperatures.

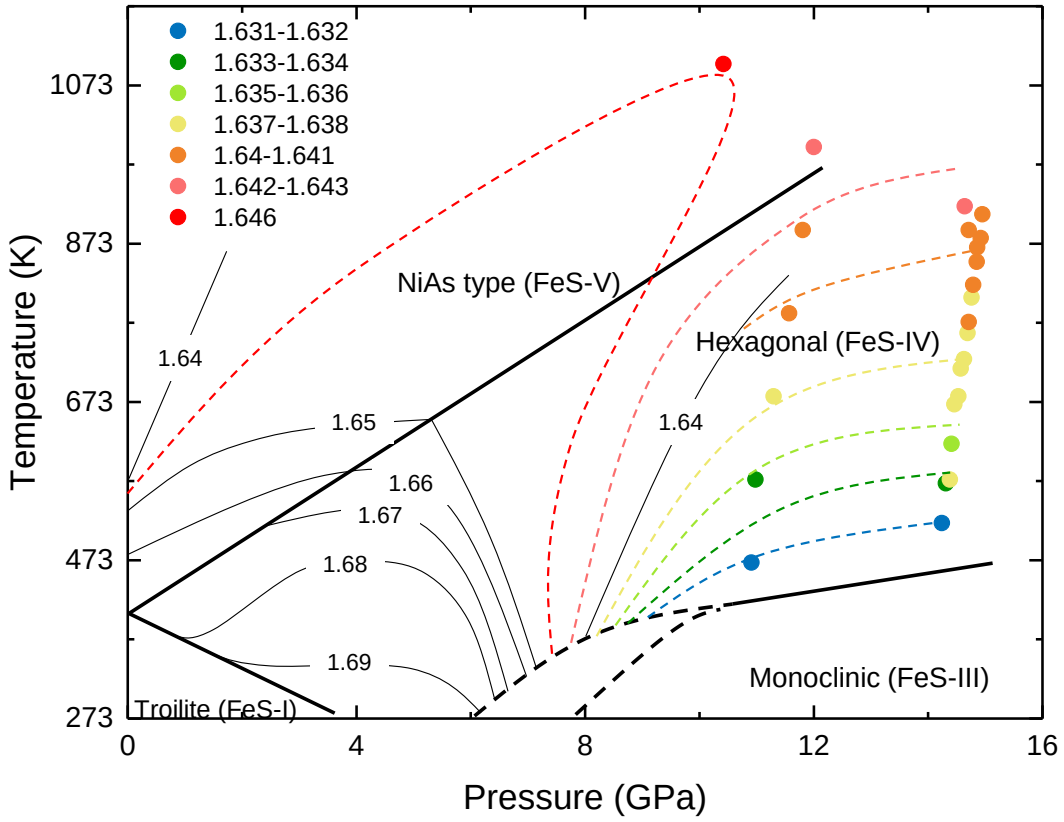

Fig. 5.12 Contours of c_f/a_f ratio of FeS as a function of pressure and temperature between room temperature and 1173 K and from 0 to 16 GPa. The bold lines (curves) indicate the phase boundaries of

different phases, and the black thin curves the contours of the c_f/a_f ratio discretized in the range from 1.64 to 1.69 (Kusaba et al., 1998). Colored points are data of this study, and the dashed curves with same color are estimated contours.

5.5 Sulfur in "middle-size" terrestrial planetary cores

The phase stability of Fe_3S_2 below melting observed in this study confirms the notion that it would be one of the possible phases in solid cores of middle-size sulfur-rich terrestrial planets, specifically for planets having a core pressure larger than 12 GPa. The upper bound of pressure stability of Fe_3S_2 is expected close to ~20 GPa, since more iron-rich products, Fe_3S and Fe_2S, have been observed at 21 GPa (Fei et al., 2001).

Although current understanding of the interior of Galilean satellites of Jupiter is rather limited, if core's pressures of Europa, Io, and Ganymede are confirmed to range from 6 to 10 GPa, the main products of a crystallizing Fe-S core would be Fe or FeS, depending on sulfur concentration. Crystallization of Fe_3S_2 requires bigger and/or denser bodies. A telluric planet in the solar system with core at relatable pressures is Mercury. The core of Mercury could account for 3/4 of its radius due to its relatively large mass and small radius (Anderson et al., 1987), and hence with pressure spanning from 5-8 GPa (estimated pressure at core mantle boundary) to 30-44 GPa (center) (Rivodini et al., 2009). Mercury's core is partially molten (Margot et al., 2007) and the Fe-S system has been largely used to model its properties (e.g. Hauck et al., 2007; Rivoldini et al., 2009; Dumberry and Rivoldini 2015). On the basis of the phase diagram Fe_3S_2 would crystallize over a large depth range in the Mercury's core. Whether the products are $Fe+Fe_3S_2$ or Fe_3S_2+FeS strongly depends on the bulk sulfur concentration in the crystallizing liquid.

5.6 Summary

Properties of Fe_3S_2, including phase stability, structure, lattice parameter and equation of state were studied by *in situ* x-ray diffraction between 12 and 15 GPa and up to the partial-melting temperature of 1109 K, and complemented by SEM analysis of the recovered samples. Fe_3S_2 was found to form above 12 GPa and 850 K. In the binary Fe-S system, it coexists with Fe or FeS depending on the sulfur bulk concentration, and it is stable till melting. It has an orthorhombic crystalline structure, with space group either PNA21, PNN2, or PNNM. Analysis of the diffraction patterns allowed determination of the lattice parameters a, b, and c and of the unit-cell volume for

all runs, without noticeable difference from run to run. Fitting the isothermal data to a second-order Birch-Murnaghan and a Vinet equation of state with K' fixed to 4 for the reference temperature at 940 K yields similar zero-pressure volume V_0 of 372.2 ±0.8 and 367.3 ±0.6 Å^3, with zero-pressure bulk modulus K_0 of 129.9 ±3.8 and 185.2 ±4.0 GPa, respectively. The two sets of fitted parameters don't make a discernable difference on the equation of state within the interested pressure range. Based on the unit-cell volume collected from 850 K to 1109 K around 14 GPa, the thermal expansion, assumed constant in this P-T range, was determined to be 26.5×10^{-5} K^{-1}.

Based on the here-refined Fe-FeS phase diagram and considering the P-T stability conditions of Fe_3S_2, this would not crystallize for small and middle-size telluric planets with core's pressure below 12 GPa. In particular, concerning the Galilean satellites of Jupiter Europa, Io, and Ganymede, if their metallic core is composed of an Fe-S alloy, the solid products core solidification would be Fe or FeS. Conversely, Fe_3S_2 could crystallize over a large depth range in Mercury's core.

A further achievement of this study have been the determination of the lattice parameters and compressional behavior of FeS from 11 to 15 GPa and 470 K to 1100 K, in both hexagonal and NiAs-type structure. We extracted reliable c_f/a_f ratio of FeS from all the runs, and depicted the dependence on pressure and temperature based on the previous data, for which our new results represent a significant supplement at higher pressures and temperatures.

Chapter 6 Conclusions and perspectives

6.1 Conclusions

As a plausible candidate material forming the Moon's core, the physical properties of liquid Fe-C-S alloys have been systematically studied by a multi-techniques experimental approach, with specific focus on the local structure, density, and liquid miscibility at pertinent pressure and temperature conditions.

The local structure and density of liquid Fe-C-S alloys were studied by in situ X-ray diffraction and absorption, from 1 to 5 GPa and 1600 to 1900 K. The compositional space was mapped by performing experiments on several starting compositions, namely Fe – 1.5 wt%C – (4, 8, 15, 22, and 30) wt%S and Fe – 3 wt%C – (4 and 8) wt%S. Structural information of the liquids were extracted from the diffuse scattering signal. The pair distribution functions $g(r)$s indicate that the local structure of the ternary liquid is mainly affected by the concentration of sulfur, with the structure becoming remarkably less ordered for S concentration above ~23 at%S. Conversely, carbon plays a minor role in perturbing the structure. The different effect of carbon and sulfur on the structure is related to the atomic size: smaller carbon atoms interstitially incorporate in liquid iron without significantly affecting the Fe-Fe bonds, while interstitial incorporation of larger sulfur atoms perturb the Fe-Fe networks when added in significant amount. Thus, at first approximation, the local structure of ternary liquids is controlled by the S content. However, the density of ternary alloys, independently determined from the analysis of the short-range portion of the distribution function and from analysis of the absorption profile, shows a co-effect of carbon and sulfur, although S more significantly decreases the density than C.

The miscibility of liquid Fe-C-S was studied by electron microscopy analysis of quench experiments performed from 2 to 6 GPa at 1600 K and 2000 K. Starting compositions over a large range of C (5-30 at%) and S (12-30 at%) content were employed to precisely determine the miscibility gaps.

The obtained density dataset was then employed to build a mixing model according to the asymmetric non-ideal Margules formulation. With the fitted interaction Margules parameters, the density of liquid Fe-C-S alloys can be modeled as a function of temperature, pressure, and light element content. This thermodynamic model was then employed, together with the determined

miscibility gaps, to discuss the carbon and sulfur content in the Moon's core starting from densities proposed by three of the latest Moon's core models and under the hypothesis of a pressure of 5 GPa and a temperature of either 1850 K or 1600 K. Out of these models, two consider the core to be fully molten, while one has a solid inner core surrounded by a liquid outer core.

In the case of the two models assuming a fully-molten core, density can be related with a relatively well-defined sulfur content (13-23 wt.% or 34-36 wt% depending on models), while carbon content is limited by the miscibility gap (<4.4 wt%). Accordingly, current uncertainties on S and C content of the Moon's core come more from the spread of proposed densities than from actual understanding of material's properties. Furthermore, on the basis of miscibility experiments, no immiscible Fe-C-S liquids can form above 5 GPa, and even at pressure below 5 GPa, only at high temperature, as with cooling the liquid composition would reach carbon solubility limit before entering the immiscible region. Accordingly, immiscibility-induced core stratification can be ruled out for the core of the Moon if made by a ternary Fe-C-S alloy.

For the model assuming a solid inner core + a liquid outer core, which could be either solid Fe + liquid Fe-C-S, or solid Fe_3C + liquid Fe-C-S, fundamental constraints come from the phase diagram the ternary Fe-C-S system. If we assume a core temperature of about 1850 K, the amounts of S and C required to match the outer core density proposed by the model appears incompatible with the existence of a solid inner core. Lower temperatures would be required to have an inner core. If the core is assumed at 1600 K, a C-bearing fcc-Fe core in coexistence with a liquid Fe-C-S outer core would be possible. On the other hand, if the bulk composition on the Moon's core lies on the carbon-rich area, an Fe_3C solid inner core could coexist with Fe-C-S liquid outer core. However, in absence of more accurate determination of the phase diagram and partial melting properties of the ternary Fe-C-S system the discussion can be only qualitative.

A second part of this Ph.D. work was devoted to the study of the subsolidus portion of the Fe-FeS phase diagram in the 11-15 GPa range, where the intermediate Fe_3S_2 phase has been reported. To this purpose four Fe-S starting compositions were selected, with nominal compositions Fe – (15, 20, 25, and 30) wt%S, and used for in situ X-ray diffraction experiments. Fe_3S_2 was observed to form around 14 GPa at temperature above 850 K, and to remain stable until the onset of melting. Isothermal decompression at 940 K, allowed locating the low-pressure phase boundary around 12 GPa. Here-determined P-T stability field implies that Fe_3S_2 crystallizes upon secular cooling of

Fe-S core of terrestrial planetary bodies only at pressures above 12 GPa. As such Fe_3S_2 is not expected to form in the core of Europa, Io, or Ganymede.

The structure of Fe_3S_2 was here determined for the first time based on in situ X-ray diffraction measurements. Fitting the peaks of Fe_3S_2 yielded an orthorhombic crystalline structure and the space group has been limited to three possibilities, PNA21, PNN2, or PNNM. Fitting the unit-cell volumes of Fe_3S_2 along an isotherm at 940 K to both second-order Birch-Murnaghan and Vinet formalism with *K'* fixed to 4 yields a zero-pressure bulk modulus K_T of 129.9 and 185.2 GPa, respectively. Unit-cell volumes collected along an almost isobaric path at ~14 GPa from 850 K to 1100 K allowed the determination of the thermal expansion coefficient $\alpha = 26.5 \times 10^{-6}$ K^{-1}.

Thermo-elastic properties were also investigated for phase IV and V of FeS. The pressure and temperature dependence of c_f/c_a estimated by the experimental results are in good agreement with previously reported data, to which provide significant extension to higher pressure and temperature conditions.

6.2 Perspectives

From an experimental point of view, the reliability of assemblies is a first but fundamental requirement for the studies on liquids. Different from solids, liquids tend to escape from the sample chamber if not well sealed during the experiments. In our first runs, hBN was chosen as the sample chamber, which however was easily deformed during compression, so that severe leaks were experienced upon melting very often. Thanks to the adoption of a sapphire ring added into the sample chamber, the liquid encapsulation was largely improved. The sample retained its geometry (also instrumental for proper Beer-Lambert measurements) and only minor leaks were observed, in particular for long experiments. However, even a slight leak might cause the heater or thermocouple failure. Assemblies suitable for liquid studies are to be developed in the future work. Improvements could be achieved by modifying the shape of sapphire sample chamber from a simple ring to a cup, and testing different capsule materials for good sealing. Noteworthy, suitable X-ray transparency is a needed for many in situ experiments.

The low solubility of carbon observed in the miscibility experiments appear in contradiction with results from *in situ* synchrotron experiments. Since the experimental conditions were maintained

for tens of minutes during the *in situ* experiments, while in the case of the miscibility experiments samples were quenched few minutes after reaching the target P-T conditions, a potential reason for the apparent inconsistency is that equilibrium had not been reached in the miscibility experiments. To verify this hypothesis, time-series quench experiments would be necessary, repeating experiments on the same starting compositions and at the same P-T conditions but maintain these for different durations. We stress however that the miscibility gaps determined from our recovered samples are still valid, as the immiscible products always lie on them, regardless the chemical equilibration of the two immiscible phases (i.e. chemical equilibration only moves compositions of recovered products along the immiscibility lines).

As already mentioned, another important step ahead in the modeling of the Moon's core will be provided by the determination of ternary phase diagram of Fe-C-S system at 5 GPa. Indeed, the compatibility of compositions of liquids and solids independently matching the densities of liquid outer core and solid inner core cannot disregard the phase diagram and solid-liquid elemental partitioning.

Regarding the analysis of Fe-S data, further work remains to be done in the near future. Firstly, by exploiting not only the diffraction peaks' position but also the intensity, the atomic information of Fe_3S_2 could be solved. We have limited the possible space group to three cases, i.e. PNA21, PNN2, and PNNM, by searching with the visible peak positions. However, as these three space groups share similar number and position of the peaks, the univocal determination of the space group was not possible. A possible way out would be to search for the correct Wyckoff site and corresponding atomic position within these three space groups with the peak position and intensity of Fe_3S_2, and the solutions could be an indication for the correct space group. Another work to be carried out is the determination of the upper pressure bound for the phase stability of Fe_3S_2. In this study, we have reached 16 GPa, around the pressure limit for Paris Edinburgh press, and Fe_3S_2 was still stable. However, more iron-rich phases, Fe_3S and Fe_2S were reported stable at 21 GPa by Fei et al. (2000). It thus remains unknown if other Fe-S phases exist between 16 and 21 GPa, and where the upper pressure bound lies for Fe_3S_2.

With the InSight mission currently operating on Mars, BepiColombo on its way to Mercury, and the missions Artemis to the Moon and JUICE to Jupiter and its satellites that will be launched in

the near future, more fascinating observations are to come. These will likely lead to new evidence regarding the interior of these terrestrial planetary bodies that will call for the properties of multi-component iron alloys over an extended pressure, temperature and compositional range. Much work remains to be done for constraining the core of planetary bodies within the solar system.

References

Adachi, A., Morita, Z.I., Kitaura, M. and Demukai, N., 1970. Density of liquid iron measured by the levitation technique. *Technol Rep Osaka Univ*, *20*(908), pp.67-75.

Alvarez-Murga, M., Perrillat, J.P., Le Godec, Y., Bergame, F., Philippe, J., King, A., Guignot, N., Mezouar, M. and Hodeau, J.L., 2017. Development of synchrotron X-ray micro-tomography under extreme conditions of pressure and temperature. *Journal of synchrotron radiation*, *24*(1), pp.240-247.

Anderson, J.D., Colombo, G., Esposito, P.B., Lau, E.L. and Trager, G.B., 1987. The mass, gravity field, and ephemeris of Mercury. *Icarus*, *71*(3), pp.337-349.

Anderson, O.L., Oda, H. and Isaak, D., 1992. A model for the computation of thermal expansivity at high compression and high temperatures: MgO as an example. *Geophysical Research Letters*, *19*(19), pp.1987-1990.

Angel, R.J., Alvaro, M. and Nestola, F., 2018. 40 years of mineral elasticity: a critical review and a new parameterisation of equations of state for mantle olivines and diamond inclusions. *Physics and Chemistry of Minerals*, *45*(2), pp.95-113.

Arima, H., Ohtaka, O., Hattori, T., Katayama, Y., Utsumi, W. and Yoshiasa, A., 2007. In situ XAFS and XRD studies of pressure-induced local structural change in liquid AgI. *Journal of Physics: Condensed Matter*, *19*(7), p.076104.

Balog, P.S., Secco, R.A. and Rubie, D.C., 2001. Density measurements of liquids at high pressure: Modifications to the sink/float method by using composite spheres, and application to Fe-10wt% S. *International Journal of High Pressure Research*, *21*(5), pp.237-261.

Balog, P.S., Secco, R.A., Rubie, D.C. and Frost, D.J., 2003. Equation of state of liquid Fe-10 wt% S: Implications for the metallic cores of planetary bodies. *Journal of Geophysical Research: Solid Earth*, *108*(B2).

Bassett, W.A., Shen, A.H., Bucknum, M. and Chou, I.M., 1993. A new diamond anvil cell for hydrothermal studies to 2.5 GPa and from− 190 to 1200 °C. *Review of Scientific Instruments*, *64*(8), pp.2340-2345.

Besson, J.M., Hamel, G., Grima, T., Nelmes, R.J., Loveday, J.S., Hull, S. and Häusermann, D., 1992. A large volume pressure cell for high temperatures. *High Pressure Research*, *8*(5-6), pp.625-630.

Boccato, S., Garino, Y., Morard, G., Zhao, B., Xu, F., Sanloup, C., King, A., Guignot, N., Clark, A., Garbarino, G. and Morand, M., 2022. Amorpheus: a Python-based software for the treatment of X-ray scattering data of amorphous and liquid systems. High Pressure Research, 42(1), pp.69-93.

Boehler, R., Von Bargen, N. and Chopelas, A., 1990. Melting, thermal expansion, and phase transitions of iron at high pressures. *Journal of Geophysical Research: Solid Earth*, *95*(B13), pp.21731-21736.

Boehler, R., 1996. Fe-FeS eutectic temperatures to 620 kbar. *Physics of the Earth and Planetary Interiors*, *96*(2-3), pp.181-186.

Boulard, E., King, A., Guignot, N., Deslandes, J.P., Le Godec, Y., Perrillat, J.P., Clark, A., Morard, G. and Itié, J.P., 2018. High-speed tomography under extreme conditions at the PSICHE beamline of the SOLEIL Synchrotron. *Journal of Synchrotron Radiation*, *25*(3), pp.818-825.

Boulard, E., Denoual, C., Dewaele, A., King, A., Le Godec, Y. and Guignot, N., 2020. Following the phase transitions of iron in 3D with X-ray tomography and diffraction under extreme conditions. *Acta Materialia*, *192*, pp.30-39.

Breuer, D., Rueckriemen, T. and Spohn, T., 2015. Iron snow, crystal floats, and inner-core growth: modes of core solidification and implications for dynamos in terrestrial planets and moons. *Progress in Earth and Planetary Science*, *2*(1), pp.1-26.

Buono, A.S. and Walker, D., 2011. The Fe-rich liquidus in the Fe–FeS system from 1 bar to 10 GPa. *Geochimica et Cosmochimica Acta*, *75*(8), pp.2072-2087.

Cameron, A.G. and Ward, W.R., 1976, March. The origin of the Moon. In *Lunar and Planetary Science Conference* (Vol. 7).

Cameron, A.G.W., 2001. From interstellar gas to the Earth-Moon system. *Meteoritics & Planetary Science*, *36*(1), pp.9-22.

Canup, R.M. and Asphaug, E., 2001. Origin of the Moon in a giant impact near the end of the Earth's formation. *Nature*, *412*(6848), pp.708-712.

Chabot, N.L., Campbell, A.J., McDonough, W.F., Draper, D.S., Agee, C.B., Humayun, M., Watson, H.C., Cottrell, E. and Saslow, S.A., 2008. The Fe–C system at 5 GPa and implications for Earth's core. *Geochimica et Cosmochimica Acta*, *72*(16), pp.4146-4158.

Chen, B., Li, J. and Hauck, S.A., 2008. Non-ideal liquidus curve in the Fe-S system and Mercury's snowing core. *Geophysical Research Letters*, *35*(7).

Chudinovskikh, L. and Boehler, R., 2007. Eutectic melting in the system Fe–S to 44 GPa. *Earth and Planetary Science Letters*, *257*(1-2), pp.97-103.

Cisowski, S.M., Collinson, D.W., Runcorn, S.K., Stephenson, A. and Fuller, M., 1983. A review of lunar paleointensity data and implications for the origin of lunar magnetism. *Journal of Geophysical Research: Solid Earth*, *88*(S02), pp.A691-A704.

Coati, A., Chavas, L.M.G., Fontaine, P., Foos, N., Guimaraes, B., Gourhant, P., Legrand, P., Itie, J.P., Fertey, P., Shepard, W. and Isabet, T., 2017. Status of the crystallography beamlines at synchrotron SOLEIL. *The European Physical Journal Plus*, *132*(4), pp.1-9.

Corgne, A., Wood, B.J. and Fei, Y., 2008. C-and S-rich molten alloy immiscibility and core formation of planetesimals. *Geochimica et Cosmochimica Acta*, *72*(9), pp.2409-2416.

Crichton, W.A. and Mezouar, M., 2002. Noninvasive pressure and temperature estimation in large-volume apparatus by equation-of-state cross-calibration. *High Temperatures High Pressures(UK)*, *34*(2), pp.235-242.

Dasgupta, R., Buono, A., Whelan, G. and Walker, D., 2009. High-pressure melting relations in Fe–C–S systems: Implications for formation, evolution, and structure of metallic cores in planetary bodies. *Geochimica et Cosmochimica Acta*, *73*(21), pp.6678-6691.

Deans, S.R., 2007. *The Radon transform and some of its applications*. Courier Corporation.

De Chiffre, L., Carmignato, S., Kruth, J.P., Schmitt, R. and Weckenmann, A., 2014. Industrial applications of computed tomography. *CIRP annals*, *63*(2), pp.655-677.

Dehant, V., 2020. Detection of the Chandler wobble of Mars from orbiting spacecraft. *Geophysical Research Letters*, *47*(21), p.e2020GL090568.

Dickey, J.O., Bender, P.L., Faller, J.E., Newhall, X.X., Ricklefs, R.L., Ries, J.G., Shelus, P.J., Veillet, C., Whipple, A.L., Wiant, J.R. and Williams, J.G., 1994. Lunar laser ranging: A continuing legacy of the Apollo program. *Science*, *265*(5171), pp.482-490.

Dragomir, I., 1964. Study of the Properties of Fe-P Solutions-Surface Tension and Density. *Izv. Vysshikh Uchebn. Zavedenii Chernaya Met*, (11), pp.50-52.

Dubrovinskaia, N. and Dubrovinsky, L., 2003. Whole-cell heater for the diamond anvil cell. *Review of Scientific Instruments*, *74*(7), pp.3433-3437.

Dumberry, M. and Rivoldini, A., 2015. Mercury's inner core size and core-crystallization regime. *Icarus*, *248*, pp.254-268.

Dwyer, C.A., Stevenson, D.J. and Nimmo, F., 2011. A long-lived lunar dynamo driven by continuous mechanical stirring. *Nature*, *479*(7372), pp.212-214.

Elkins-Tanton, L.T., Burgess, S. and Yin, Q.Z., 2011. The lunar magma ocean: Reconciling the solidification process with lunar petrology and geochronology. *Earth and Planetary Science Letters*, *304*(3-4), pp.326-336.

Fei, Y., Bertka, C.M. and Finger, L.W., 1997. High-pressure iron-sulfur compound, Fe_3S_2, and melting relations in the Fe-FeS system. *Science*, *275*(5306), pp.1621-1623.

Fei, Y., Li, J., Bertka, C.M. and Prewitt, C.T., 2000. Structure type and bulk modulus of Fe_3S, a new iron-sulfur compound. *American Mineralogist*, *85*(11-12), pp.1830-1833.

Fei, Y. and Brosh, E., 2014. Experimental study and thermodynamic calculations of phase relations in the Fe–C system at high pressure. *Earth and Planetary Science Letters*, *408*, pp.155-162.

Frohberg, M.G. and Weber, R., 1964. Dichtemessungen an Eisen-Kobalt-und Eisen-Kupfer-Legierungen. *Archiv für das Eisenhüttenwesen*, *35*(9), pp.877-883.

Frost, D.J., Poe, B.T., Trønnes, R.G., Liebske, C., Duba, A. and Rubie, D.C., 2004. A new large-volume multianvil system. *Physics of the Earth and Planetary Interiors*, *143*, pp.507-514.

Fuller, M. and Cisowski, S.M., 1987. Lunar paleomagnetism. *Geomatik*, *2*, pp.307-455.

Gagnepain-Beyneix, J., Lognonné, P., Chenet, H., Lombardi, D. and Spohn, T., 2006. A seismic model of the lunar mantle and constraints on temperature and mineralogy. *Physics of the Earth and Planetary Interiors*, *159*(3-4), pp.140-166.

Garcia, R.F., Khan, A., Drilleau, M., Margerin, L., Kawamura, T., Sun, D., Wieczorek, M.A., Rivoldini, A., Nunn, C., Weber, R.C. and Marusiak, A.G., 2019. Lunar seismology: An update on interior structure models. *Space Science Reviews*, *215*(8), pp.1-47.

Genova, A., Goossens, S., Lemoine, F.G., Mazarico, E., Neumann, G.A., Smith, D.E. and Zuber, M.T., 2016. Seasonal and static gravity field of Mars from MGS, Mars Odyssey and MRO radio science. *Icarus*, *272*, pp.228-245.

Giovenco, E., Perrillat, J.P., Boulard, E., King, A., Guignot, N. and Le Godec, Y., 2021. Quantitative 4D X-ray microtomography under extreme conditions: a case study on magma migration. *Journal of Synchrotron Radiation*, *28*(5).

Goossens, S., Sabaka, T.J., Genova, A., Mazarico, E., Nicholas, J.B. and Neumann, G.A., 2017. Evidence for a low bulk crustal density for Mars from gravity and topography. *Geophysical research letters*, *44*(15), pp.7686-7694.

Hall, H.T., 1958. Some high-pressure, high-temperature apparatus design considerations: Equipment for use at 100 000 atmospheres and 3000 °C. *Review of Scientific Instruments*, *29*(4), pp.267-275.

Hamilton, V.E., Christensen, P.R., McSWEEN Jr, H.Y. and Bandfield, J.L., 2003. Searching for the source regions of Martian meteorites using MGS TES: Integrating Martian meteorites into the global distribution of igneous materials on Mars. *Meteoritics & Planetary Science*, *38*(6), pp.871-885.

Hartmann, W.K. and Davis, D.R., 1975. Satellite-sized planetesimals and lunar origin. *Icarus*, *24*(4), pp.504-515.

Hauck, S.A., Solomon, S.C. and Smith, D.A., 2007. Predicted recovery of Mercury's internal structure by MESSENGER. *Geophysical research letters*, *34*(18).

Herbert, F., Davis, D.R. and Weidenschilling, S.J., 1986. Formation and evolution of a circumterrestrial disk: Constraints on the origin of the moon in geocentric orbit. In Origin of the Moon (pp. 701-730).

Herzberg, C.T., Baker, M.B. and Wendlandt, R.F., 1982. Olivine flotation and settling experiments on the join Mg2SiO4-Fe2SiO2. *Contributions to Mineralogy and Petrology*, *80*(4), pp.319-323.

Hillgren, V.J., K. Gessmann, C. and Li, J., 2000. An Experimental Perspective on the light element in the Earth's core. *Origin of the Earth and Moon*, *30*, p.245.

Hirayama, Y., Fujii, T. and Kurita, K., 1993. The melting relation of the system, iron and carbon at high pressure and its bearing on the early stage of the Earth. *Geophysical research letters*, *20*(19), pp.2095-2098.

Hixson, R.S., Winkler, M.A. and Hodgdon, M.L., 1990. Sound speed and thermophysical properties of liquid iron and nickel. *Physical Review B*, *42*(10), p.6485.

Holder, C.F. and Schaak, R.E., 2019. Tutorial on powder X-ray diffraction for characterizing nanoscale materials. *ACS Nano 2019 13* (*7*), pp.7359-7365.

Hood, L.L., Mitchell, D.L., Lin, R.P., Acuna, M.H. and Binder, A.B., 1999. Initial measurements of the lunar induced magnetic dipole moment using Lunar Prospector magnetometer data. *Geophysical Research Letters*, *26*(15), pp.2327-2330.

Ikuta, D., Kono, Y. and Shen, G., 2016. Structural analysis of liquid aluminum at high pressure and high temperature using the hard sphere model. *Journal of Applied Physics*, *120*(13), p.135901.

Ishii, T., Shi, L., Huang, R., Tsujino, N., Druzhbin, D., Myhill, R., Li, Y., Wang, L., Yamamoto, T., Miyajima, N. and Kawazoe, T., 2016. Generation of pressures over 40 GPa using Kawai-type multi-anvil press with tungsten carbide anvils. *Review of Scientific Instruments*, *87*(2), p.024501.

Jimbo, I. and Cramb, A.W., 1993. The density of liquid iron-carbon alloys. *Metallurgical Transactions B*, *24*(1), pp.5-10.

Jing, Z., Wang, Y., Kono, Y., Yu, T., Sakamaki, T., Park, C., Rivers, M.L., Sutton, S.R. and Shen, G., 2014. Sound velocity of Fe–S liquids at high pressure: Implications for the Moon's molten outer core. *Earth and Planetary Science Letters*, *396*, pp.78-87.

Kanzaki, M., 1991. Ortho/clinoenstatite transition. *Physics and Chemistry of Minerals*, *17*(8), pp.726-730.

Katayama, Y., Inamura, Y., Mizutani, T., Yamakata, M., Utsumi, W. and Shimomura, O., 2004. Macroscopic separation of dense fluid phase and liquid phase of phosphorus. *Science*, *306*(5697), pp.848-851.

Kato, T. and Ringwood, A.E., 1989. Melting relationships in the system Fe-FeO at high pressures: Implications for the composition and formation of the Earth's core. *Physics and chemistry of minerals*, *16*(6), pp.524-538.

Khan, A., Connolly, J.A., Pommier, A. and Noir, J., 2014. Geophysical evidence for melt in the deep lunar interior and implications for lunar evolution. *Journal of Geophysical Research: Planets*, *119*(10), pp.2197-2221.

Khan, A., Liebske, C., Rozel, A., Rivoldini, A., Nimmo, F., Connolly, J.A.D., Plesa, A.C. and Giardini, D., 2018. A geophysical perspective on the bulk composition of Mars. *Journal of Geophysical Research: Planets*, *123*(2), pp.575-611.

King, A., Guignot, N., Zerbino, P., Boulard, E., Desjardins, K., Bordessoule, M., Leclerq, N., Le, S., Renaud, G., Cerato, M. and Bornert, M., 2016. Tomography and imaging at the PSICHE beam line of the SOLEIL synchrotron. *Review of Scientific Instruments*, *87*(9), p.093704.

King, A., Guignot, N., Henry, L., Morard, G., Clark, A., Le Godec, Y. and Itié, J.P., 2022. Combined angular and energy dispersive diffraction: optimized data acquisition, normalization and reduction. *Journal of Applied Crystallography*, *55*(2).

Kirshenbaum, A.D. and Cahill, J.A., 1962. The density of liquid iron from the melting point to 2500 K. *Trans. Met. Soc. AIME*, *224*.

Knibbe, J.S., Rivoldini, A., Luginbuhl, S.M., Namur, O., Charlier, B., Mezouar, M., Sifre, D., Berndt, J., Kono, Y., Neuville, D.R. and van Westrenen, W., 2021. Mercury's Interior Structure constrained by Density and P-wave Velocity Measurements of Liquid Fe-Si-C Alloys. *Journal of Geophysical Research: Planets*, *126*(1), p.e2020JE006651.

Kojitani, H., Shirako, Y. and Akaogi, M., 2007. Post-perovskite phase transition in $CaRuO_3$. *Physics of the Earth and Planetary Interiors*, *165*(3-4), pp.127-134.

Kondo, T., Sawamoto, H., Yoneda, A., Kato, M. and Matsumoto, A., 1993. Ultrahigh-pressure and high-temperature generation by use of the MA8 system with sintered-diamond anvils. *High Temperatures. High Pressures (Print)*, *25*(1), pp.105-112.

Konopliv, A.S., Binder, A.B., Hood, L.L., Kucinskas, A.B., Sjogren, W.L. and Williams, J.G., 1998. Improved gravity field of the Moon from Lunar Prospector. *Science*, *281*(5382), pp.1476-1480.

Kono, Y., Park, C., Kenney-Benson, C., Shen, G. and Wang, Y., 2014. Toward comprehensive studies of liquids at high pressures and high temperatures: Combined structure, elastic wave velocity, and viscosity measurements in the Paris–Edinburgh cell. *Physics of the Earth and Planetary Interiors*, *228*, pp.269-280.

Konopliv, A.S., Yoder, C.F., Standish, E.M., Yuan, D.N. and Sjogren, W.L., 2006. A global solution for the Mars static and seasonal gravity, Mars orientation, Phobos and Deimos masses, and Mars ephemeris. *Icarus*, *182*(1), pp.23-50.

Konopliv, A.S., Asmar, S.W., Folkner, W.M., Karatekin, Ö., Nunes, D.C., Smrekar, S.E., Yoder, C.F. and Zuber, M.T., 2011. Mars high resolution gravity fields from MRO, Mars seasonal gravity, and other dynamical parameters. *Icarus*, *211*(1), pp.401-428.

Krogh-Moe, J., 1956. A method for converting experimental X-ray intensities to an absolute scale. *Acta Crystallographica*, *9*(11), pp.951-953.

Kusaba, K., Syono, Y., Kikegawa, T. and Shimomura, O., 1998. High pressure and temperature behavior of FeS. *Journal of Physics and Chemistry of Solids*, *59*(6-7), pp.945-950.

Laneuville, M., Wieczorek, M.A., Breuer, D., Aubert, J., Morard, G. and Rückriemen, T., 2014. A long-lived lunar dynamo powered by core crystallization. *Earth and Planetary Science Letters*, *401*, pp.251-260.

Li, B., Kung, J. and Liebermann, R.C., 2004. Modern techniques in measuring elasticity of Earth materials at high pressure and high temperature using ultrasonic interferometry in conjunction with synchrotron X-radiation in multi-anvil apparatus. *Physics of the Earth and Planetary Interiors*, *143*, pp.559-574.

Li, J., Fei, Y., Mao, H.K., Hirose, K. and Shieh, S.R., 2001. Sulfur in the Earth's inner core. *Earth and Planetary Science Letters*, *193*(3-4), pp.509-514.

Li, J., Hadidiacos, C., Mao, H.K., Fei, Y. and Hemley, R.J., 2003. Behavior of thermocouples under high pressure in a multi-anvil apparatus. *High pressure research*, *23*(4), pp.389-401.

Li, L., Wang, L. and Vaughan, M.T., 2008. Elastic softening of peridotite due to the presence of melt phases at high pressure. *Physics of the Earth and Planetary Interiors*, *170*(3-4), pp.176-180.

Lin, Y., Tronche, E.J., Steenstra, E.S. and van Westrenen, W., 2017. Evidence for an early wet Moon from experimental crystallization of the lunar magma ocean. *Nature Geoscience*, *10*(1), pp.14-18.

Lognonné, P. and Johnson, C., 2007. Planetary seismology. *Treatise on Geophysics*, *10*, pp.69-122.

Lucas, L.D., 1960. Densite du fer, du nickel et du cobalt a letat liquide. *Comptes rendus hebdomadaires des seances de l academie des sciences*, *250*(10), pp.1850-1852.

Lucas, L.D. and Met, M.S.R., 1972. Density of Metals at High Temperatures in the Solid and Molten States, Part 2. *Mem. Sci. Rev. Met*, *69*(6), pp.479-492.

Lucey, P.G., Taylor, G.J. and Malaret, E., 1995. Abundance and distribution of iron on the Moon. *Science*, *268*(5214), pp.1150-1153.

Lugmair, G.W. and Shukolyukov, A., 1998. Early solar system timescales according to 53Mn-53Cr systematics. *Geochimica et Cosmochimica Acta*, *62*(16), pp.2863-2886.

Mao, H.K., Bell, P.M., Shaner, J.T. and Steinberg, D.J., 1978. Specific volume measurements of Cu, Mo, Pd, and Ag and calibration of the ruby R1 fluorescence pressure gauge from 0.06 to 1 Mbar. *Journal of applied physics*, *49*(6), pp.3276-3283.

Mao, H.K., Xu, J.A. and Bell, P.M., 1986. Calibration of the ruby pressure gauge to 800 kbar under quasi-hydrostatic conditions. *Journal of Geophysical Research: Solid Earth*, *91*(B5), pp.4673-4676.

Margot, J.L., Peale, S.J., Jurgens, R.F., Slade, M.A. and Holin, I.V., 2007. Large longitude liberation of Mercury reveals a molten core. *Science*, *316*(5825), pp.710-714.

Marshall, W.G. and Francis, D.J., 2002. Attainment of near-hydrostatic compression conditions using the Paris–Edinburgh cell. *Journal of Applied Crystallography*, *35*(1), pp.122-125.

McGovern, P.J., Solomon, S.C., Smith, D.E., Zuber, M.T., Simons, M., Wieczorek, M.A., Phillips, R.J., Neumann, G.A., Aharonson, O. and Head, J.W., 2004. Correction to "Localized gravity/topography admittance and correlation spectra on Mars: Implications for regional and global evolution". *Journal of Geophysical Research: Planets*, *109*(E7).

Mees, F., Swennen, R., Van Geet, M. and Jacobs, P., 2003. Applications of X-ray computed tomography in the geosciences. *Geological Society, London, Special Publications*, *215*(1), pp.1-6.

Mighani, S., Wang, H., Shuster, D.L., Borlina, C.S., Nichols, C.I. and Weiss, B.P., 2020. The end of the lunar dynamo. *Science advances*, *6*(1), p.eaax0883.

Morard, G., Sanloup, C., Fiquet, G., Mezouar, M., Rey, N., Poloni, R. and Beck, P., 2007. Structure of eutectic Fe–FeS melts to pressures up to 17 GPa: implications for planetary cores. *Earth and Planetary Science Letters*, *263*(1-2), pp.128-139.

Morard, G. and Katsura, T., 2010. Pressure–temperature cartography of Fe–S–Si immiscible system. *Geochimica et Cosmochimica Acta*, *74*(12), pp.3659-3667.

Morard, G., Mezouar, M., Bauchau, S., Álvarez-Murga, M., Hodeau, J.L. and Garbarino, G., 2011. High efficiency multichannel collimator for structural studies of liquids and low-Z materials at high pressures and temperatures. *Review of Scientific Instruments*, *82*(2), p.023904.

Morard, G., Garbarino, G., Antonangeli, D., Andrault, D., Guignot, N., Siebert, J., Roberge, M., Boulard, E., Lincot, A., Denoeud, A. and Petitgirard, S., 2014. Density measurements and structural properties of liquid and amorphous metals under high pressure. *High Pressure Research*, *34*(1), pp.9-21.

Morard, G., Bouchet, J., Rivoldini, A., Antonangeli, D., Roberge, M., Boulard, E., Denoeud, A. and Mezouar, M., 2018. Liquid properties in the Fe-FeS system under moderate pressure: Tool box to model

small planetary cores. *American Mineralogist: Journal of Earth and Planetary Materials*, *103*(11), pp.1770-1779.

Morita, Z.I., Ogino, Y., Kaito, H. and Adachi, A., 1970. Structure change in liquid iron detected from density measurements. *J Japan Inst Metals*, *34*(2), pp.248-253.

Mougel, B., Moynier, F. and Göpel, C., 2018. Chromium isotopic homogeneity between the Moon, the Earth, and enstatite chondrites. *Earth and Planetary Science Letters*, *481*, pp.1-8.

Mueller, H.J., Schilling, F.R. and Lathe, C., 2007. Multianvil techniques in conjuction with synchrotron radiation at Deutsches ElektronenSYnchrotron (DESY) - HAmburger SYnchrotron LABor (HASYLAB). *SPECIAL PAPERS-GEOLOGICAL SOCIETY OF AMERICA*, *421*, p.207.

Müller, H.J., Schilling, F.R., Lathe, C. and Lauterjung, J., 2006. Recent development of experimental techniques for high-pressure mineral physics under simulated mantle conditions. *High Pressure Research*, *26*(4), pp.529-537.

Nakajima, Y., Takahashi, E., Suzuki, T. and Funakoshi, K.I., 2009. "Carbon in the core" revisited. *Physics of the Earth and Planetary Interiors*, *174*(1-4), pp.202-211.

Nakamura, Y., Lammlein, D., Latham, G., Ewing, M., Dorman, J., Press, F. and Toksöz, N., 1973. New seismic data on the state of the deep lunar interior. *Science*, *181*(4094), pp.49-51.

Nakamura, Y., Latham, G., Lammlein, D., Ewing, M., Duennebier, F. and Dorman, J., 1974. Deep lunar interior inferred from recent seismic data. *Geophysical Research Letters*, *1*(3), pp.137-140.

Nishida, K., Ohtani, E., Urakawa, S., Suzuki, A., Sakamaki, T., Terasaki, H. and Katayama, Y., 2011. Density measurement of liquid FeS at high pressures using synchrotron X-ray absorption. *American Mineralogist*, *96*(5-6), pp.864-868.

Nishida, K., Suzuki, A., Terasaki, H., Shibazaki, Y., Higo, Y., Kuwabara, S., Shimoyama, Y., Sakurai, M., Ushioda, M., Takahashi, E. and Kikegawa, T., 2016. Towards a consensus on the pressure and composition dependence of sound velocity in the liquid Fe–S system. *Physics of the Earth and Planetary Interiors*, *257*, pp.230-239.

Nishiyama, N., Wang, Y., Rivers, M.L., Sutton, S.R. and Cookson, D., 2007. Rheology of ε-iron up to 19 GPa and 600 K in the D-DIA. *Geophysical research letters*, *34*(23).

Nishiyama, N., Wang, Y., Sanehira, T., Irifune, T. and Rivers, M.L., 2008. Development of the multi-anvil assembly 6-6 for DIA and D-DIA type high-pressure apparatuses. *High Pressure Research*, *28*(3), pp.307-314.

Norman, N., 1957. The Fourier transform method for normalizing intensities. *Acta Crystallographica*, *10*(5), pp.370-373.

Ohtani, E., Kagawa, N., Shimomura, O., Togaya, M., Suito, K., Onodera, A., Sawamoto, H., Yoneda, M., Tanaka, S., Utsumi, W. and Ito, E., 1989. High-pressure generation by a multiple anvil system with sintered diamond anvils. *Review of Scientific Instruments*, *60*(5), pp.922-925.

Paganin, D., Mayo, S.C., Gureyev, T.E., Miller, P.R. and Wilkins, S.W., 2002. Simultaneous phase and amplitude extraction from a single defocused image of a homogeneous object. *Journal of microscopy*, *206*(1), pp.33-40.

Pan, X., Siewerdsen, J., La Riviere, P.J. and Kalender, W.A., 2008. Anniversary Paper: Development of x-ray computed tomography: The role of Medical Physics and AAPM from the 1970s to present. *Medical physics*, *35*(8), pp.3728-3739.

Papike, J.J., Ryder, G. and Shearer, C.K., 2018. Lunar samples. *Planetary materials*, pp.719-952.

Philippe, J., Le Godec, Y., Mezouar, M., Berg, M., Bromiley, G., Bergame, F., Perrillat, J.P., Alvarez-Murga, M., Morand, M., Atwood, R. and King, A., 2016. Rotating tomography Paris–Edinburgh cell: a novel portable press for micro-tomographic 4-D imaging at extreme pressure/temperature/stress conditions. *High Pressure Research*, *36*(4), pp.512-532.

Poirier, J.P. and Tarantola, A., 1998. A logarithmic equation of state. *Physics of the Earth and Planetary Interiors*, *109*(1-2), pp.1-8.

Pollack, J.B. and Fanale, F., 1982. Origin and evolution of the Jupiter satellite system. *Satellites of Jupiter*, pp.872-910.

Powell, R.L., 1974. Thermocouple reference tables based on the IPTS-6*8* (Vol. 125). US National Bureau of Standards.

Prescher, C., Prakapenka, V.B., Stefanski, J., Jahn, S., Skinner, L.B. and Wang, Y., 2017. Beyond sixfold coordinated Si in SiO2 glass at ultrahigh pressures. *Proceedings of the National Academy of Sciences*, *114*(38), pp.10041-10046.

Qian, Y., Xiao, L., Head, J.W., van der Bogert, C.H., Hiesinger, H. and Wilson, L., 2021. Young lunar mare basalts in the Chang'e-5 sample return region, northern Oceanus Procellarum. *Earth and Planetary Science Letters*, *555*, p.116702.

Rai, N. and van Westrenen, W., 2014. Lunar core formation: new constraints from metal–silicate partitioning of siderophile elements. *Earth and Planetary Science Letters*, *388*, pp.343-352.

Rivoldini, A., Van Hoolst, T. and Verhoeven, O., 2009. The interior structure of Mercury and its core sulfur content. *Icarus*, *201*(1), pp.12-30.

Rivoldini, A., Van Hoolst, T., Verhoeven, O., Mocquet, A. and Dehant, V., 2011. Geodesy constraints on the interior structure and composition of Mars. *Icarus*, *213*(2), pp.451-472.

Runcorn, S.K., 1996. The formation of the lunar core. *Geochimica et Cosmochimica Acta*, *60*(7), pp.1205-1208.

Rutter, M.D., Secco, R.A., Liu, H., Uchida, T., Rivers, M.L., Sutton, S.R. and Wang, Y., 2002. Viscosity of liquid Fe at high pressure. *Physical Review B*, *66*(6), p.060102.

Ryzhenko, B. and Kennedy, G.C., 1973. The effect of pressure on the eutectic in the system Fe-FeS. *American Journal of Science*, *273*(9), pp.803-810.

Saito, T., Shiraishi, Y. and Sakuma, Y., 1969. Density measurement of molten metals by levitation technique at temperatures between 1800 and 2200 C. *Trans Iron Steel Inst Japan*, *9*(2), pp.118-126.

Sanloup, C., Guyot, F., Gillet, P., Fiquet, G., Mezouar, M. and Martinez, I., 2000. Density measurements of liquid Fe-S alloys at high-pressure. *Geophysical Research Letters*, *27*(6), pp.811-814.

Sanloup, C. and Fei, Y., 2004. Closure of the Fe–S–Si liquid miscibility gap at high pressure. *Physics of the Earth and Planetary Interiors*, *147*(1), pp.57-65.

Sanloup, C., Van Westrenen, W., Dasgupta, R., Maynard-Casely, H. and Perrillat, J.P., 2011. Compressibility change in iron-rich melt and implications for core formation models. *Earth and Planetary Science Letters*, *306*(1-2), pp.118-122.

Shatskiy, A., Katsura, T., Litasov, K.D., Shcherbakova, A.V., Borzdov, Y.M., Yamazaki, D., Yoneda, A., Ohtani, E. and Ito, E., 2011. High pressure generation using scaled-up Kawai-cell. *Physics of the Earth and Planetary Interiors*, *189*(1-2), pp.92-108.

Shibazaki, Y., Kono, Y. and Fei, Y., 2015. Microscopic structural change in a liquid Fe-C alloy of~ 5 GPa. *Geophysical Research Letters*, *42*(13), pp.5236-5242.

Shibazaki, Y. and Kono, Y., 2018. Effect of silicon, carbon, and sulfur on structure of liquid iron and implications for structure-property relations in liquid iron-light element alloys. *Journal of Geophysical Research: Solid Earth*, *123*(6), pp.4697-4706.

Shimomura, O., Utsumi, W., Taniguchu, T., Kikegawa, T. and Nagashima, T., 1992. A new high pressure and high temperature apparatus with sintered diamond anvils for synchrotron radiation use. *High-Pressure Research: Application to Earth and Planetary Sciences*, *67*, pp.3-11.

Shimoyama, Y., Terasaki, H., Ohtani, E., Urakawa, S., Takubo, Y., Nishida, K., Suzuki, A. and Katayama, Y., 2013. Density of Fe-3.5 wt% C liquid at high pressure and temperature and the effect of carbon on the density of the molten iron. *Physics of the Earth and Planetary Interiors*, *224*, pp.77-82.

Shimoyama, Y., Terasaki, H., Urakawa, S., Takubo, Y., Kuwabara, S., Kishimoto, S., Watanuki, T., Machida, A., Katayama, Y. and Kondo, T., 2016. Thermoelastic properties of liquid Fe-C revealed by sound velocity and density measurements at high pressure. *Journal of Geophysical Research: Solid Earth*, *121*(11), pp.7984-7995.

Singer, S.F., 1970. Origin of the Moon by capture and its consequences. *Eos, Transactions American Geophysical Union*, *51*(9), pp.637-641.

Smrekar, S.E., Lognonné, P., Spohn, T., Banerdt, W.B., Breuer, D., Christensen, U., Dehant, V., Drilleau, M., Folkner, W., Fuji, N. and Garcia, R.F., 2019. Pre-mission InSights on the interior of Mars. *Space Science Reviews*, *215*(1), pp.1-72.

Spanner, D.C., 1951. The Peltier effect and its use in the measurement of suction pressure. *Journal of Experimental Botany*, pp.145-168.

Stähler, S.C., Khan, A., Banerdt, W.B., Lognonné, P., Giardini, D., Ceylan, S., Drilleau, M., Duran, A.C., Garcia, R.F., Huang, Q. and Kim, D., 2021. Seismic detection of the martian core. *Science*, *373*(6553), pp.443-448.

Steenstra, E.S., Lin, Y., Dankers, D., Rai, N., Berndt, J., Matveev, S. and van Westrenen, W., 2017a. The lunar core can be a major reservoir for volatile elements S, Se, Te and Sb. *Scientific reports*, *7*(1), pp.1-8.

Steenstra, E.S., Lin, Y., Rai, N., Jansen, M. and van Westrenen, W., 2017b. Carbon as the dominant light element in the lunar core. *American Mineralogist*, *102*(1), pp.92-97.

Stevenson, D.J., Spohn, T. and Schubert, G., 1983. Magnetism and thermal evolution of the terrestrial planets. *Icarus*, *54*(3), pp.466-489.

Stolper, E., Walker, D., Hager, B.H. and Hays, J.F., 1981. Melt segregation from partially molten source regions: the importance of melt density and source region size. *Journal of Geophysical Research: Solid Earth*, *86*(B7), pp.6261-6271.

Strong, H.M. and Chrenko, R.M., 1971. Diamond growth rates and physical properties of laboratory-made diamond. *The Journal of Physical Chemistry*, *75*(12), pp.1838-1843.

Terasaki, H., Nishida, K., Shibazaki, Y., Sakamaki, T., Suzuki, A., Ohtani, E. and Kikegawa, T., 2010. Density measurement of Fe3C liquid using X-ray absorption image up to 10 GPa and effect of light elements on compressibility of liquid iron. *Journal of Geophysical Research: Solid Earth*, *115*(B6).

Thibault, Y. and Walter, M.J., 1995. The influence of pressure and temperature on the metal-silicate partition coefficients of nickel and cobalt in a model C1 chondrite and implications for metal segregation in a deep magma ocean. *Geochimica et Cosmochimica Acta*, *59*(5), pp.991-1002.

Tompkins, S. and Pieters, C.M., 1999. Mineralogy of the lunar crust: Results from Clementine. *Meteoritics & Planetary Science*, *34*(1), pp.25-41.

Touboul, M., Kleine, T., Bourdon, B., Palme, H. and Wieler, R., 2007. Late formation and prolonged differentiation of the Moon inferred from W isotopes in lunar metals. *Nature*, *450*(7173), pp.1206-1209.

Tsuno, K., Ohtani, E. and Terasaki, H., 2007. Immiscible two-liquid regions in the Fe–O–S system at high pressure: implications for planetary cores. *Physics of the Earth and Planetary Interiors*, *160*(1), pp.75-85.

Usselman, T.M., 1975. Experimental approach to the state of the core; Part I, The liquidus relations of the Fe-rich portion of the Fe-Ni-S system from 30 to 100 kb. *American Journal of Science*, *275*(3), pp.278-290

Utsumi, W., Funakoshi, K.I., Urakawa, S., Yamakata, M., Tsuji, K., Konishi, H. and Shimomura, O., 1998. SPring-8 beamlines for high pressure science with multi-anvil apparatus. *The Review of High Pressure Science and Technology*, *7*, pp.1484-1486.

Van Kan Parker, M., Sanloup, C., Tronche, E.J., Perrillat, J.P., Mezouar, M., Rai, N. and van Westrenen, W., 2010. Calibration of a diamond capsule cell assembly for in situ determination of liquid properties in the Paris–Edinburgh press. *High Pressure Research*, *30*(2), pp.332-341.

Vertman, A.A., Filippov, E.S. and Samarin, A.M., 1964. Density of iron nickel+ cobalt in solid+ liquid states. *Doklady Akademii Nauk SSSR*, *155*(2), p.323.

Vinet, P., Ferrante, J., Smith, J.R. and Rose, J.H., 1986. A universal equation of state for solids. *Journal of Physics C: Solid State Physics*, *19*(20), p.L467.

Vinet, P., Ferrante, J., Rose, J.H. and Smith, J.R., 1987. Compressibility of solids. *Journal of Geophysical Research: Solid Earth*, *92*(B9), pp.9319-9325.

Viswanathan, V., Rambaux, N., Fienga, A., Laskar, J. and Gastineau, M., 2019. Observational constraint on the radius and oblateness of the lunar core-mantle boundary. *Geophysical Research Letters*, *46*(13), pp.7295-7303.

Walker, D., Dasgupta, R., Li, J. and Buono, A., 2013. Nonstoichiometry and growth of some Fe carbides. *Contributions to Mineralogy and Petrology*, *166*(3), pp.935-957.

Walter, M.J., Thibault, Y., Wei, K. and Luth, R.W., 1995. Characterizing experimental pressure and temperature conditions in multi-anvil apparatus. *Canadian Journal of Physics*, *73*(5-6), pp.273-286.

Wänke, H. and Dreibus, G., 1988. Chemical composition and accretion history of terrestrial planets. *Philosophical Transactions of the Royal Society of London. Series A, Mathematical and Physical Sciences*, *325*(1587), pp.545-557.

Wang, Y., Durham, W.B., Getting, I.C. and Weidner, D.J., 2003.. *Review of Scientific Instruments*, *74*(6), pp.3002-3011.

Wang, Y., Uchida, T., Von Dreele, R., Rivers, M.L., Nishiyama, N., Funakoshi, K.I., Nozawa, A. and Kaneko, H., 2004. A new technique for angle-dispersive powder diffraction using an energy-dispersive setup and synchrotron radiation. *Journal of applied crystallography*, *37*(6), pp.947-956.

Waseda, Y., The Structure of Non Crystalline Materials: Liquids and Amorphous Solids, 1980. *McGraw-Hill Inc, New York*.

Waseda, Y., Matsubara, E. and Shinoda, K., 2011. *X-ray diffraction crystallography: introduction, examples and solved problems*. Springer Science & Business Media.

Weber, R.C., Lin, P.Y., Garnero, E.J., Williams, Q. and Lognonné, P., 2011. Seismic detection of the lunar core. *science*, *331*(6015), pp.309-312.

Wenk, H.R., Ischia, G., Nishiyama, N., Wang, Y. and Uchida, T., 2005. Texture development and deformation mechanisms in ringwoodite. *Physics of the Earth and Planetary Interiors*, *152*(3), pp.191-199.

Werner, S.C. and Tanaka, K.L., 2011. Redefinition of the crater-density and absolute-age boundaries for the chronostratigraphic system of Mars. *Icarus*, *215*(2), pp.603-607.

Wiechert, U., Halliday, A.N., Lee, D.C., Snyder, G.A., Taylor, L.A. and Rumble, D., 2001. Oxygen isotopes and the Moon-forming giant impact. *Science*, *294*(5541), pp.345-348.

Wieczorek, M.A., 2008. Constraints on the composition of the Martian south polar cap from gravity and topography. *Icarus*, *196*(2), pp.506-517.

Wieczorek, M.A., Neumann, G.A., Nimmo, F., Kiefer, W.S., Taylor, G.J., Melosh, H.J., Phillips, R.J., Solomon, S.C., Andrews-Hanna, J.C., Asmar, S.W. and Konopliv, A.S., 2013. The crust of the Moon as seen by GRAIL. *Science*, *339*(6120), pp.671-675.

Williams, Q. and Jeanloz, R., 1990. Melting relations in the iron-sulfur system at ultra-high pressures: Implications for the thermal state of the Earth. *Journal of Geophysical Research: Solid Earth*, *95*(B12), pp.19299-19310.

Williams, J.G., Konopliv, A.S., Boggs, D.H., Park, R.S., Yuan, D.N., Lemoine, F.G., Goossens, S., Mazarico, E., Nimmo, F., Weber, R.C. and Asmar, S.W., 2014. Lunar interior properties from the GRAIL mission. *Journal of Geophysical Research: Planets*, *119*(7), pp.1546-1578.

Wise, Donald U, 1963. An origin of the moon by rotational fission during formation of the earth's core. *Journal of Geophysical Research* 68.5: pp1547-1554.

Woodcock, L.V., Angell, C.A. and Cheeseman, P., 1976. Molecular dynamics studies of the vitreous state: Simple ionic systems and silica. *The Journal of chemical physics*, *65*(4), pp.1565-1577.

Xu, F., Morard, G., Guignot, N., Rivoldini, A., Manthilake, G., Chantel, J., Xie, L., Yoneda, A., King, A., Boulard, E. and Pandolfi, S., 2021. Thermal expansion of liquid Fe-S alloy at high pressure. *Earth and Planetary Science Letters*, *563*, p.116884.

Yamada, A., Inoue, T., Urakawa, S., Funakoshi, K.I., Funamori, N., Kikegawa, T., Ohfuji, H. and Irifune, T., 2007. In situ X-ray experiment on the structure of hydrous Mg-silicate melt under high pressure and high temperature. *Geophysical research letters*, *34*(10).

Yamazaki, D., Ito, E., Yoshino, T., Tsujino, N., Yoneda, A., Guo, X., Xu, F., Higo, Y. and Funakoshi, K., 2014. Over 1 Mbar generation in the Kawai-type multianvil apparatus and its application to compression of $(Mg_{0.92}Fe_{0.08})$ SiO_3 perovskite and stishovite. *Physics of the Earth and Planetary Interiors*, *228*, pp.262-267.

Zhang, J., Dauphas, N., Davis, A.M., Leya, I. and Fedkin, A., 2012. The proto-Earth as a significant source of lunar material. *Nature Geoscience*, *5*(4), pp.251-255.

Acknowledgements

First of all, I would like to thank my PhD advisor Daniele Antonangeli and Guillaume Morard for offer me this invaluable chance to study and work in IMPMC and sharing with me the knowledge and experimental experience. Thank you for always being willing and available to spend time on discussions of my data, analyses, and questions.

Thank you to Nathalie Bolfan and Dan Frost for being the reviewers of my thesis, and Livia Bove, Mark Wieczorek, Nadege Hilairet, and Nicolas Rambaux for being the members of the jury.

I would like to thank my colleague Fang, who offered a lot of helps during those first hard days right after my arrival, and Nicki, Silvia for always being willing to help during the three years. Thank you for the countless help during the sleepless nights of my beamtime. Thank you Geeth for patiently teaching me everything about the use of the multi-anvil press and Remy for the help of SEM in LMV. Thank you to Eglantine and Yann for presenting me the details of PE presses and assemblies.

I would also like to thank the beamline scientists and technicians of PSICHE, SOLEIL, and ID-27, ERSF. Thank you Laura Henry, Nicolas Guignot, and Mohamed Mezouar for timely solving all the problems during the experiments and offering the technical supports for the softwares. A special thanks to Andrew King for patiently explaining me the details of the CAESAR and answering my silly questions.

At last, I would like to say a special thanks to Attilio Rivoldini. Thank you for patiently teaching me the theories of thermodynamics and planetary science, and also for the fruitful discussion. My PhD could not have moved smoothly without your help.

Appendix A. Results for the test run on aluminum

The Al sample was cut from an aluminum wire (99.9995%, Alfa Aesar), polished on the lateral to remove the oxide layer, and loaded in a BN capsule.

The density of liquid aluminum is presented in Fig. A1, in comparison with literature data obtained with the same technique. The two points collected at PSICHE beamline are in good agreement with that in literature when extrapolated to lower temperature, collected in APS using the same diffraction method, indicating both the data collection at PSICHE beamline and the data processing are reliable.

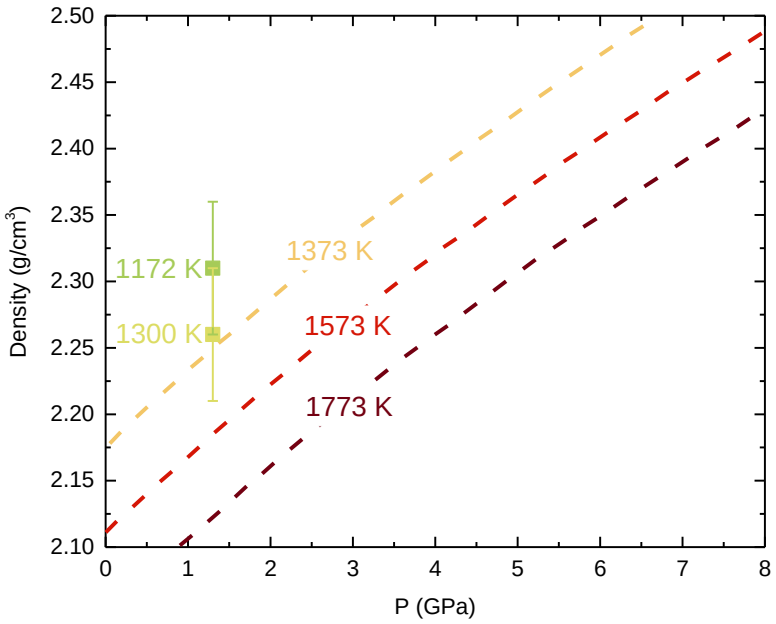

Fig. A1 Density as a function of pressure obtained in this work with the literature data (Ikuta et al., 2016). The dashed lines are isothermal density trends interpolated by experimental results. Closed squares are experimental data at lower temperature collected in the test run.

Appendix B. Submitted paper: Local structure and density of liquid Fe-C-S alloys at Moon's core conditions

Local structure and density of liquid Fe-C-S alloys at Moon's core conditions

Bin Zhao[1], Guillaume Morard[2], Eglantine Boulard[1], Silvia Boccato[1], Nicki C. Siersch[1], Attilio Rivoldini[3], Nicolas Guignot[4], Laura Henry[4], Andrew King[4], Claire Zurkowski[5], Yingwei Fei[5], Daniele Antonangeli[1]

[1]Sorbonne Université, Muséum National d'Histoire Naturelle, UMR CNRS 7590, Institut de Minéralogie, de Physique des Matériaux et de Cosmochimie, IMPMC, 75005 Paris, France

[2]Université Grenoble Alpes, Université Savoie Mont Blanc, CNRS, IRD, Université Gustave Eiffel, ISTerre, 38000 Grenoble, France

[3]Royal Observatory of Belgium, Avenue Circulaire 3, B-1180 Brussels, Belgium

[4]Synchrotron SOLEIL, L'Orme de Merisiers, Saint Aubin-BP48, 91192 Gif-sur-Yvette, France

[5]Earth and Planets Laboratory, Carnegie Institution for Science, 5251 Broad Branch Road, N.W., Washington, DC 20015, USA

Corresponding author: Bin Zhao (bin.zhao@upmc.fr)

Key points:

We measured the local structure and density of liquid Fe-C-S alloys in the range of 1-5 GPa and 1600-1900 K.

A thermodynamic model based on asymmetric Margules formalism was built based on this dataset.

We used this thermodynamic model to address three of the latest models of the Moon's core and to discuss the possible C and S content.

Abstract

The local structure and density of ternary Fe-C-S liquid alloys have been studied by the combination of *in-situ* X-ray diffraction and absorption experiments between 1 and 5 GPa and 1600 to 1900 K. The addition of up to 12 at% of carbon (C) to Fe-S liquid alloys does not significantly modify the structure, which is largely controlled by the perturbation to the Fe-Fe network induced by S atoms. The liquid density determined from diffraction and/or absorption techniques allows us to build a non-ideal ternary mixing model as a function of pressure, temperature, and composition in terms of the content of alloying light elements. The composition of the Moon's core is addressed based on this thermodynamic model. Under the assumption of a homogeneous liquid core, with an average density of either 4550 or 5812 kg/m^3 as proposed by two recent Moon models, the sulfur content would respectively be 34-36 wt% or 13-23 wt%, while the carbon content is mainly limited by the Fe-C-S miscibility gap, with an upper bound of 4.3 wt%. On the other hand, if the core is partially molten, the core temperature is necessarily lower than 1850 K estimated in the text, and the composition of both the inner and outer core would be controlled by aspects of the Fe-C-S phase diagram not yet constrained well enough.

Plain Language summary

Several geodetic and geochemical studies addressed the properties of the Moon's core. Core's density is directly related to its chemical composition, which is crucial for better understanding its origin and thermal evolution. With carbon and sulfur being considered as two plausible light elements alloyed to iron to form the core, we selected a series of Fe-C-S compositions and studied the local structure and density of corresponding liquids. The measured densities were integrated to build a thermodynamic model. Our results show that sulfur and carbon have a co-effect on the density and sound velocity of the liquid alloys, with sulfur playing a much more significant role. Consequently, the sulfur content is well constrained for a given density, which however largely differs from model to model. On the contrary, the constraints on C content remain looser, not only because of the smaller effect of C on the density but also due to the still inadequate knowledge of the Fe-C-S ternary phase diagram. While specific C and S ranges can be pointed out under the hypothesis of a fully molten core, the compositional constraints on a partially molten core are limited by the lack of knowledge of Fe-C-S phase diagram at pertinent conditions.

1.Introduction

The Moon has a unique relevance not only as the closest planetary body to the Earth, but also because its formation has had profound impacts on the Earth's history. During the past decades, numerous space missions have been launched to determine its origin, evolution, and current internal structure (e.g. Dickey et al., 1994; Konopliv et al., 1998; Hood, 1999). This interest will be further fueled by other planned and ongoing missions, including the NASA Artemis program [https://www.nasa.gov/specials/artemis/].

Despite the large amount of seismic, geodetic, and electromagnetic data collected during the past half-century, and the high accuracy measurements performed during the latest 20 years, numerous questions remain open regarding the deepest regions of the Moon, especially its core (e.g. Nakamura et al., 1974; Toksöz et al., 1974; Lognonné et al., 2003). Electromagnetic sounding data from Lunar Prospector imply that the core region is metallic (Hood et al., 1999; Shimizu et al., 2013), while Apollo seismic data indicate high attenuation of acoustic waves passing through the core region (Nakamura et al., 1973, 1974). Other more specific but fundamental core properties such as size, density, and composition still remain rather uncertain (e.g. Garcia et al., 2011; Williams et al., 2014). To date, only a few consensuses have been reached: (1) The core should be at least partially molten in line with the moonquake records and geodetic observations (Lognonné and Johnson, 2007); (2) The mean core density is below that of pure iron, in order to match the measured moment of inertia (Garcia et al., 2019; Viswanathan et al., 2019); (3) Light elements are needed in the core to decrease its crystallizing temperature and density, and sulfur is often favored as the main light element (e.g. O'Neill, 1991; Weber et al., 2011; Jing et al., 2014; Antonangeli et al., 2015). Based on joint inversion of available independent observables such as Apollo, LLR and Grail data, and comparative geochemical analysis of Moon's samples *vs*. bulk silicate Earth, several models have been put forward in recent decades, (e.g. Garcia et al., 2011; Weber et al., 2011; Kuskov et al., 2021) showing significant spreading in many of the parameters relevant for the core.

Sulfur is the most favored light element to be alloyed with iron in the Moon's core, because of its chemical affinity to iron at Moon's core conditions (siderophile behavior), and its effectiveness in decreasing the density of pure iron. Other light elements, such as oxygen and silicon, are not expected in significant concentration, as oxygen solubility into iron seems to be relatively low at the pressures pertinent to the Moon's core (Ricolleau et al., 2011), and the oxidizing conditions during the core differentiation do not favor silicon (Kilburn and Wood, 1997). On the other hand, carbon could be a potential light element component in Moon's core, although its presence and abundance are debated (e.g. Steenstra et al., 2017a and references therein). As such, the phase diagram and the thermo-elastic properties of Fe-C and Fe-S binary liquids have been intensively studied at pressures in the range of 1-10 GPa and temperatures between 1700K and 2200K, forming the basis for discussing implications for Moon's core composition, origin, and thermal evolution.

Sulfur strongly decreases the melting temperature, density, and sound velocity of liquid iron (see Morard et al., 2018 and references therein) at Moon's core conditions. The phase diagram of Fe-S has been studied at pertinent P-T conditions by analysis of recovered samples and *in-situ* X-ray diffraction (Fei et al., 1997, 2000). Sound velocity of liquid Fe-S has been studied by ultrasonics measurements (Jing et al., 2014; Nishida et al., 2016, 2020) and molecular dynamic calculations (Kuskov and Belashchenko, 2016). Density has been studied *in-situ* by the sink/float method, X-ray diffraction, and absorption (Sanloup et al., 2000; Nishida et al., 2008, 2011; Morard et al., 2018; Xu et al., 2021). Thermodynamic models of liquid Fe-S at Moon's core conditions based on these experimental data show a strong non-ideal mixing behavior between liquid Fe and FeS (Morard et al., 2018; Terasaki et al., 2019; Xu et al., 2021). Macroscopic properties can be related to the local structure of the liquid, *i.e.* how the Fe and S atoms are distributed in the short-range distance. In the binary liquid, sulfur is suggested to be incorporated interstitially in liquid iron (Shibazaki and Kono, 2018). Studies indicate that a small amount of sulfur does not significantly affect the local organization of the first coordination shells of the liquid, while the structure exhibits a progressively increased disorder for S concentration above 23.5 at% and the liquid becomes poorly organized for the end member FeS (Shibazaki and Kono, 2018; Morard et al., 2018).

Carbon is also an interstitial element in liquid iron (Shibazaki and Kono, 2018). However, as carbon atoms are much smaller in size compared to sulfur atoms, their inclusion perturbs the Fe liquid structure to a much lower extent. Unlike the disordered Fe-S alloys, Fe-C liquids at high pressure maintain a relatively well-defined local structure for C concentration up to 25 at% (Fe_3C). Consequently, the density (Shimoyama et al., 2013; Terasaki et al., 2010; Sanloup et al., 2011) and sound velocity (Shimoyama et al., 2016; Kuwabara et al., 2016) of Fe-C liquids don't markedly decrease with increasing the carbon content. A density discontinuity was first found in liquid Fe-5.7 wt% C around 6 GPa by Sanloup et al. (2011), and was attributed to a liquid-liquid phase transition of Fe-C at 5.2 GPa. This density discontinuity was reproduced on liquid Fe-3.5 wt% C (Shimoyama et al., 2013), and the phase transition was afterward supported by the observation of a subtle structural change at ~5GPa (Shibazaki et al., 2015).

While the two binary liquids have been well studied, the ternary Fe-C-S system, and in particular ternary Fe-C-S liquid alloys, remain far from being fully understood, with only a few data published on miscibility (Corgne et al., 2008; Dasgupta et al., 2009) and melting (Dasgupta et al., 2009; Deng et al., 2013). In this study, synchrotron X-ray diffraction and absorption experiments were conducted on ternary Fe-C-S liquid alloys in a Paris-Edinburgh cell up to 5 GPa and 1900 K to investigate *in situ* the effect of the simultaneous incorporation of carbon and sulfur on the local structure and density of liquid iron alloys. The measured density data have been used to establish a thermodynamic model for Fe-C-S liquid solutions, which in turn can be used to help to determine the composition of the core of the Moon and other small planetary bodies.

2.Materials and Methods

2.1 Sample preparation

Iron (99.5%, Alfa Aesar), FeS (99.98%, Alfa Aesar), and graphite powders (99%, Alfa Aesar) were grounded in an agate mortar for 30 minutes to produce samples of nominal compositions of Fe-1.5 wt% C-4 wt% S (hereafter referred to as Fe-1.5C-4S), Fe-1.5C-8S, Fe-1.5C-15S, Fe-1.5C-22S, Fe-1.5C-30S, Fe-3C-4S, and Fe-3C-8S. Mixed powders were dried in a vacuum stove at 150 ℃ for 1 hour, and loaded in BN capsules (*Beamtime0720*) or sapphire rings (*Beamtime0921*), prior to the X-ray diffraction and/or absorption experiments.

2.2 High-pressure in-situ X-ray diffraction experiments

In-situ synchrotron X-ray diffraction and absorption experiments were carried out using the newly designed UToPEC (Ultrafast Tomography Paris Edinburgh Cell) (Boulard et al, 2018) at the PSICHÉ beamline, Synchrotron SOLEIL, France. The samples were loaded into a PEC assembly (shown in Figure S2) consisting of a sapphire ring, a BN capsule, a graphite furnace, and a boron epoxy gasket, similar to the one reported in Boulard et al. (2020). Pressure was generated by a pair of tungsten carbide anvils driven by a hydraulic pump, while high temperature generation was ensured by the above-mentioned graphite resistive furnace. Temperature as a function of power was calibrated in a dedicated run before the experiments by a non-destructive cross-calibration method (e.g. Parker et al., 2010), using the thermal Equation of State (EOS) of Pt, hBN, and MgO (Zhao et al., 1997, Matsui et al., 2000, 2009) and the unit-cell volumes determined by X-ray diffraction at each power step. The error on temperature, including possible gradients, is estimated to be ±100 K. The hBN capsule, surrounding the sapphire capsule, also served as the pressure calibrant. The high brilliance polychromatic X-ray beam, with energy ranging from 10 keV to 90 keV was collimated to 25×50 μm^2 (vertical×horizontal FWHM) by two slits before the sample. The diffracted beam was collected by a Ge solid-state detector.

In each experiment, the sample was initially cold compressed to the target pressure, and then molten by heating up at a rate of 100 K/min. At temperatures above 1150 K (corresponding to 300 W), the different phases present in the sample were checked every 50 W by diffraction. The fully molten status of the sample was pinpointed by the absence of sharp diffraction peaks of solids on top of the diffuse scattering signal from the liquid, and further confirmed by tomography. Indeed, thanks to the fast computed-tomography capabilities available at the PSICHÉ beamline (Boulard et al., 2018), the status of samples can be also monitored by 3D tomography images. Figure S3 shows the sequence obtained by increasing temperature

from solid powder mixture to fully molten sample. Once fully molten, a CAESAR (Combined Angle and Energy Dispersive Structure Analysis and Refinement) scan was collected by combining the recorded energy-dispersive diffraction pattern at angles from 2.5 °to 29.5 °with a step of 0.2 °(King et al., 2022). The counting times for 2.5-10 °, 10-20 °, and 20-29.5 ° ranges were respectively 5s, 10s, and 20s, for a total duration of the whole scan of about 20 minutes. The combined energy and 2θ ranges enable a data collection over an extended wave vector (Q), up to 20 $Å^{-1}$. A preset function controlled the motion of slits in front of the Ge detector and ensured signal collection from a fixed and constant volume of the sample irrespective of the angle.

The CAESAR data were analyzed on the basis of the methodology developed by Eggert et al. (2002) and Morard et al. (2014) implemented into the software AMORPHEUS (Boccato et al., 2022) to study the local structure and density of the liquids. Briefly, the pair distribution function $g(r)$ and distribution function $F(r)$ (also referred to as reduced distribution function) are obtained from the collected $S(Q)$ by a Fourier transformation. For $r<r_{min}$ $F(r)= -4\pi r\rho$, where r_{min} is the minimum distance between two atoms due to the interatomic repulsive force, and ρ the atomic density. A figure of merit χ^2 as a function of r_{min} is defined to minimize the oscillation of $F(r)$ in the low r region. Hence, when χ^2 reaches the local minimum, the atomic density ρ is determined by the slope of $F(r)$ over $r<r_{min}$. In line with previous work (Morard et al., 2014), the error of atomic density for this method is empirically estimated to be ±3 atoms/nm^3, considering the effect of the selected Q range, the self-absorption from the sample, and the scattering background residual from the surrounding materials. For materials of present interest, this yields an uncertainty on density about ±250 kg/m^3.

2.3 High-pressure *in-situ* X-ray absorption experiments

Predefined routines allow rapidly commuting the beamline setup from diffraction mode to absorption mode, while sharing the same general optics layout. Absorption profiles were thus collected right after each diffraction acquisition. In this configuration, the height of the incident beam was reduced to 10 microns by collimating slits. An MgO polycrystalline sample was added into the optical path, between the sample and the detector, so to act as polychromator. On the downstream side, the detector was fixed at 8 °with respect to the straight beam path, and the two diffraction peaks of MgO located at 37.5 keV (200) and 53.5 keV (220) were employed to record the absorption profile while scanning the sample (the intensities of the diffraction peaks are proportional to the beam intensity transmitted across the sample). Reference incident intensity was measured by translating the sample completely out of the beam. Detailed experimental procedure was described by Henry et al. (2022). One of the main advantages of this setup is that no extra

optical paths or detectors were needed, and the absorption profile of the assembly was taken at the same experimental condition as the CAESAR scan.

Based on the Beer–Lambert law, it was possible to extract from the absorption profile the value of $(\mu\rho)_{P,T}$, the product of mass absorption coefficient and density at experimental P-T conditions. In order to disentangle the density from the absorption coefficient, we assumed the liquid to have the same absorption coefficient of the hot solid, which, in turn, is obtained from the absorption profile collected on the solid just before melting, imposing the density ρ_S inferred from energy-dispersive X-ray diffraction:

$$\rho_{P,T} = \frac{(\mu\rho)_{P,T}}{(\mu\rho)_S/\rho_S} \quad (1)$$

The details of data processing for diffraction and absorption can be found in the Supplementary Information.

3. Results

3.1 Liquid structure

Figure 1 (a) shows the pair correlation function $g(r)$ (or radial distribution function for isotropic media such as the liquids of the present study) together with partial $g(r)$ from calculations available in literature. Oscillations in the $g(r)$s become less pronounced for samples with 22.1 at% S or more, consistent with previous studies on Fe-S binary liquids (Shibazaki and Kono, 2018; Morard et al., 2018; Xu et al., 2021), in which the liquids were reported to show a more disordered structure for the S content of 23.5 at% S, 29.4 at% S, and 25.1 at% S, respectively. On the other hand, inclusion of up to 18 at% of carbon in the ternary liquid seems not to have a detectable impact on the local structure, as signatures of the second and third coordination shells are still distinguishable. The modification of the structure is controlled by the interstitial inclusion of more massive S atoms that perturb the Fe-Fe network, while smaller C atoms can enter in interstitial sites between Fe atoms without significant effect on the local structure. This is further supported by the variation in the atomic density shown in Figure S4. The atomic density with increasing S or C content shows opposite trends, highlighting the different effect of sulfur and carbon. Conversely, we note that the atomic density of Fe-Si liquids does not significantly change with Si content, as Si atoms substitute iron atoms.

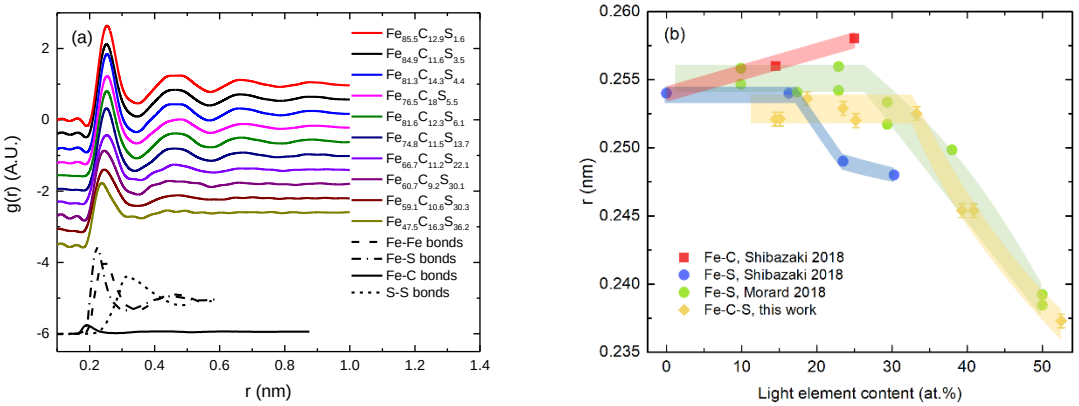

Figure 1 (a) Radial distribution function measured for Fe-C-S ternary liquids in the 1-5 GPa and 1700-1900 K range. Data are shown for increasing sulfur content (from the top to bottom) and compared to the partial $g(r)$ showing the individual contribution of Fe-Fe, Fe-S, and S-S bonds, calculated for a binary Fe-S liquid alloy with 23 at% S (Morard et al., 2018), and the partial $g(r)$ illustrating the Fe-C bonds calculated for a binary Fe-C alloy with 20 at% C (Lai et al., 2017). (b) First peak positions of the ternary alloys in comparison with results obtained for binary Fe-C and Fe-S at similar P-T condition (1.5-5.2 GPa and 1600-1980 K in Morard 2018, and 3-5 GPa, 1600-2000 K in Shibazaki 2018). Colored areas are guides for the eye.

The most prominent feature in the $g(r)$ is the position (r_1) and intensity of the first peak, corresponding to the first coordination sphere. r_1 as a function of total light element content is plotted in Figure1 (b) and compared with results from literature obtained for binary liquids. Within the experimental uncertainties the r_1 value of Fe-S liquids is not observed to vary with S content for S addition up to ~20-25 at%, while it significantly decreases for higher concentration. As suggested by the calculated partial $g(r)$, this is likely due to the increased contribution of the shorter and covalent Fe-S bonds (Figure 1 (a)). Since the scattering intensity is proportional to the square of the atomic number, the contribution from Fe-Fe and Fe-S bonds in the case of $Fe_{66.7}C_{11.2}S_{22.1}$ account, respectively, for ~65% and ~27% of the total signal (see Morard et al., 2008 and references there in), while the contribution from other bonds is negligible. Therefore, the formation of shorter Fe-S bonds moves the first peak position of the total $g(r)$ towards lower r value, while other bonds hardly have any visible effect. For binary Fe-C liquids, the addition of carbon seems to move r_1 towards higher values according to available experimental data (Shibazaki and Kono, 2018), in apparent contrast with molecular dynamic calculations that indicate short Fe-C bonds (Lai et al., 2017). This discrepancy may imply that the addition of carbon might have a more complex perturbation effect other than simply forming the Fe-C bonds.

Our results of r_1 as a function of total light element content follow a trend qualitatively similar to that reported for the binary Fe-S by Morard et al., 2018 and Shibazaki and Kono, 2018, with a closer agreement

with values reported in the former. The similar trend for Fe-S and Fe-C-S liquids at the same total light element content indicates that the Fe-S bonds still play a dominant role in determining the structure of the ternary liquid. Up to 18 at% of C does not modify the two-regime behavior observed for binary Fe-S liquid alloys, nor the light element threshold defining the change in the regime. Thus, in this context C seems to play the same role as S in decreasing the r_1 value, in agreement with the length of the calculated Fe-C bonds (Lai et al., 2017), but in apparent contrast with the experimental r_1 value reported for the Fe-C liquids (Shibazaki and Kono, 2018).

3.3 Density

Table 1 summarizes the densities measured at the experimental conditions. Absorption measurements were only conducted in the second of the two synchrotron beamtimes (*Beamtime0922*). Densities obtained by diffraction and by absorption are consistent, with remarkable agreement in the cases of S-rich samples (e.g. measurements on $Fe_{60.7}C_{9.2}S_{30.1}$ and $Fe_{47.5}C_{16.3}S_{36.2}$), and the difference for measurements even on $Fe_{74.8}C_{11.5}S_{13.7}$ is smaller than 8% between the two methods. When the two methods yield slightly dissimilar results, densities measured by diffraction are systematically lower than those measured by absorption. A possible reason is that collected diffraction signal is contributed from a sulfur-rich portion of the sample. In fact, the diffraction method would be more sensitive to local inhomogeneity compared to absorption if the diffracting volume is comparable in scale to the size of inhomogeneous regions (a few tens of microns). On the other hand, as the absorption profile is taken on the whole sample, the error from local inhomogeneity has been almost eliminated (*i.e.* the massive absorption coefficient is averaged). Finally, and irrespective of the above consideration, we note that both values are used to build the thermodynamic model.

Table 1 Samples' composition, experimental P-T conditions, measured density and density rescaled to 1850 K, for both diffraction and absorption experiments.

Atomic proportion (%)			Exp. T (K)	Pressure (GPa)	ρ by diffraction (kg/m^3)	ρ rescaled to 1850K (kg/m^3)	ρ by absorption (kg/m^3)	ρ rescaled to 1850K (kg/m^3)
Fe	C	S						
Beamtime0720								
84.9	11.6	3.5	1895	2.15	6780	6800	/	/
85.5	12.9	1.6	1690	1.06	6900	6800	/	/
81.3	14.3	4.4	1722	2.29	6740	6680	/	/
			1895	2.09	6600	6620	/	/
76.5	18.0	5.5	1625	2.52	6590	6490	/	/
			1895	2.17	6430	6460	/	/
Beamtime0921								
81.6	12.3	6.1	1760	3.86	6550	6510	6830	6790
			1850	3.70	6460	6460	6460	6460
74.8	11.5	13.7	1610	4.92	6200	6110	6710	6610
			1720	4.70	6180	6130	6630	6570
			1805	4.57	6110	6100	6550	6530
66.7	11.2	22.1	1760	3.72	/	/	5950	5920
			1850	3.62	5620	5620	6030	6030
59.1	10.6	30.3	1760	3.44	5020	4990	5220	5200
			1850	3.31	5160	5160	5200	5200
60.7	9.2	30.1	1760	4.76	/	/	5590	5560
			1850	4.35	5550	5550	5510	5510
47.5	16.3	36.2	1760	4.7	/	/	5140	5110
			1850	4.42	4970	4970	5060	5060

3.4 Thermodynamic model

A thermodynamic solution model of the Fe-C-S liquid was built based on the thermal EOSs of the end members, Fe, FeS, and Fe_3C (parameters provided in Table S2) with their interactions modeled by an asymmetric Margules formulation.

In an asymmetric Margules formulation, the non-ideality of the Gibbs energy of the component *i* of a mixture is described by the addition of an excess contribution:

$$G_i = G_{i0} + G_{i,ex}(W) \quad (2)$$

where G_i is the Gibbs energy of component i, G_{i0} the Gibbs energy at standard state, and $G_{i,ex}(W)$ the excessive Gibbs energy. W is the interactive Margules parameter which is assumed linear with pressure and temperature:

$$W(P,T) = W_0 + T \times W_S + P \times W_V \tag{3}$$

Deriving the Gibbs energy with respect to pressure yields the volume. The volume of Fe-C-S liquids using Fe, FeS, and Fe_3C as end members is written as

$$V_{FeCS} = X_{Fe_3C}V_{Fe_3C} + X_{FeS}V_{FeS} + X_{Fe}V_{Fe} + X_{Fe_3C}V_{ex(\,Fe_3C)} + X_{FeS}V_{ex(\,FeS)} + X_{Fe}V_{ex(\,Fe)} \tag{4}$$

The additional terms are excessive contributions to the volume, which are functions of the fraction of each component. For instance, the excessive volume contribution from Fe, *i.e.* $V_{ex(\,Fe)}$ is related to the other end members by:

$$\begin{aligned} V_{ex(\,Fe)} = {} & X_{FeS}^2[W_{V,Fe-FeS} + 2X_{Fe}\left(W_{V,FeS-Fe} - W_{V,Fe-FeS}\right)] \\ & + X_{Fe_3C}^2[W_{V,Fe-Fe_3C} + 2X_{Fe}\left(W_{V,Fe_3C-Fe} - W_{V,Fe-Fe_3C}\right)] \\ & + 2X_{Fe}X_{FeS}X_{Fe_3C}\left(W_{V,FeS-Fe} + W_{V,Fe_3C-Fe}\right) \\ & - 2X_{FeS}X_{Fe_3C}\left(X_{FeS}W_{V,Fe_3C-FeS} + X_{Fe_3C}W_{V,FeS-Fe_3C}\right) \\ & + \frac{X_{Fe_3C}X_{FeS}(1-2X_{Fe})}{2}(W_{V,FeS-Fe} + W_{V,Fe-FeS} + W_{V,Fe_3C-Fe} \\ & + W_{V,Fe-Fe_3C} + W_{V,Fe_3C-FeS} + W_{V,FeS-Fe_3C}) \end{aligned} \tag{5}$$

with the ternary interaction term neglected. $W_{V,i-J}$ is the volume interaction Margules parameter, which characterizes the interaction intensity of components *i* and *j* (Tsuno et al., 2011). We note that in this model the ternary interaction term is ignored. With the other two counterparts for FeS and Fe_3C, the mixed volumes given by Margules model are shown in Eq. (6).

$$\begin{aligned} \mathrm{V}_{Fe-C-S} = {} & \mathrm{X}_{Fe_3C}\mathrm{V}_{Fe_3C} + \mathrm{X}_{FeS}\mathrm{V}_{FeS} + \mathrm{X}_{Fe}V_{Fe} + \mathrm{X}_{Fe}X_{Fe_3C}^2W_{V,Fe-Fe_3C} + \mathrm{X}_{Fe}X_{FeS}^2W_{V,Fe-FeS} \\ & + X_{Fe_3C}X_{Fe}^2W_{V,Fe_3C-Fe} + X_{Fe_3C}X_{FeS}^2W_{V,Fe_3C-FeS} \\ & + X_{FeS}X_{Fe}^2W_{V,FeS-Fe} + X_{FeS}X_{Fe_3C}^2W_{V,FeS-Fe_3C} \\ & + \frac{X_{Fe}X_{Fe_3C}X_{FeS}\left(3-2X_{Fe}-2X_{Fe_3C}-2X_{FeS}\right)}{2}(W_{V,Fe-Fe_3C} + W_{V,Fe-FeS} \\ & + W_{V,Fe_3C-Fe} + W_{V,Fe_3C-FeS} + W_{V,FeS-Fe} + W_{V,FeS-Fe_3C}) \end{aligned} \tag{6}$$

The fitted parameters to the experimental data are listed in Table 2. Based on Eq. (4) all relevant thermodynamic properties of Fe-C-S solutions can be computed from standard thermodynamic relations.

The thermal expansion coefficients of each composition can be calculated according to its definition:

$$\alpha = \left(\frac{1}{V}\right)\left(\frac{\partial V}{\partial T}\right) \tag{7}$$

For comparison, the density measured at different temperature conditions are rescaled at the reference value of 1850 K by making use of the thermal expansion coefficients, and the comparisons between ideal and non-ideal models are shown in Figure2. The fitted Margules parameters for Fe and Fe_3C are close to 0 indicating that Fe and Fe_3C mix almost ideally at here-considered conditions. Comparing to the ideal mixing model in Figure 2 (a), the densities provided by Margules model in Figure 2 (b) are in overall better agreement with the experimental data. Also, note that ternary alloy with high light element content at low pressure (< 3 GPa) proved to be immiscible, hence only high-pressure data were collected for the sulfur-rich samples. Finally, we stress that although the here-established mixing model well account for the available experimental data and is suitable for density calculations for the Fe-C-S liquid system as a function of pressure and/or composition in the 0-5 GPa range, it may no longer be valid at higher pressure, since the density discontinuity of Fe-C liquid due to a phase transition at 5.2 GPa (Sanloup et al., 2000).

Table 2 Fitted interaction Margules parameters

$W_{V,Fe-Fe_3C}$	0.2 ±0.2
W_{V,Fe_3C-Fe}	0 ±0.2
$W_{V,Fe-FeS}$	-2.2 ±0.4
$W_{V,FeS-Fe}$	-1.0 ±0.4
W_{V,Fe_3C-FeS}	-3.0 ±0.2
$W_{V,FeS-Fe_3C}$	0.8 ±0.2

* All the parameters are in cm^3/mol

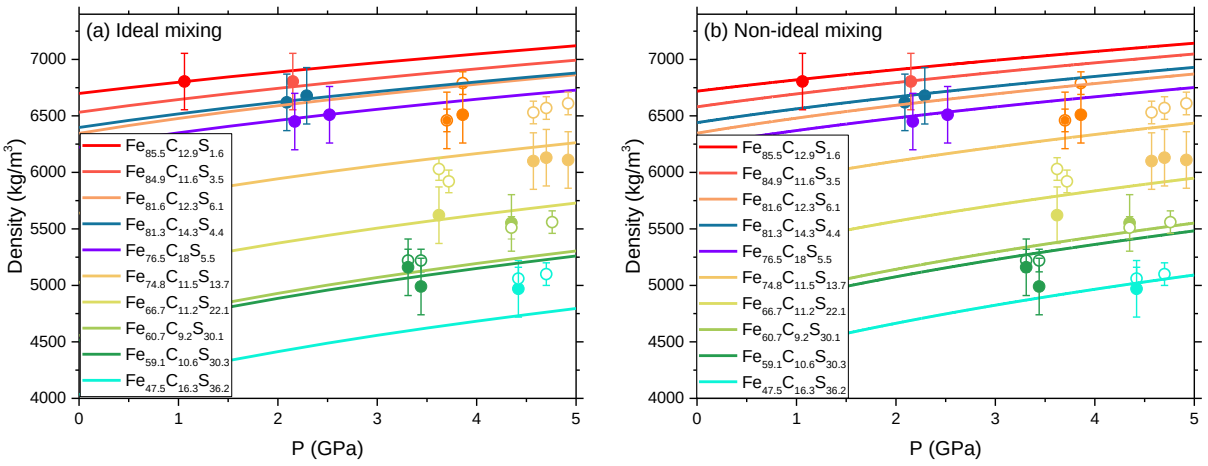

Figure 2 Density at 1850 K computed for selected compositions in the liquid Fe-C-S ternary system according to ideal (a) and non-ideal (b) thermodynamic models. (a) Ideal mixing model constructed based on the properties of Fe, Fe_3C and FeS end members (Table S2). (b) Non-ideal mixing model based on the Margules mixing rule. Open circles and filled circles are results from absorption and diffraction measurements, respectively. The experimental uncertainties are mainly from the limited Q range, self-absorption, and r_{min} fluctuation in the case of diffraction, and from minor sample deformation and fitting procedure for absorption.

The density calculated for the liquid Fe-C-S ternary alloys at 5 GPa as a function of the light element content is shown in Figure3 (a) and compared with data for binary Fe-S and Fe-C alloys from literature. The uncertainties are from the fitting of the Margules parameters, which yielded ±35 - ±75 kg/m^3 on the density. The most recent studies on Fe-S liquid by diffraction (Morard et al., 2018) and absorption (Terasaki et al., 2019) are in good agreement and provide higher density compared to earlier studies, (Sanloup et al.,2000), while results on Fe-C liquid by absorption are all within mutual uncertainties (Terasaki et al., 2010; Sanloup et al., 2011; Shimoyama et al., 2013). The density of Fe-C-S alloys plots in between those of binary alloys, indicating a co-effect of sulfur and carbon in decreasing the density of pure iron. As alloys with high light element content reach the miscibility limit at low pressure (see Dasgupta et al., 2009), the carbon content considered in this study is restricted to less than 18 at%, so to model a homogeneous ternary liquid. The density is thus largely controlled by the sulfur content, with the effect due to carbon inclusion minor as the direct consequence of the limited proportion of carbon in the modeled alloys.

3.4 Sound velocity calculation

The compressional sound velocity of the ten compositions investigated in this study can be calculated at 5 GPa and 1850K in an internally consistent way based on our thermodynamic model, following the equation

$$v_p = \sqrt{\frac{K_T(1+\alpha\gamma T)}{\rho}} \tag{8}$$

where γ is the Grüneisen parameter, α the thermal expansion coefficient calculated by eq. (7), ρ the extrapolated density of the ternary alloy by the mixing model, and K_T the isothermal bulk modulus calculated by its definition and the mixing model, Eq. (5):

$$K_{1850K,P} = \left[-V\left(\frac{dP}{dV}\right)\right]_{1850K} \tag{9}$$

Since there is no experimentally determined γ for Fe-S, Fe-C, or Fe-C-S, the γ of ternary Fe-C-S samples are calculated as:

$$\gamma = \frac{K_T V \alpha}{C_P - K_T V T \alpha^2} \tag{10}$$

where the C_P is the heat capacity at constant pressure of the ternary alloys, determined by the values of all the end members:

$$C_P = \frac{\partial(\sum_i x_i\, Q_i)}{\partial T} = \sum_i x_i\, C_{P,i} \tag{11}$$

where Q is the amount of heat and the subscript *i* represent each end members. The C_P of Fe, FeS, and Fe_3C are calculated with Eq. (10) using the parameters provided in Table S2. The calculated thermo-elastic properties are provided in Table S3.

Here we note that using other parameterization of the bulk modulus of the alloys (e.g. Chen et al. 2014; Morard et al, 2018) and/or a value of γ=1.72 (e.g. Kuwabara et al., 2016; Shimoyama et al., 2016) fixed to that experimentally determined for liquid Fe (Anderson and Ahrens, 1994) lead to a ~15% higher compressibility, and consequently higher velocities, without modifying the reported trend.

Figure 3 (b) shows the calculated sound velocity compared with the data from literature for the Fe-S and Fe-C binary systems. The errors are from the fitting of Margules parameters and the uncertainties of γ. The ternary data show some scatter, but follow the trend defined for Fe-S alloys. We also note that the points showing higher values of sound velocity with respect to a linear trend are those with larger C fraction (e.g. the point at x=23.5, for which C content is 18 at%). While difficult to independently address the effect of S and C on velocities, the sound velocity of the liquid ternary alloy would offer a useful reference to model seismic velocities in the Moon's core.

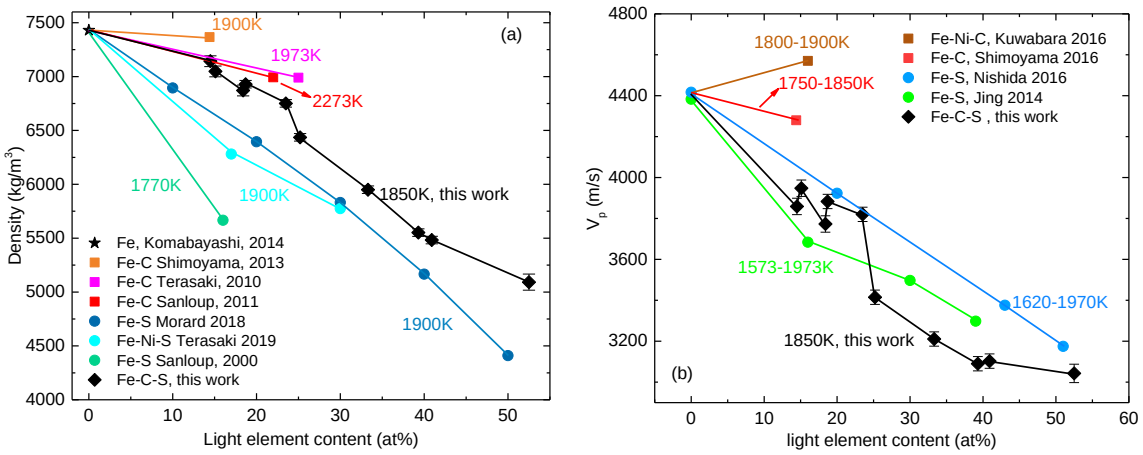

Figure 3 Density (a) and sound velocity (b) at 5 GPa modeled for the ternary Fe-C-S alloys as a function of light element content and compared with data for the binary Fe-S and Fe-C system. The reference temperature for our model is 1850 K, while the temperature of other studies is annotated adjacent to the data with the same color. Lines across the points are guides for the eye.

4 Discussion

Considering the eutectic point of planetary-core-relevant iron alloys, the relatively low temperature of the Moon's interior (*T* between 1300 K and 1900 K, e.g. Wieczorek et al., 2006) points to an Fe and S-rich core as the simplest explanation. Furthermore, the depletion of the lunar mantle in siderophile elements is possibly related to the presence of sulfur in the core (Rai and Westrenen, 2014). Accordingly, many compositional models have been put forward for the core of the Moon based on the thermo-elastic properties of Fe-S or Fe-Ni-S liquid alloys (e.g. Nishida et al., 2011; Jing et al., 2014; Antonangeli et al., 2015; Morard et al., 2018; Terasaki et al., 2019).

Based on silicate/metal partitioning, carbon has also been recently considered as a potential main light element, with up to 4.8 wt% C estimated in the lunar core (Steesntra et al., 2017a). However, the comparatively higher density of liquid Fe-C alloys (Figure 3 (a)) seems difficult to reconcile with the density of the core constrained on the basis of the geodetic data. Similarly, compressional sound velocities of liquid Fe-C and Fe-Ni-C alloys at Moon's core pressure and temperature conditions are higher than that of liquid Fe-S (Figure 3 (b)), with significant implications for the inversion of the seismological data.

Absence of data on the ternary Fe-C-S system so far has largely limited the discussion and the models to the binary systems. Current dataset allows a step forward. The local structure of ternary Fe-C-S liquid here experimentally determined for the first time, show that the shape of the $g(r)$ and in particular the position of the first coordination sphere evolves with increasing light element content following the same trend of

Fe-S liquids. As a first order approximation, the limited substitution of sulfur with carbon (~18 at%) doesn't affect the local structure of the ternary liquid. However, the two elements have different quantitative effects on density and sound velocities (Fig 3). Indeed, S lowers both density and sound velocity of liquid iron more significantly than C, as readily visible from the experimental data of Fe-C and Fe-S liquids with the same atomic proportion.

According to these considerations, assessing the amount of C in the core of the Moon on the sole basis of density and/or sound velocity constrained by seismological or geodetical observations is not straightforward. Additional constraints such as element partitioning and bulk C content are needed to understand the role of C in the core. On the other hand, the possibility of carbon as a potential light element existing with sulfur in the Moon's core cannot be ruled out.

Many Moon models were built by integrating various independent observables, including seismic, electromagnetic, geodetic, and geochemical data. Great efforts have been made to interpret these observables in terms of composition, but discrepancies still exist among studies, particularly concerning the core (Garcia et al., 2019; Viswanathan et al., 2019; Kuskov et al., 2021 and references therein). To discuss the possible content of sulfur and carbon in the Moon's core, a density contour is plotted in Figure4, where densities proposed by three of the latest Moon models (see table 3 and associated references for more details) are correlated to sulfur and carbon content based on here-presented results. While the three models would require distinct sulfur content in the core, the carbon content cannot be uniquely constrained. The Moon's core is assumed at 5 GPa and 1850 K. Note that in Kuskov et al. (2021) the Moon's core is modeled with a solid inner core surrounded by a liquid outer core, so that the solutions' space reported in Figure 4 corresponds to the C and S content in the outer core, while a fully molten core was assumed in the other two models.

Table 3 Reference models of the Moon's core here considered for discussion. Garcia19 is from model 2 in Garcia et al., (2019); Viswanathan19 is from Viswanathan et al., (2019), and Kuskov21 is from model E in Kuskov et al., (2021).

	Garcia19	Viswanathan19	Kuskov21
Main data source	Seismic T_s, T_p Geodetic M, I/MR^2, k_2 Electromagnetic ρ_a	Geodetic M, I/MR^2, k_2; Crustal thickness and density	Seismic T_s, T_p Geodetic M, I/MR^2, k_2; Geochemical bulk concentration of FeO and Al_2O_3
Core status	Fully molten	Fully molten	Solid inner core + liquid outer core
Density of the (outer) core	4550 kg/m^3	5812 kg/m^3	6200 – 7000 kg/m^3

While both Garcia19 and Viswanathan19 assume an entirely liquid core, Garcia19 suggests two Moon's models with the core density ~22% lower than in Viswanathan19, resulting in a nearly pure FeS core. As the two models in Garcia19 proposed quite similar core densities (4480 *vs.* 4550 kg/m^3), the model 2, using an updated geodetic dataset, is taken for discussion here. As Fe, FeS, and Fe_3C were employed as end-members for the thermodynamic model, the mixing limit (*i.e.* the maximum light-element content) is defined by the curve linking FeS and Fe_3C in Figure 4. A ±3% variation with respect to the proposed density in Garcia19 reflects only into a ~2 wt% variation of required sulfur content, while allowing for some carbon (below 0.5 wt%). If this model were confirmed, the required sulfur content would be pinned to 34-36 wt%, while the carbon content would be constrained by the ternary liquidus as a function of C and S content.

In the model Viswanathan19, the core oblateness as a function of radius was derived from two models, one with LLR-fitted polar MOI, and the other with a hydrostatic core model. The overlapped region indicates the core properties compatible with both models, which yield a core radius in the range of 381 ±12 km with a density of 5812 kg/m^3. The proposed density and the corresponding C and S contents are shown in Figure 4. Carbon content spans from 0 to 4.4 wt%, reaching the miscibility gap (as this model assumes a homogeneous liquid core, the carbon content is not supposed to exceed this limit), and correspondingly, the sulfur content is constrained within 13-23 wt% (variation of ±3% on the nominal density).

The model Kuskov21 assumes a partially molten core, with the density of the liquid outer core in the range of 6200-7000 kg/m^3 (and the density of the solid inner core in the range 7500–7700 kg/m^3). The pseudo binary Fe(Ni)-S was considered in this paper, with a solid inner core composed of iron (plus nickel and light elements at trace level) and an outer liquid core made of Fe-S. We can then reconsider this model in the light of our results on the ternary Fe-C-S. Both, Fe and Fe_3C are denser than the Fe-C-S liquids from which they crystallize and would be suitable candidates for an inner core, with the actual crystallizing phase controlled by the bulk concentration of carbon in the liquid.

(i) For a bulk composition on C-poor side, Fe would be the first crystallizing solid phase, leaving a Fe-C-S liquid outer core. Whether an Fe inner core would grow from the center (bottom-up), or Fe formed at the top of the core would snow across the liquid core (top-down) depends on total light element content, in particular the S content (Xu et al., 2021).

(ii) For a bulk composition with intermediate light element content (e.g. the Fe-5 wt% C-5 wt% S, see Dasgupta et al., 2009), Fe_3C would be the first solid phase to crystallize to form a solid inner core, leaving a Fe-C-S liquid outer core until the entire available C is consumed. In a similar manner, S content is expected to largely control the top-down *vs*. bottom-up crystallization regime.

(iii) For a bulk composition on C-rich side (e.g. the Fe-4.35 wt% C-7.85 wt% S, see Deng et al., 2013), graphite will first form during the core cooling process and float upward to the core-mantle boundary, followed by the crystallization of Fe_3C during the continuous temperature decrease to form an inner core. When applied to the model of Kuskov21, only the latter stage is considered. Case (iii) can thus be brought back to case to (ii).

Experiments on the Fe-C-S ternary system have supported the above-outlined three crystallization regimes, which are strongly dependent on the bulk C and S content. We stress, however, that with a limited number of experiments conducted only with a few specific compositions, the C threshold between the C-poor and C-rich side, *i.e*. the eutectic point, and how it modifies with sulfur content, remain poorly constrained.

A solid inner core of fcc-iron with the density of 7500-7700 kg/m^3 was proposed in the model of Kuskov2021. In this case, further limits in the amounts of light elements, beside the above-mentioned eutectic, are placed by the liquidus (the existence of an inner core in equilibrium with melt imposes conditions below those at liquidus). Melting experiments in the Fe–S–C system indicate the liquidus temperature to decrease significantly compared to that in the Fe–S binary system by adding a very small amount of carbon into the Fe–S system (Deng et al., 2013). In absence of precise determination of the phase diagram of the Fe-C-S system, the ternary composition at liquidus temperature = 1850 K is estimated as linear interpolation between results for the Fe-C and Fe-S binary systems and shown as shaded area in the Fe corner (Figure 4). The entire compositional space corresponding to the density of the outer core proposed in Kuskov21 lies outside this corner for a core at 1850K. In other words, a relatively hot core at 1850 K could hardly support a solid inner core. If a colder core is assumed, the C and S content at liquidus are expected to significantly increase, enabling an overlap between the solutions in the compositional space accounting for proposed outer core density and existence of Fe inner core. However, the limited knowledge of the phase diagram and melting relations of the ternary Fe-C-S system do not currently allow for a quantitative discussion.

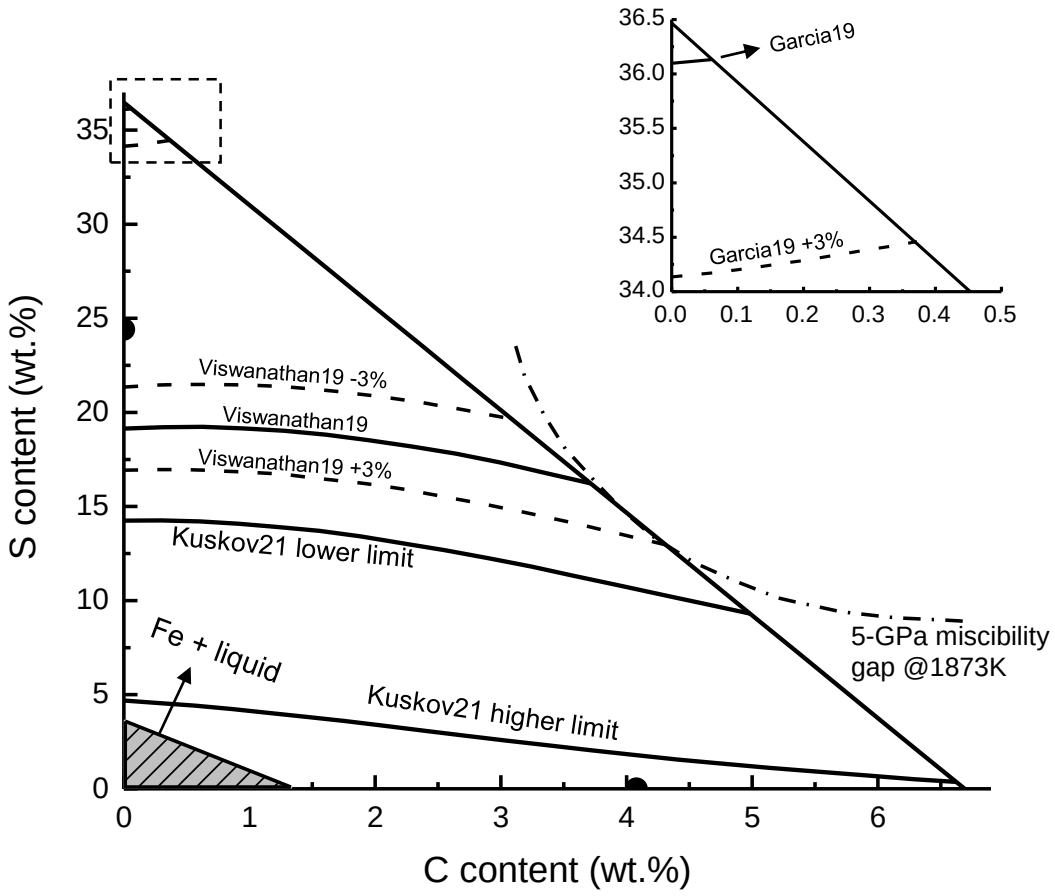

Figure 4 The carbon and sulfur content distribution within the liquid (outer) core assumed at 5 GPa and 1850 K and having density according to three recent Moon's models: Garcia19 (Garcia et al., 2019), Viswanathan19 (Viswanathan et al., 2019), and Kuskov21 (Kuskov et al., 2021). A ±3% variation is considered with respect to the density proposed in Garcia19 and Viswanathan19. Inset: Zoom-in of light element distribution for Garcia19. The shaded triangle shows the composition range for which solid Fe phase (+C at solid solubility limit) is expected in coexistence with Fe-C-S liquid. The dotted-dash curve is the miscibility gap at 5 GPa and 1873 K for Fe-C-S liquid alloys by Dasgupta et al. (2009). Eutectic compositions for the Fe-S (Buono et al., 2011) and Fe-C (Fei and Brosh, 2014) binary system at 1850 K are also shown by the closed circles on the axes.

5 Conclusions

Liquid structures and densities of Fe-C-S alloys have been studied by a multi-techniques approach at high pressure and high temperature, up to 5 GPa and 1900 K, over a large range of carbon and sulfur composition. The experimental data were employed to establish a non-ideal thermodynamic solution model for density and other thermo-elastic properties of liquid ternary alloys as a function of pressure and composition, which provides a useful database to discuss the composition of the core of small telluric planetary bodies.

Local structure, density and sound velocity of the ternary Fe-C-S liquids have been compared to those of binary Fe-C and Fe-S liquids. Although both interstitial, S and C affect the liquid structure differently, with $g(r)$ of ternary Fe-C-S liquid very close to the $g(r)$ of binary Fe-S liquid with the same light element content. At first approximation, the local structure of ternary liquids is thus controlled by the S content. Conversely, both density and sound velocity of ternary alloys show a co-effect of carbon and sulfur. With specific regards to density, values of ternary alloys are distributed between the upper and lower values provided, respectively, by Fe-C and Fe-S alloys having the same total amount of light elements. Still, the effect of S is more significant, lowering both density and sound velocities of the ternary Fe-C-S liquids with respect to pure Fe more significantly than C, as evident from the direct comparison of properties of ternary alloys with the same total amount of light elements but different C *vs*. S proportions.

Based on the acquired knowledge of the thermo-elastic properties of Fe-C-S alloys, and the derived thermodynamic model, we discussed the simultaneous presence of carbon and sulfur in the Moon's core. Three of the latest Moon's models have been considered, which propose different core states (fully molten vs. partially molten) and have quite different core densities, and thus light element content. Carbon, differently from sulfur, is hardly constrained on the sole basis of density and/or sound velocity. If the Moon's core is assumed to be composed of a homogeneous Fe-C-S liquid, the maximum carbon content limited by the miscibility gap, here estimated at 5 GPa and 1850 K around 4.3 wt% depending on sulfur content. On the contrary, sulfur content estimates on the basis of the proposed densities depend upon the considered model and are in a 13-23 wt% range (Viswanathan et al., 2019) or 34-36 wt% for model 2 in Garcia et al. (2019), well above upper limits proposed on the basis of core differentiation models (e.g. Rai and van Westrenen, 2014). This apparent incompatibility between a light, S-rich core advocated by geophysical observations and an S-poor core put forward by core-differentiation models, metal-silicate partitioning and elemental abundances in the bulk silicate Moon, remains to be addressed. On the other hand, if the core were not fully molten (e.g. model E in Kuskov et al., 2021), in the Fe-C-S system, a solid inner core would be made of Fe or Fe_3C depending on whether the bulk C content is on the C-poor or C-rich side of the eutectic. The currently limited knowledge of the phase diagram and melting properties of the ternary Fe-C-S system allows only for a qualitative discussion. The existence of a solid inner core puts more constraints on core's temperature since it must be below the liquidus. If we assume a core temperature of about 1850 K, the amounts of S and C required to match the outer core density proposed in model E by Kuskov et al. (2021) make the existence of a solid inner core rather unlikely. As the liquidus temperature at the Fe-rich side decreases with increasing S or C content, a cooler core can accommodate more light elements in the liquid outer core while having a C-bearing fcc-Fe core, in qualitative agreement with the model of Kuskov21. However, in this case, the light element budget strongly depends on a detailed

understanding of the phase diagram and partial melting properties of the ternary Fe-C-S system, and the knowledge of the bulk composition of the proto-core, for which further studies are needed.

CRediT authorship contribution statement

Bin Zhao: Conceptualization, Data curation, Formal analysis, Investigation, Visualization, Writing – original draft, review & editing

Guillaume Morard: Conceptualization, Methodology, Investigation, Supervision, Project administration, Writing – review & editing

Eglantine Boulard: Methodology, Investigation, Writing – review & editing

Silvia Boccato: Investigation, Software, Writing – review & editing

Nicki C. Siersch: Investigation, Writing – review & editing

Attilio Rivoldini: Methodology, Writing – review & editing

Nicolas Guignot: Investigation, Resources, Software

Andrew King: Resources, Software

Laura Henry: Resources, Software

Claire Zurkowski: Resources, Writing – review & editing

Yingwei Fei: Resources, Writing – review & editing

Daniele Antonangeli: Conceptualization, Methodology, Investigation, Supervision, Project administration, Writing – review & editing, Funding acquisition

Data availability statement

Raw experimental data, the Python and Matlab code for data analysis have been published in the Zenodo online repository (Zhao et al., 2022).

Acknowledgements

The authors wish to thank Im ène Est ève for her help with sample analysis by SEM, and Michel Fialin and Nicolas Rividi for their help during microprobe analysis. Yann Le Godec is acknowledged for fruitful discussions and his help for the definition and preparation of the PEC assembly. We also thank James Badro and Nicolas Wehr for preliminary tests in piston cylinder press, Anat Shahar for kindly delivering our samples to the Earth and Planets Laboratory, Washington DC, and Emma Bullock for technical assistance. This project has received funding from the European Research Council (ERC) under the European Union's Horizon 2020 research and innovation Programme (grant number 724690). YF acknowledges NASA's support (80NSSC20K0337). The Scanning Electron Microscope (SEM) facility at IMPMC is supported by R égion Ile de France grant SESAME 2006 N◦I-07-593/R, INSU-CNRS, Institute de Physique (INP)–CNRS, University Pierre et Marie Curie–Paris 6, and by the French National Re-search Agency (ANR) grant ANR-07-BLAN-0124-01. The authors acknowledge synchrotron SOLEIL for the provision of beamtime under proposals 20191835 and 20210144.

References

Anderson, W.W., & Ahrens, T.J. (1994). An equation of state for liquid iron and implications for the Earth's core. *Journal of Geophysical Research: Solid Earth*, *99*(B3), 4273-4284. https://doi.org/ 10.1029/93JB03158

Antonangeli, D., Morard, G., Schmerr, N.C., Komabayashi, T., Krisch, M., Fiquet, G., et al. (2015). Toward a mineral physics reference model for the Moon's core. *Proceedings of the National Academy of Sciences*, *112*(13), 3916-3919. https://doi.org/10.1073/pnas.1417490112

Boccato, S., Garino, Y., Morard, G., Zhao, B., Xu, F., Sanloup, C., King, A., et al. (2022). Amorpheus: a Python-based software for the treatment of X-ray scattering data of amorphous and liquid systems. *High Pressure Research*, *42*(1), 69-93. https://doi.org/10.1080/08957959.2022.2032032

Boulard, E., King, A., Guignot, N., Deslandes, J.P., Le Godec, Y., Perrillat, J.P., et al. (2018). High-speed tomography under extreme conditions at the PSICHE beamline of the SOLEIL Synchrotron. *Journal of Synchrotron Radiation*, *25*(3), 818-825. https://doi.org/10.1107/ S1600577518004861

Boulard, E., Denoual, C., Dewaele, A., King, A., Le Godec, Y., & Guignot, N. (2020). Following the phase transitions of iron in 3D with X-ray tomography and diffraction under extreme conditions. *Acta Materialia*, *192*, 30-39. https://doi.org/10.1016/j.actamat.2020.04.030

Buono, A.S., & Walker, D. (2011). The Fe-rich liquidus in the Fe–FeS system from 1 bar to 10 GPa. *Geochimica et Cosmochimica Acta*, *75*(8), 2072-2087. https://doi.org/10.1016/j.gca.2011.01.030

Chen, J., Yu, T., Huang, S., Girard, J., & Liu, X. (2014). Compressibility of liquid FeS measured using X-ray radiograph imaging. *Physics of the Earth and Planetary Interiors*, *228*, 294-299. https://doi.org/10.1016/j.pepi.2013.12.012

Corgne, A., Wood, B.J., & Fei, Y. (2008). C-and S-rich molten alloy immiscibility and core formation of planetesimals. *Geochimica et Cosmochimica Acta*, *72*(9), 2409-2416. https://doi.org/10.1016/ j.gca.2008.03.001

Dasgupta, R., Buono, A., Whelan, G., & Walker, D. (2009). High-pressure melting relations in Fe–C–S systems: Implications for formation, evolution, and structure of metallic cores in planetary bodies. *Geochimica et Cosmochimica Acta*, *73*(21), 6678-6691. https://doi.org/10.1016/ j.gca.2009.08.001

Deng, L., Fei, Y., Liu, X., Gong, Z., & Shahar, A. (2013). Effect of carbon, sulfur and silicon on iron melting at high pressure: Implications for composition and evolution of the planetary terrestrial cores. *Geochimica et Cosmochimica Acta*, *114*, 220-233. https://doi.org/10.1016/j.gca.2013.01.023

Dickey, J.O., Bender, P.L., Faller, J.E., Newhall, X.X., Ricklefs, R.L., Ries, J.G., et al. (1994). Lunar laser ranging: a continuing legacy of the Apollo program. *Science*, *265*(5171), 482-490. https://doi.org/10.1126/science.265.5171.482

Eggert, J.H., Weck, G., Loubeyre, P., & Mezouar, M. (2002). Quantitative structure factor and density measurements of high-pressure fluids in diamond anvil cells by x-ray diffraction: Argon and water. *Physical Review B*, *65*(17), p.174105. https://doi.org/10.1103/PhysRevB.65.174105

Fei, Y., Bertka, C.M., & Finger, L.W. (1997). High-pressure iron-sulfur compound, Fe3S2, and melting relations in the Fe-FeS system. *Science*, *275*(5306), 1621-1623. https://doi.org/10.1126/ science.275.5306.1621

Fei, Y., Li, J., Bertka, C.M., & Prewitt, C.T. (2000). Structure type and bulk modulus of Fe3S, a new iron-sulfur compound. *American Mineralogist*, *85*(11-12), 1830-1833. https://doi.org/10.2138/am-2000-11-1229

Fei, Y., & Brosh, E. (2014). Experimental study and thermodynamic calculations of phase relations in the Fe–C system at high pressure. *Earth and Planetary Science Letters*, *408*, 155-162. https://doi.org/10.1016/j.epsl.2014.09.044

Garcia, R.F., Gagnepain-Beyneix, J., Chevrot, S & Lognonné, P. (2011). Very preliminary reference Moon model. *Physics of the Earth and Planetary Interiors*, *188*(1-2), 96-113. https://doi.org/10.1016/j.pepi.2011.06.015

Garcia, R.F., Khan, A., Drilleau, M., Margerin, L., Kawamura, T., Sun, D., et al. (2019). Lunar seismology: An update on interior structure models. *Space Science Reviews*, *215*(8), 1-47. https://doi.org/10.1007/s11214-019-0613-y

Henry, L., Guignot, N., King, A., Giovenco, E., Deslandes, J.P., & Itié, J.P. (2022). In situ characterization of liquids at high pressure combining X-ray tomography, X-ray diffraction and X-ray absorption using the white beam station at PSICHÉ. *Journal of synchrotron radiation*, *29*(3). https://doi.org/10.1107/S1600577522003411

Hood, L.L., Mitchell, D.L., Lin, R.P., Acuna, M.H., & Binder, A.B. (1999). Initial measurements of the lunar induced magnetic dipole moment using Lunar Prospector magnetometer data. *Geophysical Research Letters*, *26*(15), 2327-2330. https://doi.org/10.1029/1999GL900487

Hubbell, J H., & Seltzer, S M. (1995). Tables of x-ray mass attenuation coefficients and mass energy-absorption coefficients 1 keV to 20 meV for elements z = 1 to 92 and 48 additional substances of dosimetric interest. United States.

Jing, Z., Wang, Y., Kono, Y., Yu, T., Sakamaki, T., Park, C., et al. (2014). Sound velocity of Fe–S liquids at high pressure: Implications for the Moon's molten outer core. *Earth and Planetary Science Letters*, *396*, 78-87. https://doi.org/10.1016/j.epsl.2014.04.015

Kilburn, M.R., & Wood, B.J. (1997). Metal–silicate partitioning and the incompatibility of S and Si during core formation. *Earth and Planetary Science Letters*, *152*(1-4), 139-148. https://doi.org/10.1016/S0012-821X(97)00125-8

King, A., Guignot, N., Henry, L., Morard, G., Clark, A., Le Godec, Y., et al. (2022). Combined angular and energy dispersive diffraction: optimized data acquisition, normalization and reduction. *Journal of Applied Crystallography*, *55*(2). https://doi.org/10.1107/S1600576722000322

Knibbe, J.S., Rivoldini, A., Luginbuhl, S.M., Namur, O., Charlier, B., Mezouar, M., et al. (2021). Mercury's Interior Structure Constrained by Density and P-Wave Velocity Measurements of Liquid Fe-Si-C Alloys. *Journal of Geophysical Research: Planets*, *126*(1), p.e 2020JE006651. https://doi.org/10.1029/2020JE006651

Komabayashi, T. (2014). Thermodynamics of melting relations in the system Fe-FeO at high pressure: Implications for oxygen in the Earth's core. *Journal of Geophysical Research: Solid Earth*, *119*(5), 4164-4177. https://doi.org/10.1002/2014JB010980

Konopliv, A.S., Binder, A.B., Hood, L.L., Kucinskas, A.B., Sjogren, W.L., & Williams, J.G. (1998). Improved gravity field of the Moon from Lunar Prospector. *Science*, *281*(5382), 1476-1480. https://doi.org/10.1126/ science.281.5382.1476

Kuskov, O.L., & Belashchenko, D.K. (2016). Thermodynamic properties of Fe-S alloys from molecular dynamics modeling: Implications for the lunar fluid core. *Physics of the Earth and Planetary Interiors*, *258*, 43-50. https://doi.org/10.1016/j.pepi.2016.07.006

Kuskov, O.L., Kronrod, E.V., Matsumoto, K., & Kronrod, V.A. (2021). Physical Properties and Internal Structure of the Central Region of the Moon. *Geochemistry International*, *59*(11), 1018-1037. https://doi.org/10.1134/S0016702921110069

Kuwabara, S., Terasaki, H., Nishida, K., Shimoyama, Y., Takubo, Y., Higo, Y., et al. (2016). Sound velocity and elastic properties of Fe–Ni and Fe–Ni–C liquids at high pressure. *Physics and Chemistry of Minerals*, *43*(3), 229-236. https://doi.org/10.1007/s00269-015-0789-y

Lai, X., Chen, B., Wang, J., Kono, Y., & Zhu, F. (2017). Polyamorphic transformations in Fe-Ni-C liquids: Implications for chemical evolution of terrestrial planets. *Journal of Geophysical Research: Solid Earth*, *122*(12), 9745-9754. https://doi.org/10.1002/2017JB014835

Lognonné, P., Gagnepain-Beyneix, J., & Chenet, H. (2003). A new seismic model of the Moon: implications for structure, thermal evolution and formation of the Moon. *Earth and Planetary Science Letters*, *211*(1-2), 27-44. https://doi.org/10.1016/S0012-821X(03)00172-9

Lognonné, P., & Johnson, C. (2007). Planetary seismology. *Treatise on Geophysics*, *10*, 69-122.

Matsui, M., Parker, S.C., & Leslie, M. (2000). The MD simulation of the equation of state of MgO: Application as a pressure calibration standard at high temperature and high pressure. *American Mineralogist*, *85*(2), 312-316. https://doi.org/10.2138/am-2000-2-308

Matsui, M., Ito, E., Katsura, T., Yamazaki, D., Yoshino, T., Yokoyama, A., et al. (2009). The temperature-pressure-volume equation of state of platinum. *Journal of Applied Physics*, *105*(1), p.013505. https://doi.org/10.1063/1.3054331

Morard, G., Sanloup, C., Guillot, B., Fiquet, G., Mezouar, M., Perrillat, J.P., et al. (2008). In situ structural investigation of Fe-S-Si immiscible liquid system and evolution of Fe-S bond properties with pressure. *Journal of Geophysical Research: Solid Earth*, *113*(B10). https://doi.org/10.1029/ 2008JB005663

Morard, G., Garbarino, G., Antonangeli, D., Andrault, D., Guignot, N., Siebert, J., et al. (2014). Density measurements and structural properties of liquid and amorphous metals under high pressure. *High Pressure Research*, *34*(1), 9-21. https://doi.org/10.1080/08957959.2013.860137

Morard, G., Bouchet, J., Rivoldini, A., Antonangeli, D., Roberge, M., Boulard, E., et al. (2018). Liquid properties in the Fe-FeS system under moderate pressure: Tool box to model small planetary cores. *American Mineralogist: Journal of Earth and Planetary Materials*, *103*(11), 1770-1779. https://doi.org/10.2138/am-2018-6405

Nakamura, Y., Lammlein, D., Latham, G., Ewing, M., Dorman, J., Press, F., et al. (1973). New seismic data on the state of the deep lunar interior. *Science*, *181*(4094), 49-51. https://doi.org/10.1126/science.181.4094.49

Nakamura, Y., Latham, G., Lammlein, D., Ewing, M., Duennebier, F., & Dorman, J. (1974). Deep lunar interior inferred from recent seismic data. *Geophysical Research Letters*, *1*(3), 137-140. https://doi.org/10.1029/GL001i003p00137

Nishida, K., Terasaki, H., Ohtani, E., & Suzuki, A. (2008). The effect of sulfur content on density of the liquid Fe–S at high pressure. *Physics and Chemistry of Minerals*, *35*(7), 417-423. https://doi.org/10.1007/s00269-008-0236-4

Nishida, K., Ohtani, E., Urakawa, S., Suzuki, A., Sakamaki, T., Terasaki, H., et al. (2011). Density measurement of liquid FeS at high pressures using synchrotron X-ray absorption. *American Mineralogist*, *96*(5-6), 864-868. https://doi.org/10.2138/am.2011.3616

O'neill, H.S.C. (1991). The origin of the Moon and the early history of the Earth—A chemical model. Part 1: The Moon. *Geochimica et Cosmochimica Acta*, *55*(4), 1135-1157. https://doi.org/10.1016/0016-7037(91)90168-5

Parker, M., Sanloup, C., Tronche, E.J., Perrillat, J.P., Mezouar, M., Rai, N., et al. (2010). Calibration of a diamond capsule cell assembly for in situ determination of liquid properties in the Paris–Edinburgh press. *High Pressure Research*, *30*(2), 332-341. https://doi.org/10.1080/ 08957959.2010.484283

Rai, N., & van Westrenen, W. (2014). Lunar core formation: new constraints from metal–silicate partitioning of siderophile elements. *Earth and Planetary Science Letters*, *388*, 343-352. https://doi.org/10.1016/ j.epsl.2013.12.001

Ricolleau, A., Fei, Y., Corgne, A., Siebert, J., & Badro, J. (2011). Oxygen and silicon contents of Earth's core from high pressure metal–silicate partitioning experiments. *Earth and Planetary Science Letters*, *310*(3-4), 409-421. https://doi.org/10.1016/j.epsl.2011.08.004

Sanloup, C., Guyot, F., Gillet, P., Fiquet, G., Mezouar, M., & Martinez, I. (2000). Density measurements of liquid Fe-S alloys at high-pressure. *Geophysical Research Letters*, *27*(6), 811-814. https://doi.org/10.1029/1999GL008431

Sanloup, C., Van Westrenen, W., Dasgupta, R., Maynard-Casely, H., & Perrillat, J.P. (2011). Compressibility change in iron-rich melt and implications for core formation models. *Earth and Planetary Science Letters*, *306*(1-2), 118-122. https://doi.org/10.1016/j.epsl.2011.03.039

Shibazaki, Y., Kono, Y., & Fei, Y. (2015). Microscopic structural change in a liquid Fe-C alloy of~ 5 GPa. *Geophysical Research Letters*, *42*(13), 5236-5242. https://doi.org/10.1002/2015GL064271

Shibazaki, Y., & Kono, Y. (2018). Effect of silicon, carbon, and sulfur on structure of liquid iron and implications for structure-property relations in liquid iron-light element alloys. *Journal of Geophysical Research: Solid Earth*, *123*(6), 4697-4706. https://doi.org/10.1029/2018JB015456

Shimizu, H., Matsushima, M., Takahashi, F., Shibuya, H., & Tsunakawa, H. (2013). Constraint on the lunar core size from electromagnetic sounding based on magnetic field observations by an orbiting satellite. *Icarus*, *222*(1), 32-43. https://doi.org/10.1016/j.icarus.2012.10.029

Shimoyama, Y., Terasaki, H., Ohtani, E., Urakawa, S., Takubo, Y., Nishida, K., et al. (2013). Density of Fe-3.5 wt% C liquid at high pressure and temperature and the effect of carbon on the density of the molten iron. *Physics of the Earth and Planetary Interiors*, *224*, 77-82. https://doi.org/10.1016/j.pepi.2013.08.003

Shimoyama, Y., Terasaki, H., Urakawa, S., Takubo, Y., Kuwabara, S., Kishimoto, S., et al. (2016). Thermoelastic properties of liquid Fe‐C revealed by sound velocity and density measurements at high pressure. *Journal of Geophysical Research: Solid Earth*, *121*(11), 7984-7995. https://doi.org/10.1002/2016JB012968

Steenstra, E.S., Lin, Y., Rai, N., Jansen, M., & van Westrenen, W. (2017a). Carbon as the dominant light element in the lunar core. *American Mineralogist*, *102*(1), 92-97. https://doi.org/10.2138/am-2017-5727

Steenstra, E.S., Lin, Y., Dankers, D., Rai, N., Berndt, J., Matveev, S., et al. (2017b). The lunar core can be a major reservoir for volatile elements S, Se, Te and Sb. *Scientific reports*, *7*(1), 1-8. https://doi.org/10.1038/s41598-017-15203-0

Terasaki, H., Nishida, K., Shibazaki, Y., Sakamaki, T., Suzuki, A., Ohtani, E., et al. (2010). Density measurement of Fe3C liquid using X-ray absorption image up to 10 GPa and effect of light elements on compressibility of liquid iron. *Journal of Geophysical Research: Solid Earth*, *115*(B6). https://doi.org/10.1029/2009JB006905

Terasaki, H., Rivoldini, A., Shimoyama, Y., Nishida, K., Urakawa, S., Maki, M., et al. (2019). Pressure and composition effects on sound velocity and density of core-forming liquids: Implication to core compositions of terrestrial planets. *Journal of Geophysical Research: Planets*, *124*(8), 2272-2293. https://doi.org/10.1029/2019JE005936

Toksöz, M.N., Dainty, A.M., Solomon, S.C., & Anderson, K.R. (1974). Structure of the Moon. *Reviews of geophysics*, *12*(4), 539-567. https://doi.org/10.1029/RG012i004p00539

Tsujino, N., Nishihara, Y., Nakajima, Y., Takahashi, E., Funakoshi, K.I., & Higo, Y. (2013). Equation of state of γ-Fe: Reference density for planetary cores. *Earth and Planetary Science Letters*, *375*, 244-253. https://doi.org/10.1016/j.epsl.2013.05.040

Tsuno, K., Frost, D.J., & Rubie, D.C. (2011). The effects of nickel and sulphur on the core–mantle partitioning of oxygen in Earth and Mars. *Physics of the Earth and Planetary Interiors*, *185*(1-2), 1-12. https://doi.org/10.1016/j.pepi.2010.11.009

Viswanathan, V., Rambaux, N., Fienga, A., Laskar, J., & Gastineau, M. (2019). Observational constraint on the radius and oblateness of the lunar core‐mantle boundary. *Geophysical Research Letters*, *46*(13), 7295-7303. https://doi.org/10.1029/2019GL082677

Weber, R.C., Lin, P.Y., Garnero, E.J., Williams, Q., & Lognonné, P. (2011). Seismic detection of the lunar core. *science*, *331*(6015), 309-312. https://doi.org/10.1126/science.1199375

Wieczorek, M.A., Jolliff, B.L., Khan, A., Pritchard, M.E., Weiss, B.P., Williams, J.G., et al. (2006). The constitution and structure of the lunar interior. *Reviews in mineralogy and geochemistry*, *60*(1), 221-364. https://doi.org/10.2138/rmg.2006.60.3

Williams, J.G., Konopliv, A.S., Boggs, D.H., Park, R.S., Yuan, D.N., Lemoine, F.G., et al. (2014). Lunar interior properties from the GRAIL mission. *Journal of Geophysical Research: Planets*, *119*(7), 1546-1578. https://doi.org/10.1002/2013JE004559

Xu, F., Morard, G., Guignot, N., Rivoldini, A., Manthilake, G., Chantel, J., et al. (2021). Thermal expansion of liquid Fe-S alloy at high pressure. *Earth and Planetary Science Letters*, *563*, p.116884. https://doi.org/10.1016/j.epsl.2021.116884

Zhao, B., Morard, G., Boulard E., Boccato S., Siersch, N., Rivoldini, A., et al. (2022). Local structure and density of liquid Fe-C-S alloys at Moon's core conditions [Dataset]. *Zenodo*. http://doi.org/10.5281/zenodo.7030984

Zhao, Y., Von Dreele, R.B., Weidner, D.J., & Schiferl, D. (1997). P-V-T Data of hexagonal boron nitride h BN and determination of pressure and temperature using thermoelastic equations of state of multiple phases. *International Journal of High Pressure Research*, *15*(6), 369-386. https://doi.org/10.1080/08957959708240481